

**SOLVOTHERMAL LIQUEFACTION OF ORANGE PEELS AND
CATALYTIC UPGRADING OF BIOCRUDE INTO TRANSPORTATION
FUEL OVER A HYBRID CATALYST**

Ishaq Kariim

**A Thesis Submitted in Fulfilment of the Requirements for the Degree of Doctor of
Philosophy in Materials Science and Engineering of the Nelson Mandela African
Institution of Science and Technology**

Arusha, Tanzania

August, 2024

ABSTRACT

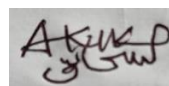
The efficient valorization of biomass for energy-derived biocrudes is essential for effective waste management. However, the production of biocrudes with high energy and reduced oxygen contents during the liquefaction process requires further improvement. This study investigates the impact of reaction temperature, residence time, and ratio of ethanol to acetone on the energy compositions and bio-product's yield enhancement were investigated under non-catalytic and catalytic process with further upgrading. The biocrudes obtained via the non-catalytic liquefaction were characterized for elemental composition, bio-oil compositions, functional group, molecular weight and thermal stability to understand the effects of process parameters on the biocrudes' compositions. An improved bio-oil with High Heating Value (HHV) (38.18 MJ/kg) and lower oxygen: carbon (O/C) ratio (0.11) were obtained at 430 °C, 35 min and 50% ethanol with a significant boost in the enhancement factor, deoxygenation, and percentage hydrogenation of 2.63, 36.88%, and 77.87%, respectively. The presence of ketones with composition of 32.58 area% suggests the needs for the removal of oxygen from the bio-oil. Using a central composite design (CCD), catalyst dosage (3-6 wt.%) and reaction temperature (330-430°C) were optimized, maintaining constant orange feedstock weight (10g), reaction time (15 minutes), and a solvent ratio of 3:1 (acetone to ethanol). Optimal biofuel yield (71.09 wt.%), solid residue (28.18 wt.%), biomass conversion (71.82 wt.%), and gas yield (40.14 mL/g) were achieved at 430°C and 3 wt.% catalyst loading. The Fe/CNSs catalysts possess high selectivity to acid formation. High correlation coefficients indicated the model's strong fit with experimental data. The hydrodeoxygenation (HDO) of cyclohexanone under both catalytic and non-catalytic conditions involved mechanisms such as hydrogenation, decarboxylation, decarbonylation, and dehydration. The NiCeMo catalysts shows an even particle dispersion where 11.3 area % of hydrocarbon and highest conversion of ketones and phenols were obtained. However, the performance of NiCeMo catalysts for HDO was hampered by the Guerbet reaction, which led to the formation of side products which are primarily alcohols. Modifying the acidity and using water as a solvent could potentially increase the HHV of the biofuel hence, promote the usage for transportation purposes. Biofuel produced through the non-catalytic process demonstrated a higher energy value of 38.18 MJ/kg, highlighting orange peels as a viable renewable energy resource.

DECLARATION

I, Ishaq Kariim, do hereby declare to the Senate of the Nelson Mandela African Institution of Science and Technology that this thesis titled “*Solvothermal Liquefaction of Orange Peels and Catalytic Upgrading of Biocrude into Transportation Fuel over Hybrid Catalyst*” is my own original work and that it has neither been submitted nor being concurrently submitted for degree award in any other institution.

Ishaq Kariim

26/08/2024



Candidate name

Date

Signature

The above declaration is confirmed by:

Prof. Thomas Kivevele

26/08/2024



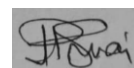
Supervisor 1

Date

Signature

Prof. Hulda Swai

26/08/2024



Supervisor 2

Date

Signature

Prof. In-Gu Lee

26/08/2024



Supervisor 3

Date

Signature

COPYRIGHT

This thesis is copyright material protected under the Berne Convention, the Copyright Act of 1999 and other international and national enactments, in that behalf, on intellectual property. It must not be reproduced by any means, in full or in part, except for short extracts in fair dealing; for researcher private study, critical scholarly review or discourse with an acknowledgement, without written permission of the Deputy Vice-Chancellor for Academic, Research and Innovation, on behalf of both the author and the Nelson Mandela African Institution of Science and Technology.

CERTIFICATION

The undersigned certify that they have read and hereby recommend for acceptance by the Senate of the Nelson Mandela African Institution of Science and Technology a thesis titled “*Solvothermal Liquefaction of Orange Peels and Catalytic Upgrading of Biocrude into Transportation Fuel over Hybrid Catalyst*” in fulfilment of the requirements for the Degree of Doctor of Philosophy in Materials Science and Engineering (Energy Materials) at Nelson Mandela African Institution of Science and Technology, Arusha Tanzania.

Prof. Thomas Kivevele

26/08/2024



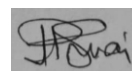
Supervisor 1

Date

Signature

Prof. Hulda Swai

26/08/2024



Supervisor 2

Date

Signature

Prof. In-Gu Lee

26/08/2024



Supervisor 3

Date

Signature

ACKNOWLEDGEMENTS

All powers and adorations belong to Allah, the omnipotent and omniscience who through His mercies, the PhD program was successfully completed. I thank Him for his guidance and protection throughout my research activities to completion.

I would like to express my deepest gratitude to the Partnership for Skills in Applied Sciences, Engineering and Technology - Regional Scholarship and Innovation Fund (PASET-RSIF) for sponsoring my PhD studies and for the Federal University of Technology, Minna, Nigeria for granting me the fellowship to undertake this study. Your support has been instrumental in allowing me to pursue my academic and research goals. I am also profoundly thankful to the Nelson Mandela African Institution of Science and Technology (NM-AIST) for offering me admission and providing an enabling environment for my research. The resources, guidance, and facilities available at NM-AIST have been crucial to the progress and success of my work.

I would like to express my deepest gratitude to Prof. Thomas Kivevele, Prof. Hulda Swai, and Prof. In-Gu Lee for their invaluable guidance, support, and encouragement throughout my PhD research. Their expertise and insightful advice have been instrumental in shaping this work, and their unwavering commitment to my academic and professional development has been truly inspiring. I am immensely grateful for the time and efforts they have devoted in supervising my research, and for their continuous support in overcoming the challenges encountered along the way. Thank you for making this journey a rewarding and enriching experience.

I am profoundly grateful to my lovely wife, Mrs. Abdulkariim Ruqayat Oyenike for her unwavering patience, understanding, and support throughout my PhD journey. Your strength and resilience in shouldering the responsibilities of taking care of my children during my absences have been extraordinary. Thank you for your love, encouragement, and sacrifices, which have been the cornerstone of my success. This achievement would not have been possible without you by my side- my 'mentor' (ori re wa ni'be). To my second wife, Mrs. Aishat Idowu Omolola, your patience, endurance, and understanding have been truly remarkable. Words cannot fully express my gratitude for your perseverance and unwavering support throughout this journey. Your contributions have been invaluable, and I am deeply thankful for everything you have done.

I would like to extend my heartfelt gratitude to my children, Abdullah Ishaq Abdulkariim, Maryam Ishaq Abdulkariim, Muhammad Ishaq Abdulkariim, Khadijah Ishaq Abdulkariim, Rufaydah Ishaq Abdulkariim, and my ‘Mama’ Dudu; Maryam Jimoh for their incredible endurance and understanding throughout my PhD period. Your patience and support during my absences have meant the world to me, even though being away from you felt like a bittersweet necessity. Thank you for your love, resilience, and for making this journey possible.

I would like to extend my sincere appreciation to my fellow PASET-RSIF scholars, who are too numerous to mention individually, and my lab mates at KIER, South Korea. Special thanks to Dr. Wajahat Kazmi Waheed and Wasi Syed Mohamad for their invaluable contributions through rigorous knowledge sharing and advice. Your support, collaboration, and friendship have greatly enriched my research experience. Thank you for your encouragement and insightful discussion.

I would like to express my deepest gratitude to my father, Mallam Abdulkariim Adigun, and my mother, Hajia Abdulkarim Amudat Aduke, for their unwavering dedication in providing me with a strong foundation of knowledge and their constant guidance throughout my life. Your support, encouragement, and sacrifices have been instrumental in my academic journey. Thank you for instilling in me the values of perseverance and hard work. This achievement would not have been possible without your love and support. May Allah grant both of you Firdaus (Aaaamin).

DEDICATION

This thesis is dedicated with deep gratitude to the memory of my beloved parents, who passed away during the final stage of my PhD journey.

TABLE OF CONTENTS

ABSTRACT.....	i
DECLARATION	ii
COPYRIGHT.....	iii
CERTIFICATION	iv
ACKNOWLEDGEMENTS.....	v
DEDICATION.....	vii
TABLE OF CONTENTS.....	viii
LIST OF TABLES.....	xii
LIST OF FIGURES	xiv
LIST OF ABBREVIATIONS AND SYMBOLS	xviii
CHAPTER ONE	1
INTRODUCTION	1
1.1 Background of the Study.....	1
1.2 Statement of the Problem.....	5
1.3 Rationale of the Study	6
1.4 Research Objectives	6
1.4.1 General Objective.....	6
1.4.2 Specific Objectives.....	7
1.5 Research Questions	7
1.6 Significance of the Study	7
1.7 Delineation of the Study.....	8
CHAPTER TWO	10
LITERATURE REVIEW	10
2.1 Introduction.....	10
2.2 Supercritical Solvents.....	11
2.2.1 Physical Properties of Supercritical Ethanol and Acetone.....	11

2.3	Biomass as Feedstock for Biofuel Production	14
2.3.1	Biomass Conversion	16
2.3.2	Crude Bio-oil.....	21
2.3.3	Heavy Fuel Oil	24
2.4	Effects of Bio-oil Physiochemical Properties on Biofuel Performance.....	24
2.5	Homogenous and Heterogenous STL Process	28
2.5.1	Homogeneous Catalytic Process	28
2.5.2	Heterogeneous Catalytic Process	31
2.6	Upgrading of Crude Bio-oil	32
CHAPTER THREE		35
MATERIALS AND METHODS.....		35
3.1	Materials.....	35
3.2	Proximate Analyses of the Orange Peels	35
3.2.1	Determination of Moisture Content (MC)	35
3.2.2	Determination of Ash Content (ACi).....	36
3.2.3	Determination of Volatile Matter (VM).....	36
3.2.4	Determination of Fixed Carbon (FC).....	37
3.2.5	Evaluation of the Lignocellulose Composition.....	37
3.3	Ultimate Analysis and HHV Evaluation	38
3.4	Solvothermal Liquefaction of Orange Peels	38
3.4.1	Biocrude Separation	39
3.5	Chemical Vapor Deposition.....	40
3.5.1	Development of Ni Supported Kaolin Catalyst	40
3.5.2	Development of Carbon Nanosphere and Purification	41
3.5.3	The Fe/CNSs Development.....	41
3.6	Monometallic Ni, Fe, Zn and Ce Development over Biochar Support.....	41
3.6.1	Hydrodeoxygenation (HDO) of Cyclohexanone and Crude Bio-oil	42

3.6	Synthesis of ZSM-5	42
3.6.1	Development of NiCeMo and NiCeMo Supported CNSs and IHC.....	43
3.7	Characterization Techniques	44
CHAPTER FOUR.....		46
RESULTS AND DISCUSSION		46
4.1	Physiochemical Properties of the Orange Peels.....	46
4.2	Non-Catalytic STL	47
4.2.1	Effect of Reaction Temperature on Bio-Products' Yield.....	47
4.2.2	Effect of Reaction Time on Bio-Products' Yield.....	49
4.2.3	Effect of Solvent Ratio on Bio-Products Yield.....	51
4.3	Effect of Reaction Conditions on Biocrudes' Compositions	52
4.3.1	Effects of Reaction Temperature on Biocrude's Compositions.....	52
4.3.2	Effects of Reaction Time on Biocrude's Compositions.....	54
4.3.3	Effects of Solvent Ratio on Biocrude's Compositions	55
4.4	Energy Composition and Van-Krevelen Plot.....	57
4.5	Biocrude's Properties Correlation.....	59
4.5.1	Combustion and Molecular Weight Distribution Analysis of Biocrudes ...	63
4.5.2	Functional Groups in the Produced Biocrudes.....	67
4.6	Reaction Mechanisms and Pathways for the Non-Catalytic STL of Orange Peels	72
4.7	Catalytic STL of Orange Peels over Fe/CNSs Catalysts	72
4.7.1	Characterization of the Produced Catalysts	72
4.7.2	Optimization of Catalytic STL using Central Composite Design.....	78
4.7.3	The RSM Analysis of the Fe/CNSs Catalyzed HTL of Orange Peels	80
4.7.4	Analysis of Variance of the Developed Model	83
4.7.5	Desirability Test.....	89
4.8	Bio-crude Characterization	91
4.8.1	Compositional Analysis and Fuel Characteristics of Biocrudes	91

4.8.2	Elemental and Heating Value of Biocrudes	93
4.8.3	Total Acid Number (TAN) and Water Content of the Biocrude Produced	94
4.8.4	Functional Groups Analysis	95
4.8.5	Mechanisms of Biocrude Formation through Catalytic STL Process.....	97
4.8.6	Surface Morphology of the Solid Residue	98
4.9	Cyclohexanone Upgrading.....	100
4.9.1	Non-catalytic HDO of Cyclohexanone	100
4.9.2	Monometallic Catalysts' Characterization	110
4.9.3	Catalytic HDO of Cyclohexanone	115
4.9.4	Functional Groups Identification of the Biofuel Produced	121
4.9.5	Reaction Pathways for the Cyclohexanone Upgrading.....	126
4.10	The HZSM-5, In-situ HZSM-5/CNSs (IHC) and NiCeMo Supported IHC and CNSs Characterization	128
4.10.1	Characterization of HZSM-5 and IHC Support	128
4.11	The HDO of Crude Biofuel Over NiCeMo Supported IHC and CNSs Supports	149
CHAPTER FIVE		158
CONCLUSION AND RECOMMENDATIONS		158
5.1	Conclusion	158
5.2	Recommendations	160
REFERENCES		162
RESEARCH OUTPUTS.....		188

LIST OF TABLES

Table 1:	Feedstocks' descriptions of various generational categories of biofuels	16
Table 2:	Different thermochemical conversion routes of biomass to produce light chemicals and liquid biofuels (Brand <i>et al.</i> , 2013).....	17
Table 3:	Classification of hydrothermal process according to conversion temperature (Biller & Ross, 2016).....	18
Table 4:	Products categories of bio-oil and their respective compounds (Zhang & Zhang, 2019).....	22
Table 5:	Comparison of bio-oil and conventional fuels (Hsuan <i>et al.</i> , 2019; Kazmi <i>et al.</i> , 2024; Osman <i>et al.</i> , 2021; Yan, 2019; Uhler <i>et al.</i> , 2016)	23
Table 6:	Physiochemical characteristics of bio-oil derived from varieties of biomass feedstocks	27
Table 7:	Effects of heterogeneous catalysts on the biocrude obtained via HTL process of biomass feedstocks	34
Table 8:	Main characteristics properties of orange peels on dry basis (db) (w/w%)	46
Table 9:	Elemental analysis of biocrudes produced at different reaction conditions	56
Table 10:	The TGA result of some selected biocrude based on HHV	65
Table 11:	Peaks assignment on the effects of process parameters on the biocrude functional groups	70
Table 12:	Design matrix for the optimization process of temperature and catalyst loading and their respective responses	79
Table 13:	Response transformation and model fittings	80
Table 14:	The ANOVA of the surface response model for the catalytic HTL products yield	84
Table 15:	Statistical parameters for the catalytic HTL products	85
Table 16:	Compounds identification from the biocrude obtained at 330 °C and 430 °C reaction temperature at 3 wt.% of Fe/CNSs catalyst loading	91
Table 17:	Elemental analysis and heating value of the produced biocrude.....	93
Table 18:	The FTIR Peaks assignment extracted from Fig. 28	97
Table 19:	Comparison of the biocrude's composition and HHV for catalytic and non-catalytic STL process	100

Table 20:	Non-catalytic upgrading of cyclohexanone in the presence of ethanol as solvent at various reaction conditions.....	108
Table 21:	Physiochemical properties of the developed catalysts	114
Table 22:	Effect of catalysts on the cyclohexanone conversion at constant catalyst loading of 3g, EtOH of 90g, 10bar nitrogen and 300rpm agitation.....	120
Table 23:	The FTIR peaks assignment from the FTIR spectral of the biofuel obtained from Fig. 37.....	122
Table 24:	The FTIR peaks assignment from the FTIR spectral of the biofuel obtained from Fig. 38.....	124
Table 25:	Structural properties of the synthesized HZSM-5 and developed metal supported CNSs and hybrid	134
Table 26:	Acidic properties of the developed NiCeMo supported IHC and CNSs catalysts	148
Table 27:	Thermal properties of the developed NiCeMo supported IHC and CNSs catalysts	149
Table 28:	Effects of residence time on the compositions and the yield of the upgraded biofuel obtained at different catalysts (CNSs, HZSM-5, IHC, NiCeMo_IHC and NiCeMo_CNSs) and residence time	152
Table 29:	Elemental analysis and the HHV value of the upgraded biofuel	153
Table 30:	The FTIR peaks assignment from the FTIR spectral of the biofuel obtained from Fig. 54.....	157

LIST OF FIGURES

Figure 1:	Proposed hydrogen donation and hydroxylalkylation pathways of ethanol (scheme 1= by Nakagawa <i>et al.</i> (2003) and scheme 2 and 3 were proposed by Ross and Blessing (1979).....	14
Figure 2:	(a) Feedstocks for biofuel production from different generations (Neto <i>et al.</i> , 2019; Singh <i>et al.</i> , 2023) (b) HHV-H/C _{eff} map for solid, liquid, and gaseous fuels (Zhang, 2016).....	15
Figure 3:	Solid wastes treatment routes into bioenergy productions (Singh <i>et al.</i> , 2023)...	17
Figure 4:	(a) Main kinds of chemical bonds present in lignin (b) Monolignols and its respective lignin structural units (do Couto Fraga <i>et al.</i> , 2021)	19
Figure 5:	Reaction pathways for liquid bio-oil production using pyrolysis process of biomass feedstock (Van Nam <i>et al.</i> , 2020).....	19
Figure 6:	Reaction pathways for lignocellulose biomass conversion (Ratnasari <i>et al.</i> , 2020)	20
Figure 7:	Combined catalysts mix (Bianasari <i>et al.</i> , 2024).....	32
Figure 8:	Experimental set-up for the STL of orange peels in a stainless-steel autoclave ..	44
Figure 9:	The TGA/DTG analysis of the orange peels feedstock in N ₂ environment	47
Figure 10:	Effects of reaction temperature on bio-products' yield.....	48
Figure 11:	Effects of residence time on bio-products' yield.....	50
Figure 12:	Effects of solvent ratio on bio-products' yield.....	51
Figure 13:	Effects of reaction temperature biocrude compositions	52
Figure 14:	Effects of residence time on biocrude compositions.....	54
Figure 15:	Effects of solvent ratio on biocrude compositions	55
Figure 16:	Inherent biocrude properties relative to (a) reaction temperature (b) residence time (c) solvent ratio and (d) Van-Krevelen plot	57
Figure 17:	Correlations between: (a,c, e) physicochemical properties and (b,d,f) energy properties against carbon element index	62
Figure 18:	(a) The TGA and (b) DTG (c-f) GPC plots of biocrudes obtained with the highest HHV	64

Figure 19: The FTIR Spectral of the produced biocrude considering the effect of (a) temperature (b) residence time and (c) solvent ratio (d) proposed reaction pathways for the non-catalytic solvothermal liquefaction of orange peels into biocrude	69
Figure 20: Surface morphology of (a-b) as-received CNSs and (c-d) Fe supported carbon nanosphere.....	73
Figure 21: Elemental mapping EDS analysis of the modified carbon nanospheres (a) Analyzed points and distribution of (b) Carbon materials (c) Fe dopant (d) Ni substrate and (e) elemental analysis	75
Figure 22: The FTIR spectral of the as-received and doped carbon nanosphere.....	76
Figure 23: The BET N ₂ Adsorption-desorption isotherms and the pore size distribution of (a) As-received CNSs and (b) Fe supported CNSs catalysts	77
Figure 24: Surface and contour plots showing the effects of temperature and catalyst loading on biocrude (a-b), solid residue (c-d), gas yield (e-f) and conversion (g-h)	81
Figure 25: Normal probability graph of residuals for the HTL product yield: (a) Biocrude (b) Solid residue (c) Gaseous product and (d) Conversion; predicted vs actual for (e) Biocrude (f) Solid residue (g) Gaseous product and (h) Conversion for orange peels	88
Figure 26: Desirability plots using numerical optimization	90
Figure 27: The GC-MS Compositional classifications of the organic contents from the biocrudes	92
Figure 28: The FTIR spectra of (a) Orange peels (b) solid residue and (c) biocrude; (b-c) obtained after the catalytic STL of orange peels	95
Figure 29: Mechanism of orange peels conversion over Fe/CNSs into biocrude.....	98
Figure 30: Surface morphology of the obtained solid residue at the optimum conditions	99
Figure 31: Effects of process parameters (a) temperature; (b) residence time; (c) formic acid at 0h; (d) formic acid at 1h (e) feed loading @ 0bar and (d) feed loading at 10bar on bio-oil yield and water content.....	102
Figure 32: Effects of process parameters (a) temperature; (b) residence time; (c) formic acid at 0h; (d) formic acid at 1h (e) feed loading @ 0bar and (d) feed loading @ 10bar on biofuel composition and cyclohexanone conversion.....	104
Figure 33: The XRD crystallography of (a) Biochar (b) Ni (c) Ce (d) Zn and (e) Fe supported biochar	111
Figure 34: (a) The N ₂ adsorption-desorption and (b) Pore diameter distribution of the developed catalysts and the biochar support	113

Figure 35: The FTIR spectra of the developed monometallic catalysts and the parent biochar	114
Figure 36: Effects of transition metals on yield, total ketone conversion, cyclohexanone conversion and cyclohexanol selectivity over (a-b) Ni (c-d) Ce (e-f) Zn and (g-h) Fe supported biochar	117
Figure 37: The FTIR spectra of the produced biofuel from the non-catalytic upgrading of cyclohexanone	121
Figure 38: The FTIR spectra of the produced bio-oil from the catalytic upgrading of cyclohexanone	123
Figure 39: Reaction mechanisms for the catalytic and non-catalytic conversion of cyclohexanone	127
Figure 40: The XRD Spectral of the synthesized HZSM-5 at various reaction conditions.	129
Figure 41: (a) The N ₂ Adsorption-desorption isotherm and the (b) pore diameter distribution of various HZSM-5	132
Figure 42: The N ₂ Adsorption-desorption isotherm and the (b-c) pore diameter distribution of 2b_HZS(10)_16h, IHC, NiCeMo_IHC and NiCeMo_CNSs.....	135
Figure 43: The XRD Pattern of the synthesized catalysts (reduced and calcined) and the support material (IHC)	136
Figure 44: The HRSEM images of (a-b) 2b_HZS(10)_16h (c-d) 2c_HZS(10)_24h and (e-f) 2d_HZS(10)_48h.....	138
Figure 45: The HRSEM and Elemental composition of (a-b) IHC (c-d) NiCeMo_IHC and (e-f) NiCeMo_CNSs catalysts	140
Figure 46: Elemental mapping of (a) the constituent elements and (b) the NiCeMo on the IHC support.....	141
Figure 47: Elemental mapping of (a) the constituent elements and (b) the NiCeMo on the CNSs support.....	142
Figure 48: The HRTEM images of NiCeMo supported (a-b) IHC and (c-d) CNSs catalysts	143
Figure 49: The XPS Spectra of NiCeMo supported IHC and CNSs (a-b) Survey scans (c-d) Ni 2p ₃ and Ce 3d (e-f) Mo 3d	145
Figure 50: The NH ₃ -TPD profiles of the developed NiCeMo supported IHC and CNSs supports	147
Figure 51: The TGA/DTG profile of the developed catalysts	149

Figure 52: Effects of residence time on the compositions and the yield of the upgraded biofuel obtained at different catalysts (a) CNSs (b) HZSM-5 (c) IHC (d) NiCeMo_IHC and (e) NiCeMo_CNSs)	151
Figure 53: Gas composition obtained over the (a) NiCeMo_IHC and (b) NiCeMo_CNSs catalysts	155
Figure 54: The FTIR spectra of the upgraded biofuel	156

LIST OF ABBREVIATIONS AND SYMBOLS

AC	Ash Content
Al-MCM-41	Mobil Composition of Matter No. 41 (Aluminum-Based)
CCD	Central Composite Design
CEI	Carbon Element Index
CHN	Carbon, Hydrogen and Nitrogen
CM	Chloromethane
CNSs	Carbon Nanosphere
CNTs	Carbon Nanotubes
CR	Carbon Recovery
CRE	Carbon Recovery Efficiency
DO	Deoxygenation
DTG	Derivative Thermal Analysis
EF	Enhancement Factor
ER	Energy Recovery
FC	Fixed Carbon
FID	Field Emission Detector
FTIR	Fourier Transform Infrared Spectrophotometer
FTS	Fischer-Tropsch Synthesis
GC-MS	Gas Chromatography -Mass Spectroscopy
GHG	Greenhouse Gases
GPS	Gel Permeation Spectroscopy
HCs	Hydrocarbons
HDO	Hydrodeoxygenation
HFO	Heavy Fuel Oil
HG	Hydrogenation

HHV	High Heating Values
HMF	5-(Hydroxymethyl)Furfural
HRSEM	High-Resolution Scanning Electron Microscope
HRTEM	High-Resolution Transmission Electron Microscope
HTL	Hydrothermal Liquefaction
HZSM-5	H-ZSM-5 is the Protonic Type or H Form Of ZSM-5
ISO	International Standards Organization
IUPAC	International Union of Pure and Applied Chemistry
LCA	Life Cycle Assessment
MAHs	Monoaromatic Hydrocarbons
MC	Moisture Content
MPa	Mega Pascals
MSD	Mass Spectroscopy Detector
N-Cmpds	Nitrogen Compounds
NH ₃ -TPD	Ammonia Temperature Programmed Desorption
PAH	Polycyclic Aromatic Hydrocarbons
PEG	Polyethylene Glycol
SC	Solvothermal Carbonization
SCF	Supercritical Fluids
SDA	Structural Directing Agent
SG	Solvothermal Gasification
SSG	Supercritical Solvent Gasification
STL	Solvothermal Liquefaction Process
TCD	Thermal Conductivity Detector
TEA	Techno-Economic Analysis
TEAOH	Tetraethylammonium Hydroxide

TGA	Thermogravimetric Analysis
THF	Tetrahydrofuran
ULO	Used Lubricating Oil
VM	Volatile Matter
XRD	X-Ray Diffraction
ZSM-5	Zeolite Socony Mobil Number 5

CHAPTER ONE

INTRODUCTION

1.1 Background of the Study

Energy demand and environmental pollution have been a major challenge in the present world due to the overdependence on the conventional fuel (Syed *et al.*, 2024; Wei *et al.*, 2019; Yang *et al.*, 2021). Several contributory factors have been identified to emit gaseous pollutants into the environment through burning of conventional energy resources (Martins *et al.*, 2019; Zhang *et al.*, 2016). The high dependency on conventional energy sources such as coal and petroleum has caused global concerns and the need for improved alternative fuels is gaining huge attention globally. According to the report published by Ritchie and Roser (2020), the emission of carbon dioxide into the environment has the highest percentage of contribution to global climate change. Energy and environmental issues remain the major challenges to human being and the environment in this present decade. These challenges are on the rise due to the ever-increasing population and urbanization which have extensively increased the dependency on natural resources such as petroleum, natural gas and coal for transportation purposes (Klinger *et al.*, 2018). The finite reserves of fossil fuel coupled with the high environmental load due to the huge greenhouse gases emissions have characterized fossil fuels as non-renewable and non-energy sources. Therefore, a renewable and sustainable energy has received several attentions due to their tendency to providing a clean environment which is comparably free to inducing air pollutions.

The applications of renewable sources of energy have paved way for the remediation of greenhouse gases (GHG) emission and therefore combating the inherent challenges. Several renewable energies have been widely employed as an alternative energy source but the application of biomass feedstock has gained enormous attention. Orange, a family of citrus species is one of the major crops grown in Muhanza and Tanga district of Tanzania which contributes to about 75% of household and 70% of council's generated revenue and this has resulted to Tanzania being ranked 6th in Africa as regards citrus producer. The oranges are always being processed into fruit juice through extraction process and huge quantity of peels are discharged into the surroundings as solid wastes (Divyabharathi & Subramanian, 2021). The presence of cellulose, lignin and hemicellulose in orange peel have positioned it as an excellent feedstock for biofuel production due to the possibilities of producing several

monomers and dimers through effective conversion techniques (Divyabharathi & Subramanian, 2021). Therefore, converting orange peel into valuable products like biofuel is crucial for reducing indiscriminate burning, which negatively impacts the ecosystem, while also promoting economic growth.

The conversion of orange peels into biocrude has been investigated by several researchers using various techniques (Aboagye *et al.*, 2017; Divyabharathi & Subramanian, 2021). Examples of such techniques includes pyrolysis and solvothermal liquefaction process (Ong *et al.*, 2019; Sun *et al.*, 2020). The application of solvothermal liquefaction approach has attracted attention of researchers and bioenergy experts due to its energy efficiency and product's distribution as compared to pyrolysis process. Solvothermal liquefaction (STL) is an excellent conversion route which has the ability to transform both wet and dried feedstocks into biocrude of improved calorific value and yield (Wądrzyk *et al.*, 2023). Although, the application of liquefaction approach has received numerous attentions due to its high energy efficiency, production of biocrudes with higher heating value (HHV) among others when compared to pyrolysis process (Ong *et al.*, 2019; Sun *et al.*, 2020). Recently, the optimization of orange peels conversion into biocrude via solvothermal liquefaction process has been reported where the effects of process parameters such as temperature, residence time and total solid loading were optimized to enhance the biocrude HHV (Divyabharathi & Subramanian, 2022). Low HHV of 32 MJ/kg was obtained which implies the presence of high composition of oxygenated compounds in the biocrude that hampered the overall quality of the biocrude. Hence, there is need to explore optimal reaction conditions that can enhance the HHV effectively and efficiently. The author observed a substantially high amount of aromatic compounds which are in the form of acids, esters and ketones-oxygenated compounds. These compositions observed from the biocrude composition through the GC-MS analysis suggest the unstable nature of the biocrude and the tendency for high acidity, corrosiveness of the biocrude during storage and tanks when stored. Hence, the development of a simple but smart approach for reducing the quantity of ketones and acids in the overall biocrude composition is required.

The determination of the optimal reaction conditions to enhance a tailor biocrude compositions is crucial for achieving economic feasibility, enhancing reactor design, and guaranteeing the production of high-quality biocrude in the context of sustainable energy approach. In this regard, it is necessary to consider the interactions between process parameters on the possible influence on the enhancement of biocrude quality throughout the STL process. The effects of

residence time and reaction temperature have been widely studied on several biomass materials while the insight into the synergetic effects of organic solvents (ethanol and acetone) on the HHV, molecular weight and combustion properties of biocrude are still missing in literature (Fernandes *et al.*; 2021; Wang *et al.*, 2019).

The fascinating characteristics of ethanol and acetone at supercritical conditions have made the search into the compositional mix an intriguing adventure during the liquefaction process (Malins, 2017; Park *et al.*, 2019; Tekin & Karagöz, 2013). The available literature on orange peels conversion were domicile in the regime of pyrolysis and hydrothermal liquefaction processes with low reported HHV, making it necessary to investigate the synergetic effects of sub/supercritical conditions of ethanol and acetone on the biocrude characteristics. The effects of ethanol and acetone ratio on the biomass conversion, yield and the composition of biocrudes on the liquefaction of waste hazelnut shell using sub- and supercritical solvents as a reaction medium have been reported by Demirkaya *et al.* (2019a). Through pyrolytic cleavage, the efficiency of ethanol at supercritical conditions enhances the direct liquefaction of biomass through hydrogen donation and thereby improve the overall biomass' conversion (Brand & Kim, 2015; Demirkaya *et al.*, 2019a). The characteristics of supercritical fluids which have rendered their suitability for improved product's selectivity during the solvothermal approach include the quicker mass and heat transfer rate, density resembling that of a liquid with enhanced dissolving capabilities, and gas-like diffusion and viscosity (Durak, 2019; Park *et al.*, 2019; Tao *et al.*, 2013). Hence, the investigation of dipolar aprotic (acetone) and polar protic (ethanol) solvents at supercritical conditions would enhance the solubility of the biomass's compositions (lignin, cellulose and hemicellulose), its intermediates and products, and improved percentage hydrogenation for biocrudes with high HHV, reduced acid, enhanced esterification reaction and reduced biocrudes' viscosity (Park *et al.*, 2019).

Therefore, combining the excellent properties of ethanol and acetone during the liquefaction process of orange peels would be a novel approach to obtaining high HHV biocrude and effective hydrodeoxygenation (HDO) pathway. Literature on the dependency of process variables (temperature, time, and the concentration of ethanol in acetone) at sub/supercritical conditions on the properties of biocrudes derived from orange peels in the absence of initial nitrogen supply is lacking. A non-catalytic approach for biomass upgrading into transportation fuels with reduced ketones and acid contents might not be so feasible and hence, the development of catalysts for upward upgrading of the biocrude into a more advanced fuel is

required. The high tendency of char formation with possible characteristics of hampering the catalysts' performance through pore blockage in a one-pot approach of biomass conversion and upgrading has necessitated the investigation of a two-stage approach. Hence, the selective development of catalysts for enhanced biofuel product is an important factor in biomass valorization into transportation fuel.

Several solid acid catalysts (catalysts that demonstrate acidic characteristics and are employed to enhance chemical reactions) has been reported to enhance the HDO process of oxygenated compounds such as ketones, phenol and acids in biocrudes (Kretzschmar *et al.*, 2024; Wang & Chen, 2017; Zormpa *et al.*, 2024). The solid acid catalysts possess surface acidic sites that are capable of donating protons to reactants, thus facilitating the HDO and esterification processes (Yun *et al.*, 2024). Examples of such catalysts that have been widely employed for biocrude and/or model compounds) upgrading include the silico-aluminates and transition metal oxides catalysts used in petrochemicals and petroleum refinery industries for fuels and fine chemicals production.

Zeolites, crystalline solids composed of three-dimensional microporous particles containing aluminum and silica, represent a typical example of silico-aluminates. They have been extensively studied in both industrial settings and laboratory-scale pilot plants for biofuel production (Arumugam *et al.*, 2021; Xue *et al.*, 2019; Zheng *et al.*, 2017). Properties such as acidic properties, pore structure (diffusivity enhancement), products selectivity (precision control), thermal stability (maintain a high structural properties without changes over a prolonged period of reusability), regenerability (several reusability circle), versatility (optimization of performance through modifications) have made zeolites a high valuable catalysts for biofuel upgrading (Kurnia *et al.*, 2017; Velaga *et al.*, 2021). The presence of unique pore structures in HZSM-5 (a type of zeolite) which could be tailored to selectively transport low molecular oxygenated compounds and enhance the conversion of intermediates has presented HZSM-5 an excellent catalyst for biocrude upgrading. Due to the presence of high acidic strength in HZSM-5 catalysts, the need to incorporate a neutral solid catalyst such as carbon nanosphere (CNS) has the tendency to retard the catalytic cracking potentials which reduces the carbon contents and HHV of the upgraded biofuel and while metal modifications could enhance the HDO of the biocrudes constituents.

Several metals has been widely employed including the noble and transition metals for enhanced HDO process during the biocrude upgrading (Guo *et al.*, 2022; Jeong *et al.*, 2017;

Nolte & Shanks, 2017; Ochoa *et al.*, 2020). The upgrading approach via the HDO approach is to reduce the overall oxygen contents in the biocrude, enhance the heating value and reduced the presence of larger molecular weight compounds.

In this present study, the effects of temperature, residence time and solvent ratio (ethanol to acetone) were investigated to establish the dependency of several biocrudes' properties on the process variables during the solvothermal liquefaction (STL) of orange peels feedstock in sub/supercritical conditions. The relationships between several physiochemical parameters and the energy related quantities were presented to understand the effect of severity of process conditions on biocrude's properties and to enable the best selection of process parameters which promotes high biocrudes' quality. To evaluate the effects of carbon nanospheres on the biocrude's properties, an optimization approach using central composite design (CCD). Also, the biocrude was further upgraded in supercritical ethanol over the developed metal doped catalysts. Reaction pathway for the solvothermal conversion of the orange feedstocks into biocrude through detailed considerations of the biocrudes' compositions was proposed. For the first time, in the absence of initial gas supply during the STL of orange peels, the dependency of enhancement factor, percentage deoxygenation, carbon recovery efficiency, percentage hydrogenation, carbon element index and energy recovery efficiency on process variables were established.

1.2 Statement of the Problem

The presence of high content of oxygenated compounds which accompany the biocrude obtained from STL process of biomass is a problem that affects its usage. This oxygenated compounds retards the direct applicability of the biocrude as direct fuel in a typical combustion engine for transportation purposes (Cheng *et al.*, 2017; Patil *et al.*, 2019). The oxygen contents in the form of an acids, aldehydes, esters and ketones causes corrosion during storage, pipelines and oxidation instability (Kumar, 2017). The presence of these compounds is associated with the formation of larger molecular weight compounds that are capable of catalysts deactivation through pore blockage and the overall mass flow limitation of reactants and products in the active sites during biocrude upgrading. The use of zeolite catalyst (ZSM-5), the most widely used catalyst in petrochemical industries are characterized with coke formation during the HDO process of large molecular compounds due to the presence of high acidity and microspore in the catalyst. The formation of polycyclic aromatic hydrocarbon has been characterized with the application of zeolites and hence, retards the use of zeolites without prior modification(s).

Therefore, this study seeks to address the presence of larger molecular oxygenated compounds in biocrude prior to upgrading and develop a robust catalyst that is capable of enhancing the HDO process in supercritical ethanol with low or no formation of polycyclic aromatic (coke). To address the presence of lower content of oxygenated compounds in biocrude including the reduction of acids, the adoption of bi-solvents (ethanol and acetone) at the supercritical condition is studied at various concentration, residence time and temperature in STL process. The obtained biocrude is then subjected to HDO reaction in the presence of modified and hybrid HZSM-5/CNSs.

1.3 Rationale of the Study

The growing global demand for transportation fuel, rising fuel costs, and concerns about greenhouse gas emissions in the face of a growing population have prompted the exploration of renewable, sustainable, and cost-effective energy alternatives. Bioenergy industries have greatly utilized several harvesting techniques for renewable energy production leading to the production of advanced and sustainable fuels for transportation purposes. Biomass is one of the unique renewable materials with high tendencies to producing high quality biocrude through adequate valorization techniques. Hence, the search for an alternative which is also sustainable and renewable energy sources from the valorization of orange peels would advert the looming contributory effects of indiscriminate burning and incineration in landfills. This approach would not only protect the environment from the greenhouse gases emission and ozone layer depletion resulted from the burning process but also generate a passive income to the local farmers and orange juice producing industries. In this regard, the valorization of orange peels in supercritical solvents under the STL process and the subsequent HDO in the presence of zeolite containing catalysts would advance the overall biocrude's properties for meeting the qualities for used in transportation industries. Hence, the research is aimed at producing liquid biofuel via two-stage valorization techniques in supercritical fluids.

1.4 Research Objectives

1.4.1 General Objective

To investigate the effects of process parameters on the STL of orange peels and catalytic upgrading of biocrude into transportation fuel over a hybrid catalyst.

1.4.2 Specific Objectives

- (i) To investigate the effects of reaction conditions such as residence time, temperature, catalyst loading and solvent's ratio on the STL of orange peels feedstock in supercritical fluids.
- (ii) To evaluate the effects of Ni, Ce, Fe and Zn supported biochar on the HDO of cyclohexanone.
- (iii) To examine the effects of Ni, Ce and Mo on the CNSs and CNSs/HZSM-5 catalysts' properties.
- (iv) To evaluate the catalytic performance of the developed NiCeMo supported CNSs and CNSs/HZSM-5 catalysts for HDO of biocrude in supercritical ethanol medium.

1.5 Research Questions

- (i) What are the effects of operating parameters on the non-catalytic STL of orange peels in supercritical fluid?
- (ii) What are the influences of Ni, Ce, Fe and Zn on the percentage HDO and cyclohexanone conversion?
- (iii) Could in-situ synthesis of HZSM-5 using CNSs as a growth controlling medium and the doping using NiCeMo improve the catalytic properties of the obtained catalysts?
- (iv) What is the impact of transition metals (NiCeMo) supported CNSs and CNSs/HZSM-5 on the HDO of biocrude obtained from the STL of orange peels?

1.6 Significance of the Study

Sustainable approaches to biofuel production through biomass valorization are gaining enormous attention for producing clean energy for the transportation sector. Orange peels, waste agricultural materials whose presence and traditional disposal methods endanger the environment, call for urgent valorization methods. This research focuses on the application of orange peels as feedstock in the STL process in supercritical fluids to produce biocrude and the onward HDO process for further upgrading in supercritical ethanol. The research adds value

to the bulk of orange peels obtained by local farmers and orange juice-producing factories, contributing to the overall economy and mitigating climate change.

1.7 Delineation of the Study

The study assesses the potential valorization of orange peels as an excellent candidate for producing high-quality biocrude in supercritical fluids using the thermochemical conversion technique (STL). Prior to valorization and the upgrading stage of this research, the characteristics and properties of orange peels, both in terms of ultimate and proximate quantities, were investigated on a dry basis. The influence of reaction conditions during both non-catalytic and catalytic approaches provides insights into the optimal parameters that favor the formation of high-quality biocrude. Additionally, the impact of transition metals on the conversion of cyclohexanone, a biocrude model compound, was studied before investigating the effects of metal-supported CNSs/HZSM-5 catalysts for the HDO of biocrude into transportation fuel. Using a 5-chapter categorization, this thesis is organized into five chapters. The background of the study, problem statement, research rationale, research objectives, research questions and the significance of the research are contained in Chapter one of this thesis. The second chapter which is tagged as Chapter two elucidate a critical review of existing literature ranging from the techniques for biomass valorization into biocrude, influence of reaction conditions on the biocrude selectivity and the role of transition metals on the HDO process of biocrude and its model compounds. The materials and methods were developed to align with the specific objectives of this study, constituting Chapter Three. This explicitly describes the lists of materials and chemicals required for this study, the process descriptions for some quantities' determination and the STL process including the biocrude recovery process and bio-products' yield determinations. Furthermore, the methodologies for carbon nanosphere, HZSM-5 and the in-situ CNSs/HZSM-5 synthesis are presented in this chapter including the doping with transition metals. The chapter further contains the study of the HDO reaction of cyclohexanone model compounds prior to the direct evaluation of catalysts on the upgrading of the obtained biocrude into transportation fuel. The presentation and discussion of results are contained in Chapter four. The effects of process parameters on both the catalytic and non-catalytic valorization of orange peels were presented and discussed. The characterization of the various catalysts and the possible implications on the HDO process. Chapter five entails the conclusion and the recommendations as observed from this study. The study is aimed at enhancing pre-biocrude qualities prior to upgrading process to retards the

associated challenges with catalysts performance due to the mass transport limitations as a result of larger molecular weight compounds. All the biocrudes obtained throughout the non-catalytic STL approach were analyzed while the gas compositions as well as biochar properties and catalysts recovery and reusability were not addressed in this research; a limitation of this study. This further presents an opportunity for further researches in the area of liquid biofuel and possible use of the biochar as adsorbents for adsorption processes. In summary, this study focuses solely on the catalytic and non-catalytic STL of orange peels in supercritical fluids and the HDO of the biocrude using HZSM-5 based catalysts. Because of the lab-scale approach employed, there is a need for additional research to delve into the techno-economic analysis (TEA) and life cycle assessment (LCA) of a biocrude production plant utilizing orange peels as feedstock.

CHAPTER TWO

LITERATURE REVIEW

2.1 Introduction

The utilization of STL techniques for biomass conversion into renewable fuel can be traced back to the early 1990s. Unlike the pyrolysis process, which relies on dried biomass to achieve high yield fuels, STL is suitable for wet feedstocks. Since the research conducted by the Pittsburgh Energy Research Centre in 1970, numerous studies have investigated and refined techniques aimed at enhancing STL performance in biomass conversion. One of the primary advantages of STL over pyrolysis is its ability to process biomass feedstocks without requiring prior drying (Biller & Ross, 2016). STL involves the production of bio-oil from an aqueous slurry of biomass or organic materials, occurring within a temperature range of 280-370°C (lower than pyrolysis), under elevated pressure of 10-25 MPa, and in the presence of a solvent (Biller & Ross, 2016). According to Biller and Ross (2016), this biomass conversion process into crude bio-oil mirrors the natural pathways of fossil fuels formation at high temperatures and pressures, albeit naturally occurring underground. In the STL technique, the primary product is liquid bio-oil, accompanied by solid and gaseous by-products.

The drawbacks associated with crude bio-oil include its elevated levels of oxygenated compounds, which lead to reduced heating values, heightened oxidative instability, increased susceptibility to corrosion, and emissions of harmful pollutants such as volatile organic compounds, nitrogen oxides, and particulate matter. Additionally, these oxygenated compounds can result in compatibility issues, rendering bio-oil less suitable as a drop-in fuel option. The elevated oxygen content present in the bio-oil produced during thermochemical conversion originates from the biomass itself, which typically contains approximately 40-50 wt% oxygen. This abundance of oxygen contributes to reducing the overall heating values of the bio-oil. Supercritical STL process of biomass valorization aids in providing a suitable reaction conditions for both the conversion process as well as the provision of in-situ hydrogen for hydrodeoxygenation process (Kazmi *et al.*, 2023; Park *et al.*, 2019). The hydrogen produced at the supercritical conditions favors the production of phenolic monomers through the β -O-4 cleavage of the lignin complexes hence, increases the bio-oil yield as well as the quality. During the HDO process, the oxygen atoms are removed from the bulk of the constituents in the form of H₂O, CO₂ and CO which results in the production of liquid fuels and fine chemicals (Dyer

et al., 2022; Wang *et al.*, 2014). The potential of several organic solvents other than sub and supercritical water have been widely reported to enhance the biomass conversion into a high-quality bio-oil. Such organic solvents include the ethanol, methanol, propanol, acetone, phenol and toluene (Brand *et al.*, 2013; Park *et al.*, 2019). Introducing metal-supported catalysts with high selectivity is essential for improving the overall upgrading of bio-oil through a series of reactions, including hydrogenation, hydrodeoxygenation, decarboxylation, and decarbonylation (Janampelli & Darbha, 2018; Kubička *et al.*, 2014; Nguyen *et al.*, 2021).

2.2 Supercritical Solvents

Supercritical fluids (SCF) are species that, when subjected to and maintained at high temperature and pressure, exhibit unique properties distinct from both gases and liquids, surpassing their critical point (Shafaghat *et al.*, 2019). The distinct properties of supercritical fluids, including low viscosity, high density, and diffusivity, render them advantageous in a wide range of applications such as separation, synthesis, and extraction processes. Furthermore, supercritical fluids have the potential of been employed as reactants and also as solvent medium (Manjare & Dhingra, 2019). The dual utility of supercritical fluids offers economic advantages over other solvents, particularly in the realm of biomass conversion. Commercial applications of supercritical fluids date back to the late 1970s, where they revolutionized extraction and purification processes, offering contamination-free solutions and rapid technologies in pharmaceuticals and food industries. The effectiveness of utilizing supercritical fluids is contingent upon a thorough understanding of the phase equilibrium between the supercritical fluid and the desired solute. Designing co-solvent combinations for enhanced extraction processes under supercritical conditions offers a valuable advantage, as it contributes to improved product yield and distribution (Manjare & Dhingra, 2019).

2.2.1 Physical Properties of Supercritical Ethanol and Acetone

Unlike water at the sub and supercritical states, alcohols have superior advantages over water due to the following properties.

(i) Product separation

Crude bio-oil obtained from the liquefaction of biomass are characterized with the presence of various chemical compounds which could be classed as alcohol, ethers, esters, aromatics, hydrocarbons, ketones, phenols, nitrogen compounds and others such as Sulphur containing

aromatics (Chen & Li, 2020; Shafaghat *et al.*, 2019). Following the application of water as a solvent in the liquefaction process, complex chemical compositions are distributed within the water medium. To recover the products, a liquid-liquid extraction medium is necessary. Solvents like dichloromethane (DCM) (Koley *et al.*, 2018), ethyl acetate (Feng *et al.*, 2021) tetrahydrofuran (THF) (Zhang *et al.*, 2013) are commonly employed for phase separation. These solvents facilitate the separation of the organic-soluble phase (bio-oil) from the water-soluble phase before evaporation. When organic solvents are used as a reaction medium, they not only facilitate product recovery but also eliminate the need for phase separation. This is because the compositions of the crude bio-oil obtained from the liquefaction of biomass are soluble in organic solvents. Hence, the need for the associated cost and the high energy demand are not required.

(ii) Catalyst Activities

The use of organic solvents under supercritical conditions can be considered a strategic method for safeguarding the activity of metal-supported catalysts from deactivation caused by poisoning through leaching and hydrolysis processes. However, this approach may lead to challenges in water medium, such as the potential blockage of active sites on the catalyst materials and limitations in material transport, thereby impeding catalytic activities. Moreover, the tendency for the formation of inactive species due to water hydrolysis reactions with active catalyst sites poses a significant detriment to the catalytic liquefaction process in the presence of water. Şenol *et al.* (2005) has reported the detrimental effects of water formation during the hydrodeoxygenation process to enhance catalyst deactivation.

(iii) Enhanced Solubility

Typically, the solubility of organic compounds in water is quite low, except under supercritical conditions. At elevated temperatures and pressures, the dielectric constant of water decreases significantly from its standard value of 80. This reduction in the dielectric constant between 10-30, facilitates enhanced solubility of organic compounds in water, enabling efficient extraction and reaction processes. As crude bio-oil compounds undergo cooling following the liquefaction process, there is a tendency for condensation and segregation to occur. During this cooling process, the solvent properties of water are lost, which can affect the solubility of organic compounds. However, in the case of organic solvents such as ethanol and acetone, which have lower dielectric constants compared to water, the solubility of organic contents in crude bio-

oil is enhanced. This enhanced solubility is observed both at room temperature and under supercritical conditions, making these organic solvents advantageous for various extraction and reaction processes (Brand *et al.*, 2013; Dannhauser & Bahe, 1964; Hiejima & Yao, 2003).

(iv) Low Corrosion Potential

Water's tendency to cause corrosion calls for a careful consideration during the design of reactors for biomass liquefaction processes where water is used as a solvent. Proper reactor design and material selection are crucial to mitigate corrosion and ensure the longevity and efficiency of the process plants. However, organic solvents such as ethanol and acetone generally exhibit lower corrosive effects on reactor's walls as compared to water. This advantageous characteristic promotes the performance of organic solvents in various chemical processes, including biomass liquefaction, where corrosion can be a significant concern. Therefore, when selecting solvents for such applications, organic solvents may offer a favorable alternative due to their reduced corrosive impact.

(v) Organic solvents as catalyst and hydrogen donor

The dual-functionality and impactful role of organic solvents like ethanol and acetone have prompted extensive research into their performance under supercritical conditions, aiming to enhance the production of high-quality crude bio-oil. By facilitating in-situ hydrogen production through ethanol conversion in supercritical solvents such as ethanol and acetone, it becomes feasible to enhance the rate of biomass conversion and induce hydrodeoxygenation of its constituents in a one-pot approach (Demirkaya *et al.*, 2019b; Park *et al.*, 2019). The potency of ethanol to retard repolymerization and char/tar formation through the formation of a radical quenching agent have been presented. The initial step of the proposed mechanism involves the transfer of an α -hydrogen atom in the form of a hydride, leading to the creation of an electron-deficient species through hydroxylalkylation (Nakagawa *et al.*, 2003; Ross & Blessing, 1979). The proposed hydrogen donation and hydroxylalkylation pathways of ethanol is as presented in reaction Fig. 1.



Figure 1: Proposed hydrogen donation and hydroxylalkylation pathways of ethanol (scheme 1= by Nakagawa *et al.* (2003) and scheme 2 and 3 were proposed by Ross and Blessing (1979))

2.3 Biomass as Feedstock for Biofuel Production

The thermochemical processes, extensively studied, represent a leading technique for converting biomass into bio-oil, presenting a sustainable and environmentally friendly energy solution for transportation needs. In this thermochemical conversion process, biomass feedstocks are heated under inert conditions at atmospheric pressure. This thermal degradation results in the production of valuable products, including biofuels, biochar, and non-condensable gases such as methane, carbon dioxide, hydrogen, and other gaseous hydrocarbons (Saghir *et al.*, 2019). The quality and composition of product formation in the thermochemical valorization process of biomass are influenced by various operational parameters, including temperature, residence time, catalyst loading, and feed ratio (Varma *et al.*, 2018). The diverse structures present in biomass materials contribute to the distinct degradation profiles observed during thermal processes, particularly evident in thermogravimetric analysis. These structural complexities directly impact the properties of the resulting bio-oil (Maia & de Moraes, 2016). Because of the intricate structural characteristics of biomass materials, various compositions of bio-oil are derived. For instance, the depolymerization of cellulose and hemicellulose yields products like sugar and furan, whereas lignin decomposition predominantly generates phenolic compounds (Collard & Blin, 2014; Kleinert & Barth, 2008).

The diversity observed in the degradation profile offers valuable insight into the critical role of temperature as a controlling parameter in the thermochemical process. The intricate composition of biomass arises from constituents such as lignin (Three dimensional biopolymers made-up of high branched of polyphenolic constituents without a pristine

structure-amorphous in nature and difficult to hydrate when compared to cellulose and hemicellulose), cellulose (high molecular weight which is composed of β -glycosidic linkage of linear chain glucose with high resistivity to chemical attack due to its stability), hemicellulose (relatively lower molecular weight constituents than cellulose and consists on short and highly branched chain of five-carbon sugars), and extractives such as acids, salts and proteins- small organic polymers and molecules (Gao *et al.*, 2016; Singh *et al.*, 2013; Zhang *et al.*, 2010). The breakdown of the listed structural components leads to the creation of multiple monomers, which, following deoxygenation, result in the production of liquid biofuels and lightweight chemicals. Hemicellulose exhibits a low degree of polymerization due to its amorphous structure, resulting in its degradation occurring in two primary stages (Mlonka-m *et al.*, 2021). The thermal behavior due to hemicellulose structural make-up indicated that it contributes less to bio-oils production through thermochemical conversion. Figure 2a and Fig. 2b show the generational classifications of feedstocks for bioenergy production and the HHV- H/C_{eff} respectively, while the description is depicted in Table 1.

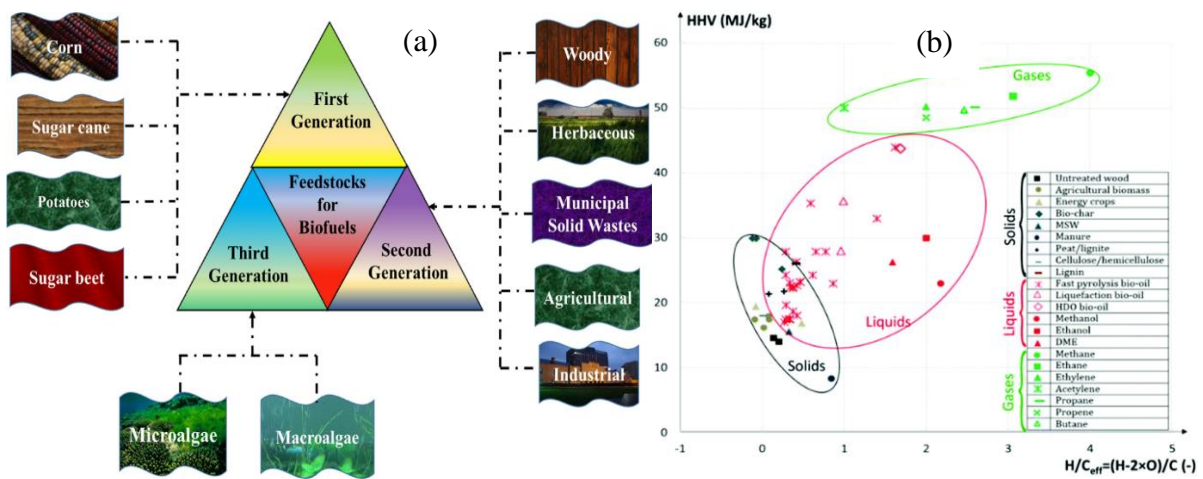


Figure 2: (a) Feedstocks for biofuel production from different generations (Neto *et al.*, 2019; Singh *et al.*, 2023) (b) HHV- H/C_{eff} map for solid, liquid, and gaseous fuels (Zhang, 2016)

Table 1: Feedstocks' descriptions of various generational categories of biofuels

Types of Biofuel	Feedstock Description	Examples
1 st generation	The biofuels obtained through this feedstock has the characteristic of competing with the feed and food industry and the agricultural land use	<ul style="list-style-type: none">• Bioethanol obtained from agricultural crops such as corn, wheat and sugarcanes.• Biodiesels derived from oil-based crops such as soybeans, palm oil, rapeseed, waste edible oils and sunflower.
2 nd generation	Biofuels in this category are obtained from non-edible food crops and/or waste residues	<ul style="list-style-type: none">• Biogas sourced from residue and wastes• Biofuels derived from biomass• Biofuels obtained from waste energy sources
3 rd generation	Obtained from micro-organisms such as algae grown in aquatic environment	<ul style="list-style-type: none">• Biofuels derived from algae conversion• Biogas obtained from algae valorization

2.3.1 Biomass Conversion

To harness the inherent energies within biomass feedstocks, it is essential to efficiently convert the components of the building blocks from complex structures into monomers and dimers. The choice of conversion technologies depends on the specific types of bioenergy being targeted (Singh *et al.*, 2023). Extensive research has been conducted in the realm of thermochemical conversion approaches to produce liquid biofuels, with the goal of developing sustainable and renewable energies that are both high-quality and cost-effective in meeting energy demands. Various thermochemical conversion techniques, including pyrolysis, liquefaction, and gasification coupled with Fischer-Tropsch synthesis (biomass-to-liquid), have been explored for the transformation of biomass into liquid biofuels and light chemicals. The operational conditions requirement for the categories of the thermochemical conversion

processes are as shown in Table 2 while the classification of liquefaction techniques is presented in Table 3.

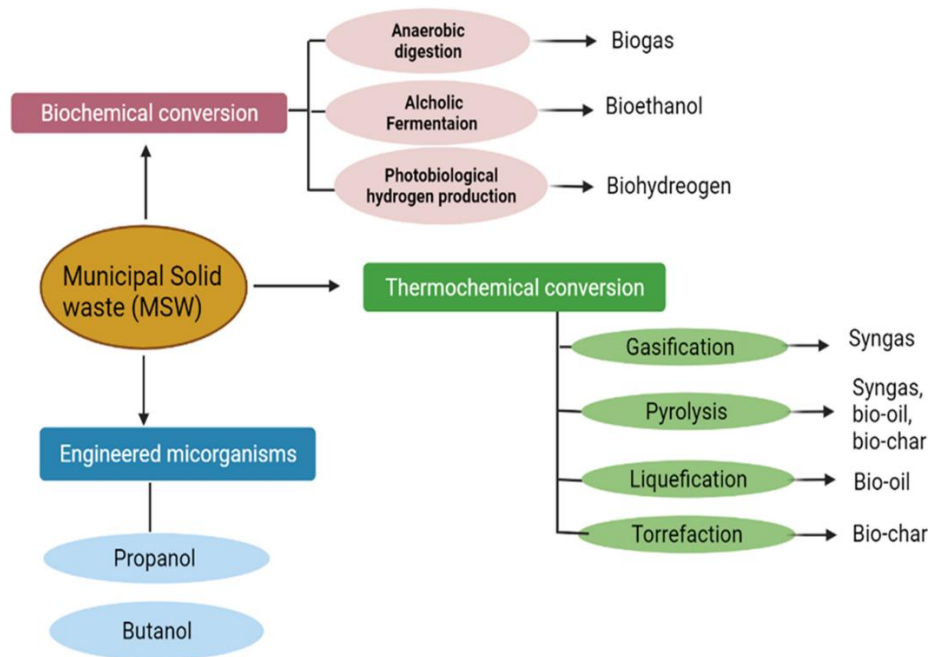


Figure 3: Solid wastes treatment routes into bioenergy productions (Singh *et al.*, 2023)

Table 2: Different thermochemical conversion routes of biomass to produce light chemicals and liquid biofuels (Brand *et al.*, 2013)

Conversion process	Temperature (K)	Pressure (MPa)	Catalyst	Drying
Gasification	873-1,573	0.1	Required in Fischer–Tropsch synthesis	Essential
Pyrolysis	723-923	0.1-0.5	Not compulsory	Essential
	523-673	5-40	Not compulsory	Not essential

Table 3: Classification of hydrothermal process according to conversion temperature (Biller & Ross, 2016)

Processes	Operating Conditions	Main product	Feed stock	Product's properties
Solvothermal Carbonization (STC)	180-250 (°C) and employing long residence times typically spanning several hours.	Biochar	Wet/dry biomass	Exhibiting characteristics similar to low-rank coal, the material is denser in energy, more readily fragmented, and displays greater hydrophobicity compared to its initial state.
Solvothermal Liquefaction (STL)	250-375	Biocrude; liquid fuel	Wet/dry biomass	The biocrude can be upgraded into a distillate range of petroleum-derived products
Solvothermal gasification (STG) or supercritical Solvent gasification (SCSG)	Above 375	Syngas	Wet/dry biomass	Typically high in either H ₂ or CH ₄ with the presence of CO ₂

The thermal conversion of lignocellulose biomass can be categorized into gasification or solvothermal liquefaction processes. Gasification involves converting biomass into synthesis gas (typically composed of CO and H₂), which can be utilized for electricity generation or for producing hydrocarbon-based fuels via Fischer-Tropsch synthesis (FTS). However, due to the complexity and high cost associated with biomass gasification and FTS integration, the utilization of commercial gasification-FTS technologies using biomass as feedstocks is limited (Munnik *et al.*, 2015). Hence, direct biomass conversion into liquid hydrocarbon fuels through solvothermal techniques offers a simpler reactor design compared to gasification-FTS processes, which involve multiple in-situ reactions. These reactions include depolymerization of complex biomass building blocks such as C-C, β -O-4, and α -O-4 bonds, as well as dehydration. These processes promote the formation of smaller monomers and/or dimers from

condensable vapors, along with the production of solid and non-condensable gaseous products. The building blocks of lignin are presented in Fig. 4a and b while the reaction pathways for the liquid bio-oil production through pyrolysis involving non catalytic and catalytic approach under the influence of HZSM-5 and Al-MCM-41 is shown in Fig. 5 and Fig. 6

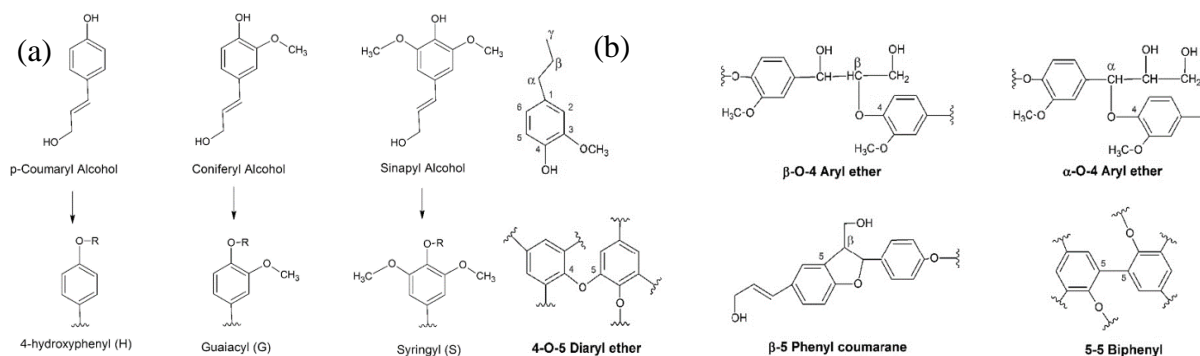


Figure 4: (a) Main kinds of chemical bonds present in lignin (b) Monolignols and its respective lignin structural units (do Couto Fraga *et al.*, 2021)

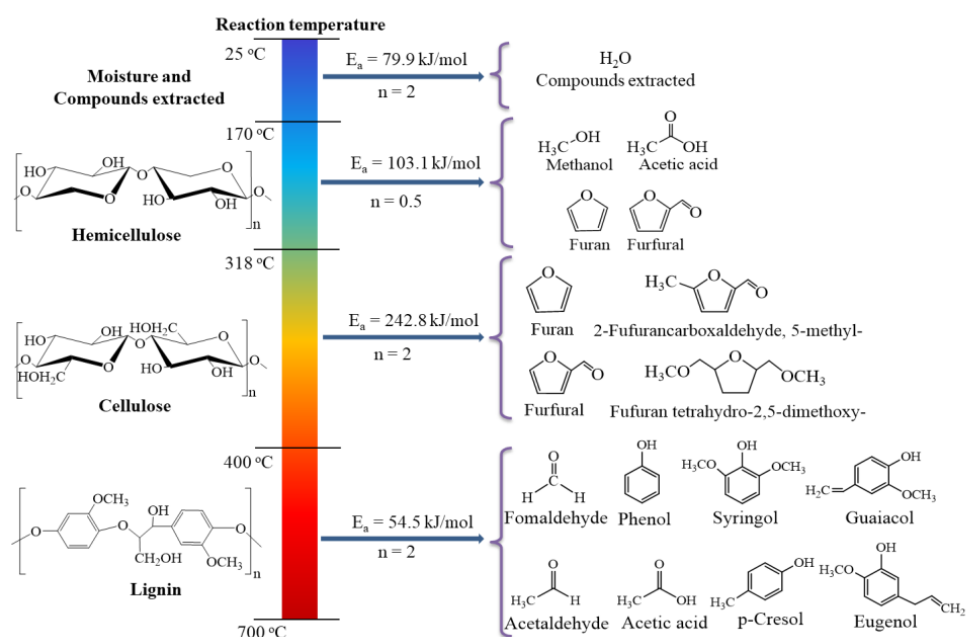


Figure 5: Reaction pathways for liquid bio-oil production using pyrolysis process of biomass feedstock (Van Nam *et al.*, 2020)

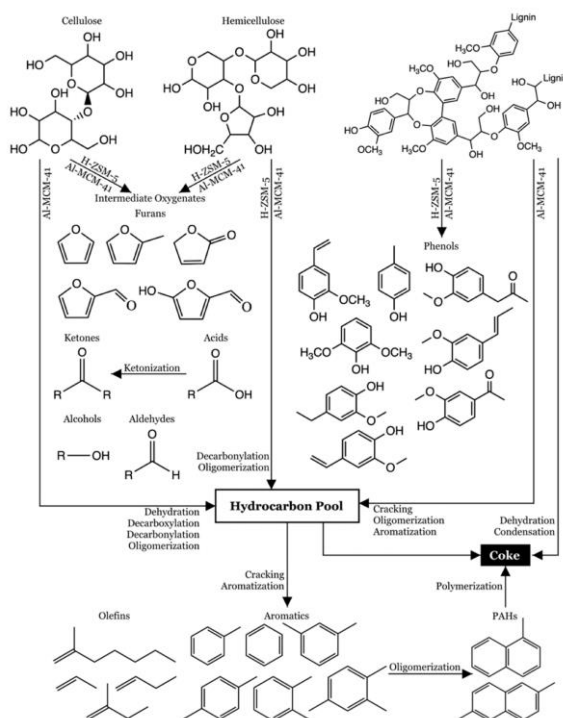


Figure 6: Reaction pathways for lignocellulose biomass conversion (Ratnasari *et al.*, 2020)

From the information presented in Fig. 5 and Fig. 6, it is evidence that catalyst plays an excellent roles in the removal of oxygen from the bulk of the bio-oil oxygenates through several reactions such as deoxygenation, hydrodeoxygenation, carbonylation, carboxylation etc. The performance characteristics of the catalysts are majorly favored in the presence of initial hydrogen supply which helps during the hydrogenation process. The adoption of solvothermal liquefaction where organic solvents capable of generating hydrogen into the reaction mixture are used, the need for the initial hydrogen supply for oxygen removal is not necessary. Hence, this present study seeks to investigate the effects of ethanol and acetone as in-situ hydrogen supply during the depolymerization and upgrading of orange peels into crude bio-oil.

The use of solvent-enhanced biomass conversion into bio-oil via thermal methods has been noted to offer several advantages over pyrolysis process. These advantages include:

- (i) Elimination of the need for feedstock drying, thereby enhancing the economic viability of the conversion process.
- (ii) Facilitation of catalyst application and subsequent improvement in product yield compared to pyrolysis processes.

- (iii) Potential for direct liquefaction without requiring a fractionation process.
- (iv) Production of bio-oil with higher heating values (HHV) due to lower water and oxygen content compared to bio-oil obtained through pyrolysis (Kim *et al.*, 2019).

2.3.2 Crude Bio-oil

Bio-oil, also referred to as crude bio-oil or biocrude, is a broad term used to describe liquid fuel derived from the conversion of biomass feedstocks under elevated temperature and pressure, particularly in solvothermal processes. Bio-oil obtained through these methods is distinguished by its high content of oxygenated compounds, which stem from the decomposition of lignin, cellulose, and hemicellulose—the primary components of biomass materials (Shah *et al.*, 2019; Srinivasan *et al.*, 2014). The abundance of oxygenated compounds in bio-oil makes it unsuitable for direct utilization in internal combustion engines for transportation or turbines for power generation. The significant presence of these compounds adversely affects the overall properties of bio-oil, including high oxidative instability, elevated acid content, increased viscosity, susceptibility to corrosion during storage and transportation, and consequently, a lower heating value (Verma & Kishore, 2017).

Bio-oil boasts several valuable properties that make its production and application an intriguing endeavor compared to conventional fuels. These properties include its biodegradability potential, relatively low toxicity, minimal or absent of sulfur content, and promising lubricity (Kazmi *et al.*, 2024; Rorrer *et al.*, 2019). Regarding the challenge posed by the high oxygen content in bio-oil, the necessity for an upgrading process to improve its properties is crucial for both commercial viability and environmental acceptance. Upgrading can be achieved through either an in-situ approach or ex-situ via a two-stage catalytic technique, where the bio-oil obtained is upgraded in a separate reactor after product recovery from biomass conversion (Kazmi *et al.*, 2024; Shu *et al.*, 2023). The products categories of bio-oil and their respective compounds are presented in Table 4 while the differences in bio-oil and conventional fuels are shown in Table 4.

Table 4: Products categories of bio-oil and their respective compounds (Zhang & Zhang, 2019)

Classifications	Compounds' type
Mono-aromatics	Benzene, phenol, cholesterol
Alkane or alkene	Cycloalkane, hexadecane, heptadecane
Fatty acids	Steric acid, palmitic acid and meristic acid
Oxygenates	Aldehydes, esters, ketones
Polyaromatics	Fluorene, naphthalene, indene
Nitrogen compounds	Pyrrols, piperidines, indoles

Table 5: Comparison of bio-oil and conventional fuels (Hsuan *et al.*, 2019; Kazmi *et al.*, 2024; Osman *et al.*, 2021; Yan, 2019; Uhler *et al.*, 2016)

Property	Bio-oil	Crude oil	Diesel	Gasoline	Heavy fuel oil (HFO)-Marine fuel
pH	2-3	-	-	-	-
Viscosity @ 40°C (cP)	40-100	180-350	1.8	0.37-0.44	30-700
Pour point °C	-15.0	21	-29.0	-60	24 to 30
Flash point °C	48–55.0	100	42.0	40	60
HHV (MJ/kg)	18-38.0	41	42.0	44	43.99
Density @ 15 °C (kg/m ³)	1200.0	0.86-0.94	820-950.0	737	960-1010
Carbon (wt%)	42-47.0	86	87.4	84.9	82.62
Hydrogen (wt%)	6–8.0	12	12.1	14.76	11.49
Nitrogen (wt%)	<0.10	0.3	392 ppm	0.08	1833 (µg/g)
Oxygen (wt%)	46-51	~0	-	-	-
Sulphur (wt%)	<0.02	2.1	1.39	-	3.5-4.5
Solid (wt%)	0.2-1.0	-	-	-	
Water (% v/v)	13-35	0.1	-	-	0.5

2.3.3 Heavy Fuel Oil

In maritime industry, the fuels consumed by ships for engine ignition are generally called the bunker fuels. The non-distillable residuals fractions obtained from the refinery of crude oils during the atmospheric distillation process are majorly the sources of the heavy fuels oil (HFO) in the 1970s. These residuals are mainly tagged as the fractions which do not sublime between 838.7 to 866.5k (Uhler *et al.*, 2016). As refining processes advance with the adoption of cutting-edge techniques like vacuum distillation, residual oils are repurposed as feedstock for further refining of lower boiling oils through catalytic cracking, coking, and thermal cracking. Consequently, the quality of the final residual oil diminishes, resulting in a decrease in volume and rendering them unsuitable as heavy fuel oils for marine industries (Uhler *et al.*, 2016).

The extraction of lower oil fractions from the residual results in a concentration of ash, metals, sulfur, water content, and higher pour point and viscosity, leading to a decline in quality. This degradation in the quality of residual fuels has prompted the blending of such fuels with other available lower boiling residuals, such as cat-cracked gas oil and automotive oil, although a controversial practice. However, this blending process helps meet the specifications required for a typical heavy fuel oil (HFO). Conversely, ISO specifications for HFO explicitly forbid the application of used lubricating oil (ULO) as blending constituents to marine fuels. Hence, the search for a renewable marine fuel that is sustainable will be an interesting adventure to meeting the ever-growing marine transportation fuels' demand. Unlike jet fuel requirement, the presence of polyaromatic hydrocarbons PAH, furan are not considered a setback in heavy fuel oil (marine fuel) for transportation although, its presence increases the average molecular weight of the fuel (Uhler *et al.*, 2016). The finding of Uhler *et al.* (2016) revolutionized the characteristic components of HFO through the application of GC-MS that shows the presence of significant quantity of aromatic compounds such as alkyl-phenanthrenes, alkyl-naphthalene and alkyl-benzenes; a product of crude oil fractionation (catalytic or thermal cracking).

2.4 Effects of Bio-oil Physiochemical Properties on Biofuel Performance

The bio-oil generated from the thermochemical conversion of biomass contains a plethora of compounds resulting from both primary and secondary cracking processes, giving rise to the formation of intermediates. Van Nam *et al.* (2020) observed that diverse composition of lignocellulose leads to variations in its degradation profile, activation energies, and degradation kinetics. Consequently, this results in the formation of biofuels with varying compositions. The

presence of oxygen and water in bio-oil obtained through the pyrolysis process renders it unsuitable for direct utilization in automobile engines, consequently resulting in a lower heating value. The direct use of bio-oil as fuel in automobile internal combustion engines has been impeded by its elevated levels of oxygen and water, reduced calorific value, inability to mix with fossil fuels due to its high polarity, inadequate stability, and limited storage duration (Attia *et al.*, 2020; Babajo *et al.*, 2019; Ding *et al.*, 2020; Ooi *et al.*, 2019).

The production of bio-oils containing high oxygen content has been reported to contribute to corrosion during crude bio-oil processing and transportation via pipelines, along with fostering microbial growth (Attia *et al.*, 2020; Steinbusch, 2010). The rise in bio-oil viscosity over time during storage has been linked to the aging process (Loong *et al.*, 2014). The oxidation instability resulting from high oxygen content during storage has hindered the effective long-term storage of bio-oil. Therefore, the presence of high oxygen content in bio-oils diminishes the quality of the fuel and its performance as a transportation fuel, consequently reducing its economic value. Labeckas *et al.* (2017) investigated the impact of physiochemical properties, such as the oxygen content of bio-oil, on combustion characteristics, ignition delay, and cyclic variation. Their findings suggested that maintaining an appropriate level of oxygen in bio-oil could enhance combustion efficiency and minimize cyclic variation. Consequently, there is a need to refine crude bio-oils into economically viable fuels suitable for internal combustion engines in automobiles, employing effective and efficient methods. The nature of depolymerization reaction occurring in the cellulose and hemicellulose resulted in an increase viscosity, molecular weight and water content in the produced bio-oil (Mortensen *et al.*, 2011).

The influence of biomass feedstocks on the physiochemical properties of bio-oil was examined, revealing that both the operational conditions of thermochemical processes and the characteristics of biomass feedstocks contribute to the properties of bio-oil. Several waste agricultural materials have been employed for the production of second-generation bio-oil over the years and Table 6 depicts the physiochemical properties of some selected bio-oil. The properties of the bio-oil obtained through the organic liquefaction process possess higher HHV over the pyrolysis reaction. Furthermore, the use of co-solvents as a reaction medium had been reported to be promising to producing higher quality bio-oil over hydrothermal, organic solvent, microwave-assisted and plasma electrolytic liquefaction processes (Kim *et al.*, 2019). This excellent characteristic performance of producing higher HHV bio-oil could further be

enhanced through reaction operating at higher temperature, extended reaction time, and higher ratio solvent to biomass and in the presence of catalysts (Yan *et al.*, 2017).

Table 6: Physiochemical characteristics of bio-oil derived from varieties of biomass feedstocks

Sample	Conversion Process	Physiochemical parameters									Ref
		C	H	O	N	S	pH	H/C	O/C	HHV (MJ/kg)	
yellow poplar	Pyrolysis	47.80	6.30	45.80	0.20	-	NR	1.57	0.72	18.05	Rezaei <i>et al.</i> (2017)
Maize Stalk	Pyrolysis	44.30	6.30	48.50	0.60	0.30	3.20	1.69	0.82	19.60	Zheng, (2008)
Sawdust	Pyrolysis	45.38±0.02	5.12±0.02	48.78±0.02	0.73±0.03	NR	NR	1.34	0.81	22.38±0.53	Cheng <i>et al.</i> (2018)
Pine wood	Pyrolysis	48.13	6.32	44.63	0.35	0.18	NR	1.56	0.70	18.57	Chen <i>et al.</i> (2016)
Wheat husk	Pyrolysis	56.30	7.80	29.70	4.80	1.40	NR	1.65	0.40	26.00	Santos <i>et al.</i> (2019)
Rapeseed cake	Pyrolysis	63.56	8.89	23.74	3.60	0.11	NR	1.67	0.28	26.70	Çulcuoğlu <i>et al.</i> (2005)
Red Oak	Pyrolysis	59.40	5.20	35.30	NR	NR	NR	1.04	0.45	NR	Choi <i>et al.</i> (2014)
Natural hay	STL	80.70	4.30	15.00	NR	NR	NR	0.63	0.14	31.5	Caprariis <i>et al.</i> (2017)
Oak	STL	69.40	6.30	24.20	NR	NR	NR	1.08	0.26	27.5	Caprariis <i>et al.</i> (2017)
Walnut shell	STL	71.20	6.30	22.50	NR	NR	NR	1.06	0.24	28.50	Caprariis <i>et al.</i> (2017)
Cellulose	STL	67.40	5.30	27.30	NR	NR	NR	0.94	0.30	24.60	Caprariis <i>et al.</i> (2017)
Sweet sorghum stalk	STL	65.60	8.27	25.21	0.85	0.08	-	1.50	0.29	25.84	Yan <i>et al.</i> (2017)

2.5 Homogenous and Heterogenous STL Process

2.5.1 Homogeneous Catalytic Process

Homogeneous catalysts allow reactions to take place under a relatively mild process condition. This enable the advancement of the understanding of the reaction mechanisms at molecular level, thus providing outstanding opportunities to enhance the catalytic processes (Kumar *et al.*, 2022). Several alkali-based and acid-based catalyst have been successfully employed for the HTL of biomass feedstocks for improved biocrude properties and yield (Kashimalla, 2022; Mishra *et al.*, 2022; Wu *et al.*, 2019). Several reports have indicated that the application of formic acid and organic acetic acid as catalyst materials have improved the yield of biocrude considerably (Liu *et al.*, 2018; Nagappan *et al.*, 2021). The dual characteristic features of formic acid and acetic acid have enhanced their performance towards improved biocrude yield and quality. Shakya *et al.* (2015) reported that, the two acids have the tendencies to behaving as a catalyst as well as reactants because, they were observed to be consumed during the chemical reactions hence, they possess no threat to the reaction mixture and no additional cost for catalyst preparation and recovery are required.

Comparing the performance of the most widely used alkali-based catalyst; Na_2CO_3 with K_2CO_3 in the conversion of woody biomass to biocrude, the latter is more promising than the former due to its ability to enhance hydrolytic depolymerization of cellulose, hemicellulose (Nagappan *et al.*, 2021; Singh *et al.*, 2013; Toor *et al.*, 2011). The performance characteristics of K_2CO_3 is promoted due to its ability to form bicarbonate and hydroxide upon reacting with water whereby, the bicarbonate acts as a secondary catalyst which aids in improved biocrude yield (Zhu *et al.*, 2015).

Zhu *et al.* (2015) have studied the influence of alkali catalyst on the properties and the yield of products through the application of HTL of barley straw. The conversion process was carried out in both the sub- and supercritical temperature ranges from 200-400 °C under the application of K_2CO_3 homogeneous catalyst material. The highest biocrude yield of 34.85 wt% with improved high heating value and the reduced O/C ratio were obtained at the reaction temperature of 300 °C under the application of K_2CO_3 catalyst. Majorly, improved phenolic compounds were promoted over carboxylic compound following the application of K_2CO_3 homogeneous catalyst which indicated that the deoxygenation reaction was favored. Also, the production and characterization of bio-oil from hydrothermal liquefaction of microalgae

Dunaliella tertiolecta cake was reported by Shuping *et al.* (2010). The study found that the biocrude's yield increased continuously with an increase in Na_2CO_3 loading up till 5 wt.% and thereafter, an observable reduction in the yield of the biocrude was observed at Na_2CO_3 dosage of 10 wt.%.

Catalytic hydrothermal liquefaction of eucalyptus to prepare bio-oils and product properties was studied by Wu *et al.* (2019). The influence of homogenous (NaOH, KOH and Pd/C) and temperature were investigated on the biocrude yield and quality on the at the liquefaction temperature of 260 and 300 °C. The yield of the observed biocrude obtained was higher in NaOH with 61.2 % at the optimum temperature of 260 °C reaction temperature. The yield of the biocrude and the biochar were observed to be inversely proportional to temperature but directly proportional to gas yield. Although, the hydrogen and carbon contents were appreciably improved while deoxygenation process was also enhanced at high temperature. The obtained compositional analysis as determined from GC-MS indicated that, further upgrading process is required to produce a transportation fuel due to the presence of large amounts of ketones, phenol, carboxylic acids and esters contents in the biocrude.

Hu *et al.* (2020) reported the effect of alkali-catalyzed liquefaction of pinewood sawdust in ethanol/water co-solvents in HTL process. Several experimental studies were conducted on the effects of co-solvent on the percentage biomass conversion and biocrude yield at reaction temperature of 300 °C, 10 wt.% of pinewood sawdust and residence time of 30 minutes. The researchers observed the highest biomass conversion of ~98% and highest yield of biocrude oil of ~48 wt.% in ethanol/water co-solvents in the absence of catalyst loading. The addition of Na_2CO_3 and NaOH was observed to retard the performance of ethanol during the liquefaction process under the process condition studied. Furthermore, the biocrude oil obtained from the ethanol-water co-solvents from the non-catalytic and homogeneous catalytic liquefaction comprises of a slightly higher molecular weight than those obtained from the application of water as solvent. Therefore, to improve the performance of HTL of pinewood sawdust, the application of ethanol as solvent was highly recommended to enable ease upgrade process during the hydrodeoxygenation process.

Lai *et al.* (2018) have studied the effects of Na_2CO_3 addition on the conversion of sewage sludge (SS) via HTL process in ethanol-water co-solvent to understand the synergy between water and ethanol medium towards improved biocrude quality and yield. The study was conducted in a 300 mL volume of stainless-steel batch autoclave reactor operating at (200-280

°C) and reaction time between (0-60 min). Highest yield of biocrude of 33.5-36.1 wt.% were observed in ethanol/water co-solvent as compared to the yield obtained in pure water and ethanol with 32.2 wt.% and 26.8 wt.% respectively. Furthermore, the presence of higher ester contents in the biocrude obtained from ethanol/water co-solvent signifies the high quality of the biocrude. The introduction of homogenous Na_2CO_3 catalyst was found to increase the yield of biocrude but adversely reduces the quality of biocrude.

The production of biocrude via hydrothermal liquefaction of birch sawdust has been reported by Malins (2017). The finding optimized the effects of several process parameters such as the feedstock to water ratio, reaction temperature, initial hydrogen pressure, residence time, catalyst loading and the nature of catalyst of $\frac{1}{2}$ - $\frac{1}{8}$, 200-340 °C, 0-10 MPa, 5-90 min, 0.25-7.0 wt.% and (NiSO_4 , Fe_2O_4 , NaOH , ZnSO_4 , Raney-nickel, Ni65%/SiO₂, Al₂O₃, Na_2CO_3) respectively on the HTL process. The optima condition of 5 wt.% of NaOH, $\frac{1}{4}$ feedstock/water ratio, 5 min of residence time, 250 rpm of agitation speed at the reaction temperature of 300 °C resulted in the highest biocrude yield and calorific value of 54.1% and 24.9 MJ/kg without the introduction of an inert gas respectively. The GC-MS analysis of the biocrude composition indicated its suitability for further upgrade into drop-in fuel.

The mechanisms of alkaline induced catalytic hydrothermal liquefaction of biomass feedstock have been proposed by Yin and Tan (2012) to comprise of three consecutive chemical reactions. These reactions include the hydrolysis of cellulose, lignin and hemicellulose (macromolecules) into monomers and oligomers (e.g. guaiacol, fructose and glucose). Then, the formed monomers are cracked into intermediates of lower molecular weight which have huge tendencies of forming the compositions of biocrude obtained during the HTL process. The third possible reaction could be the tendency of polymerization reaction which could be favored due to the limited presence of hydrogen thereby, promotes the association of free radicals forming char. Therefore, to limit char formation during the HTL process, moderate hydrogen supply is needed for the stabilization of free fragments/radicals such as 5-(Hydroxymethyl)furfural (HMF). The formation of 5-(HMF) according to the mechanisms of biocrude formation by Yin and Tan (2012) resulted in the formation of reduced biocrude yield.

The Effects of catalyst on variety compounds and chromatographic characterization on the hydrothermal liquefaction of *Glycyrrhiza glabra* L. (Licorice) was reported by Durak and Genel (2020) where the effects of boric acid (homogeneous) and zinc oxides (heterogeneous) catalysts were studied on the biocrude's yield, energy value and the nature of hydrocarbon

formation. The percentage catalysts loading was maintained at 10 wt.% on 5g feedstock in 60 ml distilled water whereby, the reactor was operated at heating rate of 10°C/min in an inert environment of nitrogen. Highest feed conversion of 35.73 wt.% was obtained over the application of boric acid as catalyst at reaction temperature of 350 °C with heating values ranging from 21.87 to 31.78 MJ kg⁻¹. It was reported that, the application of ZnO catalyst selectively favored the production of polyaromatic hydrocarbons while boric acid enhanced the formation of monoaromatic hydrocarbons (MAHs). The selectivity of ZnO catalysts to polyaromatic hydrocarbon could be due to the presence of active pores which enable cracking of long molecular chain hydrocarbon. Also, a decrease in liquid yield was observed as temperature increases above 325 °C. The decrease in light biocrude was attributed to the formation of secondary reactions coupled with depolymerization of hydrocarbon compounds which further enhances the formation of large amount gaseous product (Durak, 2020).

The synergistic effect of hydrothermal liquefaction of wheat stalk with homogeneous and heterogeneous catalyst at low temperature was reported by Chen *et al.* (2019). The mixture of homogeneous Na₂CO₃ was incorporated with Fe, a heterogeneous catalyst to enhance the catalytic performance of the HTL of wheat stalk at different temperature and residence time. High cracking efficiency of large molecular compounds were observed in Fe loaded Na₂CO₃ that the individual catalyst components. A high reaction temperature of 270 °C was obtained to favor the yield of biocrude (89.45 wt.%) when the Fe loaded Na₂CO₃ was charged while aromatics compounds and some oxygenated compounds such as ketones, alcohols, aldehydes and alkanes were the in the biocrude. The GC-MS analysis result depicts the need for further biocrude upgrading into light aromatics hydrocarbons. Overall, the major challenges in the application of homogeneous catalysts for biocrude production is catalyst recovery, reusability and the shape-selectivity controlled for target production of chemicals. Hence, the application of heterogeneous catalyst is widely used due to its economic feasibility and the shape control power for the synthesis of light chemicals and fuels.

2.5.2 Heterogeneous Catalytic Process

The efficient design of solid catalysts for the breakdown and conversion of biomass materials to achieving a sustainable economy through the production of renewable fuels and light chemicals has gain tremendous attention owing to its excellent advantages. The design and selection of catalysts is a an important consideration in the effective conversion of biomass into valuable chemicals (Bianasari *et al.*, 2024). Recently, the review published by Bianasari *et al.*

(2024) reported an improved performance of a mixed catalyst with zeolites for an enhanced structural properties and catalytic activities. Oxygenates pose a major challenge in biocrude upgrading, as they lead to instability, high acidity, and low energy density. Catalytic hydrodeoxygenation (HDO) is an essential process for eliminating these oxygenates, enhancing biocrude quality by increasing the hydrogen-to-carbon ratio and decreasing oxygen content. Various catalytic techniques and approaches are employed in HDO to effectively remove oxygenates. Each method of oxygenate removal through catalytic HDO has specific benefits, depending on the feedstock, desired output, and operational conditions. Supported metal catalysts, bifunctional catalysts, redox catalysts, and promoter-enhanced systems all play crucial roles in converting biocrude into a more stable, high-quality fuel. The selection of a catalyst and method requires careful consideration of factors such as activity, selectivity, stability, and cost to achieve efficient and sustainable biocrude upgrading.

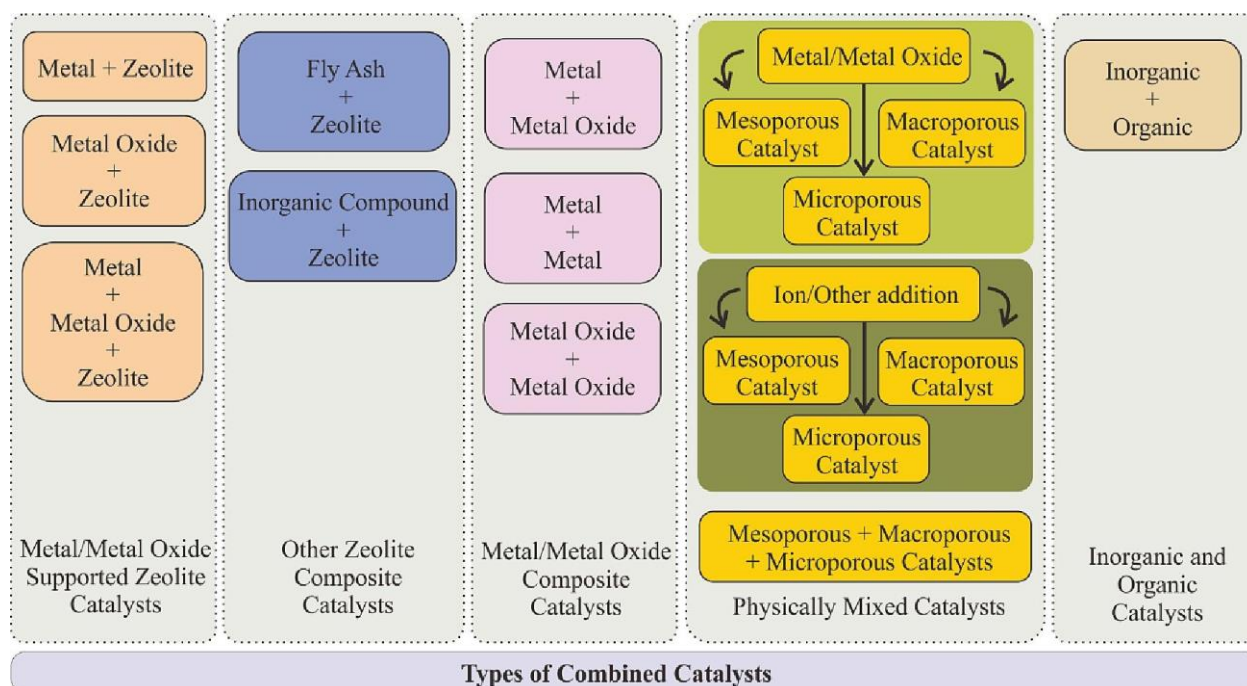


Figure 7: Combined catalysts mix (Bianasari *et al.*, 2024)

2.6 Upgrading of Crude Bio-oil

Bio-oil or biocrude upgrading is carried out to improve the hydrogen/carbon ratio (H/C). Several techniques have been adopted by various researchers towards biocrude refining. Examples of such techniques include hydrotreating, hydrocracking, thermal cracking (coking i.e. carbon rejection processes) and FCC. The high heating value of bio-oil is important parameter which determines fuel performance, hence, removing the oxygen content from the

crude bio-oil is an important adventure to producing high quality drop-in fuel for transportation purpose. The presence of large oxygenated compounds, high viscosity, high-density, high-water content, low calorific values, low C/H ratio, instability and corrosion properties of bio-oil derived from STL process have necessitated the need for upgrading to meet energy requirement and to further project bio-oil as an economic product capable of mitigating greenhouse gas effects. Several techniques have been widely reported in literature as upgrading path for oxygen removal, insights into the various methods are presented and emphasis is placed on hydrodeoxygenation process due to its efficiency and performance (Cheng, 2017; Papageridis *et al.*, 2020; Schmitt *et al.*, 2018; Taghvaei & Rahimpour, 2019; Zhang *et al.*, 2021). The presence of low content of H/C ratio in bio-oil as compared to conventional fuel (petroleum) is due to the presence of high content of oxygenates found in bio-oil feedstocks. The oxygen content's removal is a very important task to promoting biofuel as sustainable and renewable energy source (Gollakota *et al.*, 2016, 2018). The effects of heterogeneous catalysts towards improving the energy composition of biofuel derived from biomass feedstocks are presented in Table 7. Loading transition metals onto supports is essential in biocrude upgrading, enhancing catalyst effectiveness for converting bio-derived crude into higher-value fuels. Metals like nickel, cobalt, and molybdenum are dispersed on porous supports, which stabilize the particles and influence catalyst properties such as acidity and dispersion. This metal-support interaction drives key reactions like hydrodeoxygenation and hydrocracking, improving the quality of the biocrude as shown in Table 7, where the HHV values were improved. Accurate metal loading and distribution are crucial for optimal catalyst performance and efficient upgrading. Furthermore, the biofuel obtained over ethanol as solvents as shown in Table 7 possess high HHV hence, ethanol at supercritical conditions favours HDO process through enhanced catalytic reforming.

Table 7: Effects of heterogeneous catalysts on the biocrude obtained via HTL process of biomass feedstocks

S/N	Feedstock	Catalyst	Catalyst' properties			Conditions of operation				Observations				Ref
			SA (m ² /g)	Pore volume cm ³ /g	Pore size (nm)	Temp (°C)	Residence time (min)	Catalyst loading	Solvent	% yield	HHV (MJ/Kg)	H/C	O/C	
1	Alkali lignin	Ni-Co/AC	594	0.69	8.45	260-300	15	5-20 wt%	Ethanol	72	32.8	1.26	0.18	Biswas <i>et al.</i> (2021)
2	Kraft Lignin	Ni-CeO ₂ /CNF	76	0.33	17	400	15	30g	water	56	-	-	-	Aderlanio <i>et al.</i> (2018)
3	cattails biomass	Nb-AC	321	0.382	-	240-340	60	5-25g	water	32.40	29.88	1.20	1.6	Arun <i>et al.</i> (2021)
4	Gracilaria Corticata (GC) macroalgae	5% Ga/NiFe-LDO/AC	513.10	0.312	-	280	30	15wt%	ethanol	56.2	32.9	1.28	0.20	Li <i>et al.</i> (2021)
5	Dunaliella tertiolecta	Co/CNTs	-	-	-	320	30	6.6 wt. %	water	40.25	-	-	-	(Chen <i>et al.</i> , 2017)
6	Lignin	Co/CNTs	257	0.34	-	280	30	20 wt%	ethanol	66.2	33.6	-	-	Jia <i>et al.</i> (2021)
7	Spirulina	Pd/HZSM-5@MS	-	-	-	380	120	0.01g	water	37.30	29.21	1.49	0.22	Liu <i>et al.</i> (2018)
8	Spirulina microalgae	Co/CNT	257	0.34	-	290	30	20wt%	ethanol	43.6	33.6	1.39	0.29	Liu <i>et al.</i> (2021)
9	Chlorella pyrenoidosa	CNT-COOH	150.9	0.90	23.4	280	30	0.1g	water	30.5	37.6	1.62	0.10	Lu <i>et al.</i> (2020)
10	Nannochloropsis sp	Nano-Ni/SiO ₂	141.8	-	-	250	60	5wt%	water	30	37.2	1.68	0.11	Saber <i>et al.</i> (2016)
11	Pine sawdust (PSD)	HZSM-5	-	-	-	300	60	-	Water/ethanol	~64	27.51±0.07	1.48±0.02	0.33±0.15	Cheng <i>et al.</i> (2017)
12	Pine sawdust (PSD)	6%Ni/HZSM-5	-	-	-	300	60	-	Water/ethanol	~60	27.93±0.16	1.49±0.01	0.32±0.12	Cheng <i>et al.</i> (2017)
13	Pine sawdust (PSD)	12%Ni/HZSM-5	-	-	-	300	60	-	Water/ethanol	~63	27.35±0.13	1.48±0.03	0.34±0.05	Cheng <i>et al.</i> (2017)
14	macroalgae Ulva prolifera (UP)	MgO	-	-	-	280	15	10wt. %	ethanol	50.6	34.2			Xu <i>et al.</i> (2020)

CHAPTER THREE

MATERIALS AND METHODS

3.1 Materials

Orange peels were sourced from local market at Tengeru market in Arusha region of Tanzania. The orange peels were sorted via hand picking to remove any traces of solid particle while the soluble impurities were removed through washing in distilled water. The purified orange peels samples were then oven dried in a typical conventional oven at 100 °C. Thereafter, the dried sample was crushed and sieved through a 500 µm sieve. The kaolin which is used as catalyst support for CNSs growth and HZSM-5 synthesis was sourced from Pugu's deposit, Tanzania. The Kaolin was beneficiated prior to use in both cases while acetylene gas was sourced from Tanzanian supplier. Nickel (II) nitrate hexahydrate ($\text{Ni}(\text{NO}_3)_2 \cdot 6\text{H}_2\text{O}$), iron(III)nitrate nonahydrate ($\text{Fe}(\text{NO}_3)_3 \cdot 9\text{H}_2\text{O}$), Cerium(III) nitrate hexahydrate ($\text{Ce}(\text{NO}_3)_3 \cdot 6\text{H}_2\text{O}$), LUDOX[®] AS-30 colloidal silica (30 wt. % suspension in H_2O), tetraethyl ammonium hydroxide solution (35 wt.% in water) and ammonium-molybdate tetra-hydrate ($\text{NH}_4\text{Mo}_7\text{O}_{24} \cdot 4\text{H}_2\text{O}$) salts were ACS grade reagents purchased from Sigma-Aldrich. Samchun Pure Chemical Co., LTD supplied the ethanol and acetone with percentage purity of 99.5% and 99.7% respective which were used as solvent for the depolymerization/hydrodeoxygenation process and rinsing of reactor and the obtained solid residues in the spent catalysts. Sodium Hydroxide pellet (98% purity) and Ammonium nitrate (98.5%) were also supplied by Samchun Pure Chemical Co., LTD. The calcination and reduction of catalysts were performed under nitrogen (99.99%) and hydrogen (99.99%) purity respectively, both gases were supplied by Jeil Industrial Gas Co. Ltd. Korea.

3.2 Proximate Analyses of the Orange Peels

Proximate analysis was determined on orange peels materials to evaluate the moisture, ash, volatile and the fixed carbon contents. All analyses were carried out in replica of two, and the average results were reported.

3.2.1 Determination of Moisture Content (MC)

Using the ASTM D4442-16 protocol, the moisture content of the dried orange peels was determined on a dried basis. A 2 g of the sample was added into a pre-weighed ceramic crucible and the weighs were recorded. In an air-oven, the samples were dried for 2 h at 105 °C

temperature. The dried samples were then cooled using a desiccator and the final weight after the cooling were recorded. Using the equation presented in Equation 1, the moisture contents were determined.

$$\text{Moisture content} = \frac{W_b - W_c}{W_b - W_a} \times 100\% \quad (1)$$

Where W_a , W_b and W_c represent the weight of the empty crucible, the weight of the orange peels + the crucible before drying and the weight of the orange peels + the crucible after oven drying.

3.2.2 Determination of Ash Content (ACi)

According to the ASTM E1755-01 standard, the ash content was determined by adding a 2 g of the orange peels into a pre-weighed crucible and heated in a muffle furnace at a temperature of 760 °C until a noticeable white greyish matter was achieved- complete ash content observation. The calcined samples were then cooled using a desiccator and the final weight after the cooling were recorded. Using the equation presented in Equation 2, the ash contents were determined.

$$\text{Ash content} = \frac{W_c - W_a}{W_b - W_a} \times 100\% \quad (2)$$

Where W_a , W_b and W_c represent the weight of the empty crucible, the weight of the orange peels + the crucible before combustion and the weight of the orange peels + the crucible after combustion.

3.2.3 Determination of Volatile Matter (VM)

The volatile content according to the ASTM E872-82 standards was adopted where 2 g of the orange peels was heated in a pre-weighed crucible at 800 °C for a period of 7 min. The calcined samples were then cooled using a desiccator and the final weight after the cooling were recorded. Using the equation presented in Equation 3, the volatile contents were determined due to the volatilization.

$$\text{Volatile content} = \frac{W_a - W_c}{W_a} \times 100\% \quad (3)$$

Where W_a and W_c represent the weight of the sample and the weight of the samples after combustion.

3.2.4 Determination of Fixed Carbon (FC)

The fixed carbon content for the orange peels was determined using Equation 4.

$$\text{Fixed Carbon} = 100 - \%MC - \%AC - \%VC \quad (4)$$

3.2.5 Evaluation of the Lignocellulose Composition

The modified methods presented by Ayala *et al.* (2021) was adopted for the determination of the cellulose, hemicellulose, lignin and the extractive composition which makes the orange feedstock. In a typical experiment for the determination of the extractive composition, 4 g of the already dried and sieved sample was placed in a pre-weighed thimble and refluxed in 50% ethanol in acetone placed in a Soxhlet extractor's flask. The set up was refluxed for 8 h and the thimble-containing the sample was removed, dried at 105 °C overnight. The dried samples were then cooled in desiccator and thereafter, the weight loss which gives the percentage extractive was determined. The obtained products were then used as a feedstock for the determination of the water extractable where the procedures above were repeated under the application of water as a reflux medium. The experiment was performed in triplicate.

The samples obtained from the extractive determination were used in the evaluation of the percentage holocellulose content's determination. A 2 g of the extractable-free sample from the above was placed in an Erlenmeyer's flask containing 150 mL of distilled water, 1 g of sodium chlorite and 0.2 mL acetic acid placed in a water bath operating at 75 °C for 5 h. at every 1 h interval, 0.2 mL drops of acetic acid was added and a gram of sodium chlorite until a total achievable volume of 1 mL and a weight of 5 g of acetic acid and sodium chlorites were achieved. At the 5th hours of the experiment, the samples were removed from the water bath, filtered through a pre-weighed filter paper under the flow of distilled water until the yellowish coloration disappeared. The obtained samples were dried at 105 °C overnight. The dried samples were then cooled in desiccator and thereafter, the percentage weight difference gives the percentage holocellulose content.

The percentage content of the lignin was determined by the addition of 1 g of the products obtained from the extractable and refluxed in 15 mL of 75% H₂SO₄ and stirred at 400 rpm and 200 rpm for a period of 1 and 2 min respectively. The solution was poured in a 1 L flask containing 560 mL distilled water and refluxed for 4 h. the refluxed samples were filtered

through a pre-weighed filter, dried at 105 °C overnight. The dried samples were then cooled in desiccator and thereafter, the percentage weight difference gives the percentage lignin content.

In order to ascertain the cellulose content, 2 g of the samples obtained from holocellulose determination were introduced into an Erlenmeyer flask containing 10 mL of 17.5% NaOH. Subsequently, the mixture was allowed to stand at 20°C for 5 minutes. For every 5 min, a 5 mL solution of 17.5% NaOH was added until 25 mL of NaOH was achieved then, allowed to rest for 30 min. thereafter, 33 mL distilled water was introduced and the mixture was allowed to settle for a period of 1 h. Using 15 mL of acetic acid, the content in the flask was neutralized following the addition of 8.3 % NaOH until a pH=7 was achieved. The moisture was filtered through a pre-weighed filter paper and the obtained solid was oven dried at 105 °C overnight. The dried samples were then cooled in desiccator and thereafter, the percentage weight difference gives the percentage cellulose content. The percentage difference between the cellulose and holocellulose content gives the hemicellulose content.

3.3 Ultimate Analysis and HHV Evaluation

The ultimate analysis gives the percentage composition of the constituents' element such as CHNS-O in the sample materials. The elemental compositions (CHN) were characterized using CHN628 Analyzer while the Sulfur, S contents were obtained via SC-832DR (LECO. Co. USA) sulfur Analyzer. The oxygen content and the HHV was evaluated according to the relationship presented in Equation 5 and 6 (Liu *et al.*, 2018).

$$\text{Oxygen Content (\%)} = 100 - \%C - \%H - \%S - \%N \quad (5)$$

$$HHV \frac{KJ}{kg} = 0.3386C + 1.423H - 0.154O - 0.145N \quad (6)$$

Where C, H, N, O and S represents percentage composition of carbon, hydrogen, nitrogen, oxygen and sulphur respectively.

3.4 Solvothermal Liquefaction of Orange Peels

In order to determine the operating condition which, promote the effective depolymerization and HDO of the orange peels feedstocks into high quality crude bio-oil, the investigation of the effects of process parameters using a one-factor at a time optimization technique was adopted.

In all the cases of the STL experiment, a stainless-steel autoclave reactor having 500 mL volume capacity, 600 °C and 35 MPa maximum temperature and pressure respectively by Parr 4650, Illinois, USA was employed. The reactor was connected appropriately; feedstock and solvents were loaded as required using a constant weight of 10 g feedstocks and 100 mL solvents. For the first experimental case, the effects of temperature (230, 280, 330, 380, 430 and 480 °C) at constant reaction time of 15 min, 50:50 ethanol/acetone, 5 ± 1 °C/min heating rate, were investigated. Following the conclusion of the reaction, the reactor was rapidly cooled by continuously introducing water, and the resulting gas volume was determined by venting the reactor through the exhaust control valve into an inverted measuring cylinder filled with water. The solid–liquid products that had formed during the experiment were transferred into a beaker and subjected to acetone washing until a clear solution became visible. The effects of reaction time (at a constant temperature that yielded the highest biocrude) and the solvent ratio (ethanol: acetone) at a constant temperature and time (which also resulted in the highest biocrude yield). This analysis aimed to understand how different process conditions influence the yield biocrude and the energy contents. Similar methodology was adopted during the catalytic STL of the orange peels over Fe/CNSs.

3.4.1 Biocrude Separation

Solid residue containing solvent and biocrude was filtered through a pre-weighed Whatman No. 1 filter paper under vacuum. The solid residue was completely washed with acetone until droppings of colorless filtrates were observed. The retained solid residue on the pre-weighed filter paper was dried at 110 °C for a period 6 h in a convention oven and the yield of the solid residues were determined by comparing the solid residue yield with the weight of the feedstock. The solvents were recovered from the filtrate through the application of rotary evaporator operating at reduced pressure of 0.1 bar and temperature of 79 °C for a period of 2 h in a pre-weighed round-bottomed flask. The yields of the biocrudes were further estimated by comparing the retained weight to the weight of the biomass feedstock. In all the cases studied, the biocrude yield, solid residue yield, volume of gas yield (mL/g) and the biomass conversions were obtained using the expression in Equation 8-11 respectively. The deduced parameters; Equation 12-18 were obtained using the relationships presented by He *et al.* (2020) and Zhang *et al.* (2020).

$$\text{Biocrude yield } \left(\frac{w}{w} \% \right) = \frac{\text{Weight of biocrude after solvent removal}}{\text{Weight of biomass feedstock}} \times 100 \quad (8)$$

$$\text{Solid residue yield } \left(\frac{w}{w} \% \right) = \frac{\text{Weight of solid residue after drying}}{\text{Weight of biomass feedstock}} \times 100 \quad (9)$$

$$\text{Biomass conversion } \left(\frac{w}{w} \% \right) = 100 - \% \text{ Solid residue} \quad (10)$$

$$\text{Volume of gas produced } \left(\frac{mL}{g} \right) = \frac{\text{Volume of gas produced (mL)}}{\text{Weight of reactants (g)}} \quad (11)$$

$$EF = \frac{\text{HHV of biocrude}}{\text{HHV of orange feedstock}} \quad (12)$$

$$DO = \left(1 - \frac{\text{Carbon in biocrudes}}{\text{Carbon content in orange feedstock}} \right) \quad (13)$$

$$CRE = 100 - \% \text{Decarbonization} \quad (14)$$

$$HG = \frac{H \text{ in biocrude} - H \text{ in feedstock}}{H \text{ in biocrude}} \times 100 \quad (15)$$

$$ER = \frac{\text{HHV of biocrude}}{\text{HHV of feedstock}} \times \text{Biocrude yield} \quad (16)$$

$$CR = \frac{C \text{ in biocrude}}{C \text{ in feedstock}} \times 100 \quad (17)$$

$$CEI = \frac{\text{Carbon element at time } t - \text{Carbon elemnt of feedstock}}{\text{Carbon element at HHV condition} - \text{Carbon elemnt of feedstock}} \times 100 \quad (18)$$

Where; EF=Enhancement Factor; DO= Percentage Deoxygenation; CRE= Carbon Recovery Efficiency; HG=Percentage Hydrogenation; %ER=Energy recovery; CR= Carbon recovery; CEI= Carbon Element index and ERE= Energy Recovery Efficiency.

The experimental setup for the orange peels valorization is as shown in Fig. 8.

3.5 Chemical Vapor Deposition

3.5.1 Development of Ni Supported Kaolin Catalyst

Ni/Kaolin catalyst was developed via wet impregnation method. A 0.25M Ni(NO₃)₂·6H₂O in 50 mL distilled water was mixed with 10 g of kaolin sample and stirred to make an homogeneous slurry under a magnetic stirrer. The slurry was dried overnight at 105 °C, calcined at 550 °C for a period of 5 h under nitrogen flow. The calcined sample was allowed to cool, and thereafter, grinded and sieved to obtain particles with size ≤ 150 μm. The sample was kept in an airtight container for further application and characterization.

3.5.2 Development of Carbon Nanosphere and Purification

The catalyst obtained (Ni/Kaolin) was applied for the catalytic cracking of acetylene gas under nitrogen flow. About 0.5 g of Ni/kaolin catalyst was placed in a quartz crucible which was positioned into the center of the horizontal reactor. The reactor was purged through nitrogen introduction at 50 mL/min flow rate until a reaction temperature of 600 °C was achieved. At the reaction temperature, the flow rate of the nitrogen was increased to 100 mL/min while acetylene was introduced as a feed at 50 mL/min for a period of 30 min. After the completion of the reaction, the flow of the acetylene was stopped while that of the nitrogen was reduced to 50 mL/min until the reactor cools to room temperature. The produced CNSs containing catalyst particles were removed and kept for further application.

Due to the accompanied catalyst in the CNSs produced, the catalysts particles were removed through acid oxidation. Using a mixture of 3HNO₃:H₂SO₄, the as-synthesized CNSs was dispersed in the solution and stirred for a period of 1 h at 45 °C. The mixture was filtered while the oxidized CNSs was washed several times in distilled water until a neutral solution was observed. The obtained CNSs was dried at 105 °C overnight and tagged oxidized-CNSs.

3.5.3 The Fe/CNSs Development

The oxidized CNSs sample was impregnated with 0.2 mol/dm³ of the ferric nitrate nonahydrates salt in 10 mL of distilled water using wet impregnation method. The mixture was stirred for 3 h after which it was oven dried at a temperature of 110 °C for 7 h to remove water content, calcined at 450 °C for 5 h. The calcined sample was then grounded, sieved through 150 µm sieve and kept in an air-tight container.

3.6 Monometallic Ni, Fe, Zn and Ce Development over Biochar Support

The monometallic catalysts were developed to study the effects of metal particles on the HDO of oxygenated biocrude components most especially, the presence of ketones. Using the nitrate salts of the respective metals, an incipient wet impregnation method was adopted. In each case, 25 wt.% of the metal loading was carried out on 25 g of biochar as support. The procedure involves the addition of known weight of the metal salts in distilled water and the salts were allowed to completely dissolve. To the weighed support spread on a flat surface, the obtained solution was sprayed on the support and dried intermittently until the support completely absorbed all the metal solution. The impregnated support was then dried at 105 °C overnight

after which it was calcined and reduced at 450 °C and 400 °C for 4 and 8 h in N₂ and H₂ flow, respectively.

3.6.1 Hydrodeoxygenation (HDO) of Cyclohexanone and Crude Bio-oil

The above STL procedure presented during the orange peels valorization was adopted except that, a different reactor which contains a stirrer under nitrogen flow at 10 bar initial pressure was used. The gaseous products were also collected for analysis. The monometallic catalysts were employed for the HDO of the model compounds while the NiCeMo supported CNSs and IHC were used for the crude bio-oil upgrading. The weight of the catalyst was maintained at 4g and the feedstock was 10 g while the 90 g of ethanol serves as solvent and hydrogen source.

3.6 Synthesis of ZSM-5

Using the modified methods reported by Hartanto *et al.* (2019)(Hartanto *et al.*, 2019) and Hartati *et al.* (2020) , template and template free synthesis of ZSM-5 was studied at various Na₂O/Al₂O₃, crystallization temperature and time. Typically, tetraethylammonium hydroxide (TEAOH) was used as a templating agent for the shape, size and pore structure control in the ZSM-5 synthesis in a hydrothermal set-up. The synthesis route is guided by the molar ratio of the constituent' elements as indicated in Equation 7 according to Hartanto *et al.* (2019).



Sodium hydroxide, LUDOX-30 (30% SiO₂) and kaolin were used to adjust the compositionally framework of the hierarchical ZSM-5 throughout the synthesis. A 1 g of kaolin was added to a solution containing 1.94g NaOH in 30 g of distilled water and stirred for 15 minutes. Using a separate beaker, 56.91g of LUDOX-30 was continuously stirred in about 9.15 g H₂O and the resulting solution was added slowly to the first beaker under stirring. To the slurry produced, 2 g of TEAOH (in a template free approach, TEAOH was not included) was added drop wisely and the stirring continues for 8 h. The gel formed was transferred into a Teflon-lined autoclave and heated in an oven at 180 °C for 5 h (the time and the temperature were varied in this research). The mixture was allowed to cool, washed with distilled water, filtered and dried at 105 °C overnight. The obtained crystals were calcined at 550 °C for a period of 1 h for mesoporosity development through the disintegration of the structural directing agent (SDA) - TEAOH. This procedure gives Na-ZSM-5 zeolite.

The protonated HZSM-5 form of the ZSM-5 was produced through reflux in ammonium nitrate solution by cation-exchange process. A 10 g Na-ZSM-5 zeolite was mixed with 1000 mL NH_4NO_3 (1 M) and refluxed for 6 h. This procedure was repeated for three time to completely exchange the Na^+ with the H^+ to form a protonated HZSM-5 zeolite while the refluxing takes place at 80 °C. The obtained crystals were washed in distilled water severally, filtered through a vacuum pump and dried at 105 °C overnight.

The effects of dealumination kaolin were further studied where the beneficiated kaolin was subjected to 64 % sulfuric acid solution under heating at 188 °C for aluminum removal (and Al activation for bounding), pore opening and surface area enlargement. The stirring was left for 2 h while keeping the solvent: kaolin ration to 3:1. The obtained mixture was filtered while the kaolin was washed several times to attain a neutral pH, dried at 105 °C overnight, and then calcined at 550 °C for 3 h. The dealuminated kaolin obtained from this process was further subjected to the hydrothermal process to understand the effects of dealumination on the structural properties of HZSM-5 synthesis. Several HZSM-5 catalyst were produced and were coded as indicated herein: 1_HZS(5) and 1_HZNS(5). Where the “1” represents the synthesis number, HZS denotes HZSM-5 under SDA, HZNS implies the HSZM-5 without SDA and “(5)” represents the ratio of Na_2O to Al_2O_3 . In the case of the dealuminated kaolin as precursor, ‘b’ is included in the synthesis number [1b_HZS(5)]. For the in-situ synthesis of HZSM-5 under CNSs as a growth basis, the procedure for the synthesis of HZSM-5 as presented above was adopted except for the introduction of 5g of CNSs and 10 g of ethanol as a dispersant into the sodium hydroxide solution. The material obtained through this procedure is tagged, IHC.

3.6.1 Development of NiCeMo and NiCeMo Supported CNSs and IHC

Using a metal loading of 25, 10 and 5 wt% for Ni, Ce, Zn and Mo on CNSs and IHC, the respective catalysts were developed. Unlike the monometallic synthesis route presented previously, the three metal salts were mixed together and impregnated on the surfaces of the supports as presented previously. The obtained catalysts were kept in an air-tight container for further characterization and HDO potential.

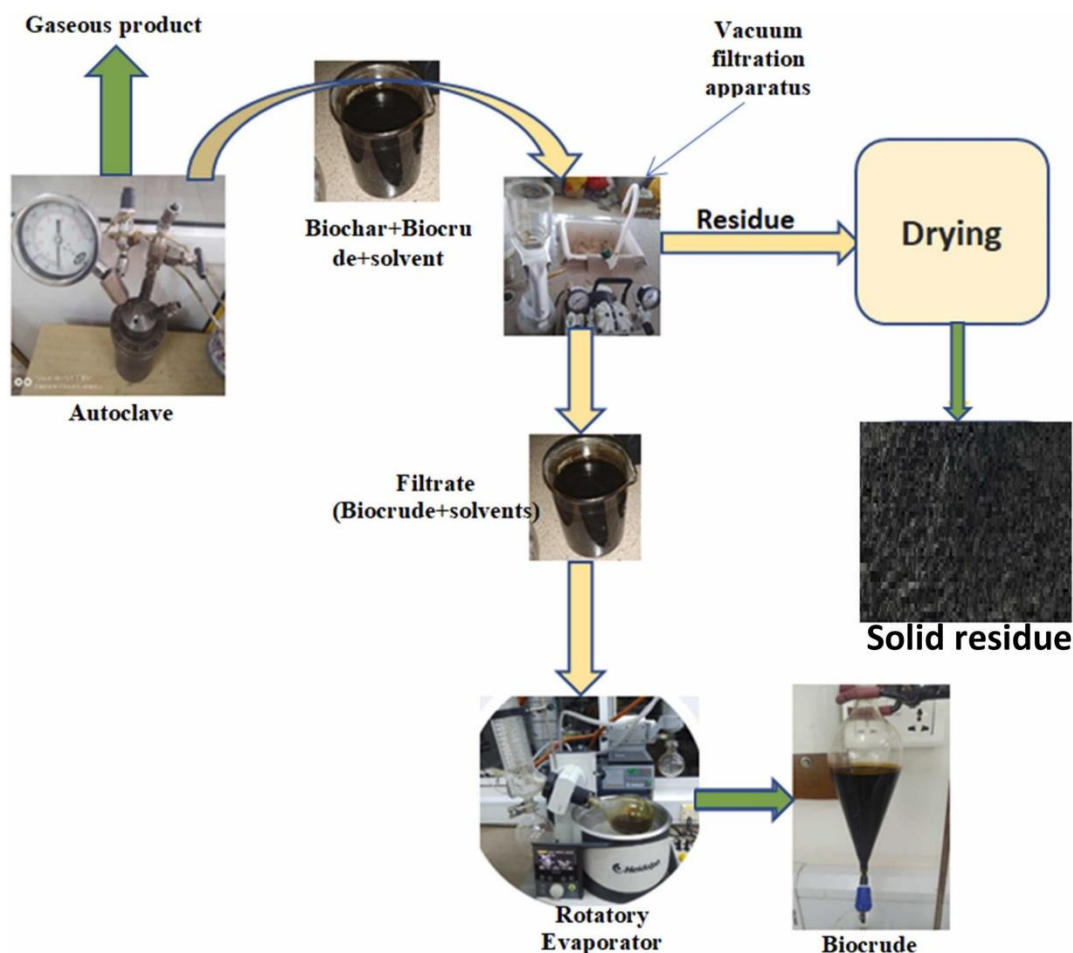


Figure 8: Experimental set-up for the STL of orange peels in a stainless-steel autoclave

3.7 Characterization Techniques

The CHN compositions were determined via CHN628 analyser while the S content was determined via SC-832DR (LECO. Co. USA) respectively. The TGA was analysed using SDT Q600 TA instrument, USA under the flow of nitrogen environment. The N_2 absorption-desorption was determined using Nova by Anton-Parr. The gas compositions were determined using GC (IGC 7200, DCScience) consisting of a carboxen 1000 column supplied by Sigma Aldrich, TCD (for H_2 , CO , CO_2 , and CH_4) and FID detector (for C_2H_4 , C_2H_6 , C_3H_6 , and C_3H_8 detection) under hydrogen (8%) and helium flow. The biocrude composition was also analysed using GC-MS by Agilent Technologies (7890 A GC system by Agilent) coupled with a Mass Detector (MSD-5977 A USA) and series an auto-injector (7683B Series Injector by Agilent) with HP-5 MS column in helium environment. In each case of the GC-MS analysis, 1.0 μL of was prepared with 1:100 split ratio, the oven temperature was program at 45 $^{\circ}C$ for a period of 5 mins, followed by a ramp to a temperature of 280 $^{\circ}C$ for a duration of 10 mins at 8 $^{\circ}C/min$. The crystallinity of the catalyst was determined using XRD by PW1800 diffractometer

operating at scanning speed of 5 °/min, 40 kV, 55 mA generator settings and under CuK α material). The functional group was analysed using Nicoletis50 FTIR spectrometer by Thermo-Fisher Scientific Instrument. The samples were prepared by mixing KBr of spectroscopic grade and the analysis was performed using the DLaTGS ATR (Diffuse Light Absorption Total Reflection) technique. The average molecular weight was conducted on the tetrahydrofuran (THF) soluble fractions using Waters e2695 Gel Permeation Chromatograph (GPC) coupled with a Viscotek VE 3580 RI detector with a Styragel HR-0.5,1,4E,4 having a column with dimension of 7.8 mm \times 300 mm. The THF at 0.6 mL/min flow rate was employed as an eluent while polystyrene standards were used for calibration. The morphologies of the catalysts were analysed via the FE-SEM coupled with EDS (also for elemental mapping) and the HR-TEM images for the internal morphologies. The Omicron Sphera II photoelectron spectrometer was used to obtain the XPS spectra under the X-ray radiation source (Al-K α) at hv value of 1486.6 eV. The total acid number (TAN) which measures the acidity of the bio-oil was determined by the amount of potassium hydroxide in milligrams that is required to neutralize the acids in one gram of the samples via potentiometric titration TAN ASTM 664 method. Also, the water content was determined via titrimetric analysis using SI analytic instrument and the volume of the base used for the analysis was recorded.

CHAPTER FOUR

RESULTS AND DISCUSSION

4.1 Physiochemical Properties of the Orange Peels

The physiochemical and compositional analysis of the orange were determined to providing an insight into its suitability as feedstock for biocrude production. The proximate compositions and the compositional parameters of the orange peels are presented in Table 8. The elemental compositions are shown in Table 8 and the thermal stability of the orange peels is depicted in Fig. 9 was presented for the initial evaluation of the suitability for biocrude production. The presence of carbon content of 41.47 wt.% implies the transfer of carbon into biocrude which ultimately improved the shared HHV. The volatility nature of the orange peels was observed in the TGA result (Fig. 9). This observation is linked to the presence of organic species which are depolymerized constituents of lignin, cellulose, and hemicellulose. At the initial stage of the analysis, between 30-160 °C, the weight loss was attributed to moisture content with 5.89 wt.%. Further increase in temperature shows two dominant peaks degradation temperature (T_p) at 220.4 °C and 321.3 °C which are attributed to hemicellulose and lignin volatilization respectively. This is in agreement with the study conducted by Hornung and Stenzel (2019). The possible valorization of the orange peels into biocrude is deducible by the volatile constituents of 57.70 wt.% observed between 30-430 °C. Two main important information could be established from this observation; that the feedstock is potent for bio-energy production and that through adequate conversion approach within the degradation temperature, biocrude of high yield and conversion could be obtained.

Table 8: Main characteristics properties of orange peels on dry basis (db) (w/w%)

Proximate analysis				HHV (MJ/kg)
MC	VC	AC	FC*	HHV
5.83 ± 0.18	89.14 ± 0.20	3.72 ± 0.55	7.13 ± 0.86	18.88 ± 0.23
Compositional analysis (w/w%)				
Cellulose	Lignin	Hemicellulose*		
39.98 ± 0.54	4.81 ± 0.43	23.79 ± 0.34		

MC= moisture content; VC= volatile content; AC= Ash content; FC=Fixed carbon by difference; 100%-VC%-AC%; Hemicellulose=100%-Cellulose%-Lignin%-Extractive%-Ash%

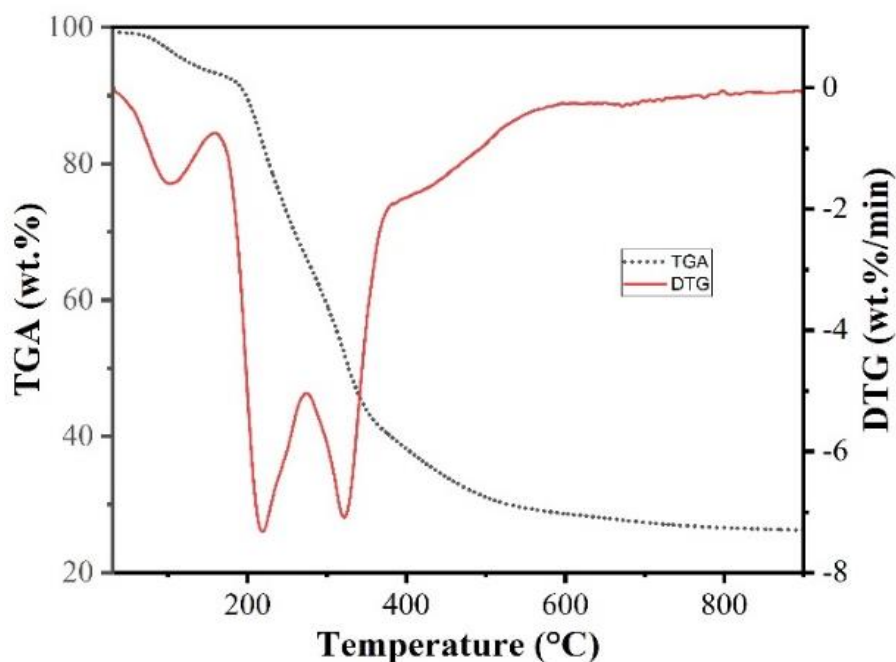


Figure 9: The TGA/DTG analysis of the orange peels feedstock in N₂ environment

The volatile contents and the energy density of the orange peels as indicated in Table 8 shows the suitability of orange peels as a feedstock for bio-oil through effective conversion process. The obtained values are closer to the values reported by Divyabharathi and Subramanian (2022) who worked on the optimization of biocrude production from orange peel feedstock via hydrothermal liquefaction process.

4.2 Non-Catalytic STL

The effects of process parameters, such as reaction temperature, reaction time, and the solvents' ratio (ethanol: acetone), were investigated on the biocrude yield, solid residue, volume of gas and the biomass conversion.

4.2.1 Effect of Reaction Temperature on Bio-Products' Yield

In order to evaluate the effects of process parameters that favor the STL of orange peels biomass, the application of one-factor at a time was adopted to establish the correlations which exist between process variables and products' yield. The effects of reaction temperature at constant feed to solvent ratio of 1:10, reaction time (15 min) and ethanol: acetone ratio (50:50) were investigated and the result is as shown in Fig. 10.

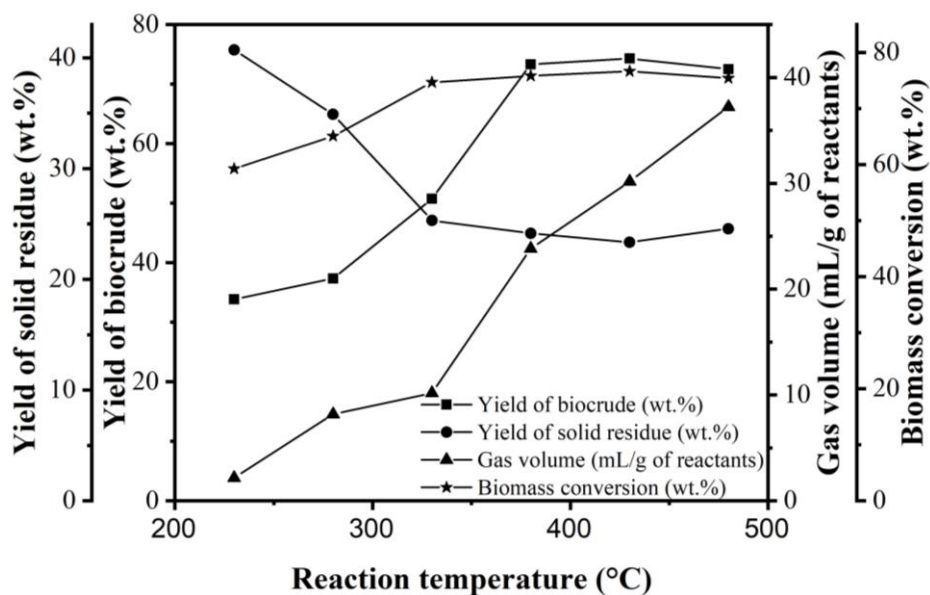


Figure 10: Effects of reaction temperature on bio-products' yield

As regards the biocrude yield, the biocrude yield was observed to increase progressively as the reaction temperature increases at constant time (15 min) and solvent ratio (50:50 of EtOH: acetone). The observable increase in biocrude yield as temperature increases is in accordance with the findings of Kazmi *et al.* (2023). The increase in biocrude yield due to an increment in temperature is attributed to an improved internal energy in the STL process and consequently promotes biomass decomposition. The percentage biocrude yield increases from 33.87 wt. % at 230 °C to 73.30 wt. % at 430 °C. The low biocrude yield of 33.87 wt. % at 230 °C could be associated with low biomass conversion due to incomplete depolymerization (degradation of higher percentage of hemicellulose and partial cellulose and lignin) at the subcritical region of the solvents (Demirkaya *et al.*, 2019b; Khampuang *et al.*, 2015). Corroboratively, the TGA thermograph of the feedstock (Fig. 9) indicates the peak degradation temperature (T_p) of 220.4 and 321.3 °C. Reaction temperature of 230 °C are considered low for optimum STL of orange peels into biocrude which inferably would produce biocrudes with lower yield and biomass conversion. Lower biocrude formations were also observed at 280 and 330 °C. Thus, the temperature was not sufficiently high enough to weaken the crystallinity of the cellulose and the lignin, preventing the hydrolysis reaction into glucose and other monomers, which could have been further be converted into aromatics. At 480 °C, the biocrude yield reduces by 0.65 wt.% compared to the biocrude yield obtained at 430 °C. The reduction in the biocrude yield

could be a result of secondary cracking reactions, which led to biocrude acting as feedstock and, therefore, promote gasification process over liquefaction.

Furthermore, the yield of biochar and the percentage conversion of orange peels exhibited an inverse relationship throughout the findings. This observation is in accordance with the findings of Demirkaya *et al.* (2019) who reported the effects of process parameters on the sub/supercritical valorization of hazelnuts. For instance, 40.71, 34.90 and 25.31 wt.% of solid residue were obtained at the reaction temperature of 230, 280 and 330 °C respectively. The temperature of 230 °C is below the peak degradation profile of lignin and the supercritical temperature of the two solvents hence, lower solvothermal cracking occurs and produces higher solid residue over biocrude formation with high acid contents. At a temperature closer to the T_p of the orange peels and at the supercritical regions on the solvents, 330 °C, the conversion was highly enhanced and resulted in a noticeable decrease in solid residue yield with 27.47 % when compared to the reaction temperature of 280 °C. The conversion follows an inverse relationship with solid residue yield in-line with the established relationship as described in Equation 10; the higher the yield of solid residue, the lower the biomass conversion.

The gas volume formation (mL/g of reactants) is an important factor which indicate the quantity of gaseous product obtained as a result of possible chemical reactions and cracking of large molecular weight compounds including the solvent during the solvothermal process (Brand & Kim, 2015). As previously described in various literature, that, the liquefaction process of biomass follows a complex reaction schemes involving decarbonylation, dehydroxylation, decarboxylation, deoxygenation and dehydration reactions which lead to CO₂, CO and H₂O formation (Li *et al.*, 2021). The biomass conversion increases as temperature increases from 59.29 to 76.65 wt.% at 230 to 430 °C as shown in Table 9. This finding is in accordance with the report of Li *et al.* (2021) who reported the effect of process variables on the thermochemical conversion of *Gracilaria corticata* microalgae into biocrude, and Biswas *et al.* (2020) who investigated the effects of temperature and solvent on bioproducts' formation.

4.2.2 Effect of Reaction Time on Bio-Products' Yield

The effects of reaction temperature at constant feed to solvent ratio of 1:10, reaction temperature (430 °C), and using an ethanol: acetone ratio (50:50) were investigated, and the results are shown in Fig. 11.

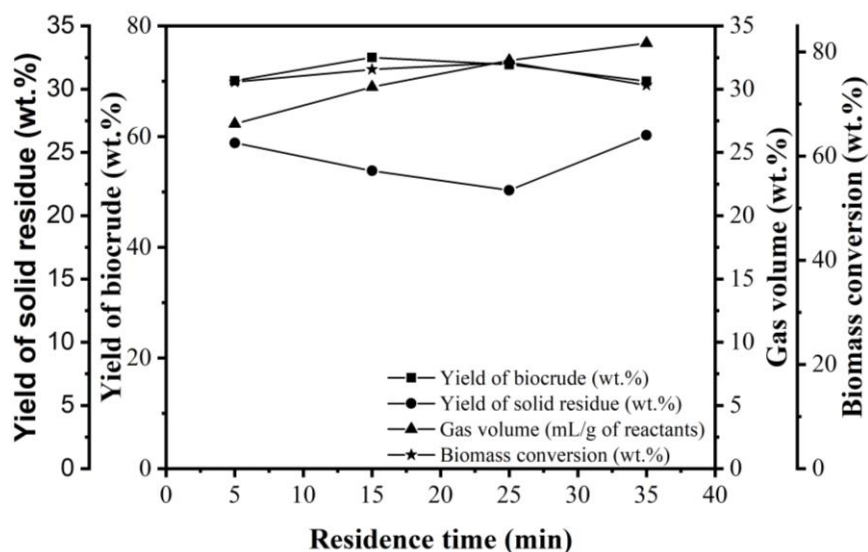


Figure 11: Effects of residence time on bio-products' yield

Residence time has been reported as an important parameters during the STL of biomass (Malins, 2017). Figure 11 shows that the yield of biocrude increased from 70.12 wt.% at 5 min to 74.30 wt. % at 15 min of the reaction time, followed by a subsequent decrease to 70.03 wt.% at 35 minutes. The first progression (5-15 min) indicates that there was enough residence time for high depolymerization of orange peels' constituents, resulting into an enhanced biomass conversion and promoting the aggregation of the produced gases into hydrocarbon monomers. According to the findings of Caprariis *et al.* (2017), the possible competition between the decompositions of the orange peels and the repolymerization reaction within biocrude's fragments during the degradation of holocellulose could lead to a reduction in the biocrude yield at longer reaction times, as observed between 25 and 35 minutes. The conversion of biocrude into volatiles, a secondary product, may account for the decrease in biocrude yield. This observation has also been reported in the findings of Bakari *et al.* (2021) who studied the effects of reaction parameters on the valorization of rice husks. At the optimal reaction time of 15 minutes, a preference for higher aggregation of gases and solid decomposition over repolymerization, condensation, and cyclization reactions was observed, which could contribute to the formation of gaseous products and solid residues. This observation is also

supported by the report of Rachel-Tang *et al.* (2017), who presented the catalytic solvolysis of biomass into biocrude.

4.2.3 Effect of Solvent Ratio on Bio-Products Yield

The effects of solvent ratio, while maintaining a constant feed to solvent ratio of 1:10, reaction temperature (430 °C), and residence time of 15 min were investigated and the results are presented in Fig. 12.

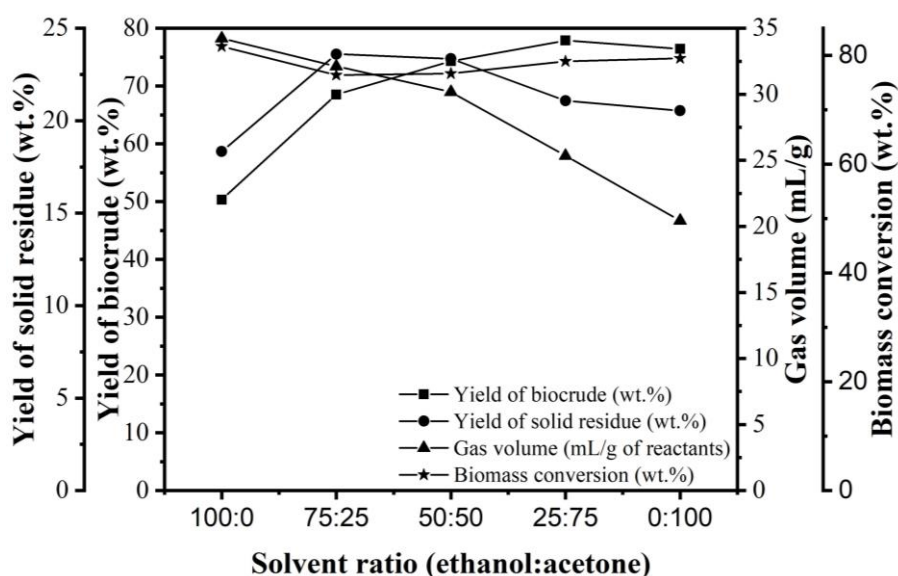


Figure 12: Effects of solvent ratio on bio-products' yield

Ethanol and acetone have been highlighted as promising solvents in the STL of biomass feedstock (Demirkaya *et al.*, 2019b; Fernandes *et al.*, 2021). From Fig. 12, the effects of solvents' ratio were studied by increasing the ratio of acetone in ethanol; 100:0, 75:25, 50:70, 27:75 and 0:100 (EtOH: acetone) during the STL of the orange peels. The products yield, while using pure ethanol under constant reaction conditions, were observed to be 50.34 wt.%, 18.34 wt%, 34.23 mL/g of reactant and 81.66 wt.% of biocrude yield, solid residue, gas product and biomass conversion, respectively. Meanwhile, the biocrude yield, solid residue yield and the gas yield obtained in pure acetone medium were 76.45 wt.%, 20.54 wt.% and 20.43 mL/g, respectively. The significant increase in the yield of biocrude derived from acetone could be linked to the improved solubility potentials of extractives and lignin, coupled with the cracking of organic soluble and intermediates at elevated temperature and the synergetic contribution of the dipolar aprotic characteristics of acetone at the supercritical conditions (Demirkaya *et al.*, 2019b). The addition of acetone to the ethanol medium enhances the biocrude yield compared

to using pure ethanol as a solvent to 68.53, 74.30, and 77.88wt% for 75:25, 50:50 and 25:75 (ethanol: acetone), respectively. The significant rise in biocrude yield upon the addition of acetone implies that acetone has contributory impact, promoting the enrichment of both polar and nonpolar soluble components in the orange peels' feedstock. At the solvent ratio of 75:25 (acetone: ethanol), the percentage biocrude yield increases as compared to pure acetone by 1.84 wt.%. This indicates the synergistic effects of acetone and ethanol as an excellent solvent mixture during the orange peels' valorization process, leading to an improvement in the biocrude yield.

4.3 Effect of Reaction Conditions on Biocrudes' Compositions

4.3.1 Effects of Reaction Temperature on Biocrude's Compositions

To determine the effect of reaction temperature quantitatively and qualitatively on the compositional make-up of the produced biocrude, GC-MS analysis was utilized, and the results are presented in Fig. 13.

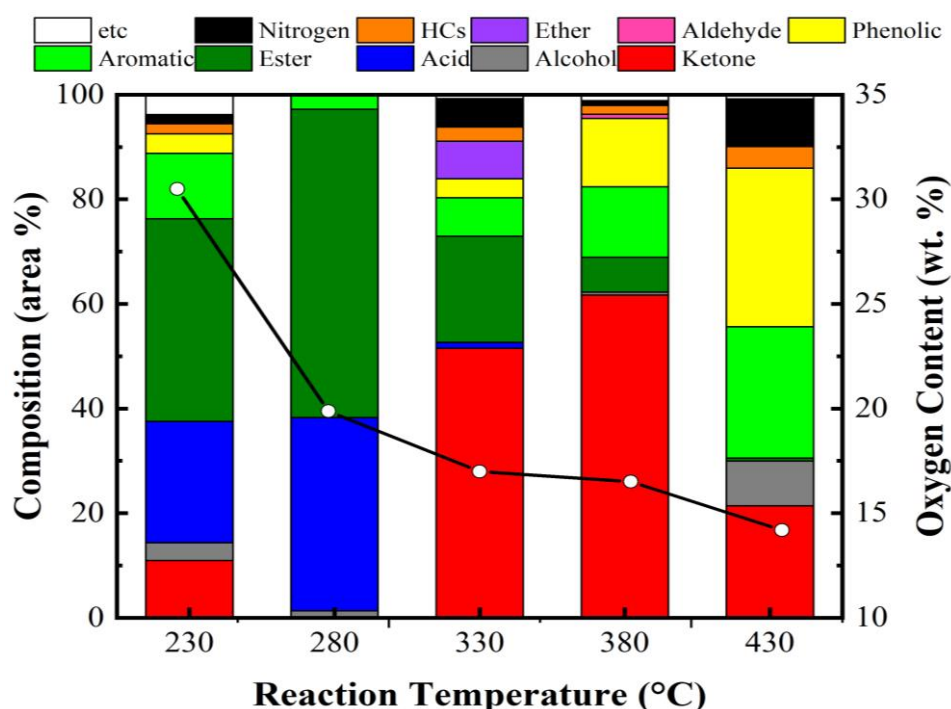


Figure 13: Effects of reaction temperature biocrude compositions

The presence of several oxygenated and non-oxygenated compounds was identified and presented based on their respective percentage area. The compositions were classified based on acid, alcohol, aldehydes, aromatics, phenols, ketones, ethers, esters, hydrocarbons, nitrogen containing compounds, and others (include heteroatoms, like chlorine, and sulfur containing

aromatic compounds). The identified compounds were produced through the depolymerization and decomposition of lignin, hemicellulose and cellulosic components of the orange peels, forming a complex mixture (Divyabharathi & Subramanian, 2021).

Although, the variation in the itemized compositions differs across various reaction conditions, providing insights into the optimum process parameters to be adopted for tailoring the biocrude properties of interest. For instance, at lower temperatures of 230 °C and 280 °C, as shown in Fig. 13, the biocrudes exhibit the highest compositions of acids and esters. This indicates that esterification and hydrolysis reactions are favored at lower reaction temperature. This observation further reveals that the production of high ester contents and acids were favored at low temperatures. The formation of ketones with percentages of 10.94%, 51.50%, 61.72%, and 21.45% at temperatures of 230°C, 330°C, 380°C, and 430°C, respectively, suggests a possible hydrogen transfer from the produced alcohol. Additionally, aldehyde formation, accounting for 0.80%, was also observed at 380°C. The possible conversion of alcohol to ketones and aldehydes through hydrogen transfer mechanism has been reported by Jun *et al.* (1998). The noteworthy observation here is the increasing trend in ketone selectivity at elevated temperatures of 330°C, 380°C, and 430°C. This indicates a substantial conversion of aromatic ethers into ketones and their derivatives, likely driven by hydrogenation and hydrolysis processes. This possible reactions phenomena is supported by the study of Meng *et al.* (2017), who investigated the synthesis of ketones from biomass-derived feedstock using solid catalysts.

As the temperature increases from 330 °C to 430 °C, the selectivity to acids formation was inhibited. This shows that, high temperature above the peak degradation temperature of orange feedstocks in the co-solvent environment retards hydrolysis reaction for acids formation. The most favorable conditions for the synthesis of aromatic ethers were observed at 330 °C, accounting for 7.15 % of the biocrude through etherification reactions. A similar observation was reported by Rorrer *et al.* (2019), where ethers were linked to the etherification reactions of acids, ketones, aldehydes and esters. Moreover, the biocrude obtained at different temperatures exhibits a lower hydrocarbon content and a higher selectivity towards oxygenated compounds, indicating the need for additional upgrading using the hydrodeoxygenation approach. The highest observable composition of hydrocarbon in all the reaction conditions shown in Fig. 13. indicates that 430 °C is the most favorable reaction condition for further study.

4.3.2 Effects of Reaction Time on Biocrude's Compositions

At the constant reaction temperature of 430 °C, with a feed to solvent ratio of 1:10, and residence time ranging from 5 to 35 minutes, and solvent ratio of 50:50 EtOH: Acetone. Like the temperature effect, various compounds were identified and classified, as illustrated in Fig. 14.

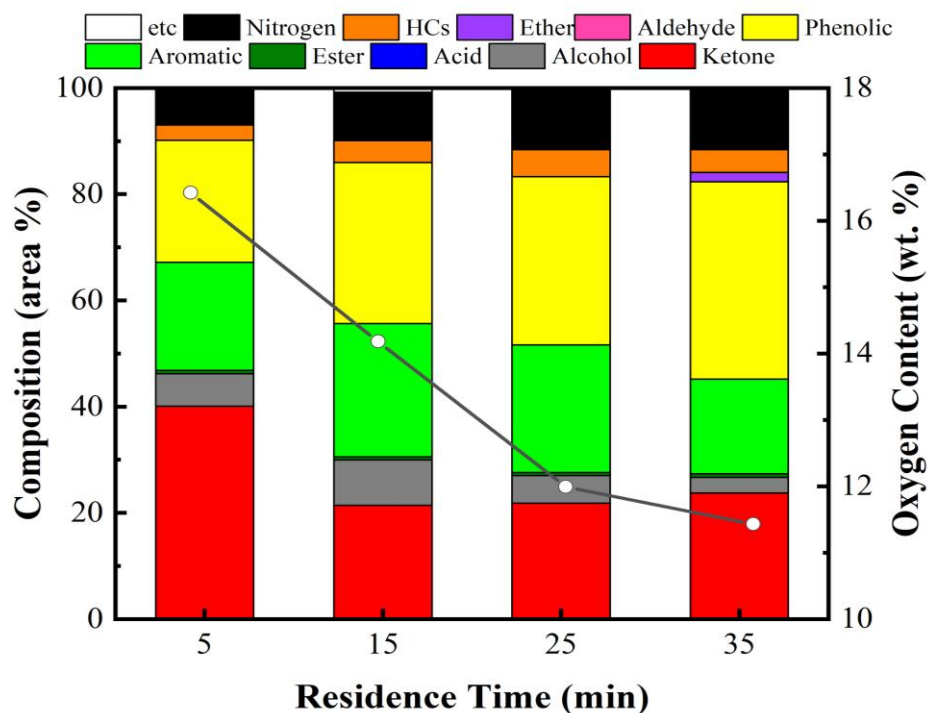


Figure 14: Effects of residence time on biocrude compositions

Notably, acids and aldehydes were not favored throughout the studied residence time at 430 °C. Primarily from Fig. 14, three main compounds; ketones, aromatics and phenolics were highly selectively produced during the studied conditions. About 40.07 % of ketones were selectively produced at the residence time of 5 min, while the concentration reduced to 21.44 % at 15 min. The formation of phenols and their derivatives were associated to the decomposition of lignin and carbohydrates through a series of reactions involving hydrolysis and subsequent methoxy- groups hydrolysis. This is in accordance with the findings reported by Carpio *et al.* (2021) who reported the effects of reaction time and temperature on the hydrothermal liquefaction of demineralized wastewater algal biomass. From the result presented in Fig. 14, the percentage composition of phenolics increases with increasing residence time. The stability of the produced ester-containing compounds and their derivatives becomes noticeable as the residence time increases, with a clear indication of a complete esterification reaction throughout the observations, resulting in no formation of acids. Hence,

high temperature solvothermal of orange peels favors the complete esterification reaction over reversed esterification. The formation of nitrogen-containing aromatics increases with prolonged residence time. This phenomenon can be attributed to the inherent instability of the aromatic intermediates produced, which exhibit a high tendency to react with nitrogen and other heteroatoms as the residence time is extended.

4.3.3 Effects of Solvent Ratio on Biocrude's Compositions

The effects of EtOH to acetone ratio on the compositional make-up of the produced biocrudes at constant reaction temperature and residence time were evaluated and the results are shown in Fig. 15.

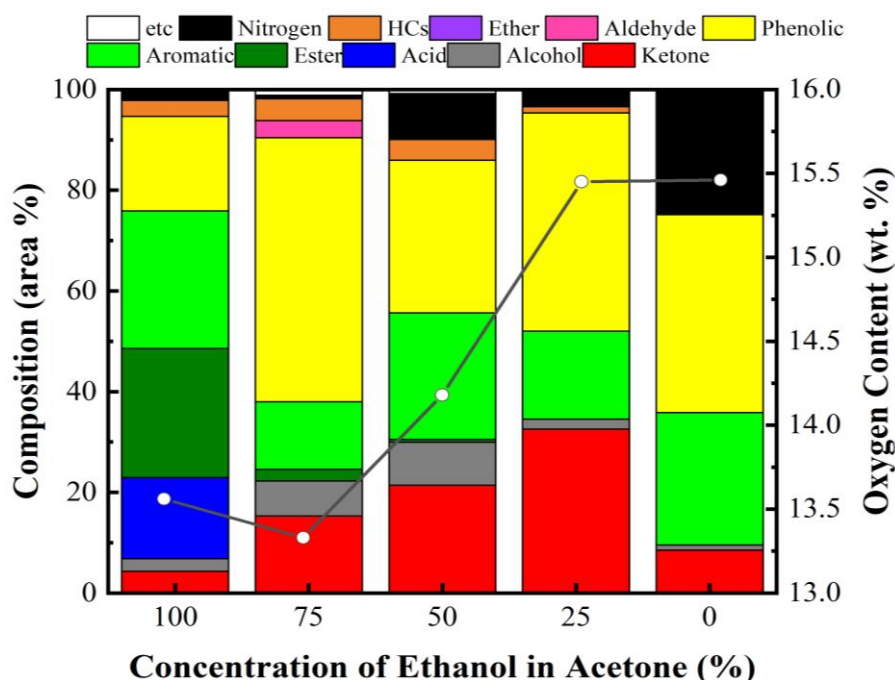


Figure 15: Effects of solvent ratio on biocrude compositions

Based on the result presented in Fig. 15, there is an increase in the percentage composition of ketones as the acetone loading on ethanol increases. For instance, at 100 % ethanol (0 % acetone), the observable presence of ketones is 4.36 % and this increases to 15.30, 21.44 and 32.58 % at 75, 50 and 25 % ethanol in acetone, respectively. This implies that the introduction of acetones in ethanol solvent enhances the ketonization reaction by improving hydrogen transfer mechanisms through solvent cracking and carboxylic acids conversion. This process is capable of promoting carbon dioxide and water formation. The biocrude produced in 100 % ethanol as solvent favors hydrolysis and reverse esterification which could be associated with the production of acids (Kazmi *et al.*, 2023).

Table 9: Elemental analysis of biocrudes produced at different reaction conditions

	Solvothermal liquefaction products				Elemental composition (%)							Deduced data from biocrude properties							
	Biocrude	Solid residue	Gas volume	Biomass conversion	N	C	H	S	O	O/C	H/C	HHV	EF	DO	CRE	HG	ER	CR	CEI
	(wt.%)	(wt.%)	(mL/g)	(wt.%)															
Orange feedstock	-	-	-	-	0.77	41.47	6.00	0.10	51.66	0.94	1.72	14.49	-	-	-	-			-
Effect of temperature																			
230,15min,50:50(A)	33.87	40.71	2.18	59.29	1.54	60.70	7.27	0.01	30.49	0.38	1.43	25.94	1.79	40.99	68.32	17.46	60.64	49.57	0.52
280,15min,50:50(B)	37.34	34.90	8.18	65.10	1.80	71.23	7.11	0.00	19.87	0.21	1.19	30.87	2.13	61.54	58.22	15.56	79.54	64.139	0.81
330,15min,50:50(C)	50.75	25.31	10.18	74.69	1.22	73.17	8.62	0.00	16.99	0.17	1.40	34.20	2.36	67.11	56.68	30.39	119.79	89.54	0.86
380,15min,50:50(D)	73.33	24.15	23.82	75.85	0.69	73.97	8.83	0.00	16.51	0.17	1.42	34.93	2.41	68.04	56.06	32.06	176.75	130.80	0.88
430,15min,50:50(E)	74.30	23.35	30.18	76.65	0.41	76.42	8.99	0.00	14.18	0.14	1.40	36.38	2.51	72.55	54.27	33.29	186.57	136.92	0.95
Effect of reaction time																			
430,5min,50:50(F)	70.12	25.76	27.27	74.24	0.40	74.36	8.81	0.00	16.42	0.17	1.41	35.09	2.42	68.21	55.77	31.92	169.79	125.74	0.89
430,15min,50:50(G)	74.30	23.35	30.18	76.65	0.41	76.42	8.99	0.00	14.18	0.14	1.40	36.38	2.51	72.55	54.27	33.29	186.57	136.92	0.95
430,25min,50:50(I)	73.01	22.01	32.27	77.99	0.41	73.49	8.80	0.00	17.30	0.18	1.43	34.63	2.39	66.51	56.43	31.79	174.51	129.40	0.87
430,35min,50:50(J)	70.03	26.36	33.64	73.64	0.64	78.42	9.51	0.00	11.43	0.11	1.44	38.18	2.63	77.87	52.88	36.88	184.52	132.44	1.00
Effect of solvent ratio																			
430,15min, 100EtOH(K)	50.34	18.34	34.23	81.66	1.31	75.87	9.26	0.00	13.56	0.13	1.45	36.55	2.52	73.76	54.66	35.23	126.97	92.10	0.93
430,15min, 75EtOH:25Acetone (L)	68.53	23.60	32.12	76.40	0.40	75.37	8.78	0.00	15.45	0.15	1.39	35.53	2.45	70.09	55.02	31.63	168.02	124.56	0.92
430,15min, 50EtOH:50Acetone(M)	74.30	23.35	30.18	76.65	0.41	76.42	8.99	0.00	14.18	0.14	1.40	36.38	2.51	72.55	54.27	33.29	186.57	136.92	0.95
430,15min, 25EtOH:75Acetone(N)	77.88	21.08	25.35	78.92	0.59	76.83	9.25	0.00	13.33	0.13	1.44	37.00	2.55	74.19	53.98	35.16	198.85	144.29	0.96
430,15min, 100Acetone(O)	76.45	20.54	20.43	79.46	0.45	75.54	8.55	0.00	15.46	0.15	1.35	35.26	2.43	70.07	54.90	29.83	186.01	139.27	0.92

4.4 Energy Composition and Van-Krevelen Plot

Table 9 shows the elemental compositions and deduced energy related parameters of the biocrudes obtained at several reaction conditions. The production of high quality biocrude via STL process has been observed to depend on various process parameters and adequate attention has been channeled to evaluate the inter-relationship that exists through several correlation factors. The HHV is one of the most important parameters which could be identified to be primarily depends on the degree of HDO process.

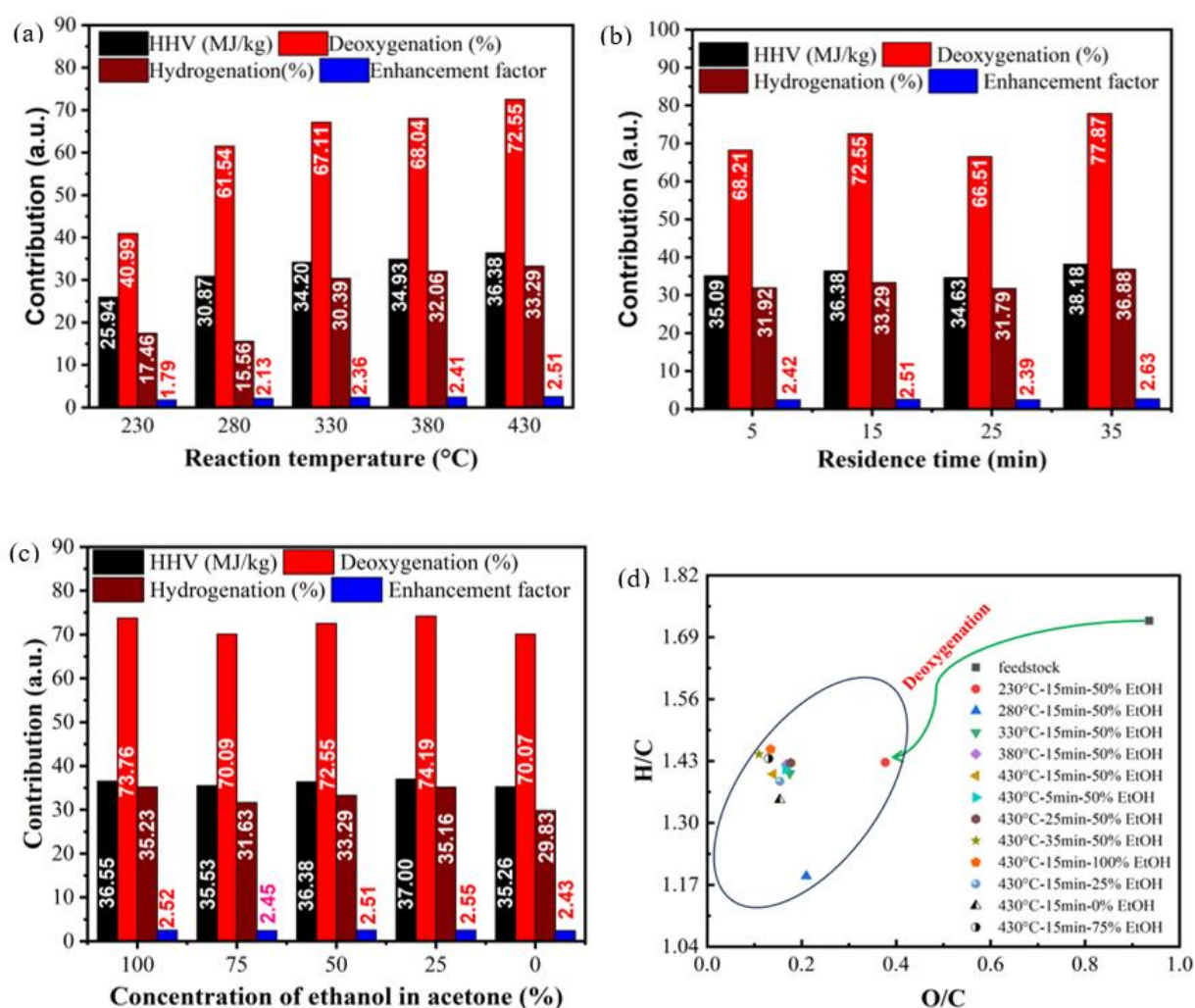


Figure 16: Inherent biocrude properties relative to (a) reaction temperature (b) residence time (c) solvent ratio and (d) Van-Krevelen plot

From Fig. 16a, the HHV (MJ/kg) increases with an increasing reaction temperature; from 26.96 to 36.38 MJ/kg at 230 to 430 °C reaction temperature. The HHV was observed to possess a direct relationship between the deoxygenation (%) and hydrogenation (%) except at the reaction temperature of 280 °C where a little decrease in the hydrogenation was observed. The

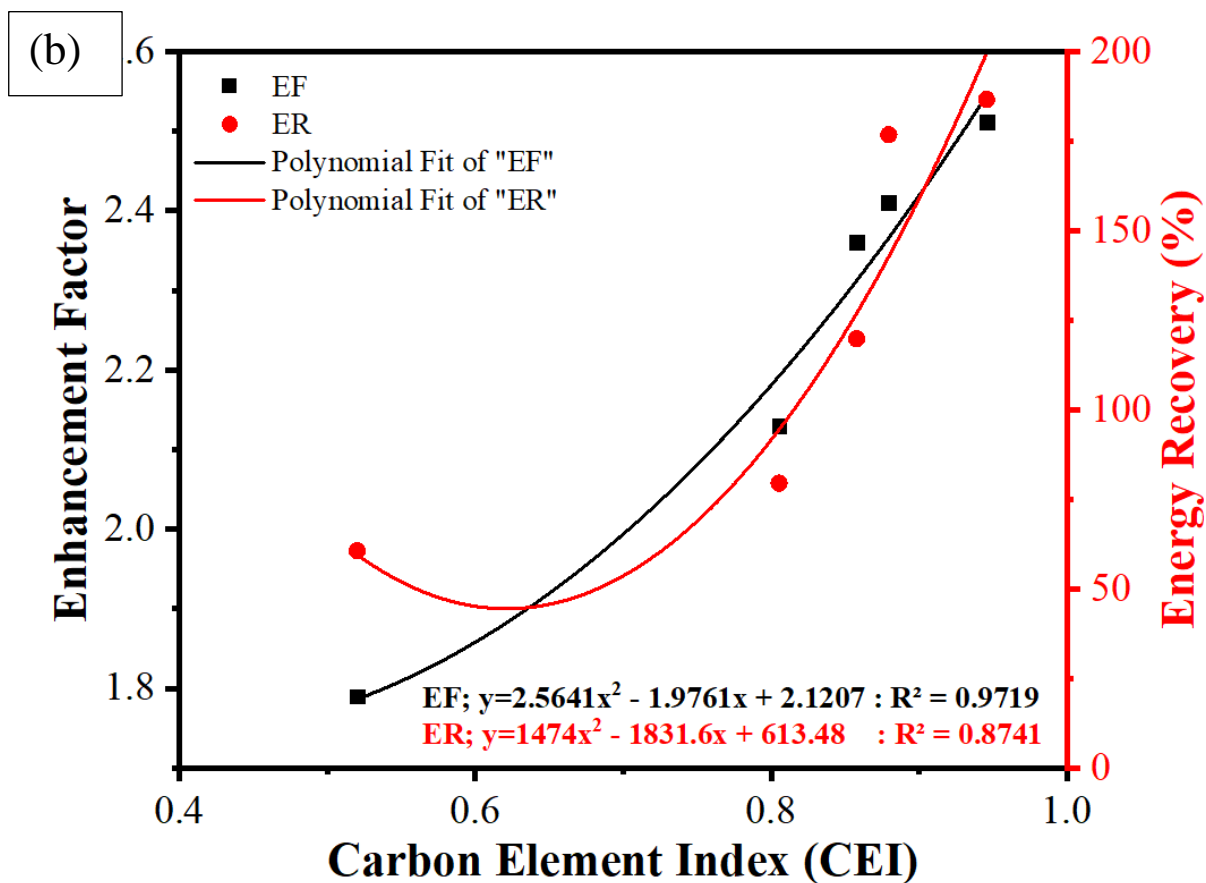
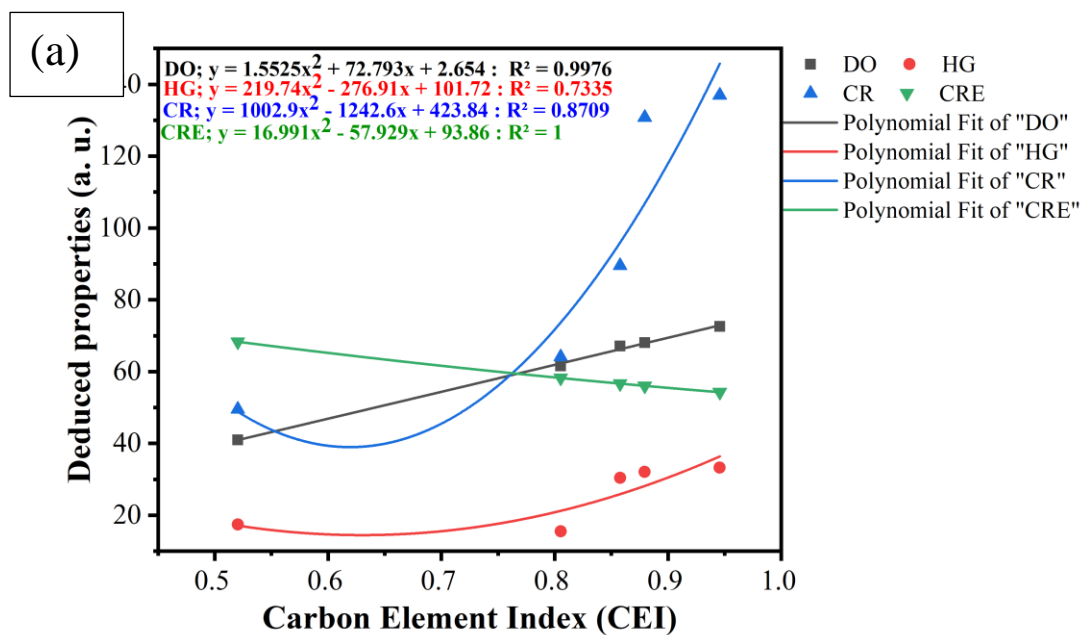
decrease in HHV is supported with the compositional results shown in Fig. 13 where reversed esterification which led to high acid formation was observed over esterification reaction. Similar observation of increasing temperature on the HHV of biocrude has been reported in various literature during the catalytic HDO of waste coffee oil in supercritical ethanol medium (Kazmi *et al.*, 2023).

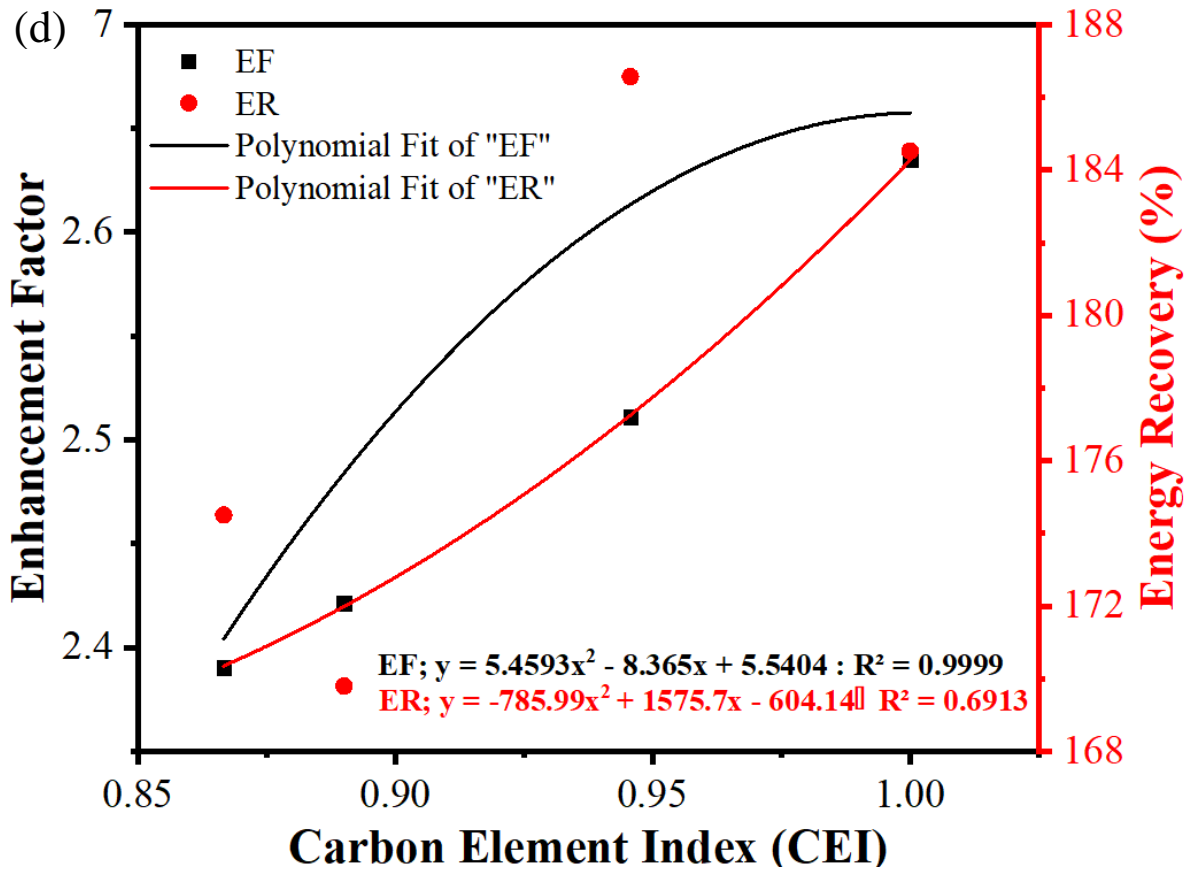
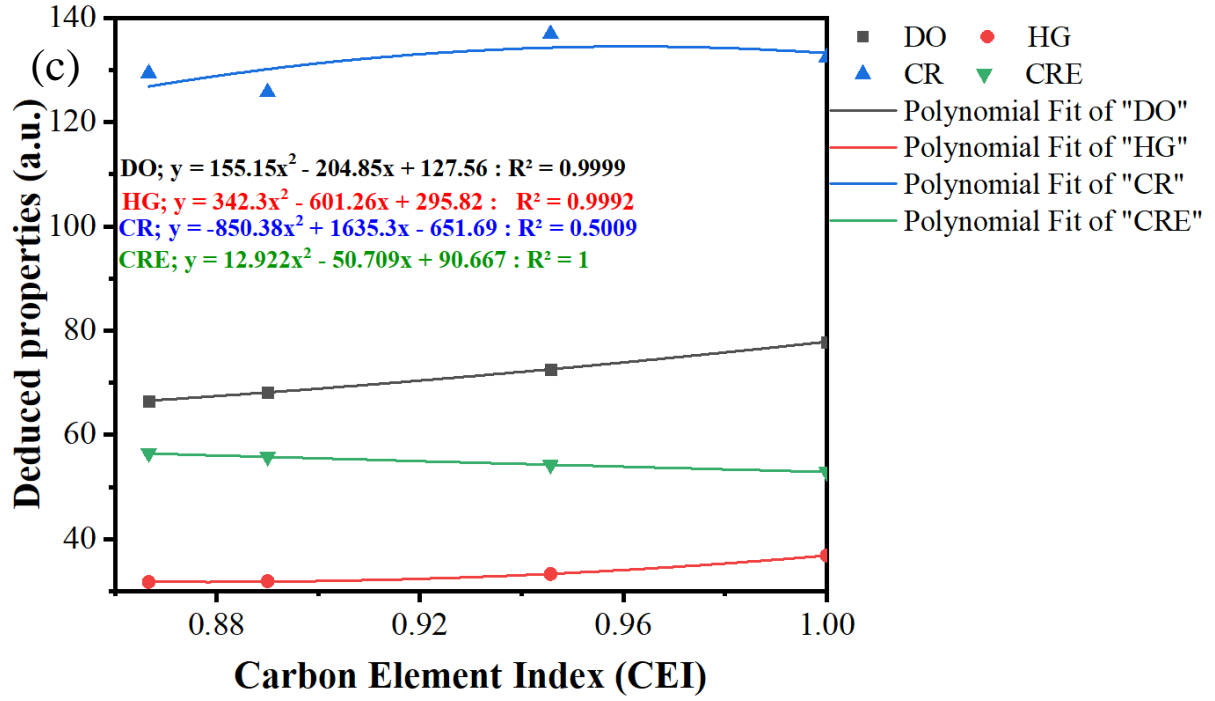
The progressive increase in HHV as temperature increases promotes the enhancement factor (EF) which compares the HHV of biocrude at a certain condition to the HHV of the initial feedstock as shown in Fig. 16b. The HHV observed at the effect of reaction time was noticed to follow a sinusoidal effect where the HHV increases from 5 to 5 min with a decrease at 25 min reaction time. This sudden decrease in the HHV could be associated with the cracking of side alkyl chains, which mostly contain H and C. As a result, an increase in the oxygen content is observed at the residence time of 25 minutes, as shown in Fig. 14 and Table 8. Highest HHV was obtained to be 38.18 MJ/kg at the reaction temperature of 430 °C, 35 min residence time and 50:50 EtOH to acetone ratio with the highest enhancement factor of 2.63. The HHV of 38.18 MJ/kg observed is higher than the reported HHV of 37.76 MJ/kg obtained during the catalytic depolymerization of orange peels over Fe supported carbon nanospheres and 25% ethanol in acetone as reported by Divyabharathi and Subramanian (2021) who reported 32MJ/kg. Furthermore, the introduction of 75 % acetone was found to improve the HHV from 36.66 MJ/kg at 100 % EtOH to 37.00 MJ/kg due to an improved deoxygenation process during the depolymerization process as depicted in Fig. 16c.

The Van-Krevelen plot which is shown in Fig. 16d shows the degree of hydrodeoxygenation (HDO) process where O/C and H/C are important parameters that depict biocrude properties. The lowest O/C ratio was observed to be 0.11 as compared to the starting orange peels with 0.94. Biocrude with the lowest O/C and H/C ratio was obtained at the reaction temperature of 430 °C, 35 min reaction time and 50:50 solvent ratio of EtOH to acetone. In order to enhance the H/C ratio of the biocrude with an O/C ratio of 0.11, it is necessary to conduct a hydrodeoxygenation (HDO) process by selectively developing a catalyst for improved conversion. Also, the decrease in oxygen and nitrogen contents in the biocrude obtained throughout the process conditions as compared to the starting orange peels feedstock are associated to the possible reactions such as dehydration and de-methanation during the solvothermal process (Liu *et al.*, 2022).

4.5 Biocrude's Properties Correlation

The percentage deoxygenation (DO), percentage hydrogenation (HG), carbon recovery (CR), carbon recovery efficiency (CRE), enhancement factor (EF) and energy recovery (ER) were correlated and fitted with carbon element index (CEI) as depicted Fig. 17. The results presented contained the fitting model, the regression line, correlation coefficient, R^2 and the fitting equation in all cases. The physiochemical properties presented were suitable to a polynomial expression $y = cx^2 + bx + a$ as adopted from the findings of He *et al.* (2020) where the effect of residence time possesses the highest correlation coefficient, R^2 of above 0.9 for the percentage DO and HG and CRE.





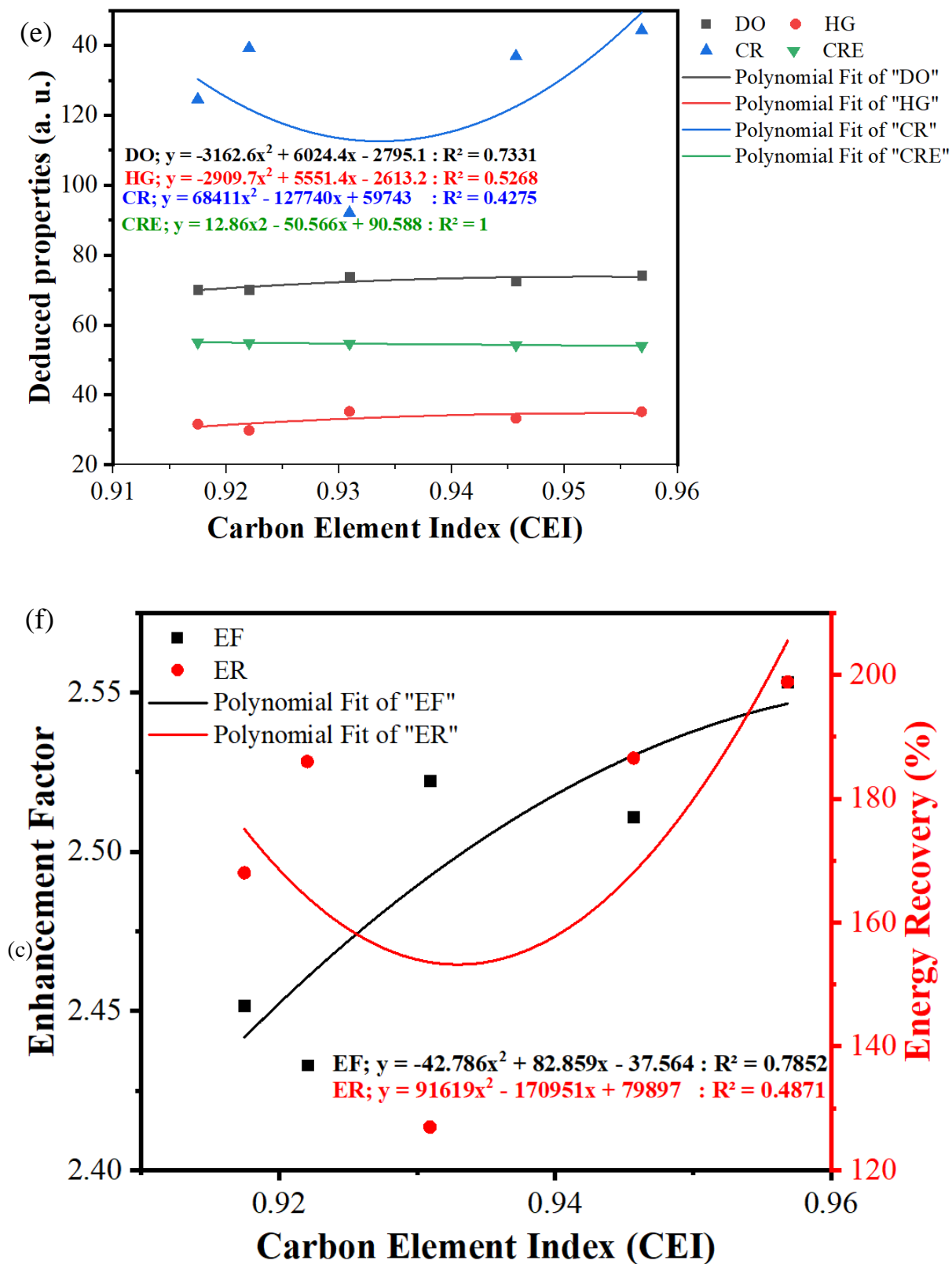


Figure 17: Correlations between: (a,c, e) physicochemical properties and (b,d,f) energy properties against carbon element index

The information from the polynomial is highly relevant to providing the severity of the liquefaction process during the investigation of the effects of residence time followed by

temperature and solvent ratio as the CEI increases. From the correlation coefficients, the b and c parameters signify the elements' sensitivity as a function of CEI and then, depends on the severity of the liquefaction conditions. The energy properties analysis of the liquefied orange peels which shows the relationship between enhancement factor and energy recovery on the carbon element index at various reaction conditions. As the severity of the process conditions increases, most especially, when the effects of temperature and time were considered, the EF and ER increases with a gradual corresponding increase in the CEI. Hence, the relationships established through the polynomial fittings help in correlating between the energy parameters (EF and ER) and the liquefaction conditions. A more direct relationships were observed in the effects of temperature and residence time on the enhancement factor where the regression coefficient, R^2 were greater than 0.9.

4.5.1 Combustion and Molecular Weight Distribution Analysis of Biocrudes

The thermogravimetric analysis is an important tool which reveals the thermal stability of biocrude, boiling point range to enable the quantification of the presence of several fractions and the inherent coke formation due to the possible presence of polyaromatics hydrocarbons in the biocrude. Figures 18a and b show the TGA and the DTG plots of biocrudes having the highest heating values in the present reaction conditions considered. The deduced data presented in Table 10 shows the variations in the thermal properties due to the different fractions contained in the biocrude.

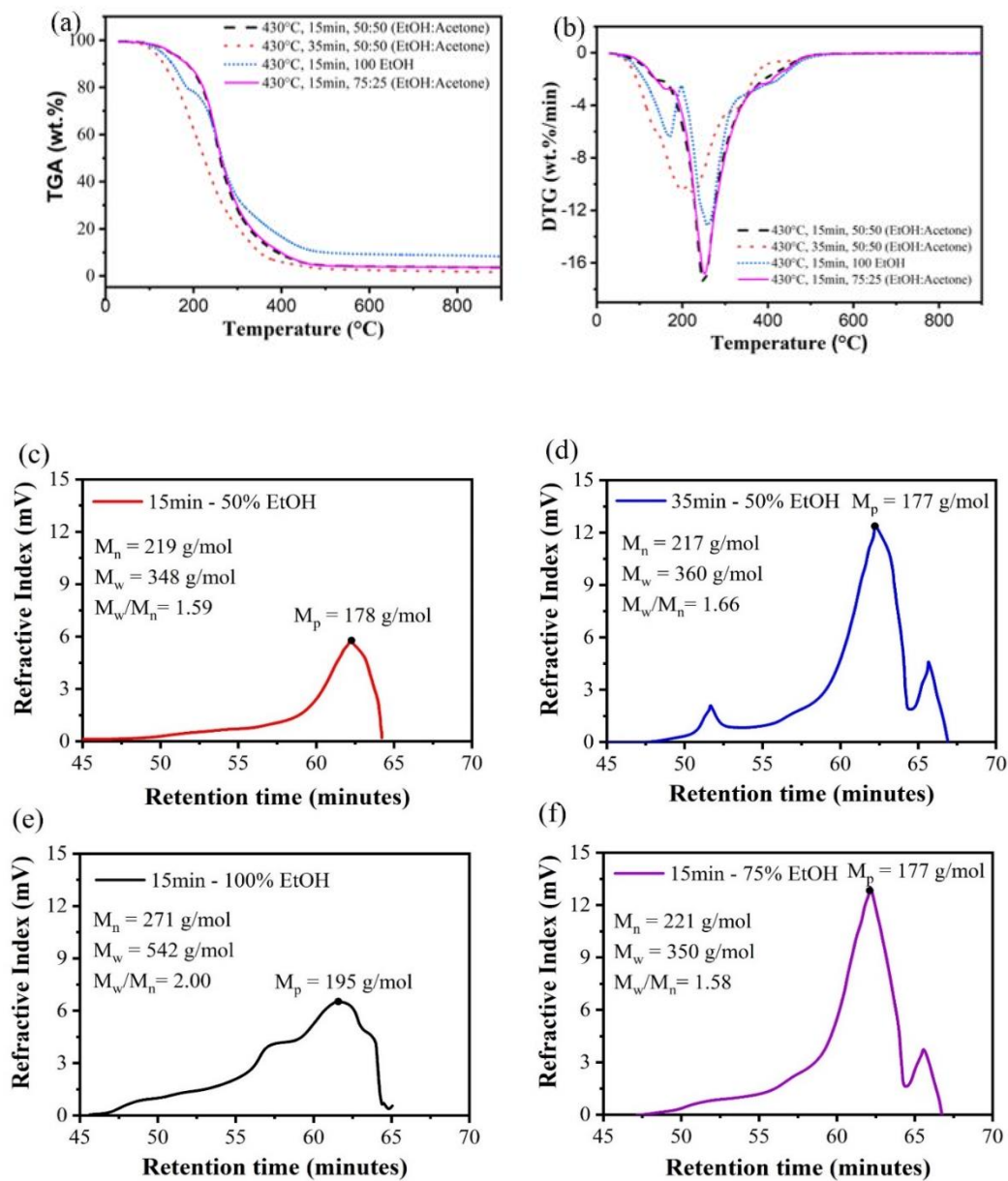


Figure 18: (a) The TGA and (b) DTG (c-f) GPC plots of biocrudes obtained with the highest HHV

Table 10: The TGA result of some selected biocrude based on HHV

Sample	Onset temp. (T_{onset}) (°C)	Peak degrad Temp, T_p (°C)	< 180 °C (Light volatiles) (wt.%)	180-360 °C Medium volatiles (wt.%)	360-550 °C Heavy oils (wt.%)	>550 °C Inorganics and coke (wt.%)	Total volatiles (30-900 °C) (wt.%)
430 °C,15min,50%EtOH50%acetone	205.20	250.40	8.54	77.11	9.62	0.57	95.84
430 °C,35min,50%EtOH50%acetone	131.80	222.60	26.99	63.52	5.86	1.160	97.65
430 °C,15min,100%EtOH	129.50	258.10	18.36	59.10	12.58	1.150	91.19
430 °C,15min,75%EtOH50%acetone	215.20	251.60	8.59	75.70	10.84	0.45	95.58

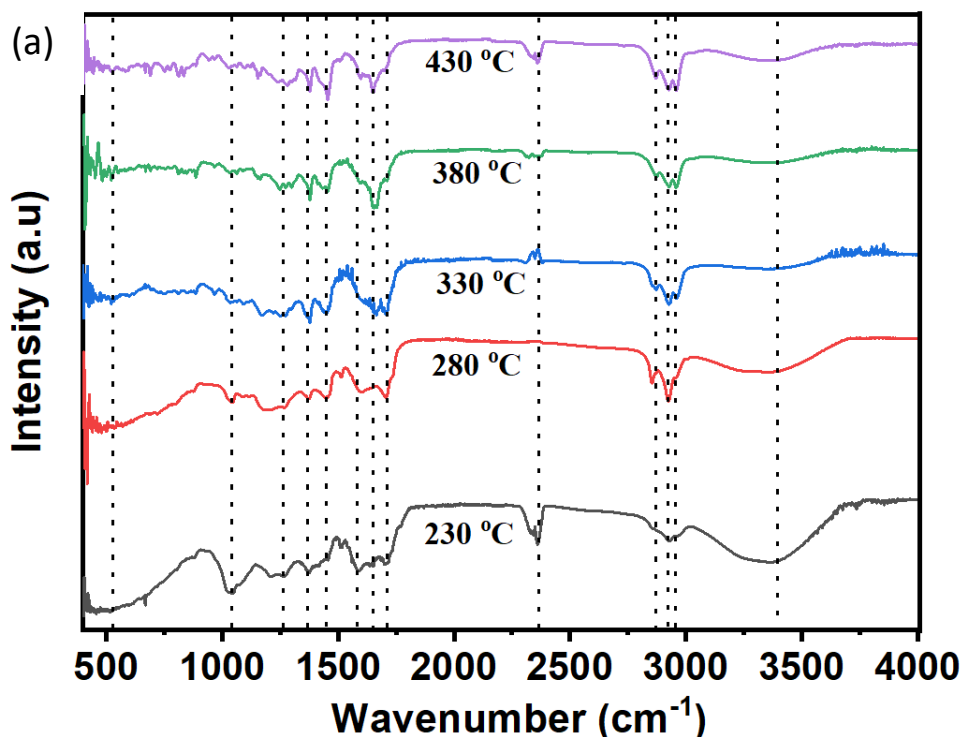
From Figs. 18a and b, the different compositions which are present in the biocrude are observable in the thermal responses and give indicated the present of different fractions of obtainable fuel-grades as a function of fractionation. The main fractions in the biocrudes were categorized into light volatiles, medium volatiles, heavy oil and inorganic and cokes with temperature ranges from $<180\text{ }^{\circ}\text{C}$, $180\text{-}360\text{ }^{\circ}\text{C}$, $360\text{-}550\text{ }^{\circ}\text{C}$ and $> 550\text{ }^{\circ}\text{C}$ respectively as presented in Table 10. From the deduced data shown in Table 10, the onset temperature, T_{onset} is the temperature at which the biocrude begins to be volatilized. Considering the effect of residence time at constant solvent ratio of 50:50 EtOH: Acetone and reaction time of $430\text{ }^{\circ}\text{C}$, the volatility increases from $205.20\text{ }^{\circ}\text{C}$ and $131.80\text{ }^{\circ}\text{C}$ as the residence time increases from 15 min to 35 min respectively. This implies that, the longer reaction time produces higher fractions of volatiles from the depolymerization of the orange peels' constituents over a shorter residence time though there is a corresponding decrease in the medium volatile components i.e., gasoline and diesel range fuel. The overall percentage volatile content of 97.65 wt.% as compared to 95.84 wt.% were obtained at 35 and 15min of residence time respectively. Also, the effect of acetone addition in ethanol to the thermal decomposition of biocrude at constant reaction temperature and residence time of $430\text{ }^{\circ}\text{C}$ and 15 minutes, respectively were observed. Therefore, to produce biocrude with high fractions of jet and diesels range fuels, the application of reaction condition with $430\text{ }^{\circ}\text{C}$, 50:50 ratio of EtOH: acetone and 15mins residence time proves superior though, a further increase in acetone content to 75% shows a slight increment in the formation of gasoline, and heavy oils production with a slight decrease in the formation of inorganics and cokes as shown in Table 10. Additionally, it was noted that the use of 100% ethanol resulted in an increased production of heavy oils in the biocrude, 12.58 wt.%, accompanied by the lowest onset temperature of 129.50°C .

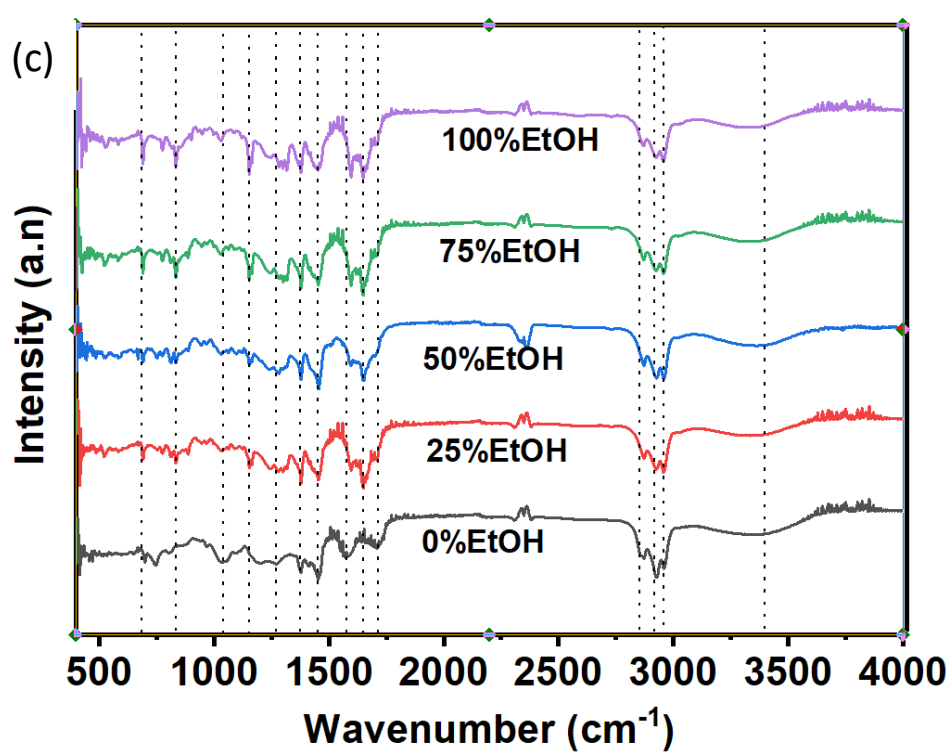
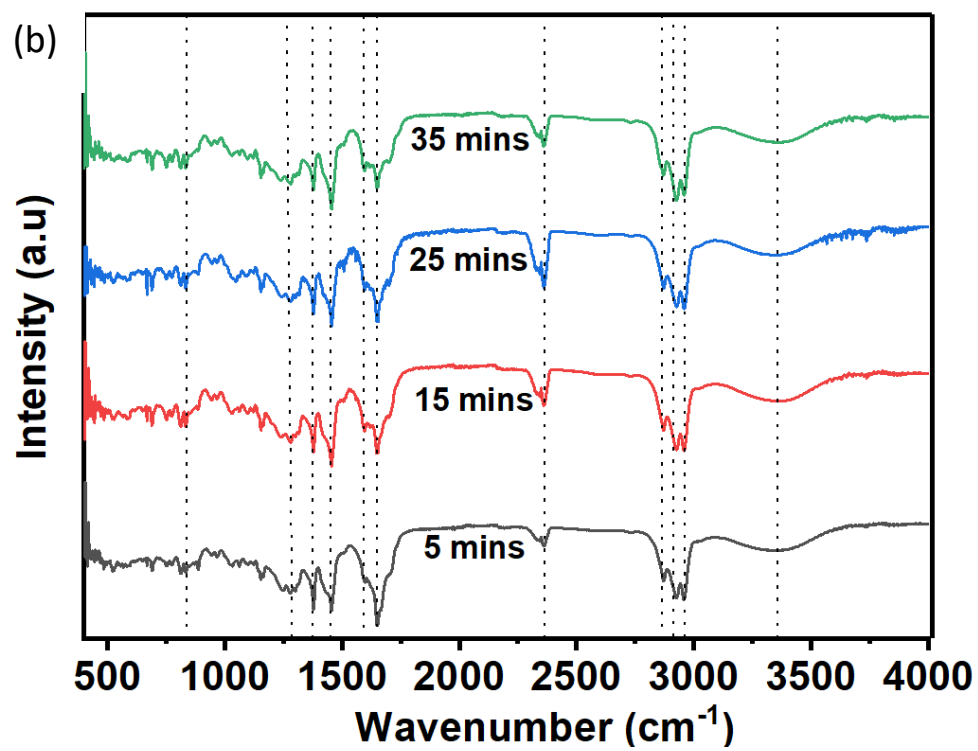
The molecular weight distribution of the biocrudes obtained with the lowest oxygen content and highest HHV were presented in Figs. 18 (c-f) where the effects of residence time and percentage ethanol loading could be understood. Based on the results presented, it can be observed that the average and peak molecular weights of the biocrudes displayed variations depending on the reaction conditions, including temperature, solvent ratio, and residence time. At 50% ethanol ratio, $430\text{ }^{\circ}\text{C}$ and different residence time of the solvothermal reaction from 15 to 35 minutes (Figs. 18c and 3d), the molecular weight increases from 348 g/mol to 360 g/mol respectively. The increase in weight could be associated with an observable increase in esters and ketones contents in the biocrude which were identified as large molecular weight compounds as contained in the GC-MS results in Fig. 14 though the higher content of phenol;

a lower molecular weight present in Fig. 3d could mean to have limited effect in the overall properties. The increase in average molecular weight in biocrude has been reported previously to depend on higher content of esters and acids (Liu *et al.*, 2022). The use of 100% ethanol as solvent in the solvothermal process resulted in esterification reaction as the most pronounced phenomenon leading to 25.60% of ester and reverse-esterification with 16.15% of acid. This higher selectivity of esters formation resulted in the highest average molecular weight compounds with 542 g/mol in the biocrude as shown in Fig. 18e. The GPC result further correlates with the TGA/DTG of the biocrude obtained which shows the highest heavy biocrude composition of 12.58wt% as shown in Table 10. The introduction of acetone at 25% concentration into the ethanol drastically reduced the average molecular weight from 542 to 350 g/mol due to an improved selectivity to phenolics compounds (light molecular weight compounds) and absence of acids formation.

4.5.2 Functional Groups in the Produced Biocrudes

The FTIR spectra of the obtained biocrudes are shown in Fig. 19 a-c where the effects of operating parameters were depicted. The FT-IR spectra of the biocrude as depicted shows a distinctive absorption peak that indicated the presence of different functional groups which corresponding to specific compounds.





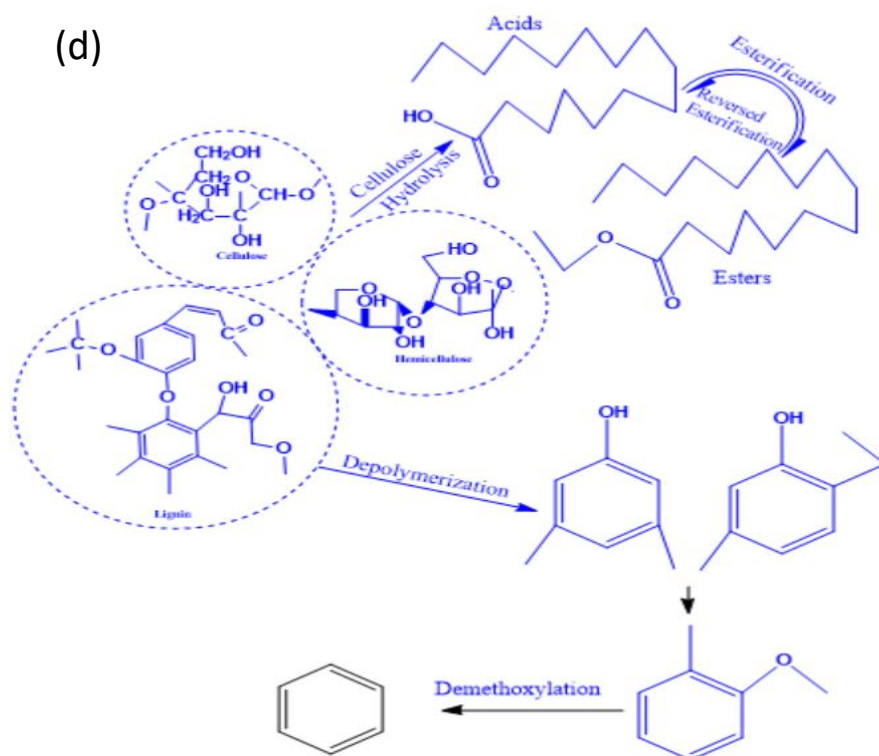


Figure 19: The FTIR Spectral of the produced biocrude considering the effect of (a) temperature (b) residence time and (c) solvent ratio (d) proposed reaction pathways for the non-catalytic solvothermal liquefaction of orange peels into biocrude

From the FTIR spectra, the peak at 3405 cm^{-1} on the effect of temperature is associated with O-H stretching vibration due to the presence of phenols, alcohols and accompanied moisture from hydrolyzed cellulose. Broader peaks were observed on the biocrudes produced at $230\text{ }^{\circ}\text{C}$ and $280\text{ }^{\circ}\text{C}$. The broader peaks formation could be associated to the presence of large amount of alcohols and water content as against those observed at $330, 380$ and $430\text{ }^{\circ}\text{C}$. The peaks observed at $2954, 2923$ and 2871 cm^{-1} are associated to the formation of $=\text{CH}$ groups due to asymmetric stretching vibration indicating the presence of alkyl groups acetone (Ali *et al.*, 2014; Matin & Aydin, 2022). The peaks at 2954 cm^{-1} become prominent from $330\text{--}430\text{ }^{\circ}\text{C}$ with similar patterns of the spectral were observed throughout the biocrudes obtained on the effect of residence time and the solvent ratio except the presence of peak at 1574 cm^{-1} at 100% . From the FTIR spectral, the details of peaks assignment for all the biocrudes are presented with the observable variation due to changes in the reaction conditions Table 11.

Table 11: Peaks assignment on the effects of process parameters on the biocrude functional groups

cm ⁻¹	Effect of temperature (°C)					Group	Class of compound
	230	280	330	380	430		
3500–3200	3363	3363	3363	3363	3356	O–H stretching	Polymeric O–H, Phenols
3200–2800	2961, 2928, 2870	2961, 2928, 2870	2961, 2928, 2870	2961, 2928, 2870	2961, 2928, 2870	C–H stretching	Alkanes-methyl group
1750–1650	1705, 1651	1705 -	1705, 1660	1705, 1660	1705, 1660	C = O stretching	Aldehydes, Ketones
1650–1590	1591	1591	-	1591	1591	C = C stretching alkene	C–C multiple bonds stretching
~1600–1450	1560, 1511	1560, 1511	- -	1560, -	1560, 1511	C = C stretching aromatic	C–C multiple bonds stretching
1470–1350	1454, 1373	1454, 1373	1454, 1373	1454, 1373	1454, 1373	C–H deformation	Alkanes-methylene group (Highest peak intensity of 1454 cm ⁻¹ at 430 °C with lowest peak intensity of 1373 cm ⁻¹ observed at 230 and 280 °C)
1300–950	1031	1031	1031	1031	1031	C–O stretching O–H bending	Phenols, primary, secondary, tertiary alcohols (Highest peak intensity observed at 230 and 280 °C)
975–525	883	883	883	883	883, 812	C–H bending	Mono-, polycyclic, substituted aromatic rings (Highest peak intensity at 380 °C)
Effect of residence time (min)							
	5	15	25	35	-		
3500–3200	3351	3356	3340	3379		O–H stretching	Polymeric O–H, Phenols
3200–2800	2961, 2928, 2870	2961, 2928, 2870	2961, 2928, 2870	2961, 2928, 2870		C–H stretching	Alkanes-methyl group
1750–1650	1705, 1651	1705, 1651	705, 1651	1705, 1651		C = O stretching	Ketones, aldehydes
1650–1590	1591	1591	1591	1591		C = C stretching alkene	C–C multiple bonds stretching
~1600–1450	1560, 1511	1560, 1511	1560, 1511	1560, 1511		C = C stretching aromatic	C–C multiple bonds stretching
1470–1350	1454, 1373	1454, 1373	1454, 1373	1454, 1373		C–H deformation	Alkanes-methylene group

cm ⁻¹	Effect of temperature (°C)					Group	Class of compound
	230	280	330	380	430		
1300–950	1281, 1154, 1028	1281, 1154, 1031	1281, 1154, 1039	1281, 1154, 1039		C–O stretching O–H bending	Phenols, primary, secondary, tertiary alcohols
975–525	886, 812	886, 812	886, 812	886, 812		C–H bending	Mono-, polycyclic, substituted aromatic rings
	Effect of ethanol's conc. (%)						
	100	75	50	25	0		
3500–3200	3352	3324	3356	3313	3360	O–H stretching	Polymeric O–H, Phenols
3200–2800	2961, 2928, 2870	2961, 2928, 2870	2961, 2928, 2870	2961, 2928, 2870	2961, 2928, 2870	C–H stretching	Alkanes-methyl group
1750–1650	1705, 1651	1705, 1651	1705, 1651	1705, 1651	1705 -	C = O stretching	Ketones, aldehydes
1650–1590	1591	1591	1591	1591	1591	C = C stretching alkene	C–C multiple bonds stretching
~1600–1450	1454	1454	1454	1454	1454	C = C stretching aromatic	C–C multiple bonds stretching
1470–1350	1373 -	1373 -	1373 -	1373 -	1373, 1404	C–H deformation	Alkanes-methylene group
1300–950	1154, 1036	1154, 1036	1154, 1036	1154, 1036	- 1036	C–O stretching O–H bending	Phenols, primary, secondary, tertiary alcohols
975–525	831, - 692	831, - 692	831, 741, 692	831 - 692	- 741	C–H bending	Mono-, polycyclic, substituted aromatic rings

4.6 Reaction Mechanisms and Pathways for the Non-Catalytic STL of Orange Peels

The proposed reaction pathways for the biocrude production during the STL process of orange peels have been presented through the products' compositions at varied reaction conditions where several reactions were observed to be taking place. Such reactions include esterification, hydrolysis, reversed-esterification, etherification, ketonization, deoxygenation and hydrogenation reactions. Within an ethanol medium, it is conceivable that cellulose depolymerization in the feedstock could transform into alcohols and esters, while there have been reports of the production of ketones and aromatic ketones (Galebach *et al.*, 2018; Tao *et al.*, 2013). Furthermore, the depolymerization of cellulose in the presence of acetone produces high content of ketones at supercritical conditions (Wang *et al.*, 2019). The ketones produced could act as an intermediate product which is capable of further conversion through metal acid catalyst via dehydration and hydrogenation into hydrocarbons pools (Serrano-Ruiz *et al.*, 2010). The existence of furan within the biocrude might result from cellulose dehydration, while the potential for alkane formation through hydrogenolysis and hydrodeoxygenation reactions is plausible (Xin *et al.*, 2020). Regarding the conversion of lignin content in biomass feedstock, it is possible to polymerize lignin into aliphatic/aromatic esters, phenolics, and ketones (Limarta *et al.*, 2018). Also, the formation of aromatic compounds (lignin monomers) has been reported to be produced through depolymerization, alkylation and hydrogenolysis reactions while repolymerization reactions could lead to the formation of char (Huang *et al.*, 2014). The formation of a high content of hetero-atom aromatics, esters, and phenols has been reported during the initial reaction period (0-30 minutes) (Riaz *et al.*, 2016).

4.7 Catalytic STL of Orange Peels over Fe/CNSs Catalysts

4.7.1 Characterization of the Produced Catalysts

The SEM images displayed in Figs. 20 (a-d) represent the structural morphologies of the as-received and the developed Fe/CNSs materials. The histograms affixed to Fig. 20b and d were obtained via the application of ImageJ software for the analysis of micrographs at the magnification of 500 nm.

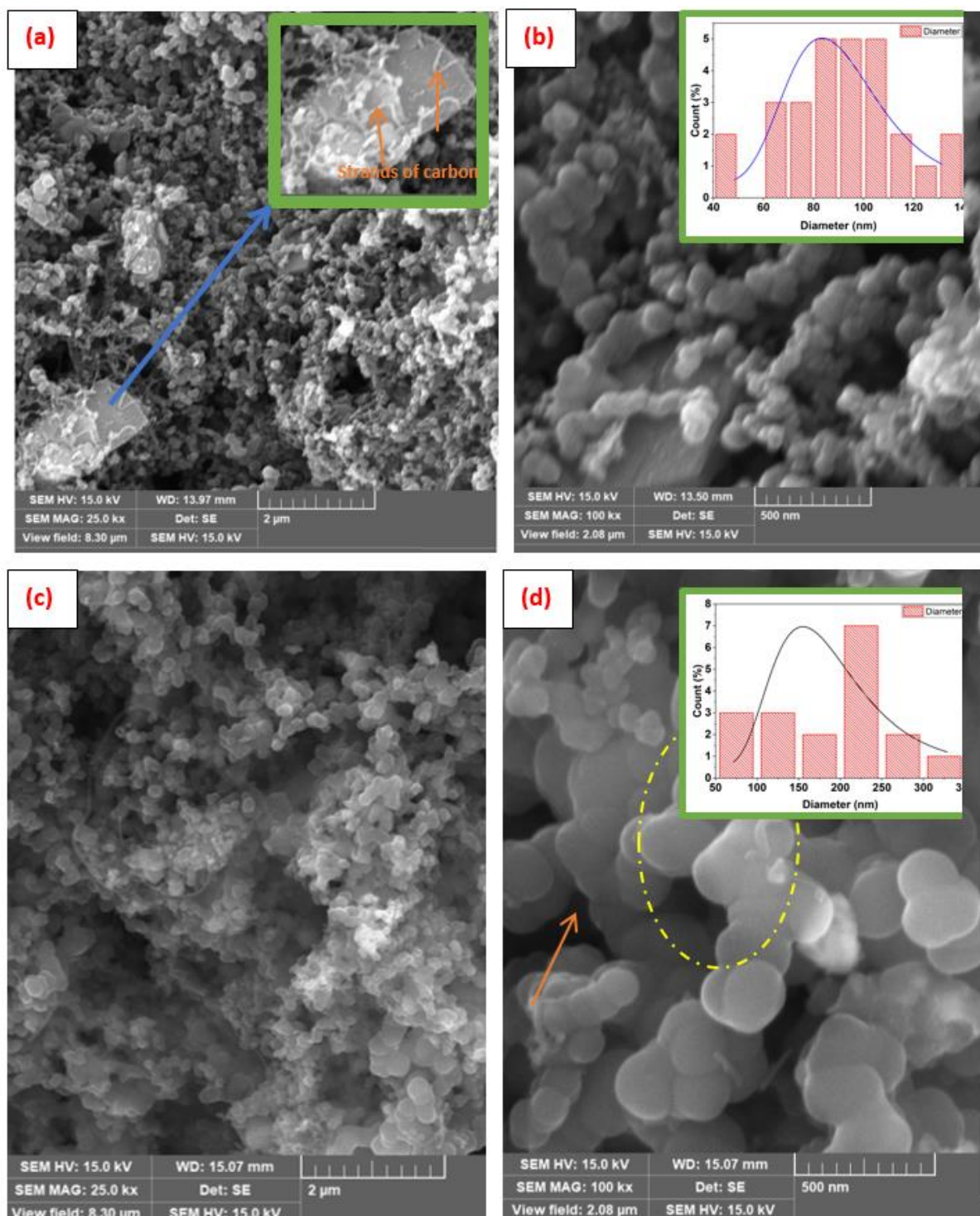


Figure 20: Surface morphology of (a-b) as-received CNSs and (c-d) Fe supported carbon nanosphere

The surface morphologies displayed in Figs. 20 (a-d) show the presence of spherical carbon materials with agglomeration. There is presence of dense particles with formation of long-strand of tubes as depicted in Fig. 20a. The presence of a slate-like surface in Fig. 20a could be attributed to the support materials employed during the CNSs synthesis. Also, the presence of

inter-particle spaces was as well observed with an illustration on Fig. 20d. The average particle sizes of the as-received CNSs and the Fe doped CNSs were estimated to be 90.85 ± 22.27 nm and 186.08 ± 64.83 nm respectively. The possible reason for the increase in the particle size after the doping process could be associated with particle agglomeration due to the formation of ferrites and oxides in the bulk of the catalysts.

Furthermore, the application of elemental mapping which gives an insight into the metals' distribution on the surfaces of the carbon nanosphere is as shown in Figs. 21 (a-b).

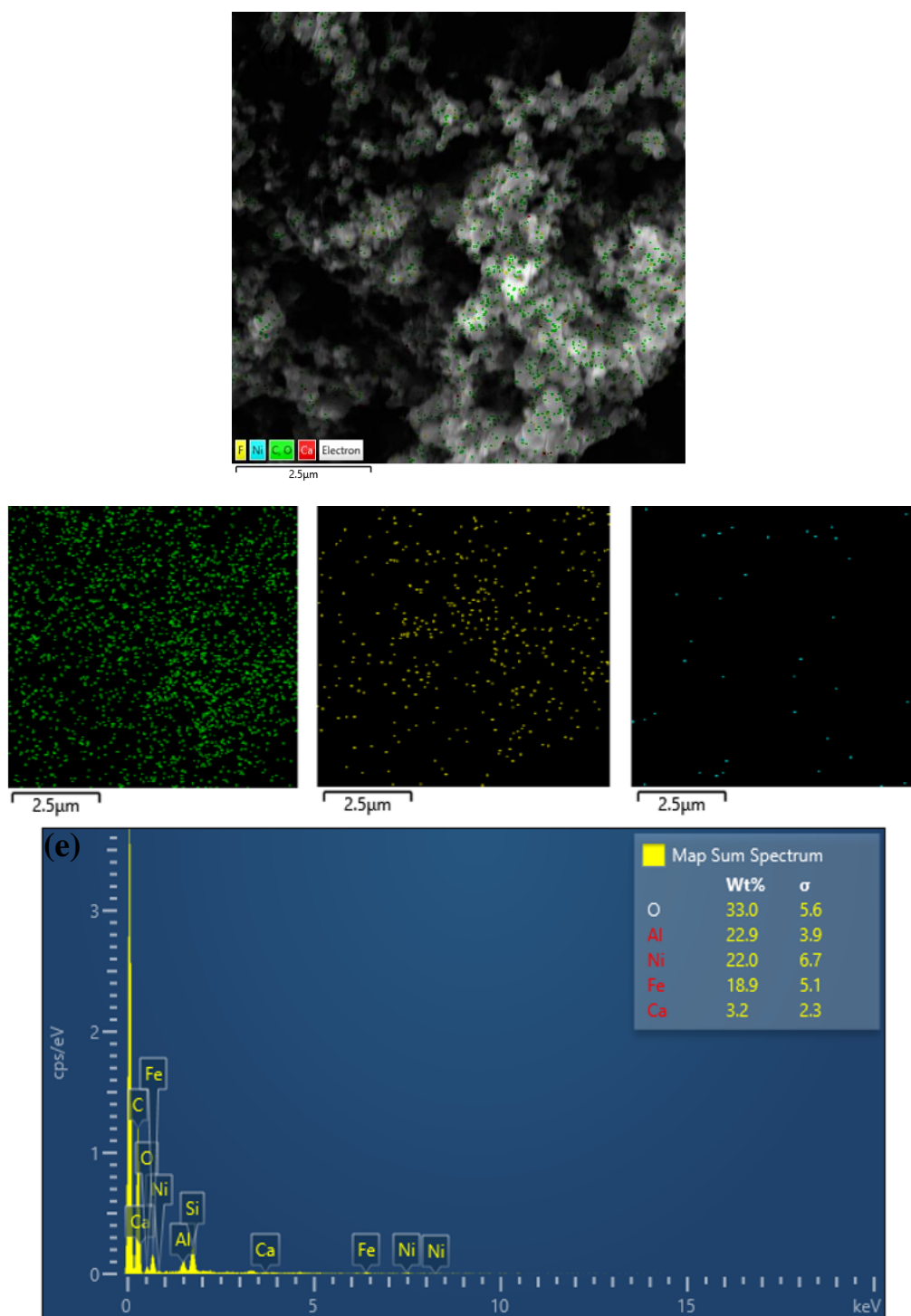


Figure 21: Elemental mapping EDS analysis of the modified carbon nanospheres (a) Analyzed points and distribution of (b) Carbon materials (c) Fe dopant (d) Ni substrate and (e) elemental analysis

The EDS layered images for both the as-received CNSs and the Fe doped CNSs depict the presence of several elements. The elemental mapping of the constituents' elements shows the dispersion of carbon (the base material), Fe (the dopant) and Ni (remnant from the catalyst adopted during the CNSs synthesis). The presence of aluminosilicate is perceived from the

presence of Si, Al and O in the CNSs. The presence of Fe was observed to be evenly dispersed on the surfaces of the carbon nanosphere particles (Fig. 21b). The even distribution exhibited by the iron particles and other elements indicated the effectiveness of the adopted doping method; wet impregnation employed in this study which could promote catalytic activities.

The functional groups present on the surface of the as-received CNSs and Fe doped CNSs are as shown in Fig. 22.

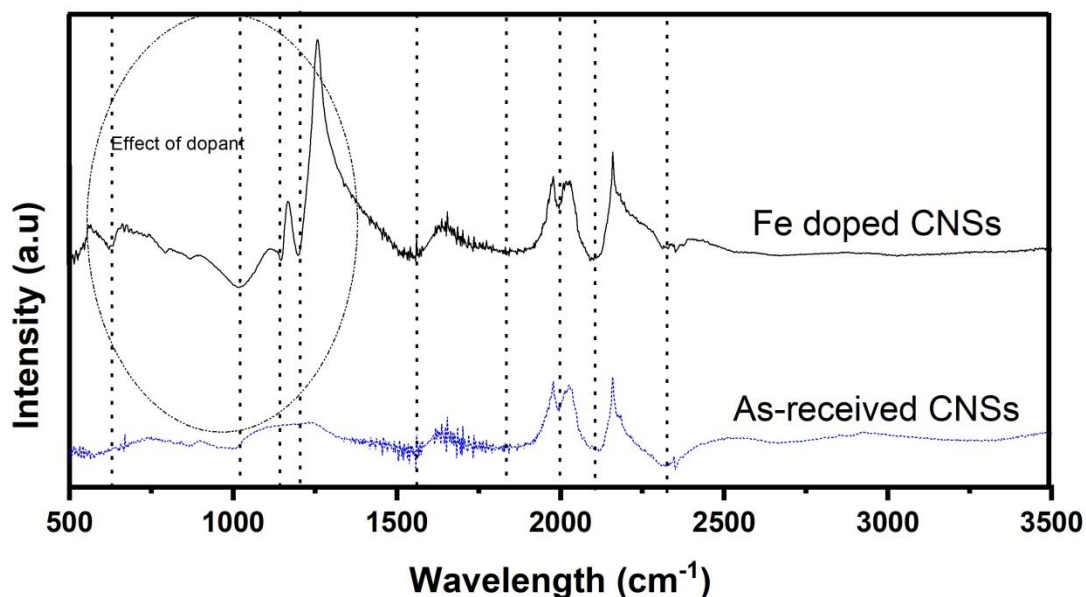


Figure 22: The FTIR spectral of the as-received and doped carbon nanosphere

The as-received CNSs and the Fe doped carbon nanosphere depicted no presence of -OH bonded group as shown in Fig. 22. This is an indication of an absence of unbound water molecules in the bulk of the materials. The presence of carboxylic and carbonyl groups (C=O stretching) is observed at the wavelength of 1830 cm^{-1} . The carboxylic group present on the surfaces of the carbon nanosphere suggested that acid purification process was employed to removing the impurities during the production process of the carbon nanosphere. The peak at 1547 cm^{-1} could be attributed to C=C stretching which is a direct indication of the hexagonal structure of the carbon nanosphere. This assertion is in accordance with the report of TermehYousefi *et al.* (2014) who reported the synthesis of multilayer carbon nanotubes from camphor oil via fast synthesis approach. The Fe doped CNSs depicts a distinct peak which indicated the successful doping process. The peaks at the wavelength 1203 and 626 cm^{-1} suggest the presence of Fe-O stretch vibration and F-O bending resulted from the possible formation of Fe_3O_4 . This assignment of peaks is similar to the finding of Panwar *et al.* (2015) who reported PEGylated magnetic nanoparticles ($\text{PEG@Fe}_3\text{O}_4$) as cost effective alternative for

oxidative cyanation of tertiary amines via C-H activation. Furthermore, the possible presence of nickel ferrite bond could be attributed to the octahedral vibration found at the wavelength of 625 cm^{-1} . The attribution of this wavenumber is similar to the observation of the report of Gopale *et al.* (2020).

The surface areas of the developed catalysts were investigated to obtain the pore volume, surface area and pore size of the catalysts. The N_2 adsorption-desorption isotherms of the catalysts are presented in Figs. 23 (a-b).

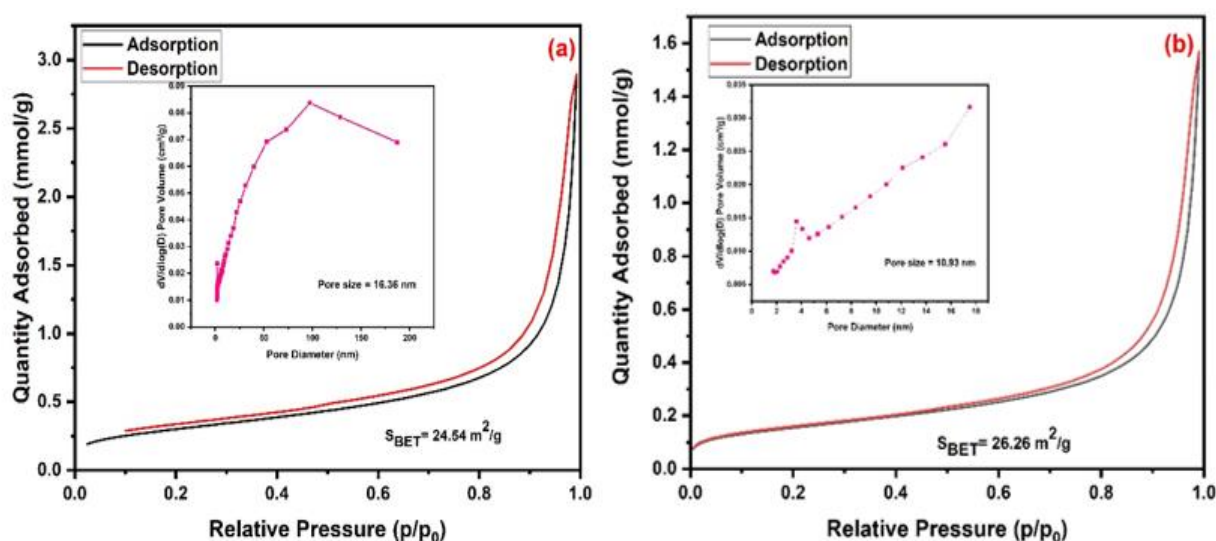


Figure 23: The BET N_2 Adsorption-desorption isotherms and the pore size distribution of (a) As-received CNSs and (b) Fe supported CNSs catalysts

From the results presented in Figs. 23 (a-b), the isotherms depicted a H3 hysteresis loop and type III isotherm according to the International Union of Pure and Applied Chemistry (IUPAC) (Bakari *et al.*, 2022). The H3 adsorption hysteresis loop depicted by the two catalysts as contained in Fig. 4a and b indicated the presence of aggregates formation of particles in a plate-like nature which gives rise to pores of slit-shaped. Also, the observation of H3 hysteresis loop could be as a result of formation of capillary condensation within the catalysts' mesopore structure leading to the presence of a wedge-shaped pores (Dhawane *et al.*, 2015; Ilo *et al.*, 2022). The surface area of the as-received CNSs and the Fe/CNSs catalysts were observed to be 24.54 and 26.26 m^2/g while the pore sizes reduced from 16.36 to 10.93 nm respectively. The reduction in pore sizes after the doping process could be associated with the formation of smaller crystallites particles on the surfaces of the support material, CNSs. The doping in the same sense could be responsible to a slight decrease in the pore volume from 0.100 cm^3/g to 0.072 cm^3/g of the as-received CNSs and Fe/CNSs catalyst respectively. The presence of higher

surface area and the presence of surface functional groups depicted by Fe/CNSs catalyst suggest its suitability as potential catalyst during the catalytic solvothermal liquefaction of orange peels feedstock for enhanced HDO process. The presence of Fe which creates an active site on the CNSs particles is expected to initiate several reactions (ethanol reforming and HDO) which are capable of enhance the overall biocrude compositions.

4.7.2 Optimization of Catalytic STL using Central Composite Design

The robust nature of central composite design technique towards optimizing process variables has been reported by several researchers (Divyabharathi & Subramanian, 2022; Yan *et al.*, 2018; Zhao *et al.*, 2021). The adopted software; Design-Expert version 13 yielded 13 experimental matrixes as shown in Table 12 from the ranges of variables (temperature and catalyst loading) which were imputed and the response transformation and model fittings are shown in Table 13. The effects of the two parameters on both the biocrude yield and conversion (the responses of maxima interest) and the solid residue and gas yield (responses of minima interest) were obvious to influencing the reaction's yields as shown in Table 12.

Table 12: Design matrix for the optimization process of temperature and catalyst loading and their respective responses

		Factor 1	Factor 2	Response 1	Response 2	Response 3	Response 4
Std	Run	A: Temperature	B: Catalyst loading	Biocrude Yield	Solid Residue	Gas Yield	Conversion
		°C	wt%	wt. %	wt. %	mL/g	wt. %
4	1	430	6	88.9	29.87	49	70.13
10	2	380	4.5	44.32	32.09	32	67.91
7	3	380	2.37	40.23	29.75	33.5	70.25
5	4	309	4.5	25.76	36.98	16	63.02
1	5	330	3	28.11	31.62	27	68.38
12	6	380	4.5	47.7	30.97	34	69.03
2	7	430	3	80.85	28.37	37.4	71.63
6	8	451	4.5	75.3	27.86	50	72.14
11	9	380	4.5	43.98	31.25	37	68.75
13	10	380	4.5	45.05	31.11	36	68.89
8	11	380	6.63	50.98	27.00	35	73.00
3	12	330	6	32.54	33.23	25	66.77
9	13	380	4.5	47.54	29.93	39	70.07

Standard deviations: Response 1= 19.74; Response 2= 2.56; Response 3= 9.05 and Response 4= 2.56

Temperature variation was observed to have more prominent effects on the responses as shown in Table 12. At the reaction temperature of 309 °C and catalyst loading of 4.5 wt.%, 25.76 wt.% of biocrude was produced with the highest solid residue yield of 36.98 wt.%. The low biocrude production at this condition implies incomplete degradation of orange peel feedstock into smaller fragments and hence, favors hydrothermal carbonization over liquefaction process where solid residue having the same properties like that of low-ranked coal is formed. Adversely, the lower temperature of operation, 309 °C further resulted to a lower percentage feed conversion of 63.02 wt. % and a corresponding reduction in the yield of gaseous products. This result is in accordance with the reports of Biswas *et al.* (2020), Durak and Genel (2020) and Ma *et al.* (2021). As the temperature increases more above the boiling points of the co-solvent, the formation of smaller molecular compounds from the orange peels feedstock through thermal cracking increases with an enhanced synergetic conversion which are induced through the pore structure of the catalyst favors an improved biocrude formation. This observation was noticeable as the temperature increases from 330-451 °C which is in accordance with the report of Divyabharathi and Subramanian (2022) due to the improved

decomposition of cellulose and hemicellulose. For instance, at 330 °C and a catalyst loading of 3 wt.%, the biocrude, gas yield and conversion as compared to 309 °C at 4.5 wt.% catalyst loading increase by 9.12 wt.% in biocrude yield, 68.75 wt.% in gas yield and 8.51 wt.% in biomass conversion. The appreciable percentage increase observed above resulted in 14.49 wt.% reduction in solid residue formation. This observation implies that higher temperature above the temperature of the solvents enhances liquefaction over carbonization process of biomass conversion. The model fitting adopted for the CCD optimization process is shown in Table 13.

Table 13: Response transformation and model fittings

Responses	Range	Ratio	Transformation	Model fitting
Biocrude yield(wt.%)	25.76-88.9	3.45	Yes; Linear regression (Inverse @ constant, =-0.5)	Quadratic
Solid residue (wt.%)	27.00-36.98	1.37	None	Reduced cubic model
Gas yield (mL/g)	16-50	3.12	None	2FI
Conversion (wt.%)	63.02-73.00	1.16	None	Reduced cubic model

4.7.3 The RSM Analysis of the Fe/CNSs Catalyzed HTL of Orange Peels

The effects of temperature and catalyst loading were visualized using a 3D surface plots (surface plots and contour plots) while the reaction time, solvent ratio and volume, mass of feed were kept constant throughout the process. The response plots showing the 3D visualization of the effects of process parameters on the considered responses are shown in Fig. 24. As the catalyst loading increases along a constant reaction temperature of 430 °C as contained in Fig. 24. The increase in the biocrude yield as shown in Fig. 24a might be attributed to the presence of Fe₂O₃ which enhances the conversion of volatile gases into a liquid fraction due to the presence of mesoporous nature of the Fe/CNSs catalyst. Furthermore, the effect of Fe supported catalyst was also noticed on the solid residue yield where the highest biochar yield was observed at lower reaction temperature of 330 °C and catalyst loading between 4.5-5.4 wt.%.

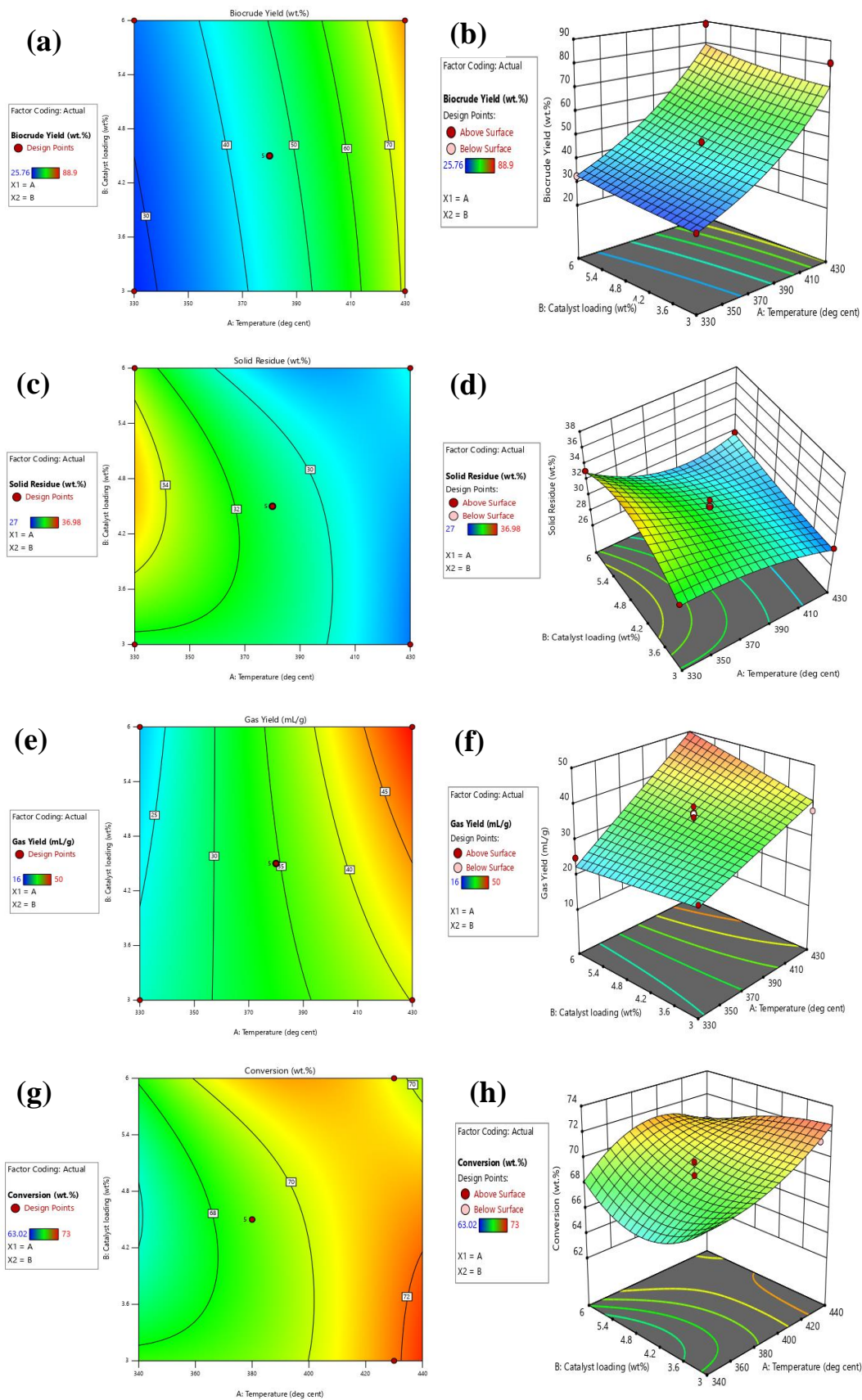


Figure 24: Surface and contour plots showing the effects of temperature and catalyst loading on biocrude (a-b), solid residue (c-d), gas yield (e-f) and conversion (g-h)

Adversely, the lowest temperature in this study, 309 °C yielded a lower biomass conversion of 63.02 wt.% and a low gaseous yield. This low observable conversion and gaseous yields could be associated with partial cracking of hemicellulose in the biomass feedstocks. As the reaction temperature increases above the super-critical temperature of the co-solvent, the cracking of large molecular building blocks of the orange peels feedstock was cracked through thermal-induced environment which breaks the inter-molecular bounds which exist in the molecules into smaller molecular compounds. In this condition, synergistically, the pore structure of the Fe/CNSs catalyst also promotes the condensation of volatiles into liquid products. An improved biocrude formation was noticeable as the temperature increases up to 430 °C with a slight reduction at 451 °C due to possible depolymerization of liquid biocrude into gaseous products. For instance, at 330 °C and catalyst loading of 3 wt.%, the biocrude yield, gas yield and percentage conversion as compared to the products obtained at 309 °C and 4.5 wt.% catalyst loading, an increase by 9.12 wt.%, 68.75 mL/g and 8.51 wt.% were observed, respectively. The appreciable percentage increase in those responses observed above were enhanced due to a corresponding reduction of 14.49 wt.% in solid residue formation; liquefaction process is favored over carbonization. This observation further implies that higher temperature above the solvents' boiling points enhances cracking process and thereby, improves the percentage conversion of orange feedstock into volatiles. Furthermore, an increase in temperature from 330 °C at 3 wt.% cat. loading to 380 °C at catalyst loading of 2.37 wt.% increase the biocrude yield from 28.11 wt.% - 40.23 wt.%, reduced the solid yield (31.62-29.75 wt.%), and enhance the biomass conversion and gas yield from 68.38-70.25 wt.% and 27-33.5 wt.% respectively.

Considering the surface and the contour plots presented in Figs. 24 (a-h), the combining effects of temperature and catalyst loading on the responses; biocrude yield, solid residue, gas yield and conversion were illustrated. From Figs. 24 (a-b), an increase in temperature from 309-430 shows a progressive increase in the percentage yield of biocrude production with a corresponding increase in gaseous yield as contained in Figs. 24 (e-f). This observation in biocrude's yield and gaseous product yield are in agreement with the report of Bakari *et al.* (2022) who reported the sub- and supercritical gasification of rice husk and Ilo *et al.* (2022) who reported the optimization of process parameters using response surface methodology to improve the liquid fraction yield from pyrolysis of water hyacinth. According to Ilo *et al.* (2022) the corresponding increase in gaseous products formation as temperature increases was attributed to (1) char disintegration into non-condensable gases and (2) disintegration of larger molecular hydrocarbon volatiles. As observed from Table 12, a reaction temperature of 451 °C

resulted to a slight decrease in biocrude yield as compared to 430 °C reaction temperature. The reduction in biocrude yield at 451 °C temperature is an indication of repolymerization of liquid-product into gaseous state and possible formation of coke with high tendency of catalyst blockage; a huge challenge in catalytic hydrocarbon liquefaction of biomass into biocrude.

The surface plots showing the effects of the operating parameters on the process variables were presented in Figs. 24 (a, c, e, and g). At constant catalyst loading throughout the experimental, an increase in temperature resulted to a progressive increase in the biocrude yield (Fig. 24a). This could be as a result of an improved degradation process of the large molecular structures in the orange peels. Similar observation of temperature increment having a noticeable effect of the bio-oil yield has been reported by Hossain *et al.* (2017). The reason for this behavior could be linked to the enhanced cracking process of the orange peels which simultaneously increases the biomass conversion, gaseous yield and inversely proportional to the solid residue's formation (Figs. 24 a, c, e and g). Furthermore, the loading of catalyst above the optimum catalyst loading while the temperature was kept constant, the biomass conversion was reduced (Fig. 24g). The reduction in the biomass conversion could be linked to the overlapping of the catalyst's active sites which therefore, hindered its performance during the cracking process.

At constant reaction temperature as observed from Figs. 24 (a-b) while the catalyst loading increases, the biocrude yields were enhanced. For examples, at the reaction temperature of 430 °C, while the catalyst loading increases from 3 wt.% to 6 wt.%, the biocrude yield increases with about 9.96 wt.% biocrude formation. This increment in biocrude formation could be attributed to the introduction of effective pore volume which is resulted from increased catalyst loading which has the tendency to aid catalytic cracking processes. Furtherance to the above observation, the percentage biomass conversion reduces with 2.09 wt.% while the gas formation increases with 31.01 mL/g. Low reaction temperature favors the production of solid residue as shown in Figs. 24 (c-d).

4.7.4 Analysis of Variance of the Developed Model

The table for the ANOVA for the statistical analysis of the observed data sets for the experimental responses is as shown in Table 14 while the statistical parameters for the catalytic STL products are depicted in Table 14.

Table 14: The ANOVA of the surface response model for the catalytic HTL products yield

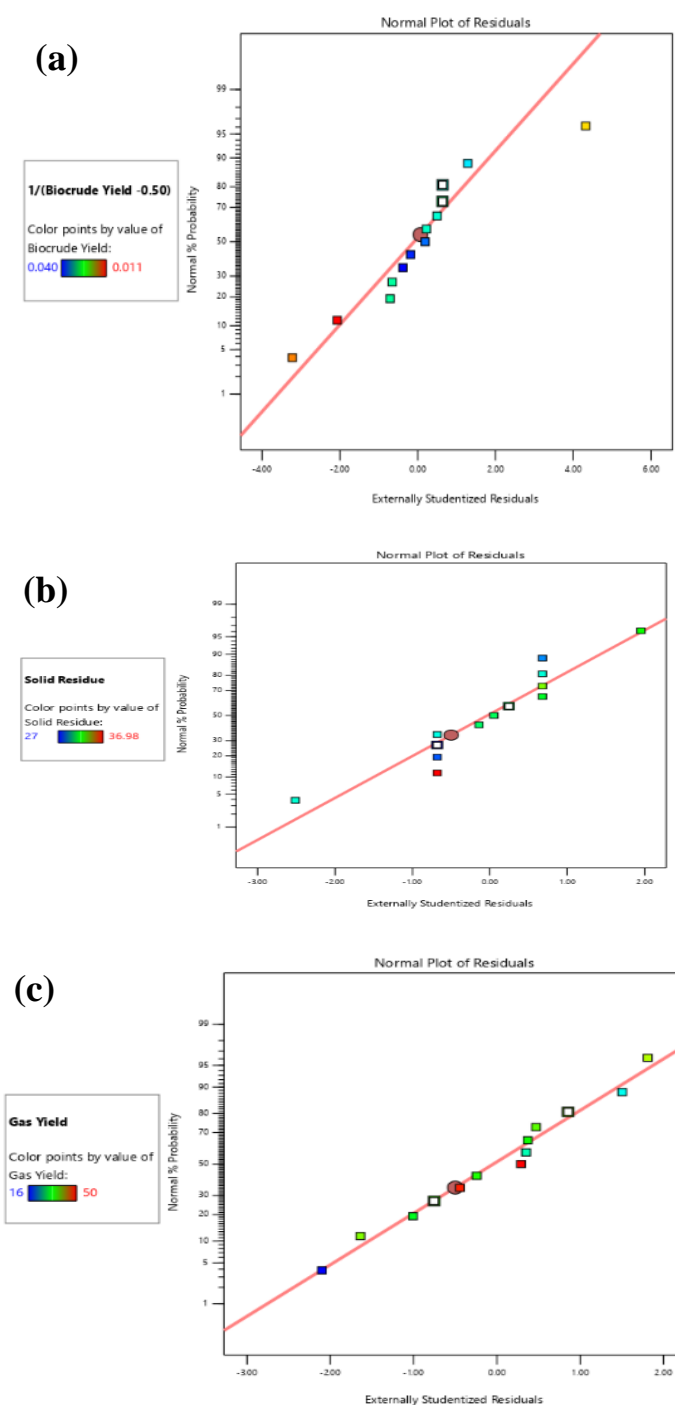
Source	Biocrude			Solid residue			Gas yield			Conversion			
	Sum of Square	F-value	p-value	Sum of square	F-value	p-value	Sum of square	F-value	P-value	Sum of square	F-value	p-value	
Model	0.0009	83.23	<0.0001	75.80	20.36	0.0022	914.38	39.56	< 0.0001	75.80	20.36	0.0022	Significance
A-Temperature	0.0008	329.02	<0.0001	41.59	78.19	0.0003	851.01	110.46	< 0.0001	41.59	78.19	0.0003	
B-Catalyst loading	0.000	11.33	0.0120	3.78	7.11	0.0445	17.13	2.22	0.1701	3.78	7.11	0.0445	
AB	3.753E-06	1.81	0.2210	0.0030	0.0057	0.9428	46.24	6.00	0.0368	0.0030	0.0057	0.9428	
A ²	0.000	10.25	0.0150	4.07	7.65	0.0395				4.07	7.65	0.0395	
B ²	4.006E-07	0.1927	0.6739	10.92	20.53	0.0062				10.92	20.53	0.0062	
A ² B	-	-	-	6.12	11.51	0.0194				6.12	11.51	0.0194	Not-significance
AB ²	-	-	-	4.88	9.17	0.0291				4.88	9.17	0.0291	
Residual	0.0000			2.66			69.34			2.66			
Lack of fit	0.0000	5.17	0.0731	0.2753	0.4620	0.5340	40.14	1.10	0.4766	0.2753	0.4620	0.5340	
Pure Error	2.982E-06			2.38			29.20			2.38			
Cor Total	0.0009			78.46			983.72			78.46			

Table 15: Statistical parameters for the catalytic HTL products

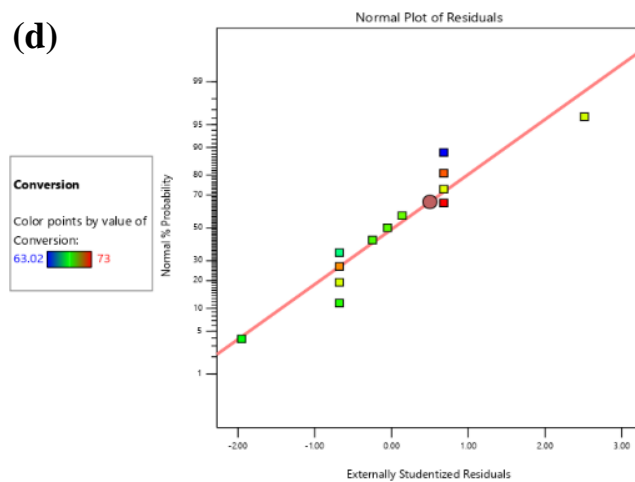
Parameters	Biocrude	Solid residue	Gas	Conversion
Standard Deviation	0.0014	0.7293	2.78	0.7293
Mean	0.0231	30.77	34.68	69.23
CV (%)	6.25	2.37	8.00	1.05
R ²	0.9835	0.9661	0.9295	0.9661
Adjusted R ²	0.9716	0.9187	0.9060	0.9187
Predicted R ²	0.9012	0.7279	0.8282	0.7279
Adeq Precision	29.2035	17.4444	19.3346	17.4444

The observed Model F-values for the four responses; yield of biocrude, yield of solid residue, gas yield and the percentage conversion were 83.23, 20.36, 39.56 and 20.36 respectively as shown in Table 14. From the above observed Model, F-values indicate that the models adopted for the ANOVA of all the four responses are significant. Furthermore, there are only a 0.01, 0.22, 0.01 and 0.22% chances for yield of biocrude, yield of solid residue, gas yield and the percentage conversion respectively that an F-value these large could occur due to the availability of noise during the experiment. Correspondingly, the responses possess P-values of 0.0001, 0.0022, 0.0001 and 0.0022 for yield of biocrude, yield of solid residue, gas yield and the percentage conversion respectively. The lower values of P-values and higher F-values indicted the significant nature of the model adopted in the analysis. These are in agreement with the observations reported by Dhawane *et al.* (2015). Also, the obtained statistical parameters for the catalytic hydrothermal liquefaction of orange peels over Fe/CNSs are depicted in Table 15. The correlation co-efficient obtained for all the responses were closer to unity as depicted in Table 15. This observation indicated that the model fitted best with the experimental data with high suitability. The closeness of the Adjusted and predicted R² values with differences less than 0.2 suggested a reasonable agreement between the factors. An adequate signal was also observed in the statistical parameters. This deduction of the presence of adequate signal was inferred due to the presence of Adeq precision which was greater than 4 in all cases of the responses. The Adequate precision of 29.20, 17.44, 19.33 and 17.44 for yield of biocrude, yield of solid residue, gas yield and the percentage conversion respectively imply that the respective models adopted for the ANOVA have the tendencies to be used in navigating the design space for the responses considered.

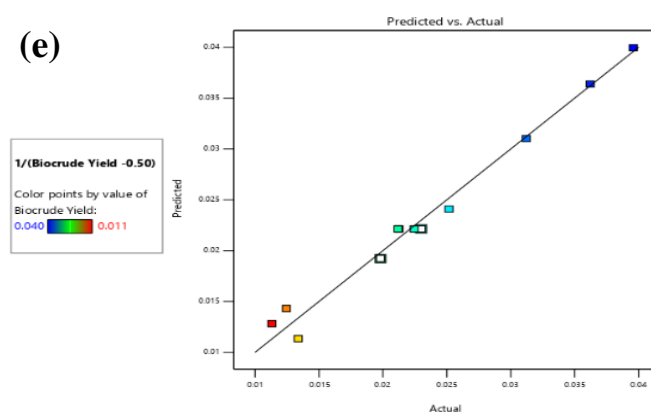
From Figs. 25 (a-d), the presences of random distribution of residual were observed to spread arbitrarily near the straight line; an indication of non-appreciable concerns and non-existence of alteration in all the considered responses (Ilo *et al.*, 2022). The plots of predicted and actual responses were also analyzed for all the responses as shown in Figs. 25Figure 25 (e-h). From the depicted results in Fig. 25, there were observable closeness of the responses in all cases (actual and residual values), an indication which shows the presence of good and robust-regression correlation between the actual and predicted values of the responses.



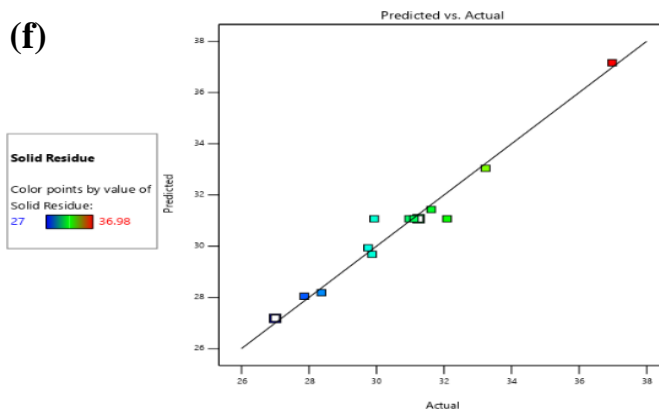
(d)



(e)



(f)



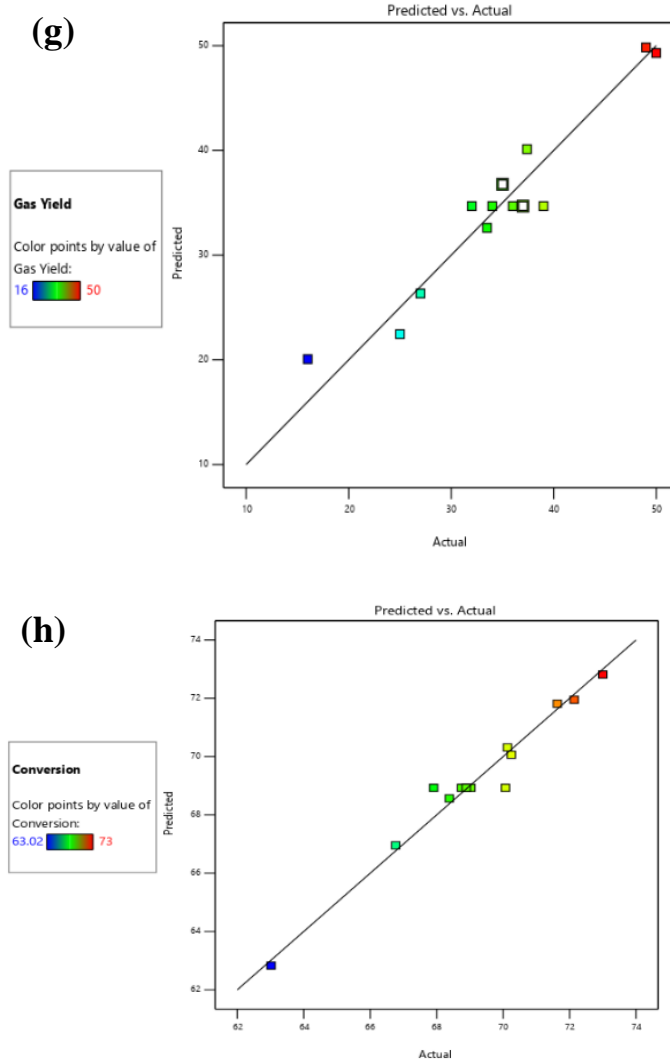


Figure 25: Normal probability graph of residuals for the HTL product yield: (a) Biocrude (b) Solid residue (c) Gaseous product and (d) Conversion; predicted vs actual for (e) Biocrude (f) Solid residue (g) Gaseous product and (h) Conversion for orange peels

The generated mathematical regression model equations after which the insignificant factors have been expunged (Equation 19-22), give the model predictions about the responses for any level of process factors under consideration. Furthermore, the final coded equations are useful for recognizing the relative impact of the process variables by comparing the factor coefficients. From Equation 19 and 21, there is an alternation between the coefficients of the variable as regards the numerical operation. This variation could indicate an inverse variation which exists between the solid residue yield and the biomass conversion.

$$1/(\text{Biocrude Yield} - 0.50) = +0.0221 - 0.0101A - 0.0017B + 0.0010AB + 0.0017A^2 \quad (19)$$

$$\text{Solid residue (\%)} = +31.07 - 3.21A - 0.9683B - 0.0275AB + 0.7605A^2 - 1.25B^2 + 1.75A^2B + 1.56AB^2 \quad (20)$$

$$\text{Gas yield (mL/g)} = +34.68 + 10.29A + 1.46B + 3.40AB \quad (21)$$

$$\text{Biomass Conversion (\%)} = +68.93 - 3.21A - 0.9683B + 0.0275AB - 0.7605A^2 + 1.25B^2 - 1.75A^2B - 1.56AB^2 \quad (22)$$

4.7.5 Desirability Test

The desirability test was carried out by setting the target of the responses. The present study aimed at optimizing the biocrude yield and the biomass conversion while the gas yield and the formation of the solid residue were set at minimum. From Fig. 26, a desirability of 0.724 was obtained; a near-idea condition for optimization of the catalytic hydrothermal liquefaction of orange peels in acetone: ethanol co-solvent.

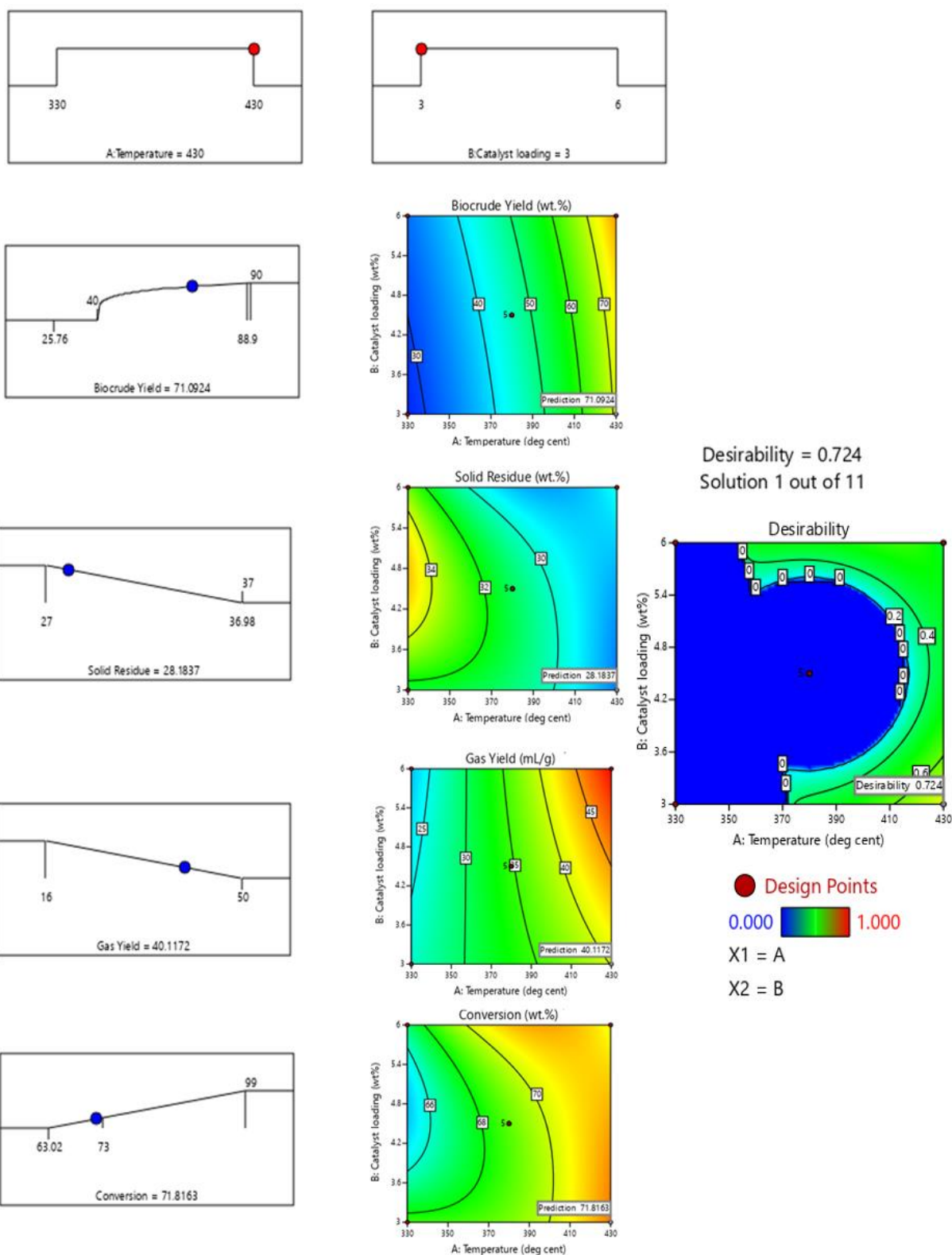


Figure 26: Desirability plots using numerical optimization

4.8 Bio-crude Characterization

4.8.1 Compositional Analysis and Fuel Characteristics of Biocrudes

The obtained biocrudes from the catalytic STL process at the optimum and at low value (-1) having a reaction temperature of 430 °C, 3 wt.% catalyst and 330 °C and 3 wt.% catalyst loading respectively. High aromatic and phenolics selectivity were observed at the optimum reaction conditions of 430 °C as compared to 330 °C with the same catalyst loading of 3 wt.% of Fe supported CNSs. The compositional distributions of the biocrudes are as depicted in Fig. 27 while the content of the biocrude at the percentage area ≥ 3 were presented in Table 16. Due to the complexity of biomass feedstock in terms of compositions, several compounds are mostly obtained from the thermochemical conversion of biomass into biocrude as shown in Table 16. This observation has been reported by several researchers and in turns, conceptualizing the mechanisms of the reaction has been a major challenge in biomass conversion.

Table 16: Compounds identification from the biocrude obtained at 330 °C and 430 °C reaction temperature at 3 wt.% of Fe/CNSs catalyst loading

Compounds identified in biocrude	% Area	
	330 °C, 3 wt.%	430 °C, 3 wt.%
	Fe/CNSs	Fe/CNSs
2-Cyclohexen-1-one, 3,5-dimethyl-	-	16.42
3-Penten-2-one, 4-methyl-	3.11	0.22
3,5-Dimethylcyclohexen-1-one	20.82	-
2-Pentanone, 4-hydroxy-4-methyl-	4.35	-
2-Pentanone, 4-hydroxy-	3.06	-
Hexadecanoic acid	6.41	5.09
Hexadecanoic acid, ethyl ester	6.91	0.37
Ethyl linoleate	3.37	-
Ethyl Oleate	5.98	-
Linoleic acid ethyl ester	3.03	-
Phenol, 3-methyl-	1.24	4.20
Phenol, 3,5-dimethyl-	1.48	10.19
Phenol, 4-ethyl-3-methyl-	-	5.66
Phenol, 5-methyl-2-(1-methylethyl)-	-	3.10
Butyl isopropyl ether	5.22	-
Pyridine, 2,4,6-trimethyl-	3.33	-

From Table 16 coupled with Fig. 27, the presence of hydrocarbons, phenolics compounds and cyclic ketones obtained from the STL of orange peels feedstock via Fe/CNSs catalyst suggests

the possibilities of obtaining high grade transportation fuel through upgrading process via hydrodeoxygenation, HDO (Cheng, 2017).

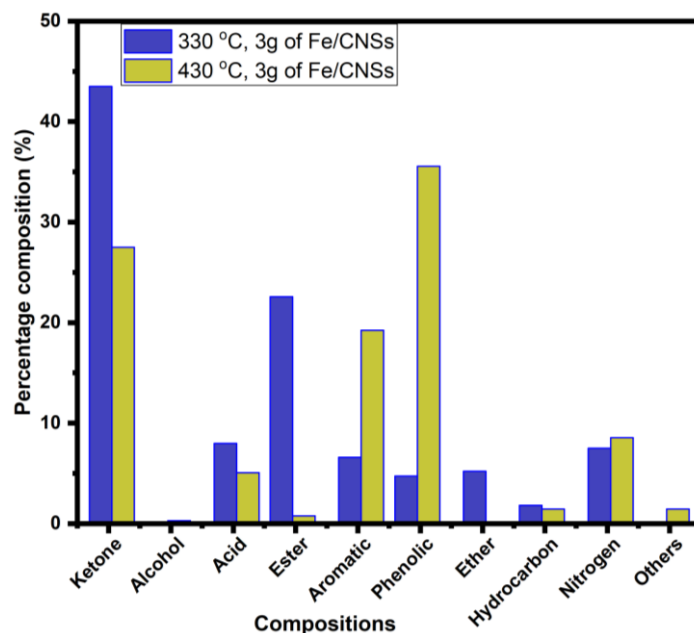


Figure 27: The GC-MS Compositional classifications of the organic contents from the biocrudes

From the result presented in Fig. 27, the selectivity of ketones and esters were favored by the Fe/CNSs at the 3:1 acetone to ethanol ratio with percentage composition of 43.53 and 22.5% respectively at the reaction temperature of 330 °C. In comparison with the reaction condition at 430 °C, the percentage composition of ketones and the esters were reduced to 27.52 and 0.79 % respectively with high selectivity of aromatics and phenolics compounds. The reduction in the percentage composition of these compounds (ketones and esters) is influenced with increasing temperature coupled with the synergetic effects of the Fe/CNSs catalyst in the ethanol and acetone medium. These conditions enhance the conversion of esters and ketones into phenolic compounds with subsequent formation of aromatics and hydrocarbon compounds via an improved repolymerization, hydrogenation, and deoxygenation reactions (Hao *et al.*, 2021). This observation of phenolic selectivity has been reported by Nguyen *et al.* (2021) who reported the catalytic activity of Fe promoted heterogeneous catalyst over *Cladophora socialis* macroalgae into fuel precursor. The formation of nitrogenous compounds with 7.53 and 8.55 % at the reaction temperature of 330 °C and 430 °C in the biocrudes is favored by the conversion of carbohydrates into monosaccharides via hydrolysis process and the subsequent reaction with proteins (Leng *et al.*, 2020). The role of the catalyst in the STL process demonstrates that Fe/CNSs catalysts enhance acid formation by initiating hydrolysis reactions,

with area percentages of 7.98% at 330°C and 5.09% at 430°C, using a 3 wt.% catalyst loading. In contrast, during the non-catalytic HTL of the orange feed, no acids were detected, and there was a lower composition of aromatic hydrocarbons, with higher selectivity of 19.26% observed at 430°C. Additionally, the presence of Fe/CNSs inhibits the formation of phenolic compounds.

4.8.2 Elemental and Heating Value of Biocrudes

From Table 17, the elemental composition, heating values and the atomic ratios of the biocrudes were presented. The parameters obtained from this table give an insight into the biocrude quality and the effectiveness of the catalyst and the reaction conditions employed during the STL process.

Table 17: Elemental analysis and heating value of the produced biocrude

Condition	C (wt.%)	H (wt.%)	N (wt.%)	S (wt.%)	O (wt.%)	H/C	O/C	HHV (MJ/kg)
330°C, 3 wt.% Fe/CNSs	71.11	8.63	1.95	0.007	14.64	1.45	0.155	33.78
430°C, 3 wt.% Fe/CNSs	78.37	9.16	1.21	0.004	10.29	1.39	0.099	37.76

The elemental composition of the biocrudes produced at the two different conditions shows that, the production of biocrude at elevated temperature of 430 °C improves the carbon and hydrogen contents in the biocrude with 10.21 and 6.14 wt. % respectively. The reduction in the oxygen, nitrogen and sulphur contents indicate an improved fuel property. The observed deoxygenation reaction which takes place during the Fe/CNSs catalyzed orange peels at elevated temperature of 430 °C leads to the reduction in the percentage composition of ketones and subsequent high content of phenolics and aromatics. This observation indicates that, the biocrude obtained at this condition is suitable as biocrude precursor for further upgrading into transportation fuel (Eboibi *et al.*, 2014). Interestingly, the higher percentage reduction in oxygen content has promoted the heating value of the biocrude obtained at higher temperature to 37.76 MJ/kg when compared to that obtained at 330 °C (33.78 MJ/kg) and the starting orange peels feedstock (18.88 MJ/kg). The obtained heating value indicated that biocrude contains higher heating value as compared to the biocrude obtained from the report of Nguyen *et al.* (2021).

4.8.3 Total Acid Number (TAN) and Water Content of the Biocrude Produced

The total acid number gives the acidity content in the biocrudes which is determined titration method by the quantity of KOH (mg) required to neutralize the acidic content in a gram of the biocrude. High amount of acid numbers in biocrude have been reported to promote corrosion during biocrude storage and transportation and rusting of tanks and machinery parts. The TAN of the biocrude obtained at 330 °C and 430 °C at 3 wt. % catalyst loading were 26.12 and 14.89 mg KOH g⁻¹ respectively. Although the obtained TAN obtained in both cases were high as compared to the standard (0.5 mg KOH/g) but relatively far below from several values reported in literature. For instance, Wang *et al.* 2(018) reported TAN values ranging from 234.65 – 268.68 mgKOHg⁻¹ during the HTL of microalgae over Ni/TiO₂ catalyst in water as solvent and 60–110 mg KOH/g was reported by Oasmaa and Meier (2015). The higher content of TAN reported could be associated with the composition of the feedstock which determined the product formation at the reaction conditions in the water medium. Therefore, the presence of water as solvent could be said to favor the formation of carbonyl groups' containing compounds in biocrude reported by Wang *et al.* 2(018). Furthermore, a more closer TAN's value of 19 mgKOHg⁻¹ of biocrude has been reported by Nguyen *et al.* (2021) during the HTL of *Cladophora socialis* macroalgae over Fe supported catalyst. From the present observations, the solvent ratio of acetone to ethanol (3:1) adopted favors lower formation of functional groups containing carboxyl functional groups such as carbohydrates, amino acids and fatty acid hence, hydrolysis reaction of lipids was not favored at higher temperature of 430 °C and 3 wt. % catalyst loading as compared to 330 °C. This observation is well supported from the acid content formation depicted in the GC-MS result shown in Fig. 8.

Water content is another important parameter in biocrude which determines the combustion properties in furnace, engines and in boilers when used as fuel. Furthermore, water content generally influences storage properties of biocrude during storage and transportation and adversely impaired engine performance at a composition above the acceptable standard. The water content from the two biocrude were obtained to be 3.68 and 0.92 wt. % for the biocrude obtained at 330 °C and 430 °C with 3 wt.% catalyst loading respectively. These values obtained were found to be below several reported values from literature which indicated the effectiveness and efficiency of the adopted process conditions and the catalyst used for the conversion process. For instance, the water content of 58.58 wt% and 43.05–72.74 wt% were obtained from the report of Wauton and Ogbeide (2021) and Khasri *et al.* (2012) respectively.

The presence of lower water content obtained at higher temperature of 430 °C and 3 wt.% catalyst loading could indicate the possibilities of Fe loading on CNSs support to inhibit the formation of secondary reaction which could have enhanced the formation of hydrated compounds. In both cases of the biocrude obtained, we observed no phase separation in the biocrude and hence, we attributed such observation further to the presence of lower amount of water content in the biocrudes (Joseph *et al.*, 2016). The adoption of reduced pressure during the evaporation process of solvent recovery could further be associated with the reduction of the inherent water contents in the biocrudes produced. Hence, producing biocrude with low water content which inferably improves the heating value of the biocrude, the need for effective catalyst and selection of process conditions are of importance.

4.8.4 Functional Groups Analysis

The biomass feedstock, solid residue and the biocrude obtained at the optimum conditions of the HTL process were examined using the FTIR technique as shown in Fig. 28.

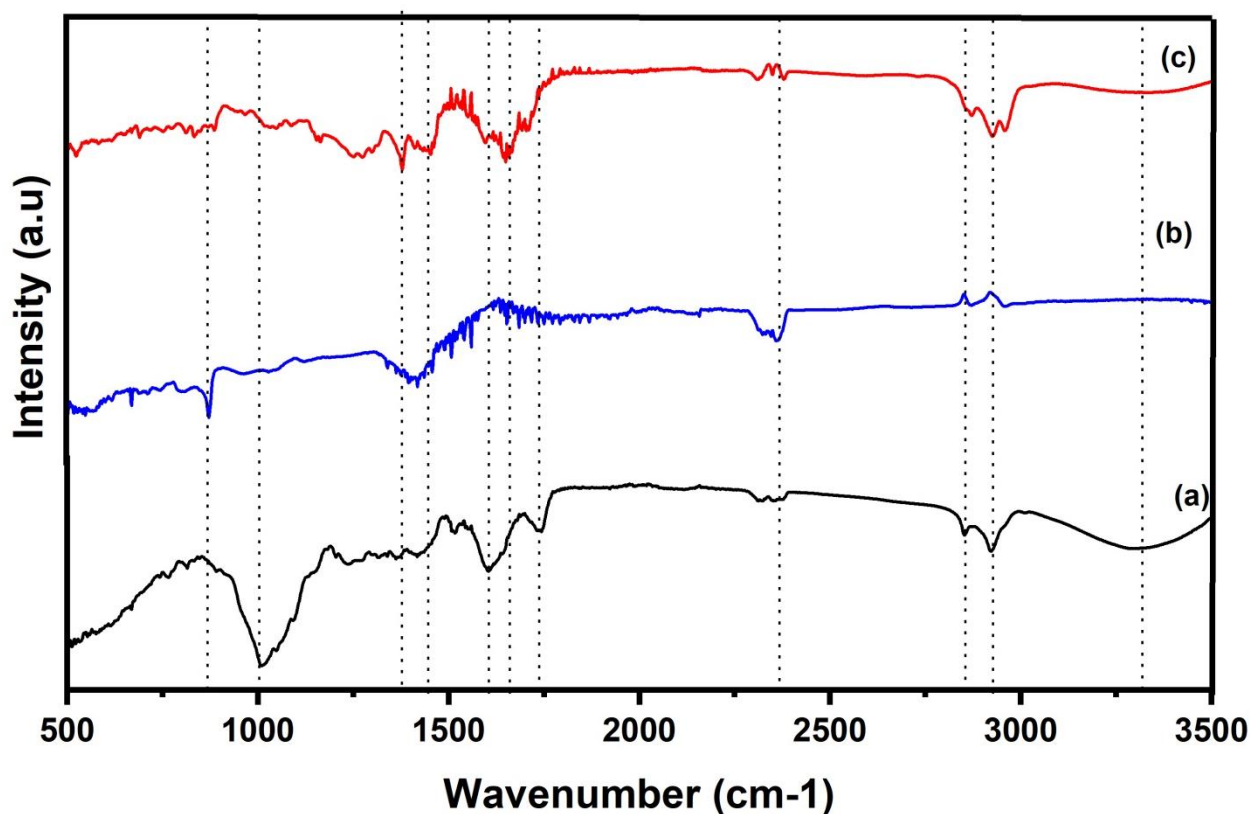


Figure 28: The FTIR spectra of (a) Orange peels (b) solid residue and (c) biocrude; (b-c) obtained after the catalytic STL of orange peels

The functional groups present on the considered materials were analyzed and the variations in the functional groups due to the thermo-conversion process were well illustrated in Table 18.

Interestingly, the presence of bonded -OH was only observed in the orange peels. The absence of -OH group in both the solid residue and biocrude could be resulted to the fact that, the adopted solvent and the catalyst enhances the instability nature of the -OH group. This similar observation of -OH bond of possible alcohols and phenols disappearance has been observed by Ma *et al.* (2021) as further indicated from the GC-MS compositions depicted in Fig. 28 and Table 18. The broadband at the wavenumber spanning from 1931-2848 and 1931-2960 cm^{-1} in the dried orange feedstock and the biocrude, respectively is an indication of the effectiveness and efficiency of the adopted processes and the catalyst material employed to extract the alkanes from the parent material. This C-H functional group is completely absence on the solid residue material while the presence of methyl C-H stretching located at the wavenumber of 2358 cm^{-1} were observed throughout the surface of the materials.

The volatility of aromatic combination bonds was well observed at the broadband of 1736 cm^{-1} ; this peak was only observed on the orange peel feedstock. The absence of this peaks in both the solid residue and the biocrude could implies that the adopted temperature of 430 °C convert the aromatic bonds components into a gaseous compound. Ketones, quinones and aldehydes, organic compounds which could only be obtained through the degradation of biomass materials were observed in the biocrude and absence in both the orange peels and the solid residue at 1711 cm^{-1} . This observation suggests that: (a) the presence of ketones cannot be noticed on the surface of biomass feedstock until it has been degraded (b) that the adopted solvent (75mL acetone and 25 mL ethanol) is excellent solvent in complete degradation of orange peels in STL setup (c) and the solid residue was completely washed during the recovery of biocrude; termed the purification process was effective. The absence of C-O stretch at the wavenumber of 1002 cm^{-1} indicating the presence of ether; an oxygenated compounds in the biocrude implies a possible reduction in the number of oxygen atom which could adversely inhibit the performance of the biocrude after the upgrading process.

Table 18: The FTIR Peaks assignment extracted from Fig. 28

Frequency (cm ⁻¹)					
IR Peaks	Orange peels	Solid residue	Biocrude	Peaks Assignment	ref
1	3320	-	-	Bonded -OH indication the presence of unstable OH from alcohols and phenols.	Ma <i>et al.</i> (2021)
2	2931-2848	-	2931-2960	C-H functional group indicating the presence of alkanes	Biswas <i>et al.</i> (2020) and Liu <i>et al.</i> (2018)
3	2358	2358	2358	Methyl C-H stretching	Zhang <i>et al.</i> (2017)
4	1736	-	-	Aromatic combination bands	Zhang <i>et al.</i> (2017)
5	-	-	1711	C = O stretch indicating the presence of Ketone, quinones and aldehydes	
6	1601	-	1657-1601	Alkenyl C=C stretching	Zhang <i>et al.</i> (2017)
7	1438	1411	1438	C=C-C aryl ring stretching	TermehYousefi <i>et al.</i> (2014) and Titirici <i>et al.</i> (2007)
8	-	-	1377	O-H bending of Phenol or tertiary alcohol	Zhang <i>et al.</i> (2017)
9	-	-	1279	O-H in-plane bending of Primary or secondary alcohol	Zhang <i>et al.</i> (2017)
10	1002	-	-	C-O stretch indicating the presence of ether; a secondary alcohol	
11	-	660-867	-	Aromatic C-H out-of-plane bending	TermehYousefi <i>et al.</i> (2014) and Titirici <i>et al.</i> (2007)

4.8.5 Mechanisms of Biocrude Formation through Catalytic STL Process

The mechanisms of biomass conversion into biocrude have been identified with a complex reaction pathway due to the presence of complex structures of organic constituents. These compositions include proteins, carbohydrates, lipids and non-cellulosic carbohydrates which is converted into smaller molecular organic structure with improved fuel properties (Hao *et al.*, 2021; Zhang *et al.*, 2021). In this present research, we have postulated mechanisms of reaction

which is presented herein to follow the reaction paths of constituents' having the high selectivity as shown in Fig. 13.

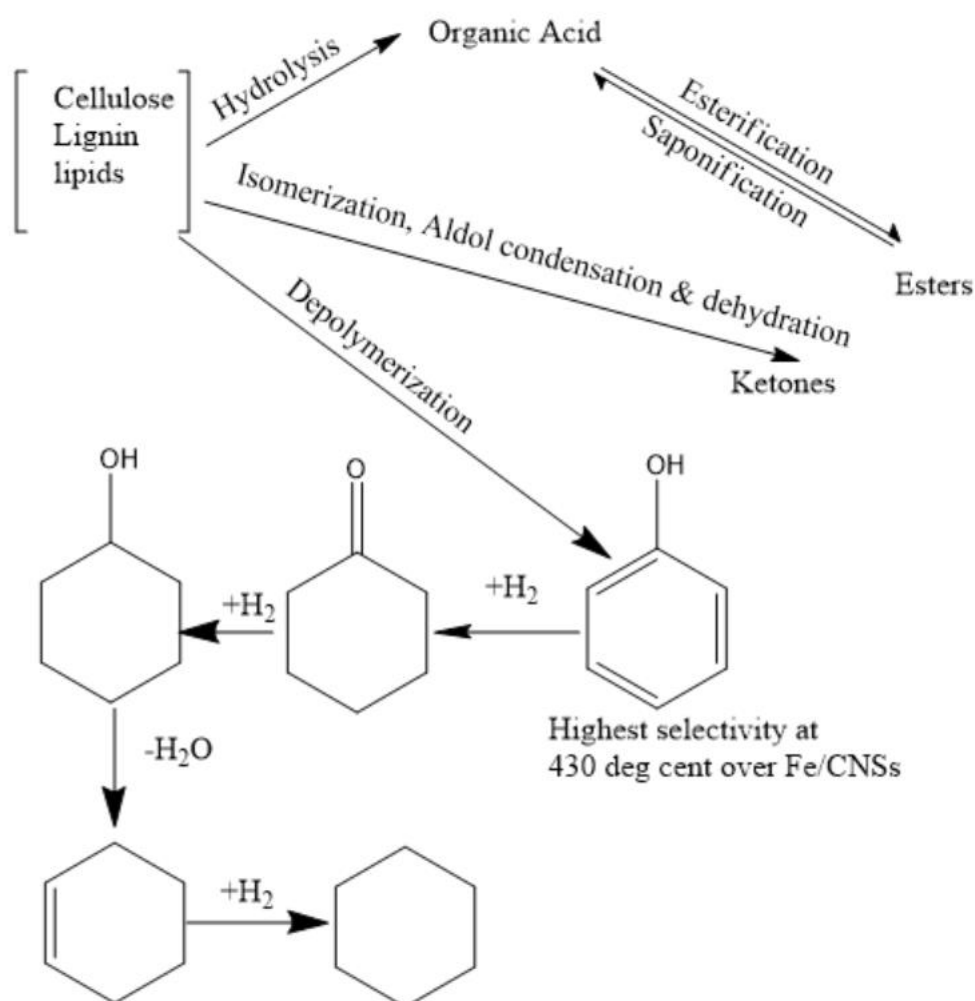


Figure 29: Mechanism of orange peels conversion over Fe/CNSs into biocrude.

4.8.6 Surface Morphology of the Solid Residue

The surface morphology of the obtained solid residue at the optimized conditions is as presented in Fig. 30.

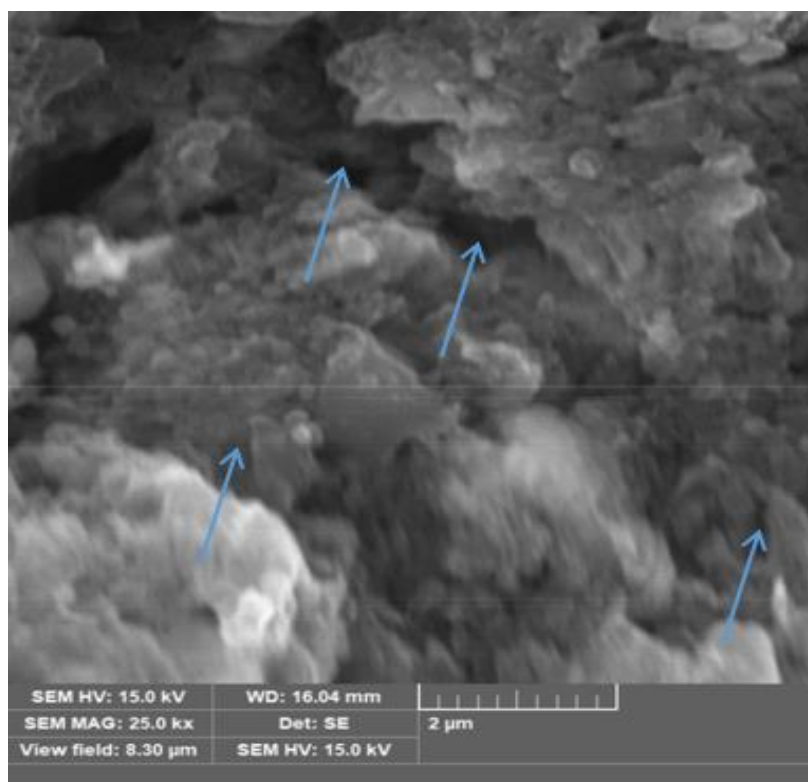


Figure 30: Surface morphology of the obtained solid residue at the optimum conditions

From the SEM image depicted in Fig. 30, the presences of pore were observed on the material. The presence of pores could be associated with the valorization process which has led to the removal of huge number of volatile constituents from the orange peels leading to the presence of pores. The present morphology of the solid residue obtained has high tendency for further modification for pore enhancement for possible use as adsorbents for catalyst support during the biocrude upgrading process. Furthermore, the pore formation on the surfaces of the solid residue is an indication of its possible use for soil improvement. Similar observation has been reported in the findings of Arafat Hossain *et al.* (2017) who studied the optimization of process parameters for microwave pyrolysis of oil palm fiber (OPF) for hydrogen and biochar production. Also, the possible use of the obtained solid residue for soil remediation and carbon sequestration are reported in the findings of Leng *et al.* (2015, 2019).

Through the comparison of the composition of the biocrude obtained from the optimization study using the Fe/CNSs as catalysts and the biocrude which gives the highest HHV value for the non-catalytic STL of the orange peels, the data are presented as shown in Table 19. Due to the high composition of hydrocarbons, low acid formation and nitrogen containing compounds formed during the STL at 430 °C, 35 min, 50:50 (ethanol:acetone), the biocrude obtained at this condition was employed for the upgrading process via HDO process.

Table 19: Comparison of the biocrude's composition and HHV for catalytic and non-catalytic STL process

Composition	330 °C, 3 wt.% Fe/CNSs	430 °C, 3 wt.% Fe/CNSs	430 °C, 35 min, 25% EtOH	430 °C, 35 min, 50% EtOH
Ketone	43.53	27.52	32.58	34.23
Alcohol	0.00	0.31	1.97	0.60
Acid	7.98	5.09	0	0.00
Ester	22.59	0.79	0	2.56
Aromatic	6.60	19.26	17.48	10.40
Phenolic	4.74	35.56	43.33	46.76
Ether	5.22	0.00	0	0.57
Hydrocarbon	1.82	1.46	1.24	3.63
Nitrogen	7.53	8.55	3.41	1.24
etc	0.00	1.47	0	0.00
HHV (MJ/kg)	33.78	37.76	37.00	38.81

4.9 Cyclohexanone Upgrading

The presence of large amount of ketones, an oxygenated compounds in the crude bio-oil samples calls for the need to develop an effective catalyst for the oxygen removal. Screening through the application of Ni, Fe, Ce and Zn on the biochar obtained at 430 °C, 35 min, 50 EtOH, the monometallic catalyst was developed and tested on cyclohexanone as a model compound. Prior to the catalytic evaluation of the cyclohexanone upgrading, non-catalytic HDO was studied at varied reaction conditions to understand the contributory effects of process parameters most especially, temperature and residence time. Ni is expected to primarily drive hydrogenation and deoxygenation reactions, while Fe is anticipated to support hydrogenation and hydrogen transfer, enhancing overall catalyst activity. Ce is likely to contribute to oxygen management and promote catalytic efficiency, and Zn is expected to improve selectivity and minimize side reactions through its Lewis acid properties.

4.9.1 Non-catalytic HDO of Cyclohexanone

The selection of cyclohexanone as a model compound for this research was guided with the presence of large cyclo-ketones in the obtained biocrudes. To understand the chemistry of the HDO process of the ketones in the absence of external hydrogen supply, the cyclohexanone model compounds was opted for. The effects of temperature, residence time, feed loading and formic acid on the HDO of cyclohexanone under the influence of EtOH as a solvent was investigated. The results from the investigation are presented in Fig. 31 where the effects of

the process parameters were studied on the yield of the biofuel and the associated water content formation.

From the results depicted in Fig. 31a, temperature possesses a high contributory effect on the biofuel formation. The biofuel yields were obtained to be 55.3, 59.7, 68.4, 72.1, 64.6 and 58.7 wt.% at 225, 250, 275, 300, 325, and 350 °C respectively at initial nitrogen pressure of 10bar and 1 h residence time. A gradual increase in biofuel was observed from the initial reaction temperatures (225-300 °C) due to an effective conversion of cyclohexanone to cyclohexanol and some accompanied products in the case of 300 °C where about 0.70 area % of ether was observed. As the temperature increases, the ethanol breaks down to producing hydrogen which aid the hydrogenation of the cyclohexanone into cyclohexanol. The water content formation during the process signifies the dependency of the hydrogenation on the temperature of the reaction where dehydration takes place. The water content increases progressively from 0.68 to 1.79 wt.% between 225-325 °C and drops to 1.03 wt.% at 350 °C. The observable drop in the water content could be attributed to the possibilities of inherent water to serve as a solvent at the supercritical conditions (220 bar) leading to the formation of hydrogen gas hence, reducing the water content. Adversely, the presence of water as a by-product of biofuel upgrading has a potential of retarding the catalytic activities during the catalytic upgrading process through the leaching of the active sites of catalysts and ultimately, catalyst deactivation by poisoning.

The results shown in Fig. 31b illustrates the effects of residence time on the cyclohexanone conversion at 350 °C reaction temperature while keeping the pressure constant at 10 bar and agitation at 300 rpm. An increase in the biofuel formation were recorded from 0-2h residence time to be 58.70, 73.60 and 78.60 wt.% respectively. The justification to the formation of an improved biofuel yield could be attributed to the elongated residence time which promotes the contact of reactant to products formation. The drop in the biofuel yield at the 3h residence time could be attributed to the possible conversion of the cyclohexanol to cyclohexanone through reverse process. This observation is evident from the compositional constituent of the obtained biofuel at 3 h where the area percentage of the cyclohexanol drops from 83.46 to 82.86 area % at 2 to 3h residence time respectively.

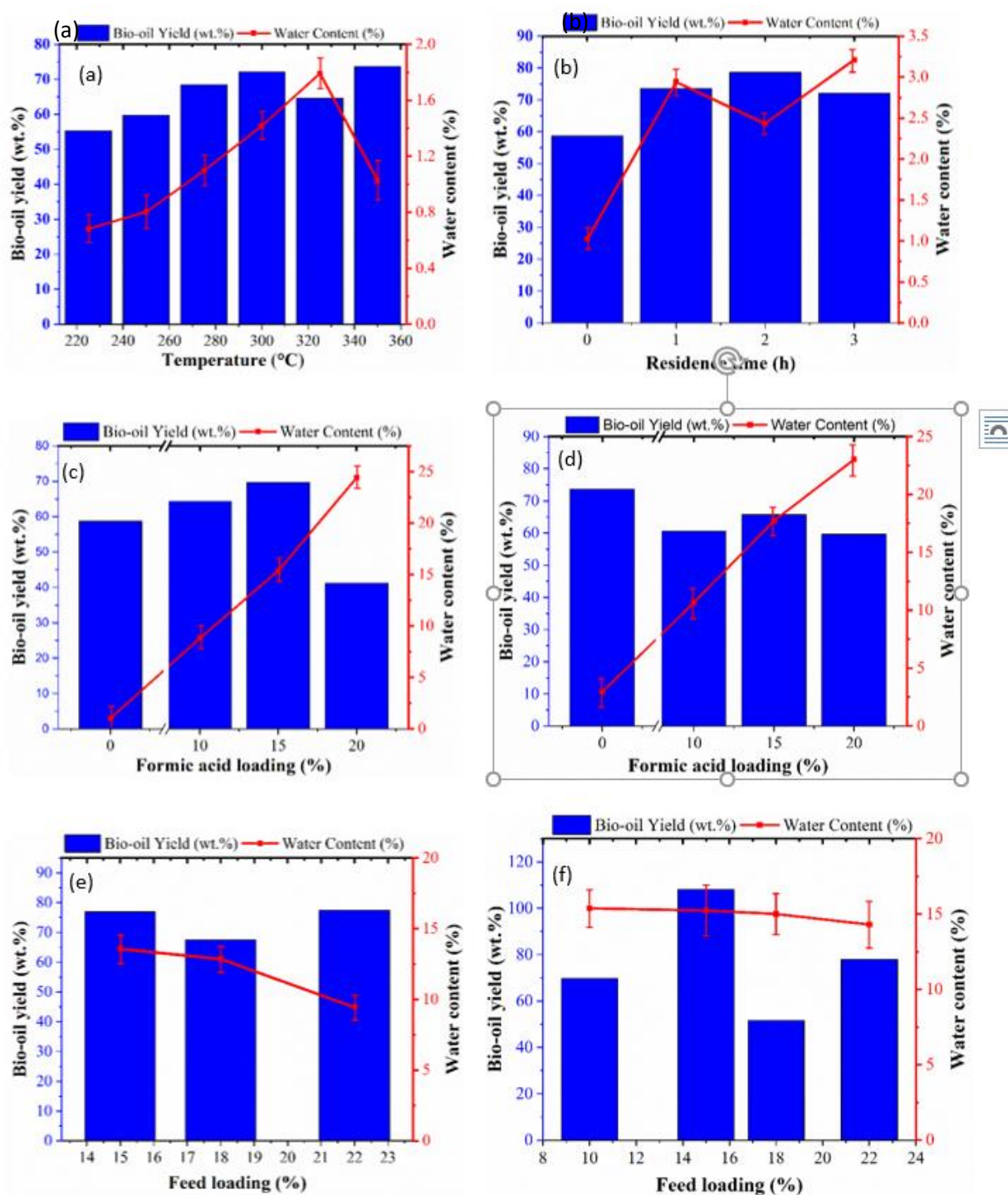


Figure 31: Effects of process parameters (a) temperature; (b) residence time; (c) formic acid at 0h; (d) formic acid at 1h (e) feed loading @ 0bar and (d) feed loading at 10bar on bio-oil yield and water content

Formic acid has been widely employed to promote the HDO of bio-oil and model compounds into an advanced fuels by several researchers due to its ability for in-situ hydrogen supply (Park *et al.*, 2019; Serrano-Ruiz *et al.*, 2010). The effects of formic acid loading at constant feed

loading are presented in Figs. 31 (c-d) for 0 and 1h residence time respectively. The introduction of formic acid has a noticeable effect on the biofuel formation. For instance, the biofuel yield of 58.7, 64.3 and 69.7 wt.% at 0, 10 and 15 wt% of formic acid respectively. This observation could be associated to the efficacy of formic acid to decompose into hydrogen which promotes the upgrading process. The decomposition of formic acid into hydrogen with associated high decarboxylation and dehydration potentials have been reported by Halleraker *et al.* (2020) and Park *et al.* (2019). The mechanisms of the formic acid dissociation at the supercritical conditions were reported to be influenced by the reaction conditions such as temperature and the introduction of water. The non-catalytic behavior of the cyclohexanone decomposition has been presented in Fig. 31a and b to produce water content, hence, the water obtained has huge tendency to impact the formic acid dissociation towards $\text{CO} + 2\text{H}_2\text{O}$ and $\text{CO}_2 + \text{H}_2 + \text{H}_2\text{O}$ (Halleraker *et al.*, 2020). This observation could be associated to the observed increase in the gas pressure during the reaction process. Corroboratively, high percentage water content was observed following the introduction of formic acid into the reaction system. The water content was observed to be 1.03, 8.82, 15.39 and 34.41 wt% at 0, 10, 15 and 20 % respectively as indicated in Fig. 31c. Similar direct proportionality of water content increment as formic acid increases was observed at the residence time of 1h according to the results in Fig. 31d. At the residence time of 1h, the biofuel yield drops considerably when compared to no-formic acid induced reaction from 73.6 to 59.6 wt% at 0 and 20 % formic loading.

The effects of feed loading at 0 and 10bar initial nitrogen supply were investigated to understand how the feed ratio at constant ethanol to formic acid affects the biofuel yield and the water formation. The obtained results as presented in Figs. 31 (e-f) indicate that, the feed ratio has a sinusoidal effect on the yield of the biofuel while an inverse proportionality was noticed on the water formation.

The effects of process parameters on the biofuel compositions and the overall cyclohexanone conversion are presented in Figs. 32 (a-f).

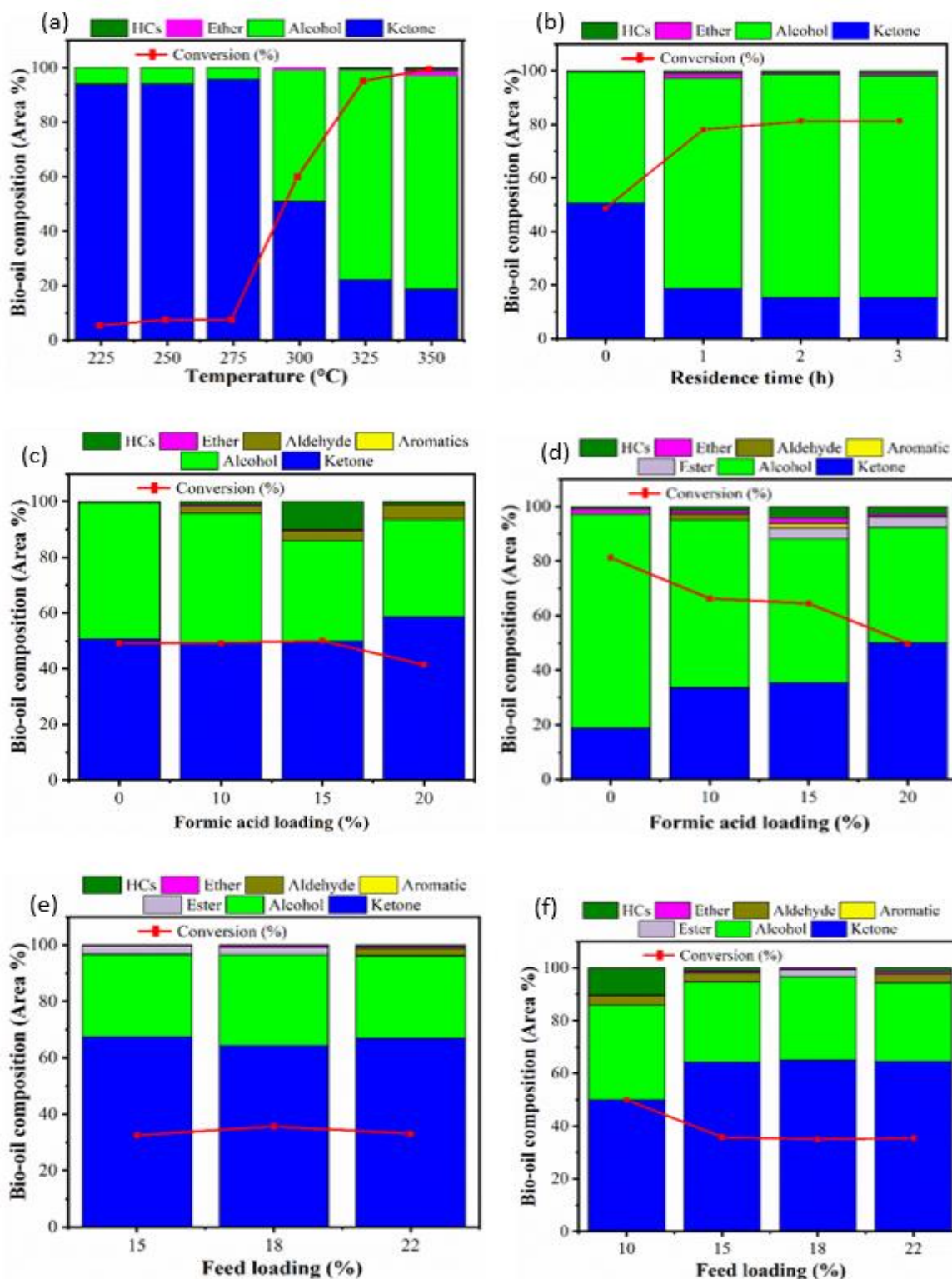


Figure 32: Effects of process parameters (a) temperature; (b) residence time; (c) formic acid at 0h; (d) formic acid at 1h (e) feed loading @ 0bar and (d) feed loading @ 10bar on biofuel composition and cyclohexanone conversion

The evaluation of the biofuel composition was carried out by GC-MS equipment and the results give an insight into the selectivity of cyclohexanol due to hydrogenation process that was

enhanced by the in-situ hydrogen production by ethanol and also formic acid. From the information provided in Fig. 32a, the percentage ketone conversion was 4.2, 5.93, 6.0, 49.01, 77.73 and 81.24 area% translating to 4.20, 5.93, 6.00, 48.31, 77.04 and 78.48 area% of alcohol at 225, 250, 275, 300, 325 and 350 °C respectively. From the results presented, the obvious contribution of temperature to the overall selectivity to cyclohexanol formation was observed. This could be associated to the increment in the internal kinetic energies for dissociation, dissociation of ethanol which forms hydrogen for hydrogenation reaction at supercritical condition of ethanol. The formation of ether was also observed at higher temperatures of 300°C, 325°C, and 350°C, with respective area percentages of 0.70, 0.15, and 1.85%. Furthermore, the presence of hydrocarbon compounds; cycloheptane was formed due to the complete hydrogenation, dehydration of cyclohexanone and cyclohexanol respectively. This observation highlights the impact of higher temperatures, specifically 325°C and 350°C, in promoting complete hydrogenation for hydrocarbon formation, resulting in 0.54 area% and 0.91 area% of cyclohexane, respectively as shown in Fig. 32a.

The formation of higher content of hydrocarbons and higher cyclohexanol selectivity at 350 °C forms the basis for the investigation of the effects of residence time on the overall conversion and upgrading of cyclohexanone model compound and the results are depicted in Fig. 32b. A significant increase in cyclohexanol conversion was observed as the residence time increased from 0 to 1 hour. Specifically, cyclohexanone conversion rates were measured at 49.26%, 81.24%, 84.65%, and 84.71% for residence times of 0, 1, 2, and 3 hours, respectively. Based on the results presented, an extended residence time improves the overall ketone conversion by allowing the reactants to have the necessary contact with hydrogen for the hydrogenation and dehydration processes. From the results presented in Fig. 32b, the HCs formation was 0.34, 0.91, 0.72 and 1.06 at 0, 1, 2 and 3 h residence time respectively. Moreover, extending the contact time enhances the selectivity for cyclohexanol formation through the hydrogenation process up to a residence time of 2 h. Beyond this 2 h mark, the selectivity for cyclohexanol decreases from 83.46 to 82.86 area% (2-3h), and an increase in hydrocarbon formation is observed at a 3 h residence. Regarding ether formation, no ether was produced at 0 h of residence time. However, a decrease in ether formation was observed as the residence time increased from 1 to 2 h, with recorded values of 1.85 and 0.47 area%, respectively with a further increase at 3 h to 0.79 area%. Interestingly, the solvothermal upgrading of cyclohexanone reported in the present findings demonstrates a high selectivity for cyclohexanol and hydrocarbon content, achieving 83.46% and 1.06 area%, respectively. This performance

surpasses the catalytic upgrading over Cu powder reported by Song *et al.* (2016) which resulted in 75.1% cyclohexanol formation. Hence, ethanol medium and a prolong residence time promote the overall hydrogenation and the subsequent dehydration process for cyclohexanol and cyclohexane production.

To study the effects of formic acid during the reaction process, the influence of formic acid loading at 0 and 1 h residence times was investigated, with the results presented in Fig. 32c and d, respectively. As shown in Fig. 32c; 0 h residence time, the introduction of formic acid impaired both conversion and selectivity to cyclohexanol, although reaction intermediates such as aldehydes were produced. With formic acid loadings of 10, 15, and 20%, the product distribution included aldehydes and ethers at 2.71, 3.58, and 4.84 area% and 0.00, 0.46, and 0.38 area%, respectively. The aldehydes were primarily composed of cyclohexane acetaldehyde when formic acid was introduced. Additionally, an increase in hydrocarbon formation was observed, reaching 0.34, 1.03, 10.10, and 1.10 area% at 0, 10, 15 and 30% formic acid loading, respectively, as shown in Fig. 32c. As presented in Fig. 32d, with a 1 h residence time, there is an improved conversion of cyclohexanone and increased selectivity for cyclohexanol compared to the 0 h residence time reaction category shown in Fig. 32c. Cyclohexanol selectivity was 78.48, 61.44, 52.69, and 42.25 area% for 0, 10, 15, and 20 % formic acid loading, respectively, while ether formation was 1.85, 1.08, 1.99, and 0.66 area% for the same loadings. Thus, the introduction of formic acid lowers the overall cyclohexanol selectivity but enhances the formation of hydrocarbon compounds due to the effective in-situ hydrogen production, which favors the hydrogenation of cyclohexanol into cycloheptane. The production of cycloheptane increases progressively with higher formic acid loading, yielding 0.91, 1.54, 4.22, and 2.84 area% at 0, 10, 15, and 20 % formic acid loading, respectively. Additionally, the formation of aromatic hydrocarbons was favored at 20 % and 15 % formic acid loading at 0 and 1 h residence time giving rise to 0.56 and 1.60 area% of aromatic compounds respectively. The aromatic compounds were primarily alkyl benzene such as (Benzene, 1,2,4-triethyl- and Benzene, 1,4-bis(1,1-dimethylethyl)-). This observation implies the enhancement of dehydrogenation and subsequent alkylation reaction resulted from the formation of active alkyl intermediates produced from the decomposition of ethanol. However, a drawback of adding formic acid is the increased gas pressure, which necessitates a larger reactor system and consequently raises operational costs.

Similarly, the effects of feed loading at a constant ethanol to formic acid ratio (70g: 20g) at 350°C and initial nitrogen supplies of 0 and 10 bar were investigated at a 0 h residence time as shown in Figs. 36 (e-f). As shown in Fig. 36, hydrocarbon production was 0.00, 0.29, and 0.59% at feed loadings of 15, 18, and 22%, respectively, while ester formation decreased from 2.95 to 2.61% as the feed loading increased from 15 to 18%. The increase in feed at constant ethanol loading affects the availability of in-situ hydrogen production for both hydrogenation and dehydration process for enhanced conversion of cyclohexanone into valuable products. It's noteworthy to state that the conversion of cyclohexanone into cyclohexanol exhibits a reverse process where process conditions determine the rate of forward and backward reactions. The obtained data during the non-catalytic cyclohexanone upgrading is as presented in Table 20.

From the results obtained during the non-catalytic upgrading of cyclohexanone into cyclohexanol and the associated hydrocarbon compounds, 350 °C reaction temperature favored the overall conversion process and selectivity to cyclohexanol and cycloheptene production. Hence, to further the study on the effects of transition metal doping on the conversion of cyclohexanone, 350 °C, 300 rpm, 10 bar of reaction temperature, agitation and initial nitrogen pressure were adopted respectively.

Table 20: Non-catalytic upgrading of cyclohexanone in the presence of ethanol as solvent at various reaction conditions

Parameters/ composition	Ketone	Alcohol	Ester	Aromatic	Aldehyde	Ether	HCs	ketones	conversion	Water content (%)	biofuel	yield (%)	Reaction Pressure (bar)	Feed Conversion (%)
Feed	100	--	-	-	-	-	-	-	-	-	-	-	-	-
Temperature														
225 °C-1hr	95.799	4.201	0.00	0.00	0.00	0.00	0.00		4.20	0.68	55.30	46.80		44.70
250 °C -1hr	94.065	5.935	0.00	0.00	0.00	0.00	0.00		5.93	0.80	59.70	75.40		40.30
275 °C -1hr	93.998	6.002	0.00	0.00	0.00	0.00	0.00		6.00	1.10	68.40	100.20		31.60
300 °C -1hr	50.991	48.313	0.00	0.00	0.00	0.70	0.00		49.01	1.42	72.10	145.20		27.90
325 °C -1hr	22.271	77.042	0.00	0.00	0.00	0.15	0.54		77.73	1.79	64.60	162.10		35.40
350 °C -1hr	18.762	78.481	0.00	0.00	0.00	1.85	0.91		81.24	1.03	58.70	219.90		26.40
residence time														
350 °C -0hr	50.744	48.918	0.00	0.00	0.00	0.00	0.34		49.26	1.03	58.70	172.90		41.30
350 °C -1hr	18.762	78.481	0.00	0.00	0.00	1.85	0.91		81.24	2.94	73.60	219.90		26.40
350 °C -2hr	15.350	83.461	0.00	0.00	0.00	0.47	0.72		84.65	2.44	78.60	186.70		21.40
350 °C -3hr	15.290	82.862	0.00	0.00	0.00	0.79	1.06		84.71	3.21	72.10	209.70		27.90
formic acid, 0hr														
90EtOH:0Formic Acid	50.744	48.918	0.00	0.00	0.00		0.34		49.26	1.03	58.70	172.90		41.30
80EtOH:10Formic Acid	95.334	0.464	0.00	0.00	2.71	0.46	1.03		4.67	8.82	64.30	178.70		35.70
70EtOH:20Formic Acid	50.028	35.906	0.00	0.00	3.58	0.38	10.10		49.97	15.39	69.70	193.70		30.30
60EtOH:30Formic Acid	58.569	34.925	0.00	0.56	4.84	0.00	1.10		41.43	24.41	41.20	233.40		58.80
formic acid, 1 h														
90EtOH:0Formic Acid	18.762	78.481	0.00	0.00	0.00	1.85	0.91		81.24	2.94	73.60	219.90		26.40
80EtOH:10Formic Acid	33.697	61.435	0.00	0.00	2.25	1.08	1.54		66.30	10.66	60.60	179.20		39.40
70EtOH:20Formic Acid	35.525	52.692	3.97	1.60	0.00	1.99	4.22		64.47	17.74	65.70	260.00		34.30

Parameters/ composition	Ketone	Alcohol	Ester	Aromatic	Aldehyde	Ether	HCS	ketones conversion	Water content (%)	biofuel yield (%)	Reaction Pressure (bar)	Feed Conversion (%)
60EtOH:30Formic Acid	50.158	42.253	3.75		0.34	0.66	2.84	49.84	23.03	59.60	292.30	40.40
feedstock loading, 10bar N ₂												
70g:20g:10g (EtOH:Facid:Cyclo-)	50.028	35.906	0.00	0.00	3.58	0.38	10.10	49.97	15.39	69.70	260.00	34.30
70g:20g:15g (EtOH:Facid:Cyclo-)	64.230	30.273	0.00	0.33	3.28	0.82	1.07	35.77	15.24	108.10	194.80	100.00
70g:20g:20g (EtOH:Facid:Cyclo-)	64.985	31.682	2.79	0.00	0.00	0.54	0.00	35.02	15.01	51.60	195.00	48.40
70g:20g:25g (EtOH:Facid:Cyclo-)	64.567	29.683	0.00	0.20	3.25	0.82	1.48	35.43	14.30	78.00	222.30	22.00
feedstock loading, 0bar N ₂												
70g:20g:15g (EtOH:Facid:Cyclo-)	67.458	29.192	2.95	0.00	0.00	0.40	0.00	32.54	13.60	76.90	173.50	23.13
70g:20g:20g (EtOH:Facid:Cyclo-)	64.326	32.259	2.61	0.00	0.00	0.51	0.29	35.67	12.88	67.60	181.90	32.45
70g:20g:25g (EtOH:Facid:Cyclo-)	66.889	29.152	0.00	0.24	2.52	0.61	0.59	33.11	9.46	77.40	200.10	22.60

4.9.2 Monometallic Catalysts' Characterization

Prior to the catalytic evaluation of cyclohexanone upgrading over metallic catalyst particles, several transition metal-based catalysts were developed on a neutral support material for details understanding of the effects of metallic particles during the upgrading process. Hence, the selection of the biochar obtained at 50% EtOH at 35 min reaction and 430 °C reaction was adopted for this study. The surface area, and the crystallinity of the monometallic catalysts (Ni, Ce, Zn and Fe) supported on biochar were investigated via BET and XRD techniques. The results shown in Figs. 33 (a-e) and Figs. 34 (a-b) represent the XRD crystallography and the BET information of the developed catalysts and the support biochar.

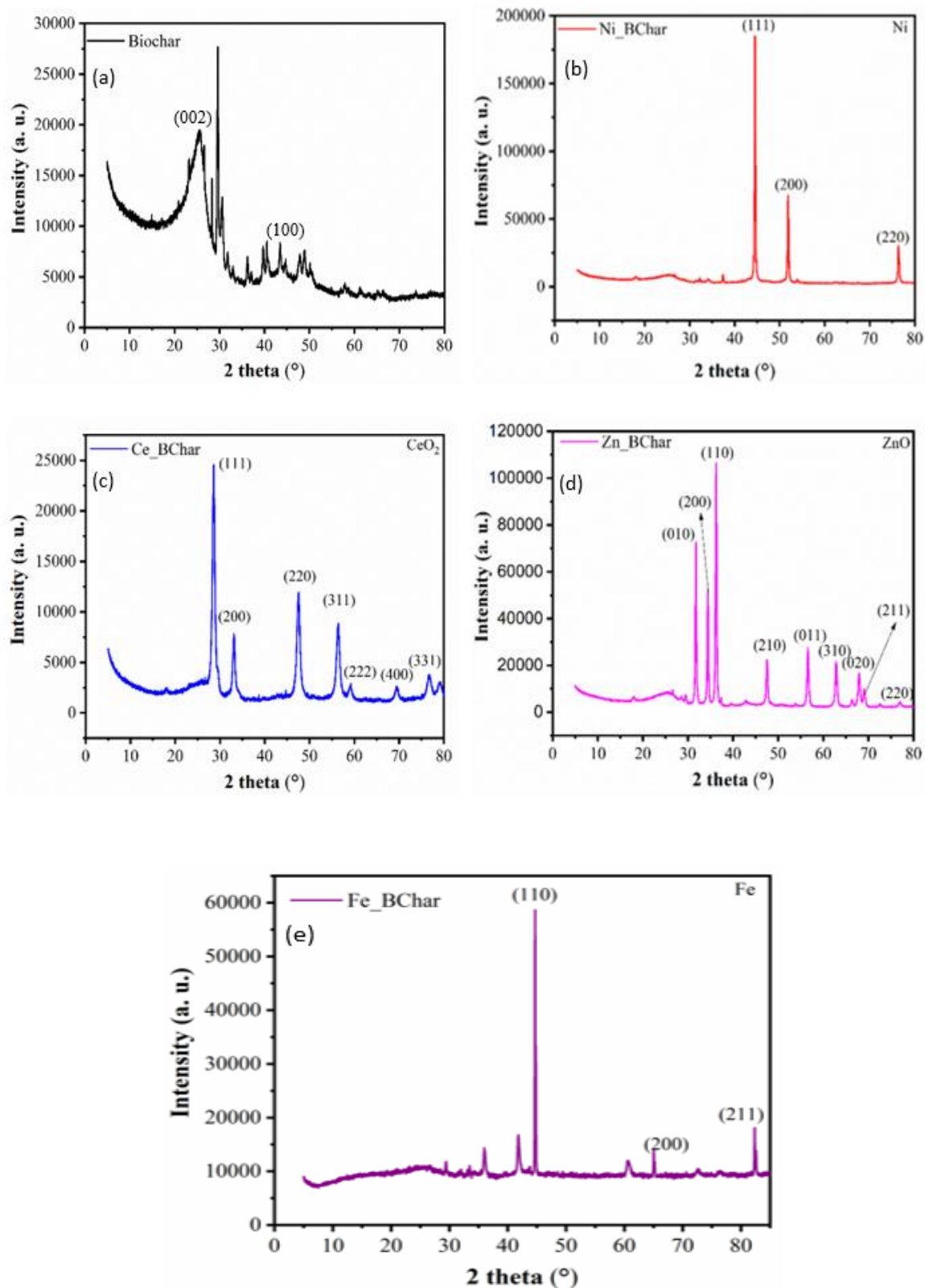


Figure 33: The XRD crystallography of (a) Biochar (b) Ni (c) Ce (d) Zn and (e) Fe supported biochar

From the results depicted in Fig. 33a, the crystallography shows a typical characteristic peaks of an amorphous carbon material with a broad diffraction angles at the 2θ of 25.50 and 44.48 ° which represent the characteristics peaks of graphitic carbon with a reflection planes assigned to (002) and (100) respectively. The observation of these peaks are in agreement with several reported diffraction peaks of an activated carbon materials (Almoneef *et al.*, 2021; Liu *et al.*, 2020; Liu *et al.*, 2010; Rodrigues *et al.*, 2020). The XRD crystallography displayed on Figs. 33 (b-e) indicate the successful doping of the respective transition metals on the biochar supports. In addition, a shift in amorphous to crystalline materials were observed throughout the doped samples. Figure 33b, three districts' peaks at the diffraction angles of 2θ of 44.48, 51.88 and 76.06 ° were observed with reflection planes corresponding to (111), (200) and (220) respectively. The peaks assignments are in accordance with the JCPDS #002-2027 of a typical cubic structure of Ni. The indexed peaks depict a characteristic peak of nickel (Ni) for a typical face-centered cubic (FCC) crystal structure.

The indexed peaks as presented in Fig. 33b is in accordance to the findings of Jayaseelan *et al.* (2014) who reported the effect of sub-acute exposure to nickel nanoparticles on oxidative stress and histopathological changes in Mozambique tilapia, *Oreochromis mossambicus*. In addition, as contained from the result presented in Fig. 33c, the Ce supported biochar possesses a unique diffraction angle at 2θ of 28.58, 33.06, 47.50, 56.30, 59.04, 69.38 and 76.80 ° which according to the JCPDS #001-1734 correspond to (111), (200), (220), (311), (222), (400) and (331) of cubic crystal structure of CeO₂ particles. This observation is in accordance with the report of Priya *et al.* (2018); Schimming *et al.* (2015). Also, the presence of crystalline Zn particles was observed with the corresponding peaks assignment at 2θ of 31.62, 34.34, 36.28, 47.6, 56.56, 63.38, 66.7, 67.87, 69.22, 72.54 and 77.42 ° which by the JCPDS #000-9340 correspond to the reflection planes of (010), (200), (110), (210), (011), (310), (020), (211), (120), (400) and (220) respectively. The peaks assignment indicates the formation of a hexagonal crystals which compose of a sharp and strong diffraction peak as depicted in Fig. 33d. Furthermore, the successful doping of the biochar with Fe was further revealed with the XRD diffraction shown in Fig. 33e. From the diffraction angles presents in the Fig. 33e, at the 2θ of 44.78, 64.88 and 82.22 ° corresponds to the cubic structure of Fe according to the JCPDS # 002-1567 with reflection planes at (110), (200) and (211) respectively.

From the obtained data from the Scherrer equation, the crystallite size of the respective monometallic catalysts was calculated. The crystallites (grain) sizes were found to 29.31, 9.44,

22.08 and 25.44 nm for Ni, Ce, Zn and Fe supported biochar respectively. The small cubic crystallites size of 9.44 nm possessed by the ceria supported biochar could be responsible for its improved cyclohexanone conversion which is reported under the catalytic upgrading over ceria supported biochar.

The N₂ adsorption-desorption isotherms and the pore size distributions of the parent biochar and the developed monometallic catalysts are presented in Fig. 34 a and b respectively. In all cases of the isotherms presented in Fig. 34a, a type IV physio-sorption isotherms with a mesoporous behavior with H4 hysteresis loops were depicted. This observation of identification is in accordance with the report of Kazmi *et al.* (2023) and Park *et al.* (2019).

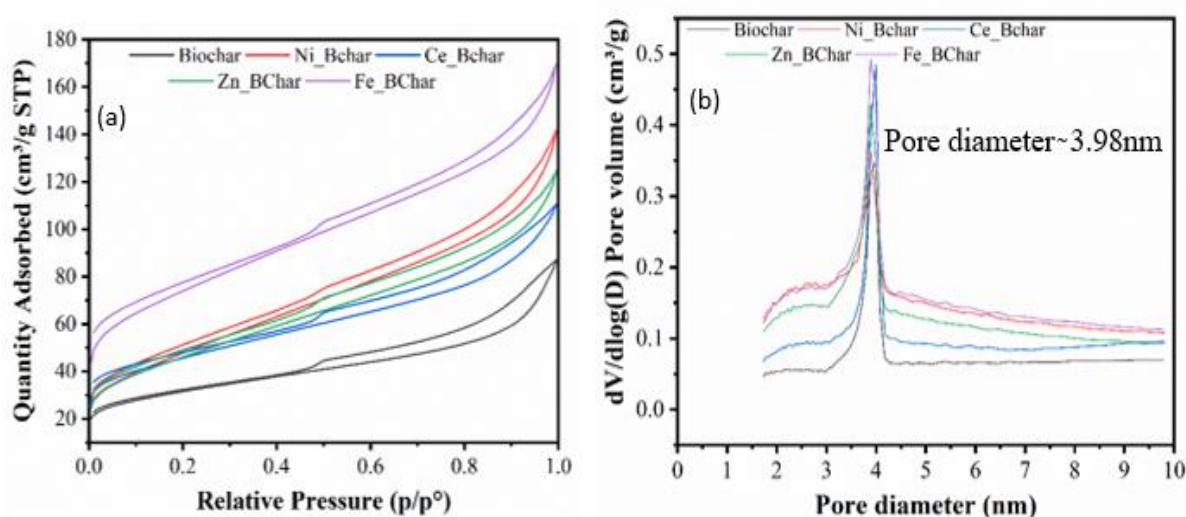


Figure 34: (a) The N₂ adsorption-desorption and (b) Pore diameter distribution of the developed catalysts and the biochar support

Generally, the adsorption isotherms reveal the interaction between the adsorbent and adsorbate, helping to clarify the adsorption mechanism (Wang *et al.*, 2020). The quantity of the adsorbed gases in all cases of the doping catalyst appears higher than the parent support materials while Fe supported biochar having the highest adsorption behaviors. This observation of Fe/Bchar with enhanced adsorption capacity could be related to the pore volume of 0.2631 cm³/g and the surface area of 263.65 m²/g as compared to other catalysts (detailed information of the physiochemical properties are found in Table 21. Moreover, no structural changes were observed in any of the doped catalysts when compared to the parent biochar. This indicates that the catalyst production procedure, specifically the wet impregnation method, does not affect the overall structural quality of the biochar sample Fig. 34. The average pore diameters were

estimated to be 3.98 nm which indicates the mesoporosity of the catalyst materials as indicated in Fig. 34b.

Table 21: Physiochemical properties of the developed catalysts

S/N	Catalyst	S_{BET} (m^2g^{-1})	V_p (cm^3g^{-1})	D_p (nm)
1	Biochar	112.86	0.14	6.85
2	Ni/Biochar	175.15	0.22	5.41
3	Ce/Biochar	162.27	0.17	5.63
4	Zn/Biochar	166.82	0.19	5.26
6	Fe/Biochar	263.65	0.26	4.93

S_{BET} = BET surface area

V_p = Single point desorption total volume of pores

D_p = BJH adsorption average pore diameter (4V/A)

The surface functional groups of the associated catalysts were analyzed via FTIR spectrophotometer and the results obtained are recorded in Fig. 35.

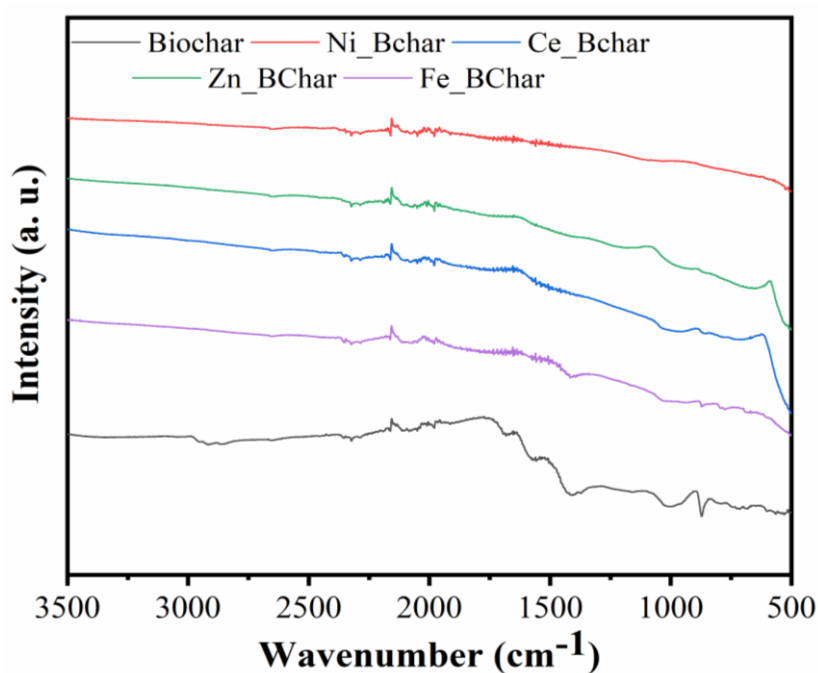


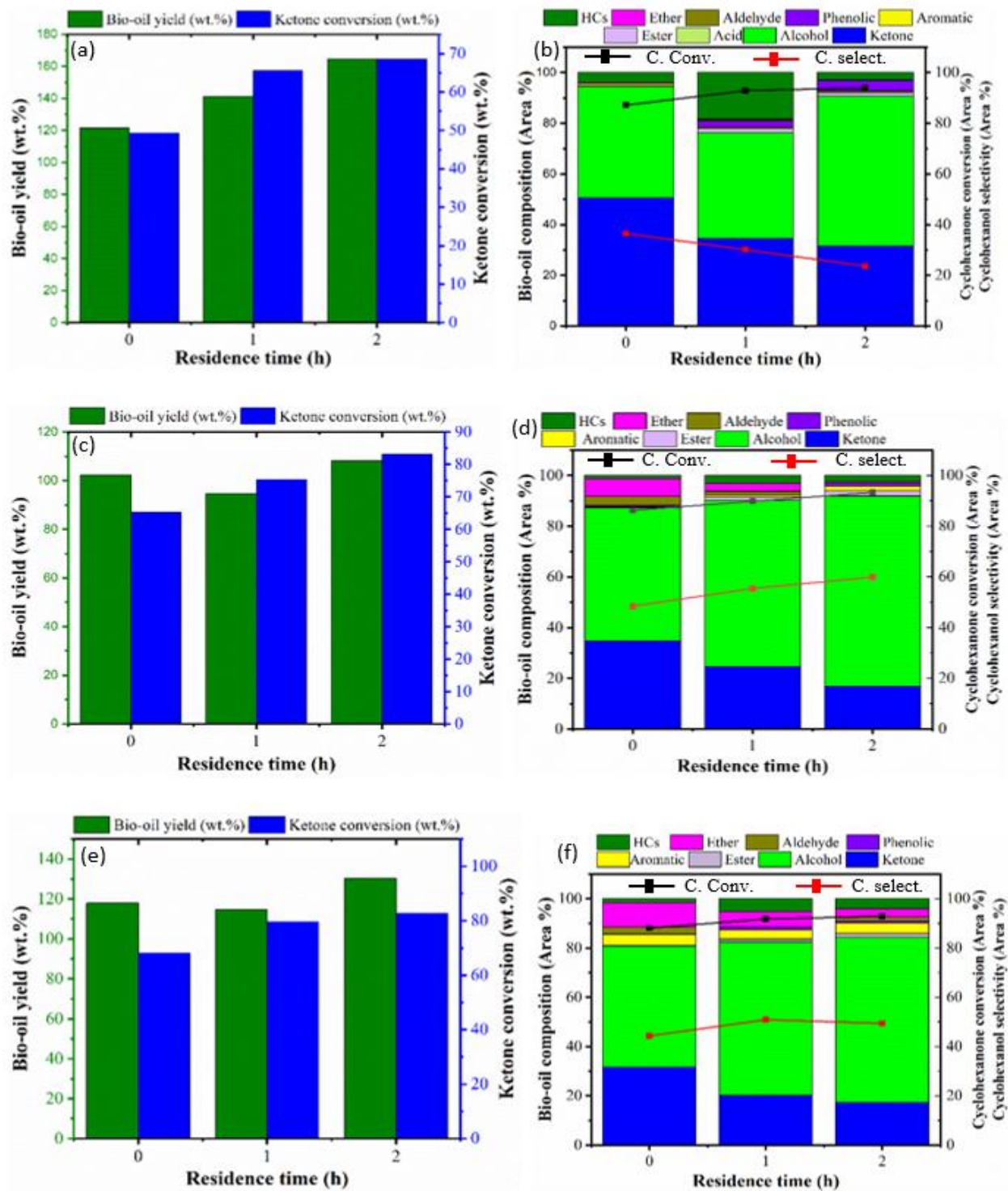
Figure 35: The FTIR spectra of the developed monometallic catalysts and the parent biochar

The FTIR results presented in Fig. 35 indicate the presence of several functional groups on the surfaces of the developed catalysts. Throughout the developed catalysts material, the formation of –OH group functional group compounds were absent due to the absence of peaks around the

3400 cm^{-1} wavenumbers. This could indicate the successful removal of both the physisorbed and chemisorbed in the samples. The presence of peak at the wavenumber of 2902 cm^{-1} was only noticeable on the biochar sample. This peak is associated with the C-H stretching. This peak assignment is in accordance with the report of Gouda *et al.* (2023), Liu *et al.* (2020) and Riyanto *et al.* (2020) and its only found on the biochar sample. Also, the peaks at 2306 cm^{-1} corresponds to the $\text{C}\equiv\text{C}$ bound which is present in all the catalyst materials including the biochar. This peak assignment is in accordance with the report of Riyanto *et al.* (2020). In addition, on the biochar sample, the presence of vibrational peak at 1673 and 1567 cm^{-1} were present and assigned to the $\text{C}=\text{O}$ stretching vibration of carboxylic groups and $\text{C}=\text{C}$ of aromatics in accordance to the findings of Gouda *et al.* (2023) and Liu *et al.* (2020), respectively. The presence of C-H asymmetric and symmetric vibrations which according to Gouda *et al.* (2023) and Riyanto *et al.* (2020) are associated to the peak located at the wavenumber of 1422 cm^{-1} as observed on the biochar and the Fe supported biochar catalyst. All the catalysts except the Ni supported biochar possess a vibrational peaks at 1012 cm^{-1} which is a characteristic peaks of C-O while the peak found on the biochar at 870 cm^{-1} is linked to the stretching vibration of C-H out of plane on the biochar (Gouda *et al.*, 2023). The peak at 721 cm^{-1} are associated with the C-C, C-H and $-\text{OH}$ out of plane on the biochar, Ce and Zn supported biochar (Liu *et al.*, 2020). The characterized monometallic catalysts were evaluated for their catalytic upgrading of cyclohexanone in the presence of nitrogen supply and also, at the supercritical condition of ethanol for hydrogen generation.

4.9.3 Catalytic HDO of Cyclohexanone

The developed catalyst was subjected to the catalytic hydrogenation of cyclohexanone model compound to understand the effects of several active's catalyst components on the selectivity and conversion of cyclohexanol and cyclohexanone respectively. Considering the efficiency of 350 °C reaction temperature as obtained from the non-catalytic process, the catalytic study was based on this reaction temperature. In this study, interest was based on the contributory effects of residence time on the developed catalysts at constant reaction temperature, initial nitrogen supply, agitation and catalyst loading of 350 °C, 10bar, 300rpm and 3g of catalysts. The effects of the catalysts are presented in Figs 36 (a-h).



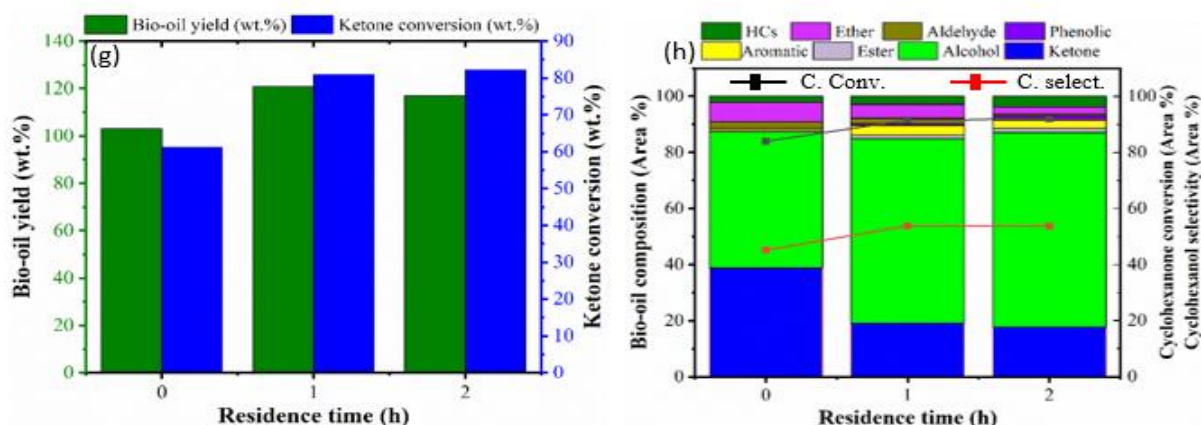


Figure 36: Effects of transition metals on yield, total ketone conversion, cyclohexanone conversion and cyclohexanol selectivity over (a-b) Ni (c-d) Ce (e-f) Zn and (g-h) Fe supported biochar

In this experimental category, the effect of residence time on various catalysts were presented to evaluate the catalytic activities of the transition metals on the biochar support Fig. 36 (a-h). From the information presented on Fig. 36a, an increase in residence time increases the yield of the biofuel and the percentage ketone conversion over the Ni supported biochar catalyst. Interestingly, highest biofuel yields were obtained during the catalytic evaluation of Ni supported biochar catalysts. For instance, the bio-oil yields were 121.50, 141.10 and 164.40 wt% at 0, 1 and 2 h residence time respectively were obtained. The performance of Ni to resulting in the production of high biofuel content signifies the efficiency of Ni to catalyze the conversion of ethanol into biofuel's components. As the residence time increases, the reactants and the solvent—which in this case serves a dual purpose by providing in-situ hydrogen and acting as a co-reactant—produce more products (Manjare & Dhingra, 2019). Additionally, the extended contact between the catalyst and reactants enhances the conversion of cyclohexanone.

The cyclohexanone content in the biofuel decreases as the residence time increases, showing values of 50.63, 34.43, and 31.44% at 0, 1, and 2 h, respectively, while the total alcohol formation corresponds to 43.99, 41.87, and 59.25%. From the Fig. 36b, the percentage selectivity to cyclohexanol formation was obtained to reduce; 36.53, 30.09 and 23.64 area% at 0, 1 and 2 h residence time respectively. This observation indicates the severity of extended residence time on the hydrogenation of cyclohexanone to inhibit the formation of cyclohexanol. Notably, non-catalytic cyclohexanone conversion does not produce phenolic compounds, unlike the catalytic process, which results in biofuel containing phenolics. Figure 36b illustrates that phenolic formation increases to 2.59 and 4.07% at 1 and 2 h of residence time, respectively.

The selectivity for hydrocarbon formation without an external hydrogen supply suggests the excellent potential of the catalytic performance of Ni-supported biochar in upgrading cyclohexanone into advanced biofuel. The study shows that hydrocarbon content increases from 3.94 to 18.27% when the residence time is extended from 0 to 1 h, before decreasing to 2.80% at 2 h, as shown in Fig. 36b. the characteristic properties of Ni which provides it with an excellent reaction properties includes the efficiency of particle dispersions, the existence of strong interaction and affinity with hydrogen produced from the ethanol decomposition which enhances the hydrogenation and dehydrogenation reactions and the ability to maintain catalytic properties at elevated temperature.

The effects of Ce supported biochar on the biofuel yield, the conversion and selectivity efficiencies were presented in Fig. 36c and d. The biofuel yields were obtained as 102.40, 94.70 and 108.20 wt.% with corresponding total ketones conversion of 68.27, 79.78 and 83.20 area% at 0, 1 and 2 h residence time. Comparing the respective ketone conversion with the results obtained over the Ni supported biochar catalysts, the Ce supported catalysts possesses an excellent conversion and selectivity to cyclohexanol formation. A progressive increase in the overall alcohol formation were highly improved which ranges from 52.50 to 75.14 area% at the residence time of 0-2 h. The results revealed the positive influence of Ce supported biochar as an effective catalyst for cyclohexanone conversion into cyclohexanol through hydrogenation and subsequent dehydration into a little pool of hydrocarbon compounds. The hydrocarbon produced were lower compared to the selectivity of Ni based biochar catalyst throughout the considered reaction time. In all the catalysts studied in the category of experiment, the Ce based biochar catalyst yielded the most alcohol and cyclohexanol selectivity and total ketone conversion of 75.14, 59.87 and 83.20 area% respectively.

The characteristic properties that make cerium (Ce) an excellent catalyst for the hydrogenation of cyclohexanone through in-situ hydrogen production from ethanol at supercritical conditions include its high redox potential, which allows for easy switching between Ce^{3+} and Ce^{4+} . This switchability contributes to its high oxygen storage capacity and enhances hydrogen transfer. Additionally, cerium oxide (CeO_2) can create and maintain oxygen vacancies within its cubic structure, providing active sites for catalytic processes and promoting the adsorption and activation of reactant molecules such as hydrogen and ketones. CeO_2 's resistance to particle sintering ensures its stability under reaction conditions. Its amphoteric properties, enabling it to act as both an acid and a base, facilitate the hydrogenation reactions of cyclohexanone and

the in-situ dissociation of hydrogen. Furthermore, the facile electron transfer process stabilizes key reaction intermediates and activates molecular hydrogen, thus enhancing the overall hydrogenation reaction. Hence, the conversion of cyclohexanone and the selectivity to cyclohexanol were favorable to the catalytic performance of Ce supported biochar catalyst. Furthermore, the lower crystallites sizes of 9.44 nm and the pore size of 5.63 nm could be further be associated with the enhanced performance recorded during the conversion of cyclohexanone over Ce supported biochar catalyst.

The Zn and Fe supported biochar yielded the highest total ketone conversion at the residence time of 1 h to producing 79.78 and 80.92 area% total ketones respectively. In the two cases of the Zn and Fe supported biochar, the total ketone conversions were 68.27, 79.78 and 82.79 area% and 61.26, 80.99 and 82.31 area% for Zn and Fe supported biochar catalysts respectively (Fig. 36 f-h). Comparing the hydrocarbon selectivity in the two catalysts, the Zn supported biochar exhibited a more selectivity to hydrocarbon formation with 5.22 area% at 2 h residence time, an amount second to the highest recorded value during the Ni supported biochar evaluation. Furthermore, the Zn supported biochar catalysts enhances the biocrude formation and aromatics selectivity of 130.2 wt.% and 4.65 area% respectively at the residence time of 2 and 1 h. Hence, from the tested catalysts in this category of catalytic evaluation of Ni, Ce, Zn and Fe supported biochar, Zn possesses the affinity to high aromatic formation. The reason to the formation of high contents of aromatic rings could be that, Zn supported biochar could display Lewis's acidity, enabling them to activate ketones by interacting with the carbonyl oxygen. The information presented in Table 22 shows the experimental parameters as obtained from all the experimental runs during the catalytic upgrading of cyclohexanone in supercritical ethanol. The Ni exhibited a selectivity of 18.27% towards hydrocarbon production at a reaction time of 1 hour at 350°C. Meanwhile, Ce-supported biochar enhanced the hydrogenation process due to its oxygen vacancy sites and redox properties, leading to the highest observed cyclohexanone conversion and alcohol selectivity.

Table 22: Effect of catalysts on the cyclohexanone conversion at constant catalyst loading of 3g, EtOH of 90g, 10bar nitrogen and 300rpm agitation

	Ketone	Alcohol	Acid	Ester	Aromatic	Phenolic	Aldehyde	Ether	HCs	Total ketone conversion	% conv. of cyclohexanone	Cyclohexanol selectivity	HCs Selec	Aromatics select	biofuel Yield (wt.%)	Gas Pre (bar)	Coke (wt.%)	Gas V (L)
Feed	100	0	0	0	0	0	0	0	0	100	0	0	0	0	-	-	-	-
Ni_BChar																		
350-0h	50.63	43.99	0	0.2	0.64	0	0	0.6	3.94	49.37	87.16	36.53	3.94	0.64	121.5	189.9	0.05	0.03
350-1h	34.43	41.87	0	1.6	0.42	2.59	0.57	0.26	18.27	65.57	92.86	30.09	18.27	0.42	141.1	203.6	0.04	0.09
350-2h	31.44	59.25	0	1.51	0.57	4.07	0.36	0	2.8	68.56	93.98	23.64	2.8	0.57	164.4	201.4	0.01	1.41
Ce_BChar																		
350 -0hr	34.7	52.5	0	0.28	0.38	0.41	3.51	7	1.23	65.3	86.26	48.45	1.23	0.38	102.4	185	1.5	0.85
350 -1hr	24.61	65.56	0	1.45	0.29	0.48	1.42	3.17	3.02	75.39	89.8	55.41	3.02	0.29	94.7	180.3	1.9	0.07
350-2hr	16.8	75.14	0	2.08	1.83	1.26	0.58	0	2.32	83.2	93.31	59.87	2.32	1.83	108.2	195.3	1.7	0.27
Zn_BChar																		
350-0h	31.73	49.13	0	0.11	4.65	0	2.95	9.77	1.65	68.27	88.08	44.36	1.65	4.65	117.8	184.6	2.1	0.79
350-1h	20.22	62.31	0	1.16	3.69	1	0	6.5	5.12	79.78	91.84	50.88	5.12	3.69	114.7	188.2	1.6	0.4
350-2h	17.21	67.08	0	1.63	4.24	0.76	1.79	3.34	3.95	82.79	92.85	49.42	3.95	4.24	130.2	189.7	2.4	0.02
Fe_BChar																		
350 -0hr	38.74	48.59	0	0.51	0.71	0.19	2.07	7.16	2.03	61.26	83.98	45.18	2.03	0.71	103.2	185.2	1.7	0.37
350 -1hr	19.01	65.92	0	1.32	3.19	0.79	1.93	5.03	2.81	80.99	91.52	53.8	2.81	3.19	120.8	191.1	1.6	0.41
350-2hr	17.69	69.47	0	1.53	2.67	1.55	0.66	2.72	3.71	82.31	92.02	53.69	3.71	2.67	117.1	186.2	7	0.62

4.9.4 Functional Groups Identification of the Biofuel Produced

The biofuel produced during the reaction conditions under the non-catalytic and catalytic conditions were evaluated to determine the presence of different functional groups- fingerprints on the biofuel. The results of the analysis for the non-catalytic and catalytic approaches are as presented in Figs. 37 (a-c) and Figs. 38 (a-c) while the peak assignments were depicted in Table 23 and Table 24 respectively.

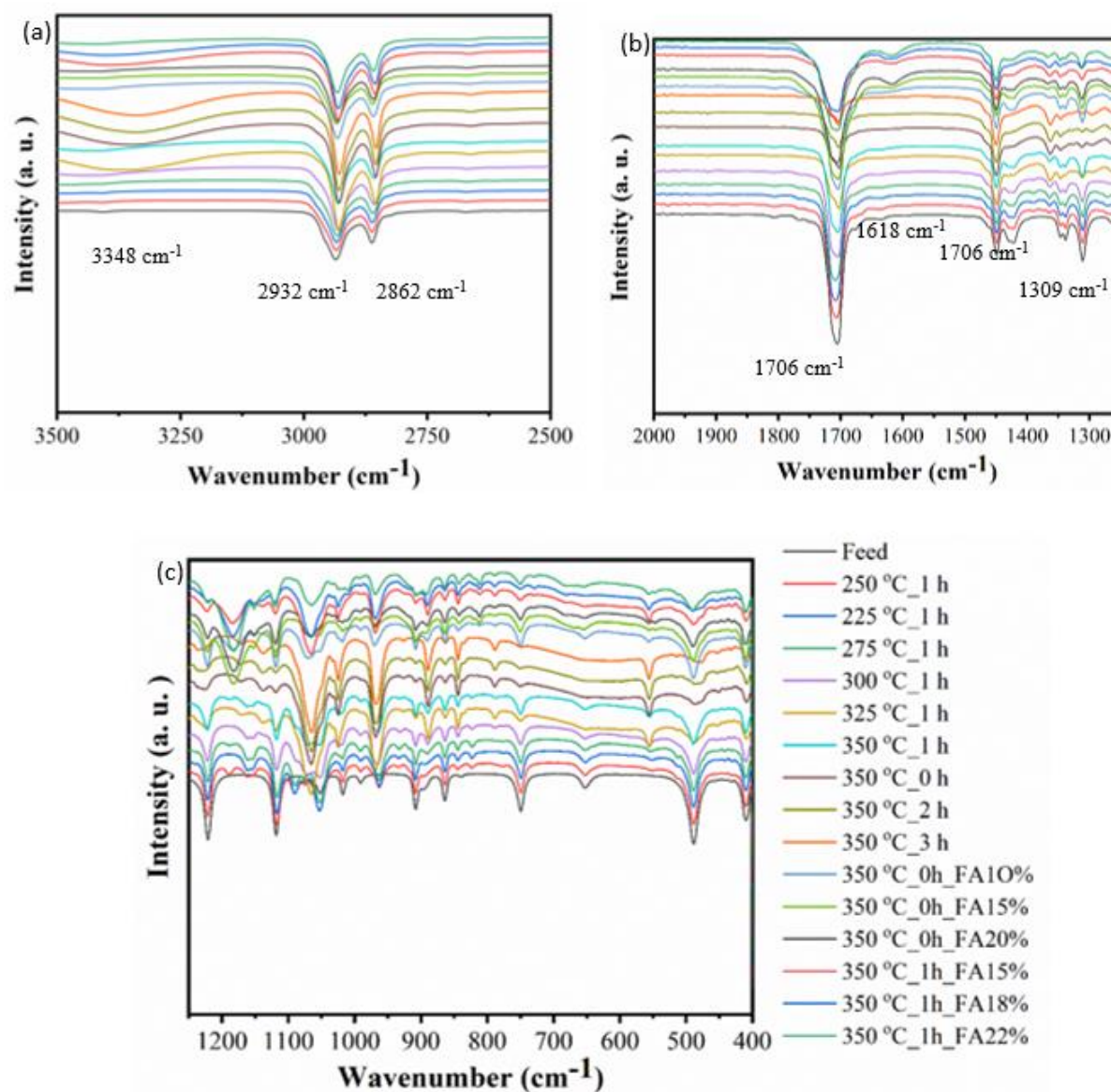


Figure 37: The FTIR spectra of the produced biofuel from the non-catalytic upgrading of cyclohexanone

Table 23: The FTIR peaks assignment from the FTIR spectral of the biofuel obtained from Fig. 37

Wave number range (cm ⁻¹)	Wavenumber (cm ⁻¹)	Functional group	Class of compounds	Observation
3600-3200	3348	O-H stretching	Phenol, alcohols, water	Peaks were observed on the bio-oil obtained at 15%FA, 1h at 350 °C and 0, 1, 2 and 3 h reactions at 350 °C. This observation could be based on the dehydration process leading to high water formation at higher FA loading
3000-2800	2932	C-H stretching	Alkanes (methyl groups)	Peaks were observed on all samples at varied intensity
2980-2800	2862	C-H stretching	Aliphatic	Peaks were observed on all samples at varied intensity
1850-1650	1706	Conjugated and unconjugated C=O stretching	Ketones, aldehyde, carboxylic acid	Peaks were observed on all samples at varied intensity
1650-1580	1618	C=C stretching	Alkenes and aromatics	Present on bio-oil obtained from 15, 20%FA for 0h at 350 °C and 15, 18 and 22 %FA for 1h at 350 °C.
1470-1350	1450	C-H and O-H bending (deformation)	Alkanes (methylene groups)	Peaks were observed on all samples at varied intensity
1300-950	1300-950	C-O stretching	Primary, secondary and tertiary alcohols	Peaks were observed on all samples at varied intensity
950-650	950-650	C-H out of plane bending	Aromatics (mono, polycyclic, substituted)	Peaks were observed on all samples at varied intensity

The FTIR spectral of the biofuel produced from the catalytic upgrading of cyclohexanone over Ni, Ce, Zn and Fe supported biochar are as shown in Figs. 38

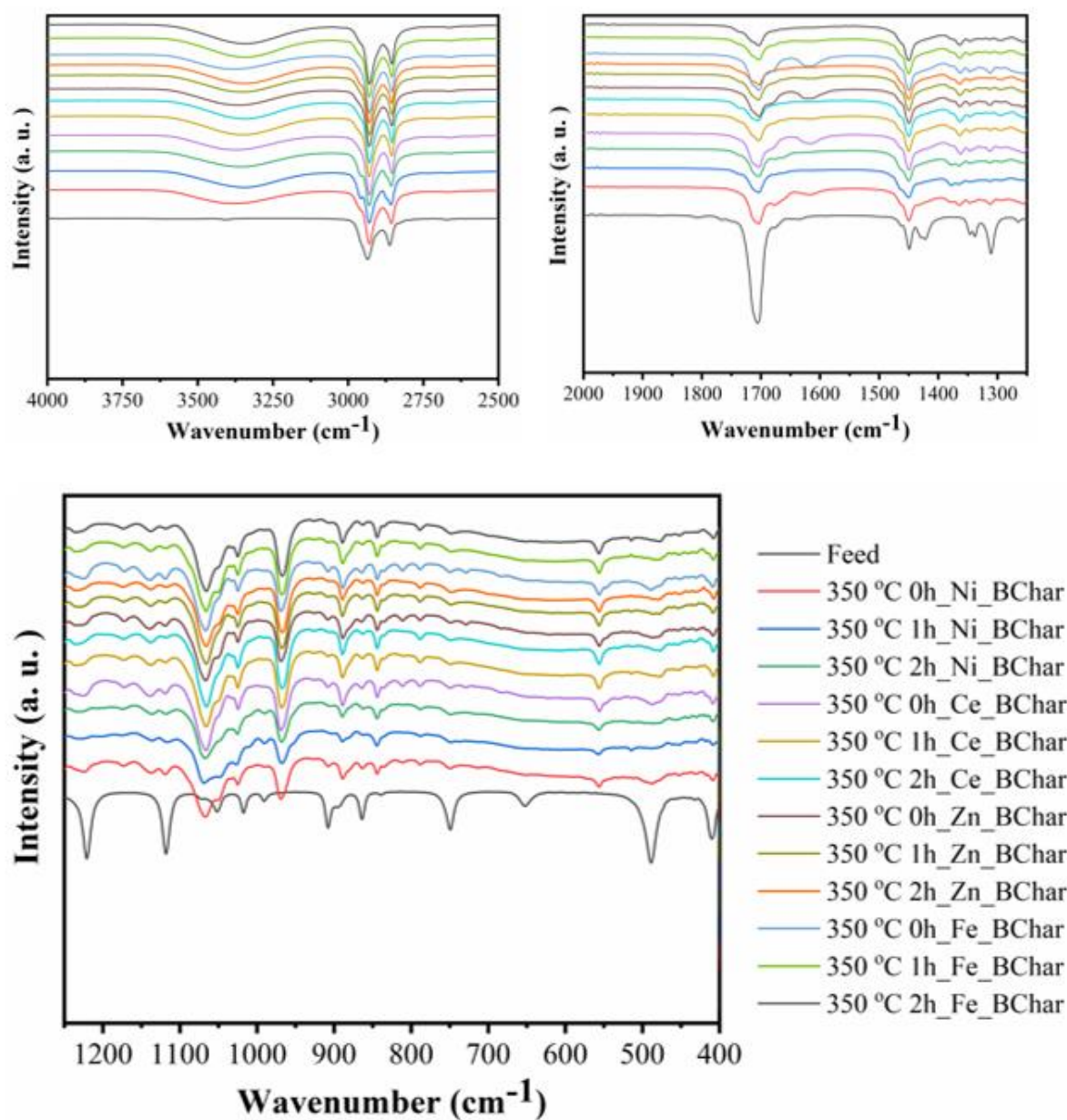


Figure 38: The FTIR spectra of the produced bio-oil from the catalytic upgrading of cyclohexanone

Table 24: The FTIR peaks assignment from the FTIR spectral of the biofuel obtained from Fig. 38

Wave number range (cm ⁻¹)	Wavenumber (cm ⁻¹)	Functional group	Class of compounds	Observation
3600-3200	3344	O-H stretching	Phenol, alcohols, water	Peak were observed on all the bio-oil obtained except the cyclohexanone feed. This indicated a successful upgrading process where high content of cyclohexanol were obtained.
3000-2800	2932, 2856	C-H stretching	Alkanes (methyl groups) and Aliphatic	Peaks were observed on all samples
1850-1650	1704	Conjugated and unconjugated C=O stretching	Ketones, aldehyde, carboxylic acid	Peaks were observed on all samples with the cyclohexanone feed having the highest intensity. This could be linked to the presence of high content of ketones in the bulk of the feed
1650-1580	1618	C=C stretching	Alkenes and aromatics	Present on bio-oil obtained at the 0 h residence time throughout the catalysts materials. This signifies the characteristic properties of all the catalysts resulted into dehydrogenation of the C-C chain in the cyclohexanone.
1470-1350	1450, 1421, 1365	C-H and O-H bending (deformation)	Alkanes	Peaks at 1450 cm ⁻¹ were observed on all samples while the peak at 1421 cm ⁻¹ was only present on the cyclohexanone feedstock. The peak at 1365 cm ⁻¹ was present on all the bio-oil except the feed; indicating the successful hydrogenation process.

Wave number range (cm ⁻¹)	Wavenumber (cm ⁻¹)	Functional group	Class of compounds	Observation
1300-950	1263, 1254, 1220, 1119, 1067, 969	C-O stretching	Primary, secondary and tertiary alcohols	Peaks at 1263 and 1220 cm ⁻¹ were observed only on the feed while, the presence of peak at 1254, 1067 and 969 cm ⁻¹ were observed on all the bio-oil samples except the feed. This could indicate the presence of C-O bond in cyclohexanol which was absent in cyclohexanone. The peaks at 1119 cm ⁻¹ was present in all the samples with the highest intensity on the feed.
950-650	950-650	C-H out of plane bending	Aromatics (mono, polycyclic, and substituted)	Peaks were observed on all samples at varied intensity

4.9.5 Reaction Pathways for the Cyclohexanone Upgrading

The quantitative and the qualitative analysis in this category of experiment give an insight into the overall conceptualization of the reaction pathways which guide the conversion of cyclohexanone to the formation of alcohols and hydrocarbons pools during both the catalytic and non-catalytic approach. According to the results obtained at lower reaction temperature, the gradual hydrogenation of cyclohexanone takes place at the non-catalytic conditions and the percentage of cyclohexanol formation increases as temperature increases. This observation could be linked to the enhanced hydrogen production at higher temperature as the supercritical condition of ethanol is approached where its decomposition is promoted. The mechanisms are therefore similar to the established pathways which were reported by Song *et al.* (2016). During this experiment, the catalytic contributory effects of ethanol as a dual-purpose fluid were observed prior to the introduction of metal supported biochar catalysts.

However, an improved conversion of cyclohexanone and selectivity to hydrocarbon were at peak following the introduction of the metal supported catalysts. In a conceptualized simple reaction pathway (first reaction pathway), in-situ hydrogen production was enhanced over the metal supported catalysts which was further adsorbed on the surfaces of the metal particles. Simultaneously, the absorption of cyclohexanone onto the surface of the metal catalysts takes place, with its oxygen atoms and carbonyl carbon. Thereafter, the adsorbed cyclohexanone molecules were attacked by the highly reactive hydrogen atom, adding to the carbonyl carbon atom. Successively, another hydrogen atom from the surface of the metal particles attacks the oxygen atom, forming a hydroxyl group. This process eventually yields the formation of cyclohexanol through a reaction called the hydrogenation process. The produced cyclohexanol are stable compounds which required further in-situ upgrading approach. Through dehydration process and hydrogen addition, the C-OH group is capable of being cleaved to produce hydrocarbon compounds (in this case, the formation of cyclohexene; an unsaturated hydrocarbon was observed with alkyl- group attached) and further hydrogenation and dehydrogenation into saturated hydrocarbon and aromatic benzene respectively. The formation of alkylated benzene was as a result of the in-situ formation of alkyl intermediates which have high tendency to react with benzene. In the second path of the reaction mechanisms, the decarboxylation, decarbonylation and alkyl ring alkylation of the parent cyclohexanone produces alkyl-cyclopentene. Hence, the overall reaction pathway for the first conceptualized reaction mechanisms is termed the hydrodeoxygenation reaction (HDO) where both the

hydrogenation and dehydration for oxygen removal take place. The reaction mechanisms is as presented in Fig. 39.

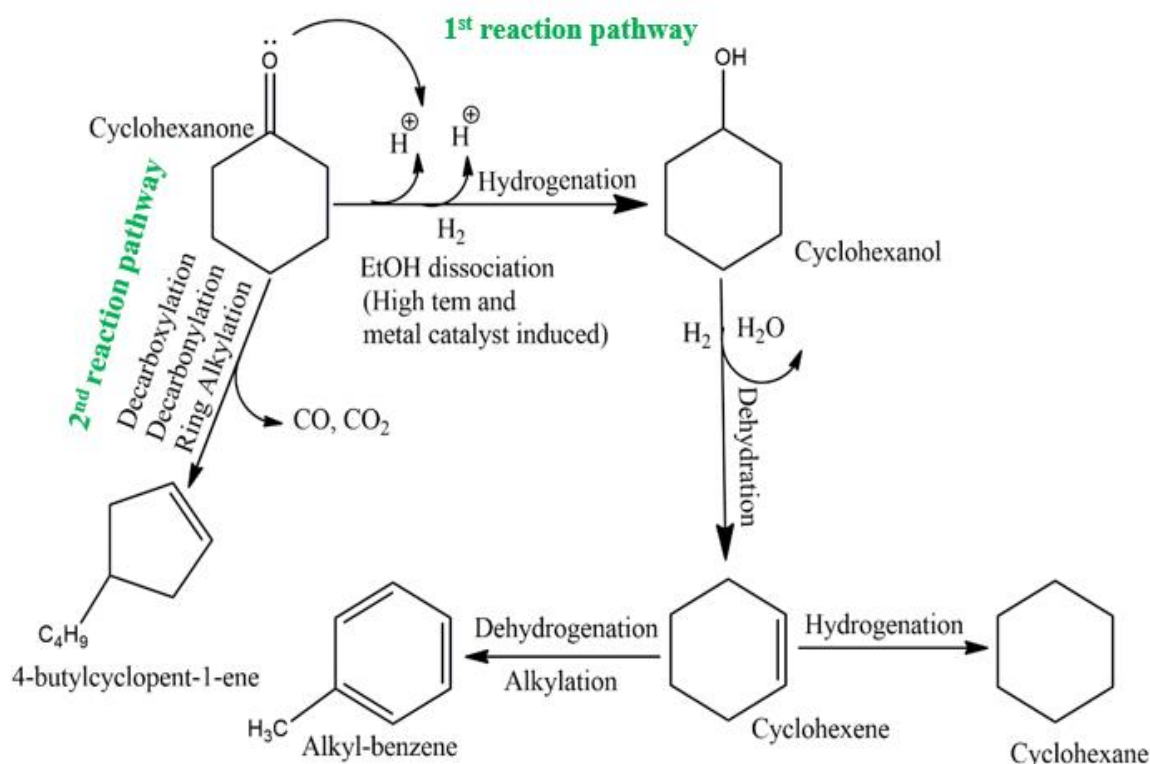


Figure 39: Reaction mechanisms for the catalytic and non-catalytic conversion of cyclohexanone

From the details understanding of the catalytic and non-catalytic upgrading of cyclohexanone, a biofuel model compounds, the intricate metal selection and catalyst development approach is achieved. The results obtained in this section has helped to further transfer the knowledge to the real biocrude obtained during the solvothermal valorization of orange peels to convert the ketones content into a less oxygen containing compounds. This would aid in presenting the biofuel as a sustainable substitute to fossil fuel energy resources for transportation purposes. Considering the catalytic performance of Ni, Ce and Zn, the doping process in the next study was guided while Mo was adopted as promoter. The tendencies of Mo do effectively disperse metals for enhanced catalysts properties has been presented by several researcher Kazmi *et al.* (2024) and Park *et al.* (2019).

4.10 The HZSM-5, In-situ HZSM-5/CNSs (IHC) and NiCeMo Supported IHC and CNSs Characterization

This section outlines the development of a NiCeMo-supported IHC (In-situ protonated ZSM-5 in CNSs) catalyst. Given Ni's excellent performance in hydrocarbon selectivity and Ce's ability to achieve high cyclohexanone conversion into alcohol, combining these two metals as the active components of the catalyst is crucial. To address the tendency for agglomeration on the IHC support, Mo is incorporated as a promoter. The molecular sieve properties of zeolite will enhance material transport, while the integrated CNSs will improve catalyst stability during the HDO process. Overall, the catalyst composition is designed to enhance ethanol reforming and the hydrogenation of ketones and phenols, aiming for the production of low-oxygenated biofuels in supercritical ethanol.

4.10.1 Characterization of HZSM-5 and IHC Support

This section presents the characteristics properties of the developed support materials and the doped catalysts to evaluate their respective properties for the catalytic conversion of the crude biofuel into transportation fuel. The characterization techniques adopted in this section include the XRD, XPS, FTIR, SEM/EDS/Mapping, TEM, BET, NH_3 -TPD and TGA for the crystallinity, oxidation states, functional groups, surface morphology/elemental analysis/elemental mapping, internal morphology, structural properties, acidity and the thermal stability respectively.

The XRD spectral of the developed HZSM-5 using various loading of $\text{Na}_2\text{O}/\text{Al}_2\text{O}_3$ ratios, crystallization time and with and without structural directing agent (SDA) are shown in Fig. 40.

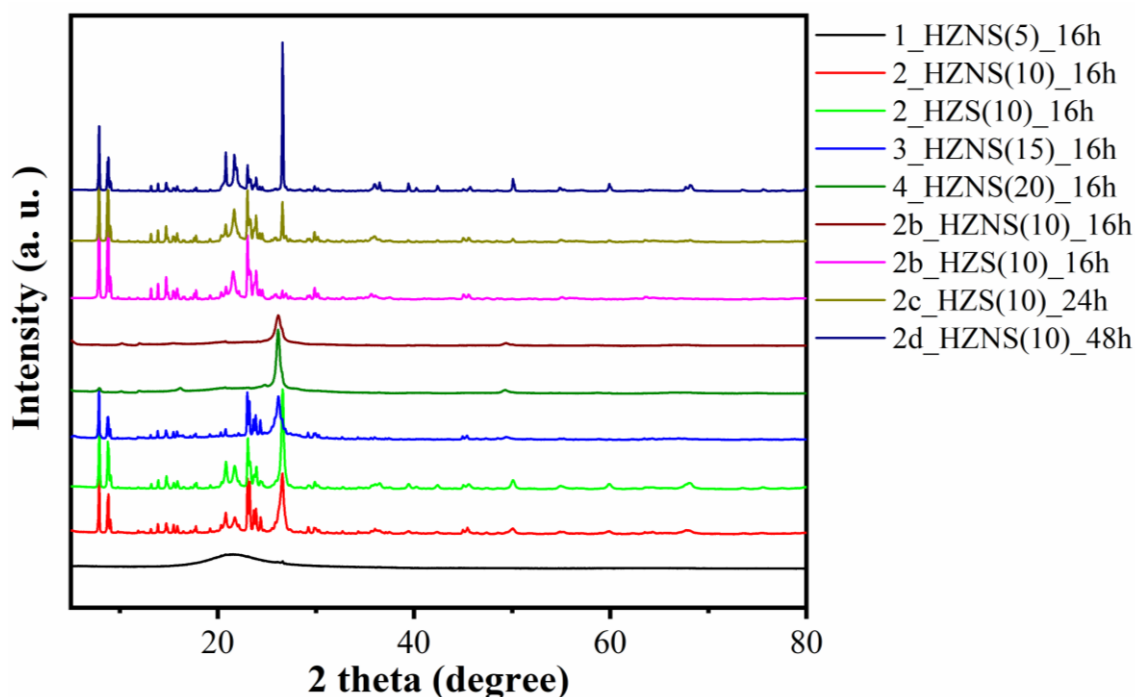


Figure 40: The XRD Spectral of the synthesized HZSM-5 at various reaction conditions

The XRD patterns shown in Fig. 40 illustrate the impact of synthesis conditions on the formation of HZSM-5. At a low $\text{Na}_2\text{O}/\text{Al}_2\text{O}_3$ ratio of 5 and a crystallization temperature of 16°C , under the influence of a structure-directing agent (SDA), zeolite materials are not produced. The resulting material's structure resembles that of typical mesoporous silica, as evidenced by its XRD spectrum. Similar observations were reported by Hartanto *et al.* (2019), indicating that a low $\text{Na}_2\text{O}/\text{Al}_2\text{O}_3$ ratio of 5 is insufficient for zeolite synthesis. At low $\text{Na}_2\text{O}/\text{Al}_2\text{O}_3$ ratio of 5, NaOH was just available to break the kaolin components into smaller particles without the ability to aid the zeolite formation. This is due to the presence of insufficient Na^+ ions to aid the mineralization process while creating a preferred alkaline medium for the zeolite growth. Similar observation has been reported by Hartanto *et al.* (2019). Increasing the sodium hydroxide loading to achieve a $\text{Na}_2\text{O}/\text{Al}_2\text{O}_3$ ratio between 10 and 15, either with or without an SDA, resulted in the formation of HZSM-5 zeolites with structures consistent with the MFI zeolite pattern. This suggests that a higher $\text{Na}_2\text{O}/\text{Al}_2\text{O}_3$ ratio between 10 and 15 helps maintain the structural properties of HZSM-5 zeolite during the hydrothermal treatment. Also, sufficient amount of Na^+ were available at the $\text{Na}_2\text{O}/\text{Al}_2\text{O}_3$ ratio between 10 and 15 and hence, the mineralization of kaolin and the required alkaline environment which promote the formation of primary building block of zeolite particles is created. A further increase in the $\text{Na}_2\text{O}/\text{Al}_2\text{O}_3$ ratio to 20 (4_HZSN(20)_16h) disrupts the formation process of HZSM-5 material and hence, different crystalline phase was observed.

Beneficiated kaolin without dealumination, as indicated by the XRD patterns in 16h, 2_HZSN(10)_16h, 2_HZS(10)_16h, and 3_HZSN(10)_16h, demonstrates the potential to produce crystalline HZSM-5 material. However, the primary challenge that necessitated the use of the dealumination process was the observed low surface area of the resulting HZSM-5 (where the macroporosity of the material produced at 1_HZNS(5)_16h is presented. Also, highest surface area of 281.17 m²/g was obtained at the 2b_HZS(10)_16h over dealuminated kaolin substrate as aluminum source. The reported increase in the surface area as compared to the 2_HZS(10)_16h could be attributed to the activity of the aluminum through the acid treatment process and the pore opening induced during the dealumination process. A further increase in the crystallization time to 24 and 48 h retards the surface areas and the pore volume to 225.67 and 106.14 m²/g and 0.1227 and 0.0580 cm³/g respectively, due to possible agglomeration of particles. In addition, the formation of hierarchical pore was associated to the nature of isotherms obtained at the 16, 24 and 48 h crystallization time under the influence of SDA where intra-crystalline mesopores were introduced in-situ. Isotherms of similar nature has been reported by Hartati *et al.* (2020) and Zhang *et al.* (2018). Moreover, presence of high degree of microporosity was observed in the zeolites produced at the 2b_HZS(10)_16h and 2c_HZS(10)_24h reaction conditions as shown in Fig. 41a where the peak pore diameters were 3.78 and 3.86 nm respectively. It could be stated generally that, the formation of hierarchical pore in HZSM-5 depends on the nature/state of aluminum loading (in this case, the dealuminated kaolin promoted the hierarchically forms HZSM-5), the introduction of SDA, and the crystallization time (16-24 h in this present study). Additionally, the formation of high mesoporous HZSM-5 zeolite was favored by the reaction condition at the 2_HZS(10)_16h as depicted in Fig. 41a. This assertion is aided by the adsorption-desorption isotherms exemplified by this obtained HSZM-5 and the intensity of the peaks formed at the pore diameter of 4.07 nm as shown in Fig. 41b.

The combined information derived from the adsorption-desorption isotherms coupled with the pore diameter distribution help for the classification of the porosity of the produced HZSM-5 support. The introduction of the SDA into the reaction condition at the Na₂O/Al₂O₃ ratio of 10 over the beneficiated kaolin as aluminum source aligned the formation of the pores within a unit category. For instance, the HZSM-5 obtained at the reaction conditions of 2_HZSN(10)_16h produces hierarchical zeolite with peak pore diameter distributed ranges were 2.01, 2.32 (dominant peak), 2.65, 3.15 and 3.87 nm as shown in Fig. 41b. The structural properties of the synthesized zeolites and the NiCeMo supported catalyst are shown in Table

25. When using beneficiated kaolin as the alumina source for HZSM-5 synthesis, the sample identified as 2_HZNS(10)_16h yielded the highest surface area. To further optimize the synthesis conditions, a $\text{Na}_2\text{O}/\text{Al}_2\text{O}_3$ ratio of 10 was applied to dealuminated kaolin. The dealumination process, carried out with 68% sulfuric acid at 188°C , not only facilitated the removal of aluminum and modification of the kaolin's pore structure but also activated the aluminum for enhanced reactivity during the crystallization stage. As reported by Chon *et al.* (1979), sulfuric acid treatment significantly enhances the adsorption properties of kaolin. The HZSM-5 produced using the beneficiated kaolin are coded with “2b, 2c and 2d” at various crystallization time and with and without the application of SDA at the initial stage of the synthesis (10)_16h. The XRD pattern obtained at 2b_HZSN(10)_16h shows a dissimilar XRD pattern as compared to the HZSM-5 produced using the same synthesis conditions except with the nature of the kaolin which serves as the alumina source. The introduction of SDA into the reaction at the $\text{Na}_2\text{O}/\text{Al}_2\text{O}_3$ ratio of 10 under the influence of SDA yielded a HZSM-5 with a noticeable MFI structure and an enhanced surface area. To further investigate the effects of the crystallization time, the crystallization time was extended to 24 and 48 (2c_HZS(10)_24h and 2d_HZS(10)_48h). In both the two cases and the case of 16 h time under the influence of dealuminated and SDA, the XRD patterns of the HZSM-5 were preserved and maintained and were similar to other findings.

The structural characterization of the HZSM-5 zeolite was determined and the adsorption-desorption isotherms which give an insight into the structural composition and the volume capacity of the HZSM-5 zeolites including the pore diameter distributions are presented in Figs. 41 a and b.

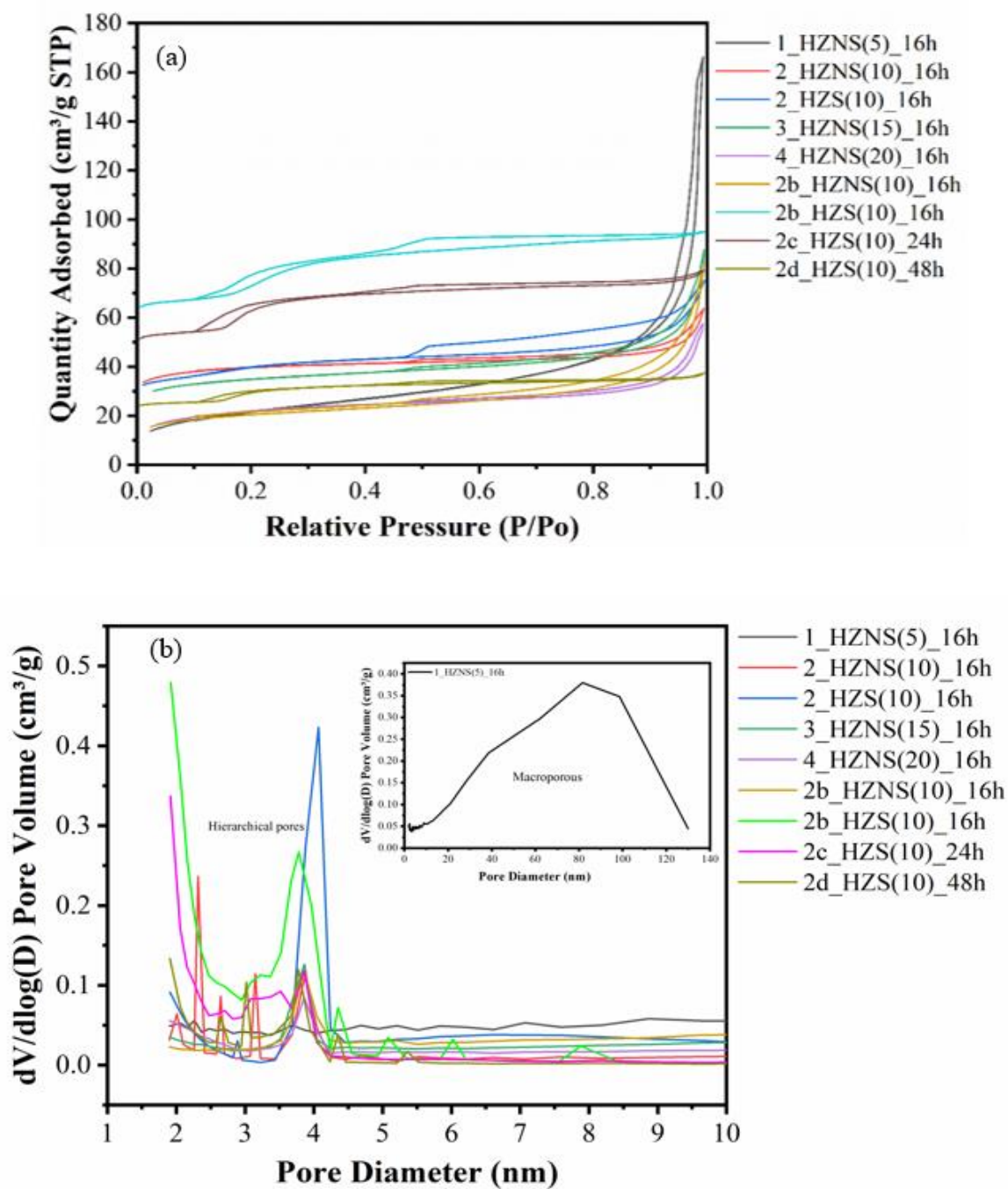


Figure 41: (a) The N₂ Adsorption-desorption isotherm and the (b) pore diameter distribution of various HZSM-5

From the results presented in Fig. 41a, the dependency of synthetic conditions on the structural composition of HZSM-5 are shown. Although, in some instances, the tendency of maintain the XRD pattern are feasible while similar XRD patterns could not necessarily contains zeolites with similar structure as shown through the comparison of the information deduced from Fig. 40 and Fig. 41a. The N₂ adsorption isotherms depicted at the Na₂O/Al₂O₃ ratio of 5 and 20 are categorized as type II with H2 hysteresis loop base on the IUPAC nomenclature. A vertical increase in the uptake of nitrogen between p/p₀ of 0.82-0.99 and 0.45-0.99 relative pressure suggest the distribution of narrow pores within the materials. The presence of isotherms with type II and IV have been characterized with hierarchical porous materials whose pores span through micro- to meso- and also to macro-. The HZSM-5 produced at the Na₂O/Al₂O₃ ratio of 10 under the influence of SDA shows the characteristics isotherms of zeolite.

According to the International Union of Pure and Applied Chemistry classification of adsorption isotherm, the 2_HZS(10)_16h exhibited a type IV isotherm; a characteristics feature of a mesoporous structure and a slit-like structures originated from voids in the interparticle arrangement of a typical zeolite crystals; a direct indication of a H4 hysteresis loop (Wang *et al.*, 2013). In all the developed materials, the presence of micropore is attributed to micropore filling at low P/P₀ while a significant nitrogen uptake at the P/P₀ ranging from 0.42 to 0.99 signifies the presence of pronounced micro-mesoporosity (Kamil & Cheralathan, 2020; Vu & Armbruster, 2019). The mesoporosity is further indicated with the pore size distribution which are presented in Fig. 41b. The details of the pore diameter distribution are contained in the Fig. 41b where the macroporosity of the material produced at 1_HZNS(5)_16h is presented. Also, highest surface area of 281.17 m²/g was obtained at the 2b_HZS(10)_16h over dealuminated kaolin substrate as aluminum source. The reported increase in the surface area as compared to the 2_HZS(10)_16h could be attributed to the activity of the aluminum through the acid treatment process and the pore opening induced during the dealumination process.

A further increase in the crystallization time to 24 and 48 h retards the surface areas and the pore volume to 225.67 and 106.14 m²/g and 0.1227 and 0.0580 cm³/g respectively, due to possible agglomeration of particles. In addition, the formation of hierarchical pores was associated to the nature of isotherms obtained at the 16, 24 and 48 h crystallization time under the influence of SDA where intra-crystalline mesopores were introduced in-situ. Isotherms of similar nature has been reported by Hartati *et al.* (2020) and Zhang *et al.* (2018). Moreover, presence of high degree of microporosity was observed in the zeolites produced at the

2b_HZS(10)_16h and 2c_HZS(10)_24h reaction conditions as shown in Fig. 41a where the peak pore diameters were 3.78 and 3.86 nm respectively. It could be stated generally that, the formation of hierarchical pore in HZSM-5 depends on the nature/state of aluminum loading (in this case, the dealuminated kaolin promoted the hierarchically forms HZSM-5), the introduction of SDA, and the crystallization time (16-24 h in this present study).

Additionally, the formation of high mesoporous HZSM-5 zeolite was favored by the reaction condition at the 2_HZS(10)_16h as depicted in Fig. 41a. This assertion is aided by the adsorption-desorption isotherms exemplified by this obtained HZSM-5 and the intensity of the peaks formed at the pore diameter of 4.07 nm as shown in Fig. 41b. The combined information derived from the adsorption-desorption isotherms coupled with the pore diameter distribution help for the classification of the porosity of the produced HZSM-5 support. The introduction of the SDA into the reaction condition at the $\text{Na}_2\text{O}/\text{Al}_2\text{O}_3$ ratio of 10 over the beneficiated kaolin as aluminum source aligned the formation of the pores within a unit category. For instance, the HZSM-5 obtained at the reaction conditions of 2_HZSN(10)_16h produces hierarchical zeolite with peak pore diameter distributed ranges were 2.01, 2.32 (dominant peak), 2.65, 3.15 and 3.87 nm as shown in Fig. 41b. The structural properties of the synthesized zeolites and the NiCeMo supported catalyst are shown in Table 25.

Table 25: Structural properties of the synthesized HZSM-5 and developed metal supported CNSs and hybrid

Sample	$S_{\text{BET}} (\text{m}^2\text{g}^{-1})$	$V_p (\text{cm}^3\text{g}^{-1})$	$D_p (\text{nm})$
1_HZNS(5)_16h	79.29	0.2570	17.17
2_HZNS(10)_16h	151.83	0.0595	9.42
2_HZS(10)_16h	143.36	0.1162	6.43
3_HZNS(15)_16h	131.16	0.1357	12.24
4_HZNS(20)_16h	76.14	0.0890	8.99
2b_HZNS(10)_16h	75.34	0.1268	13.43
2b_HZS(10)_16h	281.17	0.1469	2.60
2c_HZS(10)_24h	225.67	0.1227	2.92
2d_HZS(10)_48h	106.14	0.0580	3.14
IHC	285.71	0.1795	5.19
NiCeMo_IHC	266.54	0.2141	7.78
NiCeMo_CNSs	56.28	0.1766	16.50

The composition and process conditions that resulted in the formation of HZSM-5 zeolite with the highest surface area were adopted for the controlled synthesis of HZSM-5. This approach was used to produce an in-situ hybrid material consisting of carbon nanotubes (CNSs) as a shape-controlling material as contained in Fig. 42.

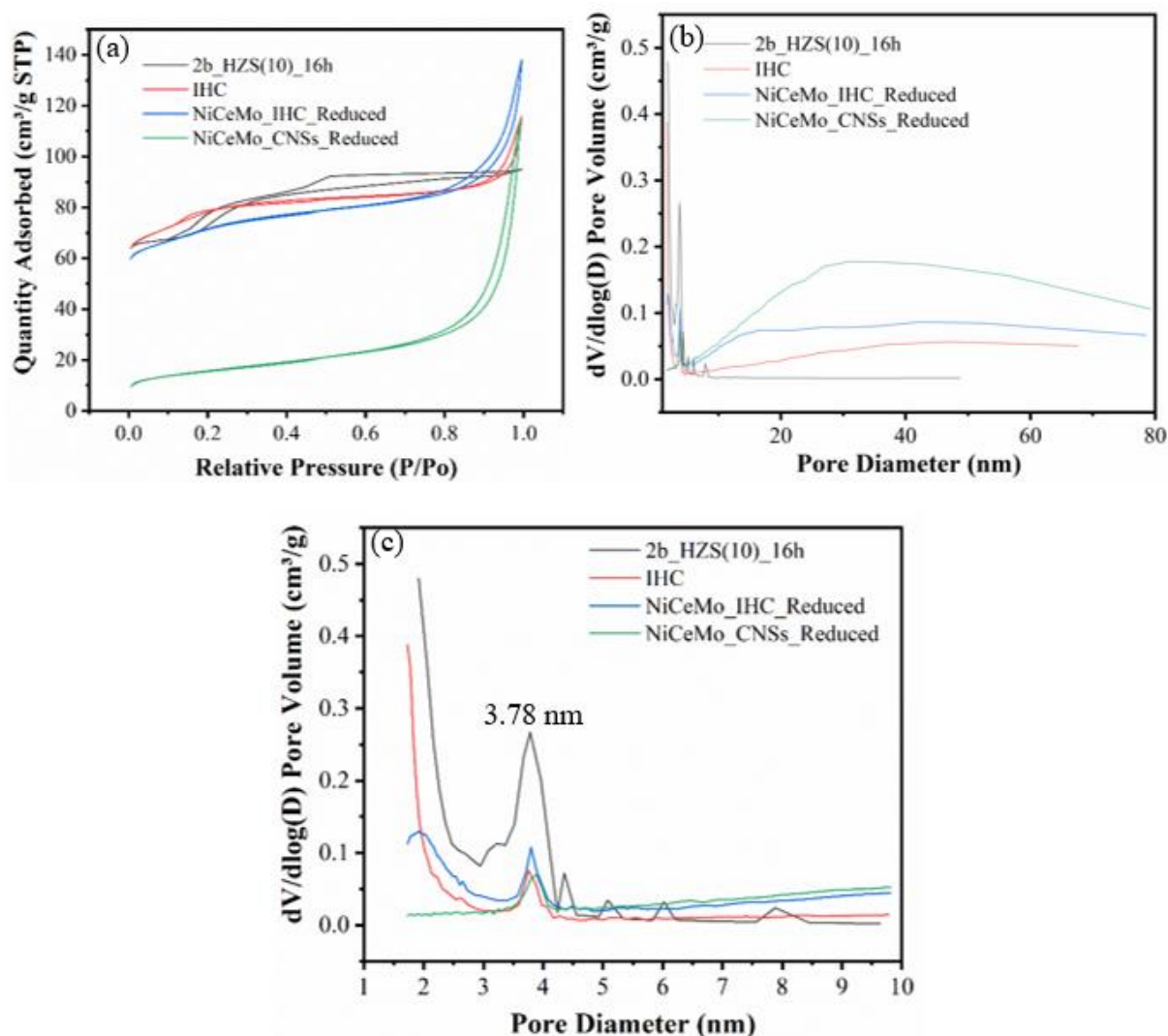


Figure 42: The N₂ Adsorption-desorption isotherm and the (b-c) pore diameter distribution of 2b_HZS(10)_16h, IHC, NiCeMo_IHC and NiCeMo_CNSs

The introduction of ethanol during the in-situ nucleation process of HZSM-5 to producing HZSM-5/CNSs (IHC), facilitates the dispersion of CNSs and also promotes the defects on the CNSs wall. The defect which is observed on the SEM images Fig. 44 enhance the surface area. The surface area increase from 281.17 (2b_HZS(10)_16h) to 285.71 m²/g (IHC) while the pore volumes were also obtained to improve from 0.1469 to 0.1795 cm³/g. The modification of the HZSM-5 with the CNSs changes the structural composition of the obtained hybrid sample as shown in Fig. 42a. The N₂ adsorption-desorption isotherms of IHC, NiCeMo_IHC

and NiCeMo_CNSs depict a characteristics behavior of a hierarchical material Fig. 42c. The reduction in the BET surface area recorded following the doping process are in line with the similar report of Li *et al.* (2018). The hierarchical structure of the obtained HZSM-5 based catalysts and the parent zeolite are contained with the observation of the presence of dominant pore diameter at 3.78 nm. The doping process was noticed to affect the nature of the isotherm due to the pore filling. The presence of several distribution of pore diameter's ranges were noticed in the material produced at 16 h crystallization time under the influence of dealuminated kaolin as shown in Fig. 42c.

The XRD patter of the hybrid IHC and the metal supported IHC and CNSs catalysts are shown in Fig. 43. From the XRD pattern presented in Fig. 43, the pattern of the XRD obtained were preserved following the in-situ development of IHC in both the reduced and calcined catalysts.

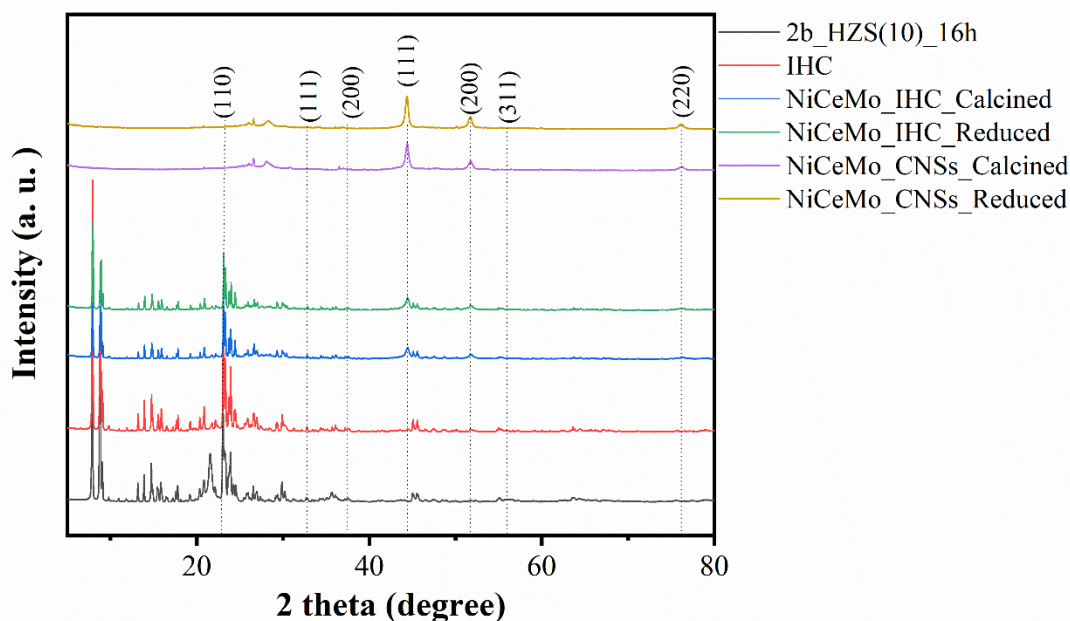


Figure 43: The XRD Pattern of the synthesized catalysts (reduced and calcined) and the support material (IHC)

The successful doping of the metal catalysts and the promoter, Mo were also noticed on the surface of the IHC and CNSs supports. The powdered XRD patterns as presented in Fig. 43 for both the calcined and reduced form of NiCeMo_IHC revealed a uniform diffraction peak with variation in peaks intensity where the pattern of the parent IHC was maintained. The observation of perseverance of the XRD pattern of the parent IHC is in accordance with the N₂

adsorption-desorption isotherm presented in Fig. 42. Similar observation of the effects of NiCe doping on ZSM-5 to maintain the typical MFI structure has been reported by Li *et al.* (2018).

The diffraction peaks at the 2-theta angle of 23.01° (110) and 56.31° (311) are characteristics diffraction angles of MoO and CeO₂ were indexed according to the JCPDS # of 004-1990 and 001-1731 of a monoclinic and cubic structured material respectively. This appearance of the diffraction angle at the 23.01° (110) and 56.31° (311) are noticeable throughout the calcined catalyst. The peaks formation at the 2 theta angles of 44.49° (111), 51.85° (200) and 76.38° (220) are associated to the presence of cubic structured Ni according to the JCPDS # 002-2027. This observation is predominantly obtained over the reduced catalysts where the introduction of hydrogen for the reduction of oxygen to water takes place at 400 °C. The tendency of the nickel to react with the cerium during the calcination was observed due to the peak's formation at the 2-theta angle of 35.12° (220) and 41.50° (311). These peaks were indexed according to the JCPDS # 007-1242 of a typical CeNi₂ crystals. The reduced catalyst further depicts a unique diffraction angle at 32.11° (111) and 37.25° (200) which indicate the presence of reduced Ce metals on the respective catalysts. According to the JCPDS # 001-9248 of a cubic structured Ce metal.

The surface morphologies of the developed HZSM-5 supports under the influence of the dealuminated kaolin at varied crystallization time and constant SDA are presented in Fig. 44 (a-f).

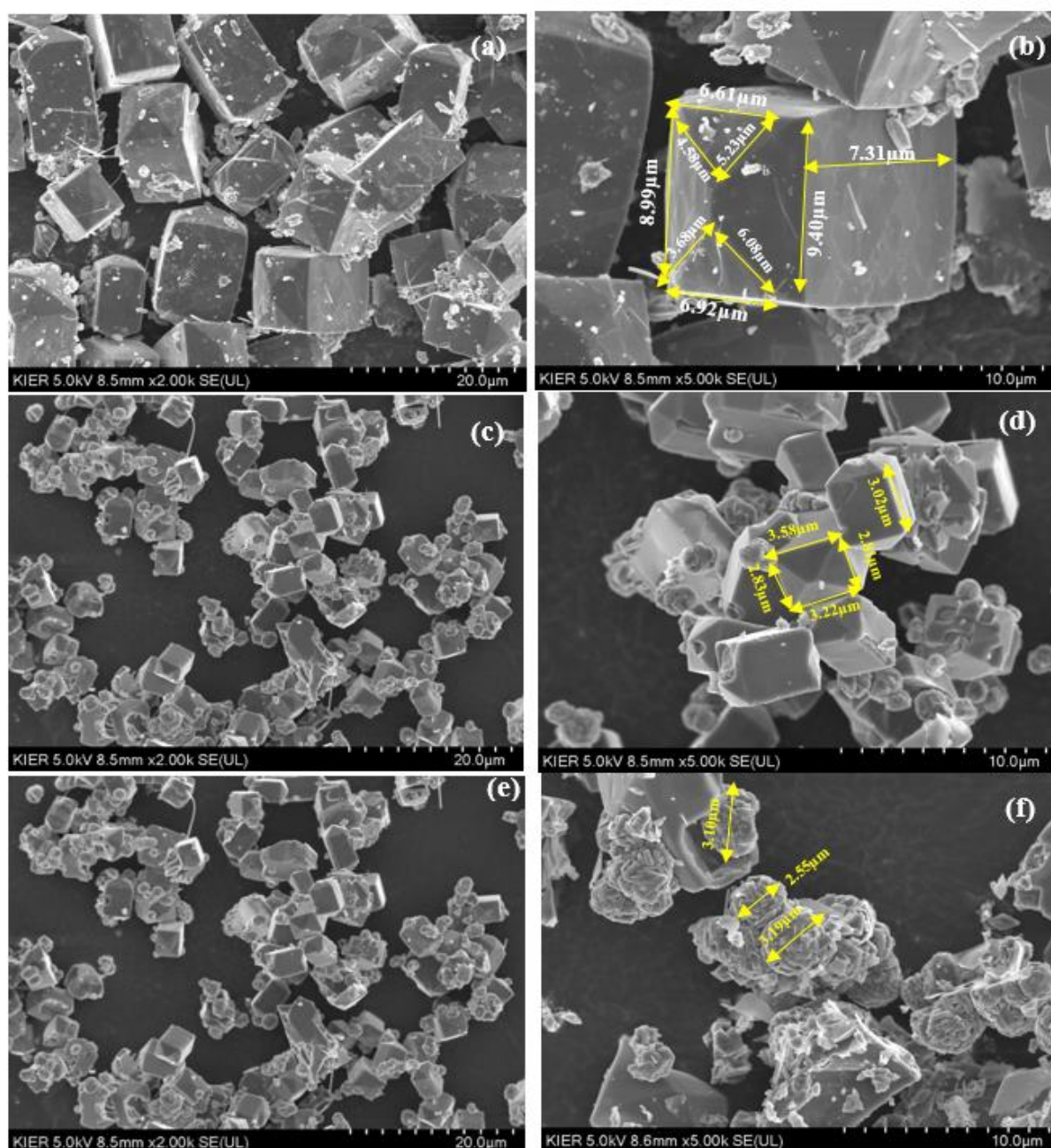


Figure 44: The HRSEM images of (a-b) 2b_HZS(10)_16h (c-d) 2c_HZS(10)_24h and (e-f) 2d_HZS(10)_48h

The images revealed a similar morphological composition of the HZSM-5 at various crystallization time except the formation of smaller and agglomeration of particles at higher time of 48 h (Fig. 44f). The particle size of the obtained HZSM-5 zeolite decreases as the crystallization time increases from 16 to 24 h. The obtained higher particle size at the crystallization time of 16 h could be attributed to the highest surface area gotten at this reaction time. Similar observation of the dependency of particle sizes on the surface area of HZSM-5 zeolites has been reported by Mohiuddin *et al.* (2016) where large aggregates with rough

exterior materials were reported. The particles formed at the lower crystallization time were found to be tightly packed when compared to those HZSM-5 synthesized at the 24 and 48 h crystallization time (Fig. 44f) a, c and e).

The formation of an intergrowth phase on the produced twinned-hexagonal crystal structure in all the HZSM-5 produced were obvious which are composed of a self-assembly of an intergrowth component while the growth increases as the crystallization time is prolonged. Similar shapes of HZSM-5 has been reported by several researchers including Zhang *et al.* (2017). An interesting observation was recorded from the HZSM-5 produced at 48 h, in this case, the formation of a simple mixture of tetragonal terminated cubic crystals (co-crystalline) were formed which is similar to the morphology of a typical HZSM-11. Spherical aggregates and hexagonal has been reported in the work of Zhang *et al.* (2017) and the obtained zeolite structure were associated to HZSM-5/11. The negative effects of this structure are the formation of HZSM-5 with low surface area as contained in the information presented in Figs. 44d and f. Furthermore, the structures of the HZSM-5 synthesized at the 16 h depicted a well-defined shape with a clearly defined identifiable edges without agglomeration.

The surface morphologies and the elemental analysis of the produced in-situ HZSM-5/CNSs (IHC) and the obtained catalysts over IHC and CNSs supports through doping with NiCeMo are presented in Figs. 45 (a-f) while the elemental mapping of the doped catalysts are presented in Figs. 46 (a-i) and Figs. 47 (a-f) for NiCeMo_IHC and NiCeMo_CNSs respectively.

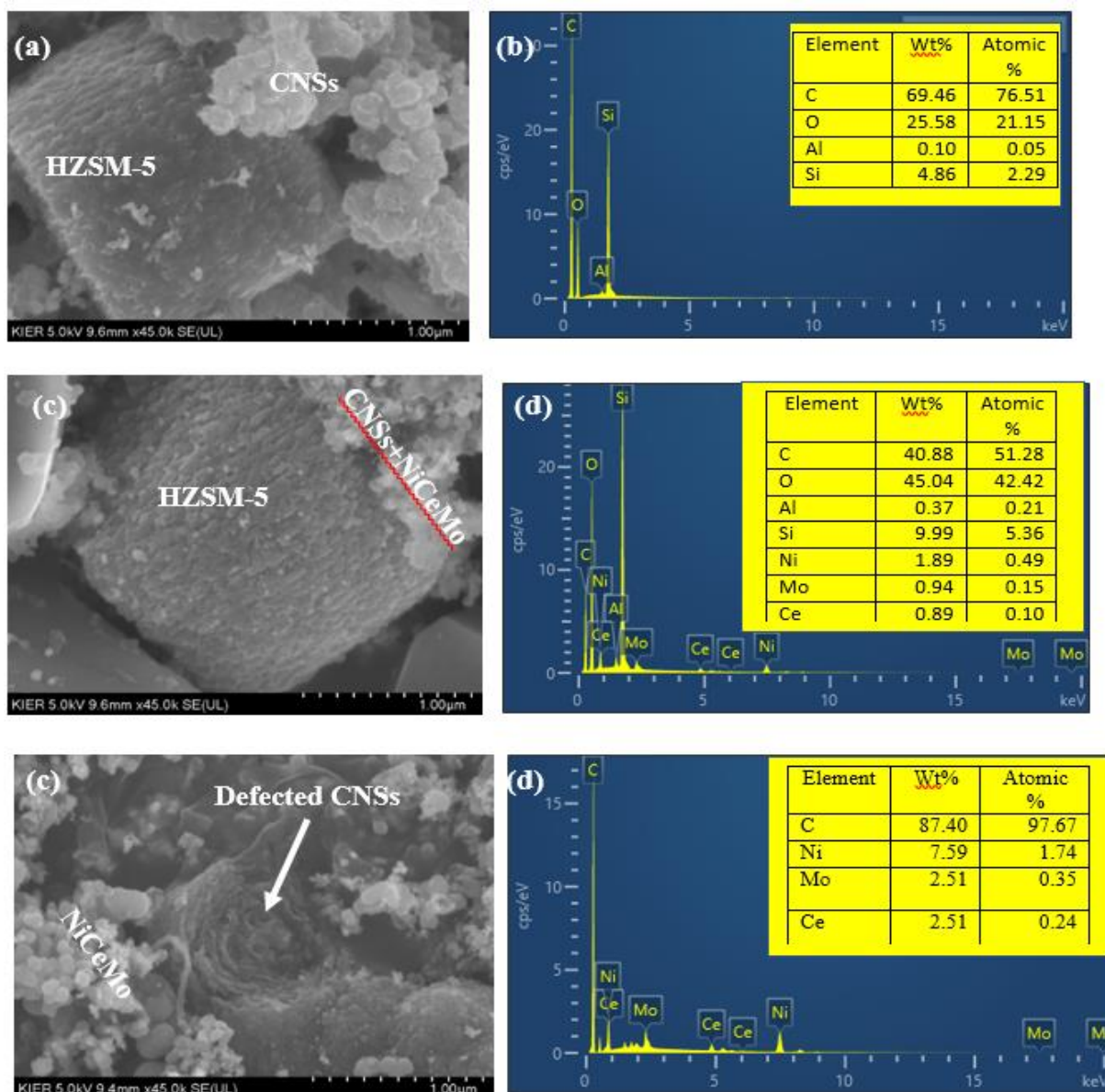


Figure 45: The HRSEM and Elemental composition of (a-b) IHC (c-d) NiCeMo_IHC and (e-f) NiCeMo_CNSs catalysts

The morphology as presented in Figs. 45a and c indicate the successful splitting of the slit (Al-Si network) in the parent HZSM-5 which could be associated to the introduction of ethanol during the synthesis process. The introduction of the CNSs as a growth directing material was able to produce a larger particle crystal with noticeable roughness. The defects induced onto the surfaces of the IHC and the CNSs samples could be responsible to the increase surface area obtained as presented in the information contained in Table 25. The formation of defect walls on the CNSs doped NiCeMo as presented in Fig. 45e is illustrated with an arrow. The opening of the CNSs which was due to defect wall is responsible for the enhancement of the surface area and the available pores for reaction. The elemental compositions of the catalysts as presented in Fig. 45d and e while that of the IHC support is presented in Fig. 45b. The Si/Al

ratio obtained from the in-situ HZSM/CNSs (HIS) is 87. From Fig. 45d, the Si/Al ratio following the doping with NiCeMo reduced to 26. The reduction in the Si/Al ratio suggests the distribution of the metals on the surfaces and also, the pores of the IHC support.

The elemental mapping which shows the metals' distributions on the surfaces of the support materials are presented. The results as presented in Figs. 46 (a-b) and Figs. 47 (a-b) and the associated individual elemental mapping indicate an effective metal dispersion for both the NiCeMo supported on IHC and CNSs particles. The effective dispersion of the active catalysts' part; NiCe is promoted by the introduction of Mo as a catalyst promoter. Similar observation on the inclusion of Mo to enhance metal dispersion has been reported in the work of Park *et al.* (2019).

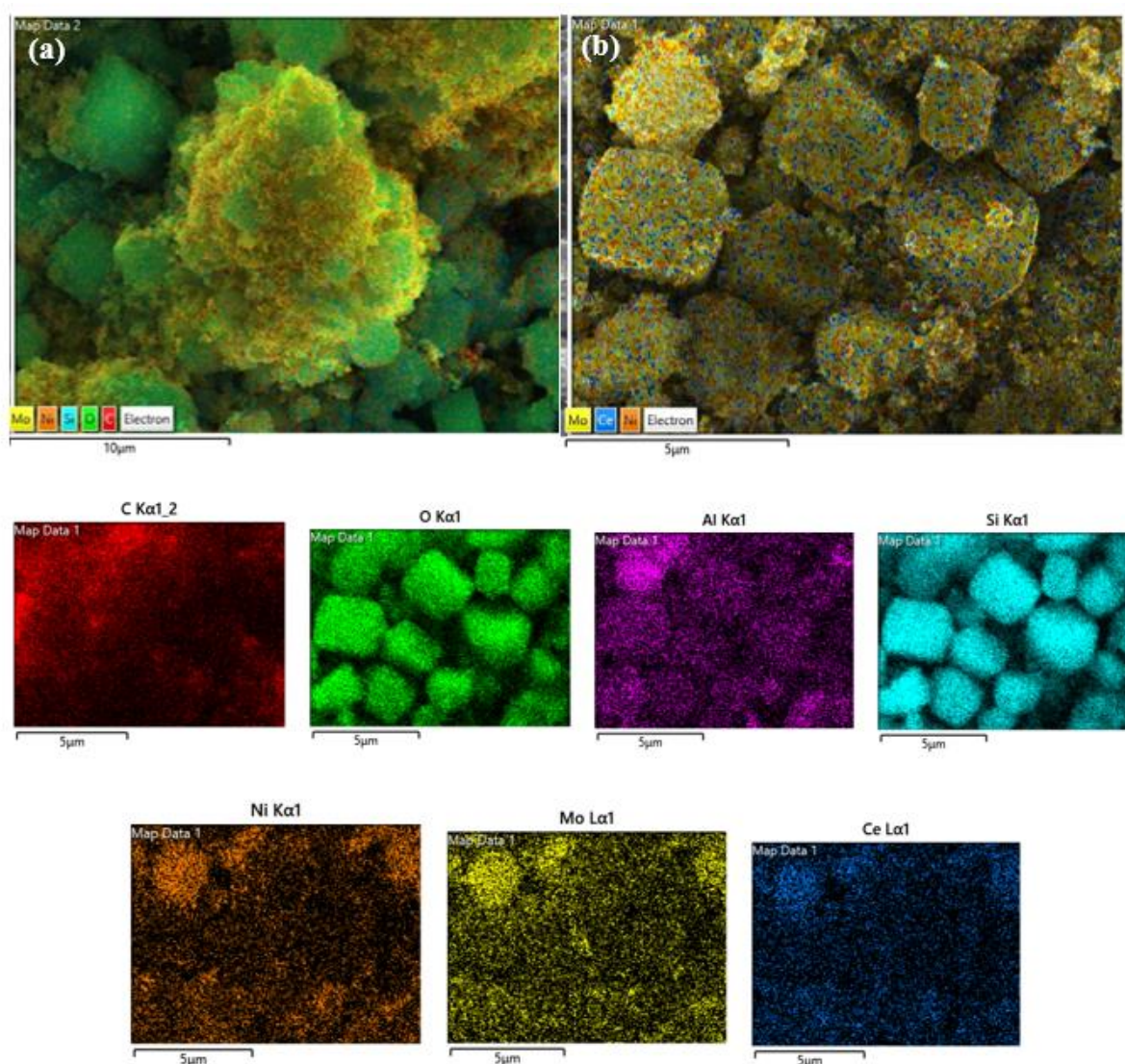


Figure 46: Elemental mapping of (a) the constituent elements and (b) the NiCeMo on the IHC support

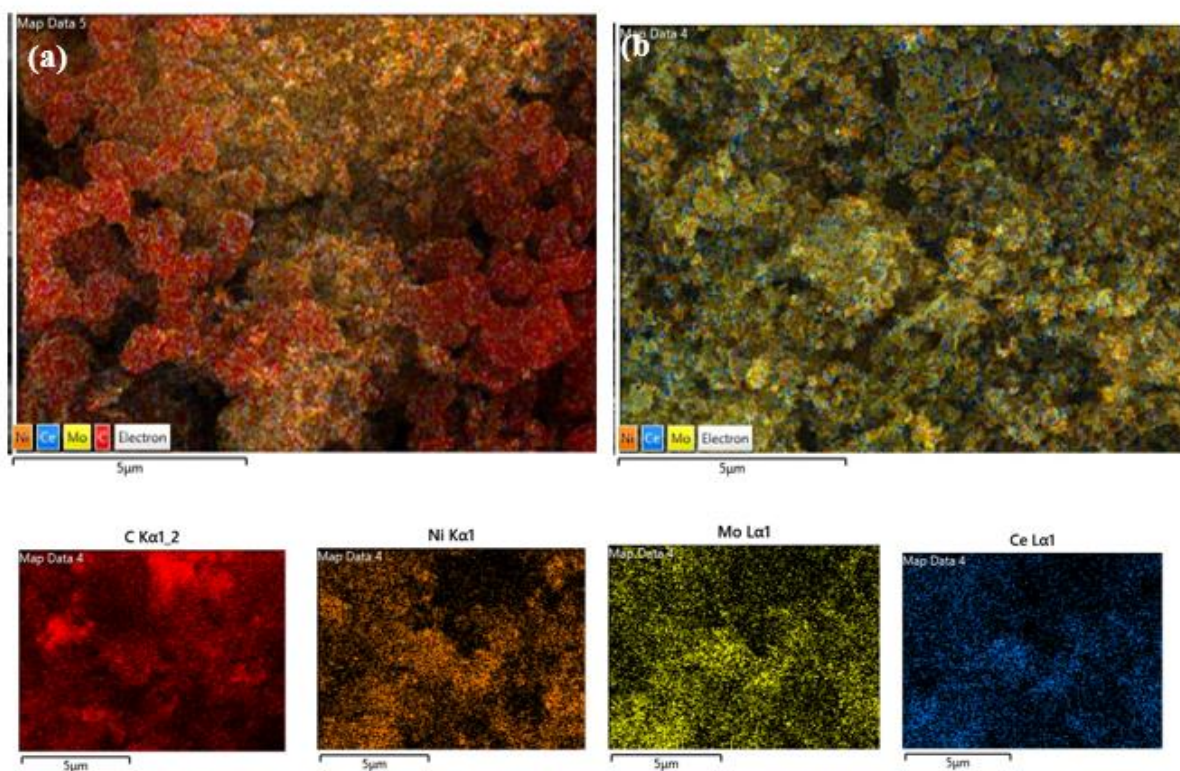


Figure 47: Elemental mapping of (a) the constituent elements and (b) the NiCeMo on the CNSs support

The internal morphologies of the developed NiCeMo supported IHC and CNSs are presented in Fig. 48 (a-d). The results presented in Fig. 48 a and c show a high dispersion of the NiCeMo on the surfaces of the IHC and CNSs supports respectively.

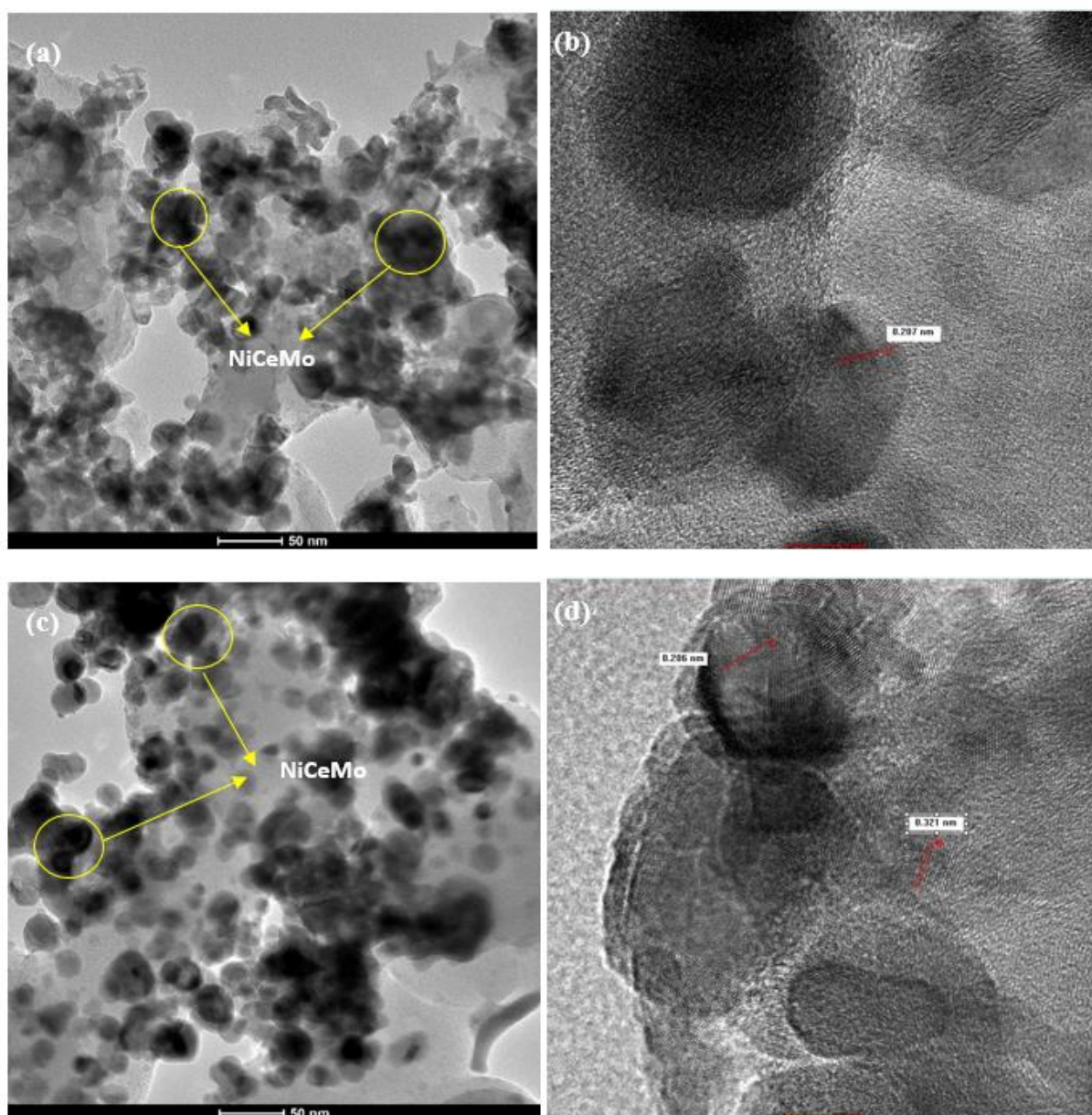


Figure 48: The HRTEM images of NiCeMo supported (a-b) IHC and (c-d) CNSs catalysts

The NiCeMo are indicated by circle in Fig. 48a and c. The lattice fringe of 0.21 nm and 0.21 nm with lattice plane (111) represents the characteristics lattice fringe of Ni on the IHC and the CNSs on Fig. 48b and d respectively. The appearances of the lattice fringe (111) suggest the effectiveness and efficiency of the reduction process in converting the NiO to Ni. The presence of CNSs support is further confirmed with the lattice fringe of 0.32 nm as depicted on Fig. 48d. The lattice fringe of the CNSs is closer to the value of 0.34 nm of the CNT reported by Lahiri *et al.* (2011). The observation of the similar lattice fringe on both the NiCeMo supported catalysts indicated that, the nature of support material has no ability to alter the lattice

orientation of metal loading. Hence, the adopted incipient wet impregnation method used for the metal loading enhances the metal distributions as sported with the HRSEM, elemental mapping and the XRD patterns of the NiCeMo supported IHC and CNSs which were presented in this study.

The XPS whose results are presented in Fig. 49 (a-f) was performed in order to determine the oxidation states of the Ni, Ce and Mo metals on the surfaces of IHC and CNSs including the metal composition of the respective support materials. In the first instance, a complete scan of the catalysts was conducted to gain an insight into the overall elemental state of the metal particles. The XPS survey scan representing the NiCeMo_IHC and NiCeMo_CNSs are presented in Fig. 49 (a-b) respectively.

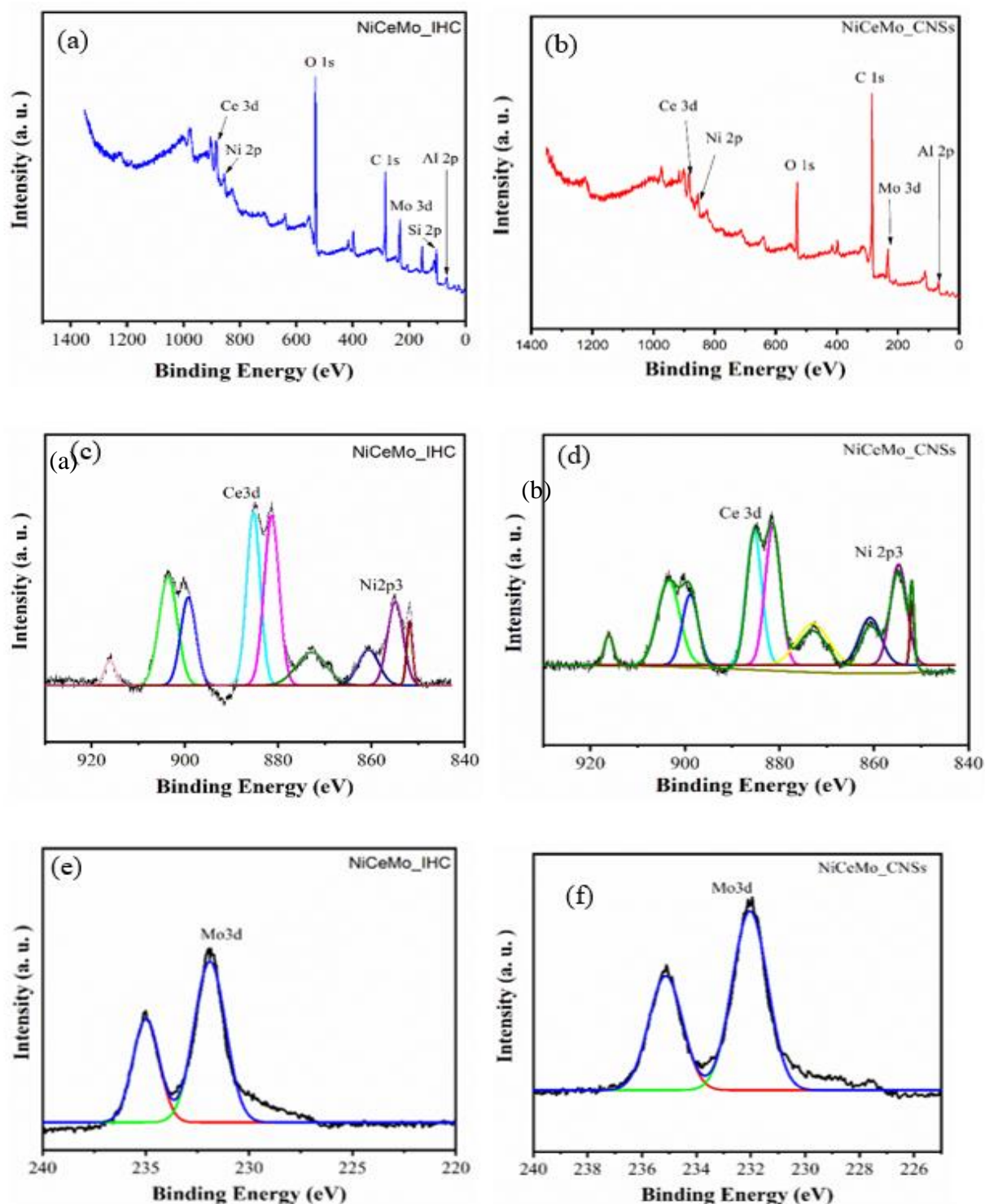


Figure 49: The XPS Spectra of NiCeMo supported IHC and CNSs (a-b) Survey scans (c-d) Ni 2p_{3/2} and Ce 3d (e-f) Mo 3d

In all the survey scan presented in Fig. 49 (a-b), the presence and the oxidation state of the constituent elements in both the catalysts were revealed. The presence of Ce, Ni and Mo dopants were present as Ce 3d, Ni 2p and Mo 3d at the binding energies of 885.15, 855.50 and 231.85 eV as shown on the XPS scan on Fig. 49 (a-b). The IHC is structurally composed of Al

and Si; these are regarded as the building block of the parent HZSM-5 zeolite coupled with the oxygen and the C from the CNSs which was employed for shape directing agent Fig. 49 (a). Carbon, C 1s has the highest intensity among the metals in the survey scan of the NiCeMo_CNSs catalysts as shown in Fig. 49b - This was due to the fact that carbon makes the highest composition in the bulk of the material.

The deconvolution peaks of the Ni 2p orbital for both the NiCeMo supported IHC and CNSs into doublets of Ni 2p_{3/2} and Ni 2p_{1/2} are presented in Fig. 49c and d respectively. The deconvoluted peaks of the two catalysts Fig. 49c and d, the observance of binding energy at 852.1, 855.5, 860.8, 872.3 and 881.5 eV (± 0.2 eV) were noticed. The peaks observed at the binding energy of 855.5 and 860.8 eV represent the presence of Ni 2p_{3/2} and Ni 2p; a shake-up satellite peak indicate the presence of Ni²⁺ on the internal pores of the NiCeMo supported catalysts (Li *et al.*, 2018; Liu *et al.*, 2024). The formation of this peak at the higher binding energy indicates the interaction of Ni with other metals and the zeolites and the CNSs. The deduction of higher energies to be a result of metal interaction is in accordance with the findings of Liu *et al.* (2024). The Ni 2p_{1/2} peak at the binding energy of 872.3 eV and the corresponding satellite peak at 881.5 eV are well observed on the two catalysts materials while the conformity of the Ni 2p_{3/2} is attributed to the presence of peaks appearance at 872.3 eV and the shake-up satellite peaks at 881.7 eV. It is noteworthy to state that, the observed binding energies are higher to the reported value by Li *et al.* (2018) which could mean that, a strong interactions exists between the catalysts composition. The presence of Ni⁰ species is related to the reduction process which was employed during the catalyst development in the presence of hydrogen environment. The spin-orbit splitting of 18.2 eV which was observed between the Ni 2p_{3/2} and the Ni 2p_{1/2} and the presence of Al_{2p} and Si_{2p} could indicate the formation of NiAl₂O₄ and Ni₂SiO₄ as a result of possible chemical formation with the parent aluminosilicate support material.

The XPS of Ce has been identified as a being complex in nature where the spectrum could be resolved into over 10 peak components (Weyrich *et al.*, 1997). The deconvolution peaks of Ce are presented along the Ni 2p XPS depicted in Fig. 49c and d. The complexity in the peak identification has been presented to involve the overlapping of the Ce⁴⁺ and the Ce³⁺ peaks due to their similar binding energies (Holgado *et al.*, 2000). The presence of the so-call u''' peak which originated from the transition of 4f⁰ from the ground state to the 4f⁰ initial state which is a characteristics peak for Ce⁴⁺. This peak is unique for the quantitative determination of the

amount of Ce^{4+} in catalysts. The spectra representing the Ce 3d region depicts a two triplets peaks at u''' , u'' and v''' , v'' where u represents the Ce $3d_{3/2}$ spin-orbit and v corresponds to the Ce $3d_{5/2}$; a characteristic peaks identification of a typical Ce^{4+} (Holgado *et al.*, 2000).

The deconvolution of the Mo 3d orbital is depicted in Fig. 49 (e-f) with two pronounced doublets links at Mo $3d_{5/2}$ and Mo $3d_{3/2}$ at 231.9 and 235.1 eV, representing the presence of five contributory Mo species (Mo^0 , Mo^{2+} , Mo^{4+} , Mo^{5+} and Mo^{6+}) (Yao *et al.*, 2017; Zheng *et al.*, 2020). Furthermore, the presence of Mo^{2+} species could be linked to the involvement of cubic structured MoNi formation on the surfaces of the catalysts following the reduction process Fig. 43.

Figure 50 shows the NH_3 -TPD patterns while the deduced acid site information is presented in Table 26 of the NiCeMo loaded IHC and CNSs catalysts after the reduction process. On the temperature region showing the desorption profile of NH_3 on the catalysts materials, the acid sites were classified as weak, moderate and strong for a temperature profile 150-200 °C, 200-400 °C and 400-700 °C respectively (Bhatti *et al.*, 2020).

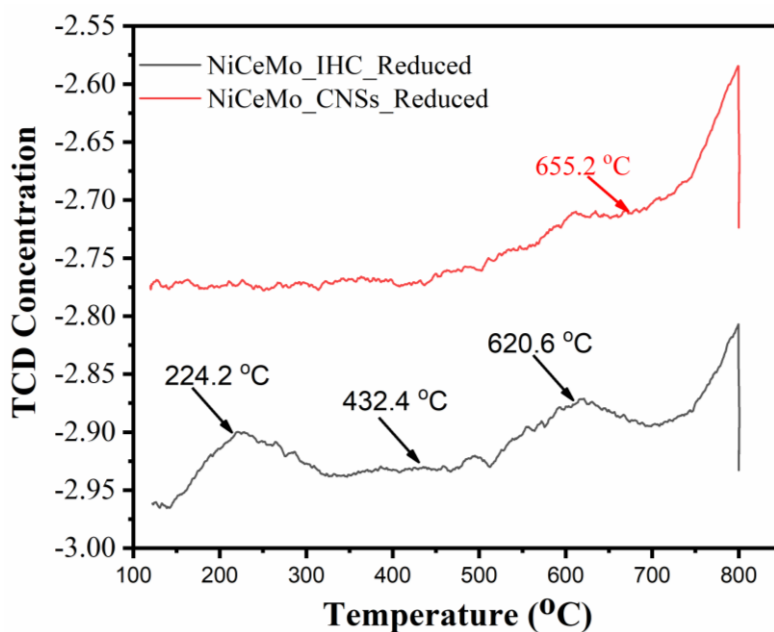


Figure 50: The NH_3 -TPD profiles of the developed NiCeMo supported IHC and CNSs supports

The presence of three distinct peaks were observed on the NiCeMo supported IHC at the temperature of 224.2, 432.4 and 620.6 °C. The presence of the peaks at the lower temperature are generally associated to the ammonia molecules that are weakly adsorbed through hydrogen bonding, in its place of acid sites while the peaks observed at the high temperature are attributed

to the strong Brønsted acid site (Li *et al.*, 2017). From the presented results in Fig. 50, the presence of moderate acid sites is formed at the temperature of 224.2 °C. The formation of the moderate acid sites at 224.2 °C is a possible indication of coordinated ammonia on the Lewis acid sites due to the weakly physio-sorption while the formation of the strong acid sites are related to the bond between the three hydrogen atoms and the three oxygen ions found in the tetrahedral framework of AlO₄ on the on Brønsted acid sites with NH₄⁺ (Kalamaras *et al.*, 2016). The presence of the highest acid sites in the two catalysts suggest that the high activities of the catalysts during the HDO process could be related to the presence of strong acidity strength. The formation of the moderate acid sites in the IHC supported catalyst could be associated with the Al-Si interaction with the metal particles. Furthermore, the NiCeMo supported CNSs shows a strong acid sites at the temperature of 655.2 °C equivalent to the 0.18567 mmol/g acidity. The effects of Ce loading has been identified to have no effects on the overall acidity of catalyst (Zhang *et al.*, 2016).

Table 26: Acidic properties of the developed NiCeMo supported IHC and CNSs catalysts

Peak number	Temp at Max. (°C)	Quantity (mmol/g)	Peak concentration (%)	Total acidity (mmol/g)
NiCeMo_IHC_Reduced	224.2	0.08833	0.05	0.31400
	432.4	0.03232	0.02	
	620.6	0.19335	0.06	
NiCeMo_CNSs_Reduced	655.2	0.18567	0.04	0.18567

The thermal behavior of the synthesized catalyst; the calcined and the reduced forms of the NiCeMo supported IHC and CNSs are presented in Table 26 while the deduced information which gives the thermal information of the catalysts to suggest the best temperature at which they could be applied without losing their thermal stability.

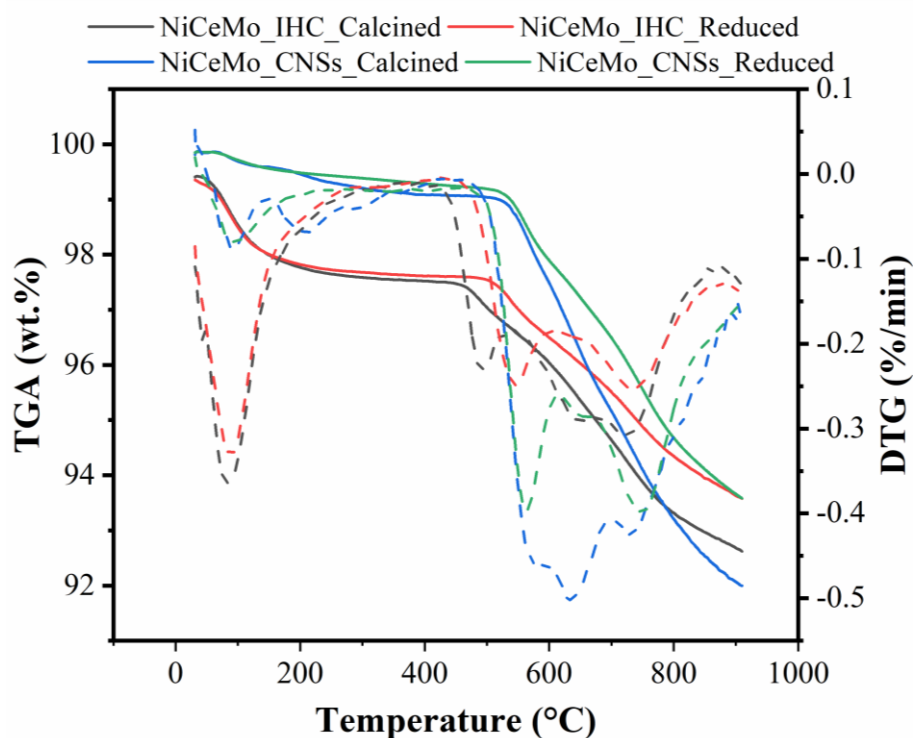


Figure 51: The TGA/DTG profile of the developed catalysts

Table 27: Thermal properties of the developed NiCeMo supported IHC and CNSs catalysts

Sample name	% Moisture	Degradation temp (°C)	Volatile (%)	Total lost (%) (31-910°C)
NiCeMo_IHC(calcined)	1.8169	410-889	4.8849	6.7878
NiCeMo_IHC(Reduced)	1.6866	410-887	4.0216	5.7772
NiCeMo_CNSs(Calcined)	0.6370	478-887	7.0267	7.8201
NiCeMo_CNSs(Reduced)	0.4813	478-887	5.6423	6.2737

4.11 The HDO of Crude Biofuel Over NiCeMo Supported IHC and CNSs Supports

The catalytic activities of the reduced forms NiCeMo_IHC and NiCeMo_CNSs were evaluated for upgrading crude bio-oil, obtained under solvothermal liquefaction conditions of 430 °C, 35 minutes, and 50% ethanol, into high-grade bio-oil. This study focused on investigating the catalysts' potential for oxygen removal from unstable ketones, primarily cycloketones, in the crude bio-oil. Under supercritical ethanol conditions, the effectiveness of the catalysts was assessed by examining their ability to dissociate ethanol and the efficiency of their acidic sites in facilitating the conversion process. An overview of the effects of temperature on the conversion of cyclohexanone revealed that the HDO process which comprises of the

simultaneous hydrogenation and dehydration process under the influence of in-situ hydrogen supply is most favored at the 350 °C reaction temperature. Hence, in this present evaluation of the NiCeMo supported IHC and CNSs catalysts, the effects of residence time (0, 1 and 2 h) at 350 °C were evaluated on the upgrading of the crude biofuel derived orange peel.

The compositions and the yield of the upgraded biofuel obtained at different catalysts (CNSs, HZSM-5, IHC, NiCeMo_IHC and NiCeMo_CNSs) and residence time are presented in Figs. 52 (a-e) and Table 28 while the elemental and the heating values are shown in Table 29.

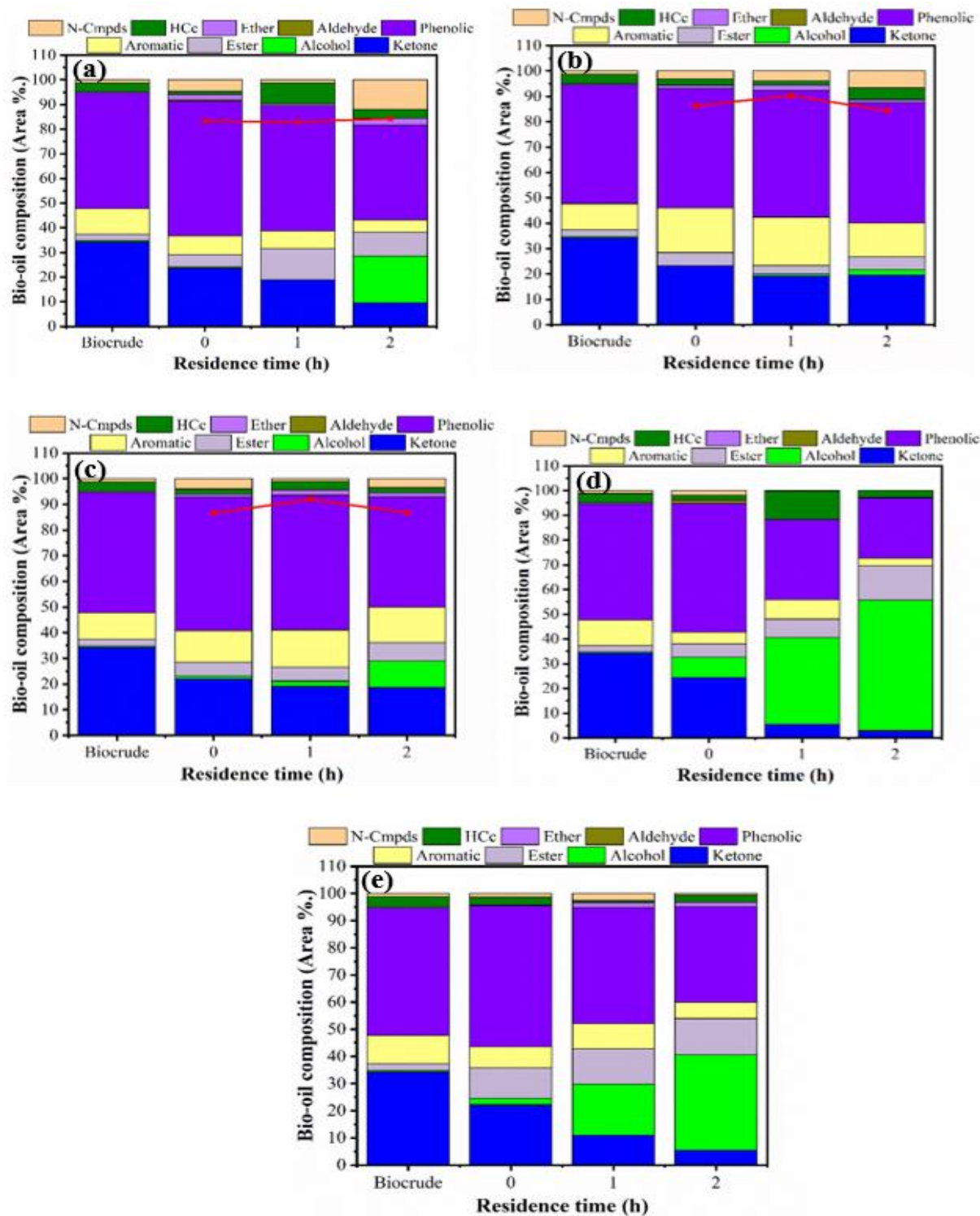


Figure 52: Effects of residence time on the compositions and the yield of the upgraded biofuel obtained at different catalysts (a) CNSs (b) HZSM-5 (c) IHC (d) NiCeMo_IHC and (e) NiCeMo_CNSs)

Table 28: Effects of residence time on the compositions and the yield of the upgraded biofuel obtained at different catalysts (CNSs, HZSM-5, IHC, NiCeMo IHC and NiCeMo CNSs) and residence time

			Ketone	Alcohol	Ester	Aromatic	Phenolic	Aldehyde	Ether	HCs	N-Cmpds	Coke, %	Yield, wt. %
		Feed	34.23	0.60	2.56	10.40	46.76	0.00	0.57	3.63	1.24	--	
Support	Temp/time	Loading											
CNSs	350,0h		23.70	0.47	4.85	7.67	54.59	0.51	2.36	1.27	4.58	3.33	83.30
CNSs	350,1h	-	18.97	0.00	12.57	7.13	50.74	0.00	0.94	8.40	1.24	7.50	83.00
CNSs	350,2h	-	9.62	18.96	9.52	5.10	38.53	0.00	2.60	3.69	11.98	0.00	84.30
HZSM-5	350,0h	-	23.28	0.00	5.19	17.51	47.07	0.00	1.30	2.57	3.09	12.50	86.30
HZSM-5	350,1h	-	19.30	0.76	3.32	19.06	49.82	0.00	2.32	1.52	3.91	0.00	90.30
HZSM-5	350,2h	-	19.51	2.20	5.01	13.42	47.48	0.00	1.08	4.62	6.68	0.00	84.30
IHC	350,0h	-	22.10	1.04	5.34	12.35	52.09	0.00	1.05	2.03	4.00	5.76	86.54
IHC	350,1h	-	19.02	2.1	5.49	14.46	52.5	0.00	2.10	3.3	1.03	6.45	91.87
IHC	350,2h	-	18.71	10.2	7.23	13.86	43	0.00	1.43	2.04	3.53	6.34	86.76
CNSs	350,0hr	NiCeMo	22.16	2.39	11.26	7.79	52.09	0.00	0.00	3.00	1.31	3.75	95.90
CNSs	350,1hr	NiCeMo	10.96	18.87	12.95	9.31	42.72	0.00	1.80	0.80	2.60	3.00	110.00
CNSs	350,2hr	NiCeMo	5.43	35.09	13.47	5.94	35.03	0.00	1.81	2.66	0.58	3.50	137.00
IHC	350,0hr	NiCeMo	24.32	8.29	5.43	4.77	51.98	1.35	0.00	1.93	1.93	6.75	103.10
IHC	350,1hr	NiCeMo	5.45	35.17	7.48	7.78	32.43	0.00	0.00	11.36	0.33	5.00	127.90
IHC	350,2hr	NiCeMo	2.92	52.82	13.93	3.03	24.41	0.00	0.28	2.61	0.00	4.50	197.20

Table 29: Elemental analysis and the HHV value of the upgraded biofuel

Support	Temp/time		N	C	H	O	O/C	H/C	HHV MJ/kg
			(%)	(%)	(%)	(%)			
		Feed	1.302	77.8603	9.0808	11.76	0.11	1.39	37.24
		Loading							
CNSs	350,0hr	NiCeMo	1.304	76.8237	8.952	12.92	0.13	1.39	36.53
CNSs	350,1hr	NiCeMo	1.122	72.8694	9.0986	16.91	0.17	1.49	34.81
CNSs	350,2hr	NiCeMo	1.135	74.0735	9.5718	15.22	0.15	1.54	36.15
IHC	350,0hr	NiCeMo	1.244	75.3697	9.023	14.36	0.14	1.43	35.92
IHC	350,1hr	NiCeMo	1.051	69.431	9.0319	20.49	0.22	1.55	33.01
IHC	350,2hr	NiCeMo	0.739	49.7873	6.5144	42.96	0.65	1.56	19.38

The results presented in Figs. 52 (a-e) show the influence of catalysts and the residence time on the HDO of the biofuel components into a low oxygen containing compounds. The performance evaluation of all the catalysts depicted a successive increase in ketone conversion as the residence time increases from 0 to 2 h. For instance, the ketone contents during the evaluation of the performance of CNSs catalysts were obtained to be 23.70, 18.97 and 9.62 Area% for 0, 1 and 2 h residence time respectively. The results with the gradual decrease in the ketone contents shows that, an increase in time favor reactants-catalysts interaction where the tendencies for an enhanced HDO process take place. Furthermore, an extended residence time promote the hydrogenation reaction for alcohol formation and the subsequent dehydration via in-situ hydrogen transfer process. Hence, the hydrogen produced during the catalytic decomposition of ethanol at the supercritical reaction conditions aid the HDO process at higher residence time. This observation is similar in all the results presented in Figs. 52 (a-e).

The optimum residence time for an enhanced hydrogenation for alcohol (18.96 Area%) and hydrocarbon (8.40 Area%) formations were observed at 2 and 1 h over CNSs catalyst, respectively. The highest biofuel yield was obtained at the residence time of 2 h to be 84.30 wt.% with 0.00 wt.% coke formation at the 3 h residence time. The shape selectivity of HZSM-5 zeolite to enhancing the production of aromatic compounds was depicted by the results presented in Fig. 52b. From Fig. 52b, the selectivity to aromatic compounds were 17.51, 19.06 and 13.42 Area% for 0, 1 and 2 h residence time respectively. The selectivity to high content of aromatic compounds of HZSM-5 could be associated to the present of high acidic sites in zeolite and the architecture of the Al-Si framework (Chaihad *et al.*, 2021; Liu *et al.*, 2019). In addition, the presence of high amount of phenols and aromatic compounds could be associated

with the high aromatization reaction during the upgrading process (Kazmi *et al.*, 2024). A shorter residence time of 0 h do not favor the hydrogenation of the ketones into alcohols but rather promotes the formation of coke (12.5 wt.%). The introduction of CNSs into the synthesis route of HZSM-5 lowers the acidity of the obtained zeolite hybrid and hence, influence its catalytic performance to promoting the biofuel yield through the suppression of gaseous formation due to cracking process.

The catalytic influence of the NiCeMo on both the hybrid IHC and the CNSs were also tested and reported in Fig. 52d and e respectively. The metal particle (Ni, Ce and Mo) have been explored to promote the HDO of biofuel into transportation fuels by various researchers (Faturachman *et al.*, 2022; Park *et al.*, 2021; Sangnikul *et al.*, 2019). The result depicted in Fig. 52d shows an excellent HDO of ketones into alcohols and the subsequent improvement in the yield of the upgraded biofuel. The yield of the biofuel and the selectivity to alcohol were obtained to be 103.10, 127.90 and 197.20 wt.%, 8.29, 35.17 and 52.83 Area% at the 0, 1, and 2 h residence time respectively. The metal loading, through the enhanced surface area and the HDO tendencies of the Ni and Ce, the EtOH's dual function as solvent and reactant was well observed.

Also, 11.36 area% of hydrocarbon was observed at the optimum residence time of 1 h over the NiCeMo_IHC catalyst material while the total ketone contents decreased to 2.92 area% at 2 h. The presence of low acidic sites on the NiCeMo_IHC and NiCeMo_CNSs retard their selectivity to aromatic compounds when compared to the pristine HZSM-5 zeolite with higher acidic sites. Unlike the NiCeMo supported CNSs catalyst, the highest hydrocarbon obtained was 3.00 area% at 0 h residence time though with a reduced coke formation. Therefore, the NiCeMo_IHC catalysts shows an excellent HDO activities for the conversion of ketones into high content alcohols and hydrocarbons with reduced aromatic, phenolic and ether contents as shown in Table 28. The performance characteristics of the NiCeMo supported CNSs could be attributed to the observed structural defect, enhanced the surface area for the metal dispersion and the overall synergetic effects of the NiCe to promote the HDO process.

The results presented in Table 29 shows the elemental and the heating values of the upgraded biofuel. The HHV of the upgraded biofuel were reduced while the O-contents increases beyond the value obtained from the feedstock. The reduction in the heating value necessitated an investigation into the liquid and gas compositions obtained during the reaction. For instance, the NiCeMo_IHC induced upgrading at the 2 h and 350 °C reaction temperature promotes the

conversion of ethanol into alcohols such as 1-butanol and 1-hexanol of high compositions in the bulk of the biofuel. This conversion process of ethanol to producing alcohol is governed by the Guerbet reaction whose products adversely increase the overall oxygen contents and subsequently the heating value of the obtained biofuel. The favorability of the NiCeMo based catalysts to side reaction, Guerbet reaction lowers the performance of the catalysts to enhancing the heating values and the lowering the oxygen contents. Controlling the formation of side products such as the alcohols would depict the upgrading process as an efficient process path to enhance the biofuel properties into a renewable energy source. The information from the gas analysis further gives an insight into the adverse effect of decarboxylation and decarbonylation reactions on the heating content of the upgraded biofuel. The gas compositions (mol) obtained during the catalytic upgrading of crude biofuel over NiCeMo supported IHC and CNSs is presented in Fig. 53: .

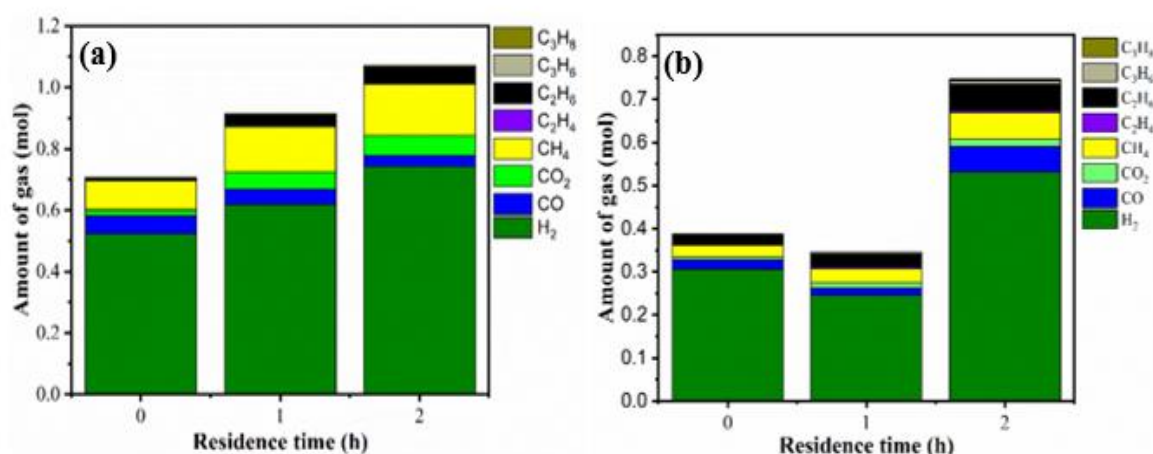


Figure 53: Gas composition obtained over the (a) NiCeMo_IHC and (b) NiCeMo_CNSs catalysts

As the residence time increases, the quantity of the overall amount of the produced gases increases as shown in Fig. 33a, for instance, the amount of hydrogen gas produced were 0.52, 0.62 and 0.74 moles at 0, 1 and 2 h residence time. The NiCeMo_IHC has a higher efficiency of hydrogen production from the decomposition of EtOH and that could be responsible for the higher HDO process which led to the production of 11.36 area% at the reaction time of 1 h. The C_2H_4 and C_3H_6 hydrogenation resulted in an increase in the production of C_2H_6 and C_3H_8 as the residence time increases. This observation enhances the formation of ethyl-substituted compounds in all cases of the catalysts. The higher content of CO and CO_2 gases are indication of the preference of the reaction process towards decarbonylation and decarboxylation

reactions. The CO and CO₂ production increase with an increase in residence time in both cases of the catalysts Figs. 53a and b. These reactions are unfavorable to producing high HHV biofuel and may have been initiated by the high acidity of the catalyst's materials. Hence, to produce a high HHV biofuel, the decarboxylation and the decarbonylation reactions should be kept at minimal through the control of catalysts' acidity. Also, the formation of lighter hydrocarbons is susceptible during the catalytic upgrading process where lower hydrocarbon fractions are produced from the primary feedstock. The limitation of the GC-MS for total quantification of the composition of biofuel with <C4 carbon contents prevent the account of this components in the biofuel.

The functional groups present in the upgraded biofuel produced using the NiCeMo supported catalysts are presented in Fig. 54Figure 54.

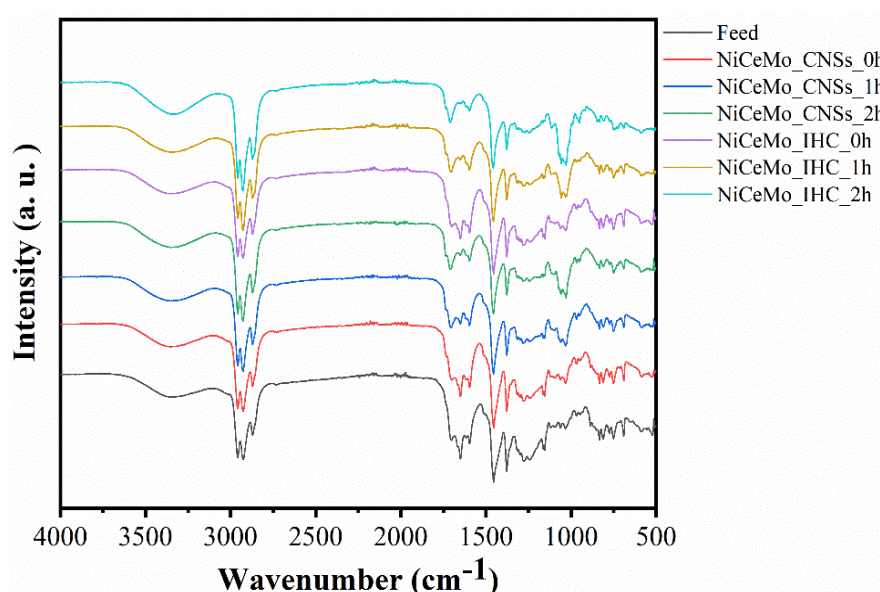


Figure 54: The FTIR spectra of the upgraded biofuel

The result presented in Fig. 54 depicts the presence of several functional groups in the produced biofuel which are similar to the feedstock, the details identification of the peaks and the peak assignments are contained in Table 30.

Table 30: The FTIR peaks assignment from the FTIR spectral of the biofuel obtained from Fig. 54

Wave number range (cm ⁻¹)	Wavenumber (cm ⁻¹)	Functional group	Class of compounds	Observation
3600-3200	3332	O-H stretching	Phenol, alcohols, water	Present in all the upgraded biofuel and the feedstock; indicating the presence of phenols and alcohol.
3000-2800	2959, 2929, 2865	C-H stretching	Alkanes (methyl groups) and Aliphatic	Present in all the upgraded biofuel and the feedstock
1850-1650	1703	Conjugated and unconjugated C=O stretching	Ketones, aldehyde, carboxylic acid	Low intensity on the feed, NiCeMo supported CNSs and IHC at 0 h residence time
1650-1580	1655, 1595	C=C stretching	Alkenes and aromatics	1655 cm ⁻¹ : High intensity on feed, , NiCeMo supported CNSs and IHC at 0 h residence time
1470-1350	1460, 1379	C-H and O-H bending (deformation)	Alkanes	
1300-950	1266, 1156, 1033	C-O stretching	Primary, secondary and tertiary alcohols	1156 cm ⁻¹ : High intensity on feed, NiCeMo supported CNSs and IHC at 0 h residence time. 1033 cm ⁻¹ : High intensity on NiCeMo supported CNSs and IHC at 1 and 2 h residence time.
950-650	834, 754, and 670	C-H out of plane bending	Aromatics (mono, polycyclic, and substituted)	670 cm ⁻¹ : Low intensity on NiCeMo supported CNSs and IHC at 2 h residence time.

CHAPTER FIVE

CONCLUSION AND RECOMMENDATIONS

5.1 Conclusion

The production of energy efficient fuel through the solvothermal liquefaction of orange peels feedstock in an autoclave reactor has been obtained. The non-catalytic valorization of orange peels through the optimization of the effects of temperature (230-430 °C), residence time (5-35 min) and the concentration of EtOH in acetone (100:0 – 0:100) were studied using one-factor at a time. The non-catalytic upgrading results shows the findings:

- (i) Orange peels was liquefied in sub/supercritical environments without N₂ supply.
- (ii) The synergetic effects of process parameters promote biocrude's quality and yield.
- (iii) Biocrude HHV with 38.1 MJ/kg was obtained at 50% ethanol, 430 °C and 35 min.
- (iv) Biocrude' volatility and molecular weight depends on process variables.
- (v) Orange peels is an excellent bio-resource material for biocrude production.

The effects of catalytic upgrading of orange peels were further investigated over Fe/CNSs catalysts material and process parameters were optimized using central composite design (CCD). This section of the study dealt with the influence of catalyst dosage (3–6 wt%) and reaction temperature (330–430 °C) were optimized on the constant weight of orange feedstock (10 g), reaction time of (15 min) and solvents' ratio of 3:1 (acetone to ethanol). The catalytic upgrading technique results shows the following findings:

- (i) Wet impregnation method favors the distribution of Fe on CNSs support.
- (ii) Optimum STL reaction conditions resulted in 71.09 wt% and 72.82 wt% of biocrude and biomass conversion respectively.
- (iii) Fe/CNSs retards the formation of oxygenates by removing C=O (of ketones) stretch bond in biocrude.
- (iv) Fe/CNSs enhances phenolics and aromatic selectivity in the biocrude at 430 °C reaction temperature and 3 wt% catalyst loading.

The non-catalytic and catalytic upgrading of bio-oil model compound; cyclohexanone was aimed at understanding the HDO effects of reaction conditions and Ni, Ce, Fe and Zn loading on the biochar obtained from the non-catalytic STL of orange peels. The results of both the studies in this category shows that:

- (i) Highest ketone conversion of 84.71 area% was achieved at the reaction conditions of 350 °C for 3 h with corresponding biofuel yield of 72.1 wt.% and water content of 3.21 wt.%; indicating the contribution of dehydration reaction during the upgrading process.
- (ii) The introduction of formic acid enhances the HDO process through hydrogenation and dehydration where 10.10 area% of hydrocarbon was obtained at 70EtOH:20FA, 350 °C for 0 h.
- (iii) At the residence time of 2 h and 350 °C, the prevalence of hydrogenation reaction leading to 83.46 area% of cyclohexanol formation
- (iv) Ni supported biochar shows an excellent cyclohexanone conversion of 93.98 area% and the highest hydrocarbon selectivity of 18.27 area% at 350 °C for 2 and 1 h respectively.
- (v) The oxygen vacancy in Ce supported biochar promotes the overall ketone conversion with total conversion of 83.20 area%.
- (vi) The presence of decarboxylation and decarbonylation reactions coupled with alkyl-substitution reactions were proposed to the formation of the observed cycloheptene; unsaturated hydrocarbon. Overall, the major reactions which promote the cyclohexanone conversion include, hydrogenation, dehydration, decarboxylation and decarbonylation reactions.

The results obtained from the catalytic upgrading of the biocrude over the NiCeMo catalysts in supercritical ethanol revealed the following findings:

- (i) The adoption of incipient wet impregnation method and the introduction of Mo as catalysts promoter enhances metal dispersion over the NiCeMo supported IHC and CNSs.

- (ii) The dealumination process employed prior to HZSM-5 synthesis enhance the surface area and activate the aluminum for reaction which promoted the hierarchical pore formation and the surface area.
- (iii) The CNSs effectively controlled the growth of HZSM-5 under the influence of SDA and ethanol as dispersant.
- (iv) The hybrid catalyst; NiCeMo supported IHC exhibited the highest conversion of ketones and phenols while producing the highest hydrocarbon content of 11.36 area% at 350 °C for a period of 1 h.
- (v) The presence of Guerbet reaction during the NiCeMo catalytic activities retards the overall heating value and improves the oxygen content.

A promising technique for valorization of orange peels feedstock into an energy-dense bio-oil has been demonstrated using a cheaper reaction pathway through efficient reaction conditions selection during the STL process. The adopted solvent (EtOH and acetone) and their respective ratio gives an insight into the dependency of the heating value of bio-oil on process parameters. The application of NiCeMo supported IHC catalyst promotes the HCs and bio-yield and enhance the H/C ratio of the upgraded biofuel while the Guerbet reaction retards the overall biofuel quality. Hence, the catalyst, NiCeMo supported IHC shows an excellent HDO potentials for use in the conversion of ethanol into a more energy dense alcohols.

5.2 Recommendations

Following the explicit investigation conducted in this study, the needs to advance the knowledge in bio-oil upgrading over metal supported catalysts are paramount. Hence, the following recommendations are made;

- (i) Effect of bi-solvents such as water: ethanol and water: acetone should be investigated for the solvothermal liquefaction of orange peels and other associated feedstock.
- (ii) The composition of gaseous products produced during the valorization of orange peels should be investigated to gain an insight into the overall reactions which control the bio-oil formation

- (iii) Investigation into the effects of process parameters on the continuous STL reactor system for orange peels valorization over the studied solvents should be carried out in order to depict the process as an economic route
- (iv) The Techno-economic analysis (TEA) and the life cycle assessment (LCA) of the crude bio-oil production and upgrading should be investigated
- (v) The control of Guerbet reaction which promotes the formation of side products should be investigated through the application of water as solvent in place of ethanol.
- (vi) The obtained liquid biofuel should be characterized for its detailed fuel properties and effort should be expedited on the combustion efficiency of the obtained fuel in a typical combustion engine.
- (vii) An efficient and effective techniques for the separation of alcohol from the bulk of the obtained biofuel after the upgrading process should be considered.

REFERENCES

- Aboagye, D., Banadda, N., Kiggundu, N., & Kabenge, I. (2017). Assessment of orange peel waste availability in ghana and potential bio-oil yield using fast pyrolysis. *Renewable and Sustainable Energy Reviews*, 70, 814-821. <https://doi.org/10.1016/j.rser.2016.11.262>
- Aderlanio Cardoso, Tomas Ramirez Reina, Isabel Suelves, José Luis Pinilla, M. M. and K. H. (2018). Effect of carbon-based materials and CeO₂ on Ni catalysts for Kraft lignin liquefaction in supercritical water. *Green Chemistry*, 20(18), 4308-4318. <https://doi.org/10.1039/C8GC02210K>
- Ali, N., Saleem, M., Shahzad, K., Saleem, R. M., & Chughtai, A. (2014). Effect of Temperature on the Bio Oil Yield from Pyrolysis of Maize Stalks in Fluidized Bed Reactor. *Journal of Pakistan Institute of Chemical Engineers*, 42(2), 79–86. <https://www.researchgate.net/publication/262376025>
- Almoneef, M. M., Jedli, H., & Mbarek, M. (2021). Experimental study of CO₂ adsorption using activated carbon. *Materials Research Express*, 8(6), 65602. <https://doi.org/10.1088/2053-1591/ac05fe>
- Anil Kumar Varma, Ravi Shankar, and P. M. (2018). A Review on Pyrolysis of Biomass and the Impacts of Operating Conditions on Product Yield, Quality, and Upgradation. In *Recent Advancements in Biofuels and Bioenergy Utilization*. 227-259 <https://doi.org/10.1007/978-981-13-1307-3>
- Arafat Hossain, M., Ganesan, P., Jewaratnam, J., & Chinna, K. (2017). Optimization of process parameters for microwave pyrolysis of oil palm fiber (OPF) for hydrogen and biochar production. *Energy Conversion and Management*, 133, 349–362. <https://doi.org/10.1016/j.enconman.2016.10.046>
- Arumugam, M., Goh, C. K., Zainal, Z., Triwahyono, S., Lee, A. F., Wilson, K., & Taufiq-yap, Y. H. (2021). Hierarchical hzsm-5 for catalytic cracking of oleic acid to biofuels. *Nanomaterials*, 11(3), 1–11. <https://doi.org/10.3390/nano11030747>
- Arun, J., Panchamoorthy, K., Sivaramakrishnan, R., Vikas, N., Abhishek, K., Gurumurthy, V., & Ramanan, K. (2021). Bioenergy perspectives of cattails biomass cultivated from municipal wastewater via hydrothermal liquefaction and hydro-deoxygenation. *Fuel*,

284(July 2020), 118963. <https://doi.org/10.1016/j.fuel.2020.118963>

- Attia, M., Farag, S., & Chaouki, J. (2020). Upgrading of oils from biomass and waste: Catalytic hydrodeoxygenation. *Catalysts*, 10(12), 1–30. <https://doi.org/10.3390/catal10121381>
- Ayala, J. R., Montero, G., Coronado, M. A., García, C., Curiel-Alvarez, M. A., León, J. A., Sagaste, C. A., & Montes, D. G. (2021). Characterization of orange peel waste and valorization to obtain reducing sugars. *Molecules*, 26(5). <https://doi.org/10.3390/molecules26051348>
- Babajo, S. A., Enaburekhan, J. S., & Rufai, I. A. (2019). Review on production of liquid fuel from co-pyrolysis of biomass with scrap/waste tire. *Journal of Applied Sciences and Environmental Management*, 23(8), 1475. <https://doi.org/10.4314/jasem.v23i8.10>
- Bakari, R., Kivevele, T., Huang, X., & Jande, Y. A. C. (2021). *Sub- and Supercritical Water Gasification of Rice Husk : Parametric Optimization Using the I - Optimality Criterion*. <https://doi.org/10.1021/acsomega.0c06318>
- Bakari, R., Kivevele, T., Huang, X., & Jande, Y. A. C. (2022). Catalytic supercritical water gasification of biomass waste using iron-doped alkaline earth catalysts. *Biomass Conversion and Biorefinery*, 0123456789. <https://doi.org/10.1007/s13399-022-02800-x>
- Bhatti, U. H., Kazmi, W. W., Muhammad, H. A., Min, G. H., Nam, S. C., & Baek, I. H. (2020). Practical and inexpensive acid_activated montmorillonite catalysts for energy-efficient CO₂ capture. *Green Chemistry*, 22(19), 6328–6333. <https://doi.org/10.1039/d0gc01887b>
- Bianasari, A. A., Khaled, M. S., Hoang, T. D., Reza, M. S., Bakar, M. S. A., & Azad, A. K. (2024). Influence of combined catalysts on the catalytic pyrolysis process of biomass: A systematic literature review. *Energy Conversion and Management*, 309(February), 118437. <https://doi.org/10.1016/j.enconman.2024.118437>
- Biller, P., & Ross, A. B. (2016). Production of biofuels via hydrothermal conversion. In *Handbook of Biofuels Production*, 509-547. Woodhead Publishing. Elsevier Ltd. <https://doi.org/10.1016/B978-0-08-100455-5.00017-5>
- Biswas, B., Bisht, Y., Kumar, J., Yenumala, S. R., & Bhaskar, T. (2020). Effects of temperature and solvent on hydrothermal liquefaction of the corncob for production of phenolic

- monomers. *Biomass Conversion and Biorefinery*, 12, 91-101. <https://doi.org/10.1007/s13399-020-01012-5>
- Biswas, B., Kumar, A., Kaur, R., Krishna, B. B., & Bhaskar, T. (2021). Catalytic hydrothermal liquefaction of alkali lignin over activated bio-char supported bimetallic catalyst. *Bioresource Technology*, 337(June), 1-8. <https://doi.org/10.1016/j.biortech.2021.125439>
- Brand, S., & Kim, J. (2015). Liquefaction of major lignocellulosic biomass constituents in supercritical ethanol. *Energy*, 80, 64–74. <https://doi.org/10.1016/j.energy.2014.11.043>
- Brand, S., Susanti, R. F., Kim, S. K., Lee, H. shik, Kim, J., & Sang, B. I. (2013). Supercritical ethanol as an enhanced medium for lignocellulosic biomass liquefaction: Influence of physical process parameters. *Energy*, 59, 173–182. <https://doi.org/10.1016/j.energy.2013.06.049>
- Caprariis, B. De, Filippis, P. De, Petrullo, A., & Scarsella, M. (2017). Hydrothermal liquefaction of biomass : Influence of temperature and biomass composition on the bio-oil production. *Fuel*, 208, 618–625. <https://doi.org/10.1016/j.fuel.2017.07.054>
- Carpio, R. B., Zhang, Y., Kuo, C. T., Chen, W. T., Schideman, L. C., & de Leon, R. (2021). Effects of reaction temperature and reaction time on the hydrothermal liquefaction of demineralized wastewater algal biomass. *Bioresource Technology Reports*, 14(February 2020), 1-10. <https://doi.org/10.1016/j.biteb.2021.100679>
- Chaihad, N., Anniwaer, A., Choirun Az Zahra, A., Kasai, Y., Reubroycharoen, P., Kusakabe, K., Abudula, A., & Guan, G. (2021). In-situ catalytic upgrading of bio-oil from rapid pyrolysis of biomass over hollow HZSM-5 with mesoporous shell. *Bioresource Technology*, 341(July), 167-183. <https://doi.org/10.1016/j.biortech.2021.125874>
- Chen, D., Li, Y., Deng, M., Wang, J., Chen, M., Yan, B., & Yuan, Q. (2016). Effect of torrefaction pretreatment and catalytic pyrolysis on the pyrolysis poly-generation of pine wood. *Bioresource Technology*, 214, 615–622. <https://doi.org/10.1016/j.biortech.2016.04.058>
- Chen, J., & Li, S. (2020). Characterization of biofuel production from hydrothermal treatment of hyperaccumulator waste (*Pteris vittata* L.) in sub- And supercritical water. *RSC Advances*, 10(4), 2160–2169. <https://doi.org/10.1039/c9ra09410e>

- Chen, Y., Cao, X., Zhu, S., Tian, F., Xu, Y., Zhu, C., & Dong, L. (2019). Synergistic hydrothermal liquefaction of wheat stalk with homogeneous and heterogeneous catalyst at low temperature. *Bioresource Technology*, 278(December 2018), 92–98. <https://doi.org/10.1016/j.biortech.2019.01.076>
- Chen, Y., Mu, R., Yang, M., Fang, L., Wu, Y., Wu, K., Liu, Y., & Gong, J. (2017). Catalytic hydrothermal liquefaction for bio-oil production over CNTs supported metal catalysts. *Chemical Engineering Science*, 161, 299–307. <https://doi.org/10.1016/j.ces.2016.12.010>
- Cheng, S. (2017). Development of Heterogeneous Catalysts for Upgrading Biomass Pyrolysis Bio-Oils into Advanced Biofuels. *South Dakota State University*
- Cheng, S., Wei, L., Alsowij, M., Corbin, F., Boakye, E., Gu, Z., & Raynie, D. (2017). Catalytic hydrothermal liquefaction (HTL) of biomass for bio-crude production using Ni/HZSM-5 catalysts. *AIMS Environmental Science*, 4(3), 417–430. <https://doi.org/10.3934/environsci.2017.3.417>
- Cheng, S., Wei, L., Alsowij, M. R., Corbin, F., Julson, J., Boakye, E., & Raynie, D. (2018). In situ hydrodeoxygenation upgrading of pine sawdust bio-oil to hydrocarbon biofuel using Pd/C catalyst. *Journal of the Energy Institute*, 91(2), 163–171. <https://doi.org/10.1016/j.joei.2017.01.004>
- Choi, Y. S., Johnston, P. A., Brown, R. C., Shanks, B. H., & Lee, K. H. (2014). Detailed characterization of red oak-derived pyrolysis oil: Integrated use of GC, HPLC, IC, GPC and Karl-Fischer. *Journal of Analytical and Applied Pyrolysis*, 110(1), 147–154. <https://doi.org/10.1016/j.jaap.2014.08.016>
- Chon, Min, C., Tsuru, T., & Takahashi, H. (1979). Changes in Pore Structure of Kaolin Mineral by Sulfuric Acid Treatment. *Clay Science*, 162, 155–162. https://www.jstage.jst.go.jp/article/jcssjclayscience1960/5/3/5_3_155/_pdf
- Collard, F. X., & Blin, J. (2014). A review on pyrolysis of biomass constituents: Mechanisms and composition of the products obtained from the conversion of cellulose, hemicelluloses and lignin. *Renewable and Sustainable Energy Reviews*, 38, 594–608. <https://doi.org/10.1016/j.rser.2014.06.013>
- Çulcuoğlu, E., Ünay, E., Karaosmanoğlu, F., Angin, D., & Şensöz, S. (2005). Characterization

- of the bio-oil of rapeseed cake. *Energy Sources*, 27(13), 1217–1223. <https://doi.org/10.1080/00908310490479592>
- Dannhauser, W., & Bahe, L. W. (1964). Dielectric constant of hydrogen bonded liquids. III. Superheated alcohols. *The Journal of Chemical Physics*, 40(10), 3058–3066. <https://doi.org/10.1063/1.1724948>
- Demirkaya, E., Dal, O., & Yüksel, A. (2019a). Liquefaction of waste hazelnut shell by using sub- and supercritical solvents as a reaction medium. *Journal of Supercritical Fluids*, 150, 11–20. <https://doi.org/10.1016/j.supflu.2019.03.019>
- Demirkaya, E., Dal, O., & Yüksel, A. (2019b). Liquefaction of waste hazelnut shell by using sub- and supercritical solvents as a reaction medium. *Journal of Supercritical Fluids*, 150, 11–20. <https://doi.org/10.1016/j.supflu.2019.03.019>
- Dhawane, S. H., Kumar, T., & Halder, G. (2015). Central composite design approach towards optimization of flamboyant pods derived steam activated carbon for its use as heterogeneous catalyst in transesterification of Hevea brasiliensis oil. *Energy Conversion and Management*, 100, 277–287. <https://doi.org/10.1016/j.enconman.2015.04.083>
- Ding, Y. L., Wang, H. Q., Xiang, M., Yu, P., Li, R. Q., & Ke, Q. P. (2020). The Effect of Ni-ZSM-5 Catalysts on Catalytic Pyrolysis and Hydro-Pyrolysis of Biomass. *Frontiers in Chemistry*, 8, 1-11. <https://doi.org/10.3389/FCHEM.2020.00790/FULL>
- Divyabharathi, R., & Subramanian, P. (2021). Biocrude production from orange (*Citrus reticulata*) peel by hydrothermal liquefaction and process optimization. *Biomass Conversion and Biorefinery*, 12(1), 183–194. <https://doi.org/10.1007/s13399-021-01383-3>
- Divyabharathi, R., & Subramanian, P. (2022). Biocrude production from orange (*Citrus reticulata*) peel by hydrothermal liquefaction and process optimization. *Biomass Conversion and Biorefinery*, 12(1), 183–194. <https://doi.org/10.1007/s13399-021-01383-3>
- do Couto Fraga, A., de Almeida, M. B. B., & Sousa-Aguiar, E. F. (2021). Hydrothermal liquefaction of cellulose and lignin: a new approach on the investigation of chemical reaction networks. *Cellulose*, 28(4), 2003–2020. <https://doi.org/10.1007/s10570-020->

- Durak, H. (2019). Characterization of products obtained from hydrothermal liquefaction of biomass (*Anchusa azurea*) compared to other thermochemical conversion methods. *Biomass Conversion and Biorefinery*, 9(2), 459–470. <https://doi.org/10.1007/s13399-019-00379-4>
- Durak, H. (2020). Hydrothermal liquefaction of *Glycyrrhiza glabra* L. (Liquorice): Effects of catalyst on variety compounds and chromatographic characterization. *Energy Sources, Part A: Recovery, Utilization and Environmental Effects*, 42(20), 2471–2484. <https://doi.org/10.1080/15567036.2019.1607947>
- Durak, H., & Genel, S. (2020). Catalytic hydrothermal liquefaction of *lactuca scariola* with a heterogeneous catalyst: The investigation of temperature, reaction time and synergistic effect of catalysts. *Bioresource Technology*, 309(March), 123375. <https://doi.org/10.1016/j.biortech.2020.123375>
- Dyer, A. C., Nahil, M. A., & Williams, P. T. (2022). Biomass:polystyrene co-pyrolysis coupled with metal-modified zeolite catalysis for liquid fuel and chemical production. *Journal of Material Cycles and Waste Management*, 24(2), 477–490. <https://doi.org/10.1007/s10163-021-01334-0>
- Eboibi, B. E., Lewis, D. M., Ashman, P. J., & Chinnasamy, S. (2014). Effect of operating conditions on yield and quality of biocrude during hydrothermal liquefaction of halophytic microalga *Tetraselmis* sp. *Bioresource Technology*, 170, 20–29. <https://doi.org/10.1016/j.biortech.2014.07.083>
- Faturachman, I., Kurniawan, H. H., Yunarti, R. T., Widjaya, R. R., Dwiatmoko, A. A., Maryati, Y., & Rinaldi, N. (2022). Pd–Ni bimetallic nanoparticles supported on TiO₂ as an efficient catalyst for catalytic transfer hydrodeoxygenation of guaiacol. *Canadian Journal of Chemistry*, 100(8), 583 – 588. <https://doi.org/10.1139/cjc-2021-0330>
- Feng, L., Li, X., Wang, Z., & Liu, B. (2021). Catalytic hydrothermal liquefaction of lignin for production of aromatic hydrocarbon over metal supported mesoporous catalyst. *Bioresource Technology*, 323(December 2020), 1-9. <https://doi.org/10.1016/j.biortech.2020.124569>

- Fernandes, A. C., Biswas, B., Kumar, J., Bhaskar, T., & Muraleedharan, U. D. (2021). Valorization of the red macroalga *Gracilaria corticata* by hydrothermal liquefaction: Product yield improvement by optimization of process parameters. *Bioresource Technology Reports*, 15(June), 1-8. <https://doi.org/10.1016/j.biteb.2021.100796>
- Galebach, P. H., McClelland, D. J., Eagan, N. M., Wittrig, A. M., Buchanan, J. S., Dumesic, J. A., & Huber, G. W. (2018). Production of Alcohols from Cellulose by Supercritical Methanol Depolymerization and Hydrodeoxygenation. *ACS Sustainable Chemistry and Engineering*, 6(3), 4330–4344. <https://doi.org/10.1021/acssuschemeng.7b04820>
- Gao, Y., Yang, Y., Qin, Z., & Sun, Y. (2016). Factors affecting the yield of bio-oil from the pyrolysis of coconut shell. *SpringerPlus*, 5(1), 1-8. <https://doi.org/10.1186/s40064-016-1974-2>
- Gollakota, A. R. K., Kishore, N., & Gu, S. (2018). A review on hydrothermal liquefaction of biomass. *Renewable and Sustainable Energy Reviews*, 81(1), 1378–1392. <https://doi.org/10.1016/j.rser.2017.05.178>
- Gollakota, A. R. K., Reddy, M., Subramanyam, M. D., & Kishore, N. (2016). A review on the upgradation techniques of pyrolysis oil. *Renewable and Sustainable Energy Reviews*, 58, 1543–1568. <https://doi.org/10.1016/j.rser.2015.12.180>
- Gopale, S. B., Kakade, G. N., Kulkarni, G. D., Vinayak, V., Jadhav, S. P., & Jadhav, K. M. (2020). X-ray diffraction, infrared and magnetic studies of NiFe₂O₄ nanoparticles. *Journal of Physics: Conference Series*, 1644(1), 1-5. <https://doi.org/10.1088/1742-6596/1644/1/012010>
- Gouda, M. S., Shehab, M., Helmy, S., Soliman, M., & Salama, R. S. (2023). Nickel and cobalt oxides supported on activated carbon derived from willow catkin for efficient supercapacitor electrode. *Journal of Energy Storage*, 61(February), 1-12. <https://doi.org/10.1016/j.est.2023.106806>
- Guo, L., Tian, Y., He, X., Qiao, C., & Liu, G. (2022). Hydrodeoxygenation of phenolics over uniformly dispersed Pt–Ni alloys supported by self-pillared ZSM–5 nanosheets. *Fuel*, 322, 8-23. <https://doi.org/10.1016/j.fuel.2022.124082>
- Halleraker, H. V., Ghoreishi, S., & Barth, T. (2020). Investigating reaction pathways for formic

- acid and lignin at HTL conditions using ^{13}C -labeled formic acid and ^{13}C NMR. *Results in Chemistry*, 2, 1-8. <https://doi.org/10.1016/j.rechem.2019.100019>
- Hao, B., Xu, D., Jiang, G., Sabri, T. A., Jing, Z., & Guo, Y. (2021). Chemical reactions in the hydrothermal liquefaction of biomass and in the catalytic hydrogenation upgrading of biocrude. *Green Chemistry*, 23(4), 1562–1583. <https://doi.org/10.1039/d0gc02893b>
- Hartanto, D., Kurniawati, R., Pambudi, A. B., Utomo, W. P., Leaw, W. L., & Nur, H. (2019). One-pot non-template synthesis of hierarchical ZSM-5 from kaolin source. *Solid State Sciences*, 87(January), 150–154. <https://doi.org/10.1016/j.solidstatesciences.2018.11.015>
- Hartati, Trisunaryanti, W., Mukti, R. R., Kartika, I. A., Firda, P. B. D., Sumbogo, S. D., Prasetyoko, D., & Bahruji, H. (2020). Highly selective hierarchical ZSM-5 from kaolin for catalytic cracking of Calophyllum inophyllum oil to biofuel. *Journal of the Energy Institute*, 93(6), 2238–2246. <https://doi.org/10.1016/j.joei.2020.06.006>
- He, Z., Zhang, F., Tu, R., Jia, Z., Cheng, S., Sun, Y., Wu, Y., Shen, X., Jiang, E., & Xu, X. (2020). The influence of torrefaction on pyrolysed biomass: The relationship of bio-oil composition with the torrefaction severity. *Bioresource Technology*, 314(June), 1-13. <https://doi.org/10.1016/j.biortech.2020.123780>
- Hiejima, Y., & Yao, M. (2003). Dielectric relaxation of lower alcohols in the whole fluid phase. *Journal of Chemical Physics*, 119(15), 7931–7942. <https://doi.org/10.1063/1.1609981>
- Holgado, J. P., Alvarez, R., & Munuera, G. (2000). Study of CeO_2 XPS spectra by factor analysis: Reduction of CeO_2 . *Applied Surface Science*, 161(3), 301–315. [https://doi.org/10.1016/S0169-4332\(99\)00577-2](https://doi.org/10.1016/S0169-4332(99)00577-2)
- Hornung, A., & Stenzel, F. (2019). Biochar - just a black matter is not enough! Biochar II: Production, Characterization and Applications. *Biomass Conversion and Biorefinery*, 1-12. <https://doi.org/10.1007/s13399-021-01284-5>
- Hsuan, C. Y., Hou, S. S., Wang, Y. L., & Lin, T. H. (2019). Water-In-Oil emulsion as boiler fuel for Reduced NO_x emissions and improved energy saving. *Energies*, 12(6), 1–14. <https://doi.org/10.3390/en12061002>
- Hu, Y., Gu, Z., Li, W., & Xu, C. (Charles). (2020). Alkali-catalyzed liquefaction of pinewood

- sawdust in ethanol/water co-solvents. *Biomass and Bioenergy*, 134(December 2019), 1-11. <https://doi.org/10.1016/j.biombioe.2020.105485>
- Huang, X., Korányi, T. I., Boot, M. D., & Hensen, E. J. M. (2014). Catalytic depolymerization of lignin in supercritical ethanol. *ChemSusChem*, 7(8), 2276–2288. <https://doi.org/10.1002/cssc.201402094>
- Janampelli, S., & Darbha, S. (2018). Selective and reusable Pt-WO_x/Al₂O₃ catalyst for deoxygenation of fatty acids and their esters to diesel-range hydrocarbons. *Catalysis Today*, 309, 219–226. <https://doi.org/10.1016/j.cattod.2017.06.030>
- Jayaseelan, C., Abdul Rahuman, A., Ramkumar, R., Perumal, P., Rajakumar, G., Vishnu Kirthi, A., Santhoshkumar, T., & Marimuthu, S. (2014). Effect of sub-acute exposure to nickel nanoparticles on oxidative stress and histopathological changes in Mozambique tilapia, *Oreochromis mossambicus*. *Ecotoxicology and Environmental Safety*, 107(September 2017), 220–228. <https://doi.org/10.1016/j.ecoenv.2014.06.012>
- Jeong, S., Yang, S., & Kim, D. H. (2017). Depolymerization of Protobind lignin to produce monoaromatic compounds over Cu/ZSM-5 catalyst in supercritical ethanol. *Molecular Catalysis*, 442, 140–146. <https://doi.org/10.1016/j.mcat.2017.09.010>
- Jia, P., Wang, J., & Zhang, W. (2021). Catalytic hydrothermal liquefaction of lignin over carbon nanotube supported metal catalysts for production of monomeric phenols. *Journal of the Energy Institute*, 94, 1–10. <https://doi.org/10.1016/j.joei.2020.09.014>
- Joseph, J., Rasmussen, M. J., Fecteau, J. P., Kim, S., Lee, H., Tracy, K. A., Jensen, B. L., Frederick, B. G., & Stemmler, E. A. (2016). Compositional Changes to Low Water Content Bio-oils during Aging: An NMR, GC/MS, and LC/MS Study. *EEnergy and Fuels*, 1-16. <https://doi.org/10.1021/acs.energyfuels.6b00238>
- Jun, C. H., Huh, C. W., & Na, S. J. (1998). Direct Synthesis of Ketones from Primary Alcohols and 1-Alkenes. *Angewandte Chemie - International Edition*, 37(1–2), 145–147. [https://doi.org/10.1002/\(SICI\)1521-3773\(19980202\)37:1/2<145::AID-ANIE145>3.0.CO;2-0](https://doi.org/10.1002/(SICI)1521-3773(19980202)37:1/2<145::AID-ANIE145>3.0.CO;2-0)
- Kalamaras, C., Palomas, D., Bos, R., Horton, A., Crimmin, M., & Hellgardt, K. (2016). Selective Oxidation of Methane to Methanol over Cu- And Fe-Exchanged Zeolites: The

- Effect of Si/Al Molar Ratio. *Catalysis Letters*, 146(2), 483–492. <https://doi.org/10.1007/s10562-015-1664-7>
- Kamil, M. S. M., & Cheralathan, K. K. (2020). Facile synthesis of hydrothermally stable mesoporous ZSM-5 zeolite from Al- SBA-16 via steam assisted crystallization. *Journal of Porous Materials*, 27(2), 587–601. <https://doi.org/10.1007/s10934-019-00839-2>
- Kazmi, W. W., Amini, G., Park, J. Y., & Lee, I. G. (2024). Catalytic upgrading of the heavy fraction of waste coffee grounds pyrolysis bio-oil using supercritical ethanol as a hydrogen source to produce marine biofuel. *Chemical Engineering Science*, 287(January), 1-13. <https://doi.org/10.1016/j.ces.2024.119761>
- Kazmi, W. W., Park, J. Y., Amini, G., & Lee, I. G. (2023). Upgrading of esterified bio-oil from waste coffee grounds over MgNiMo/activated charcoal in supercritical ethanol. *Fuel Processing Technology*, 250(April), 1-12. <https://doi.org/10.1016/j.fuproc.2023.107915>
- Khampuang, K., Boreriboon, N., & Prasassarakich, P. (2015). Alkali catalyzed liquefaction of corncob in supercritical ethanol-water. *Biomass and Bioenergy*, 83, 460–466. <https://doi.org/10.1016/j.biombioe.2015.10.022>
- Khasri, A., Ridzuan, M., Jamir, M., Sulaiman, M. H., Amran, T., & Abdullah, T. (2012). Slow Pyrolysis Of Imperata Cylindrica In a Fixed Bed Reactor. Doctoral dissertation, Universiti Teknologi Malaysia
- Kim, J. Y., Lee, H. W., Lee, S. M., Jae, J., & Park, Y. K. (2019). Overview of the recent advances in lignocellulose liquefaction for producing biofuels, bio-based materials and chemicals. *Bioresource Technology*, 279(November 2018), 373–384. <https://doi.org/10.1016/j.biortech.2019.01.055>
- Kleinert, M., & Barth, T. (2008). Phenols from lignin. *Chemical Engineering and Technology*, 31(5), 736–745. <https://doi.org/10.1002/ceat.200800073>
- Klinger, J. L., Westover, T. L., Emerson, R. M., Williams, C. L., Hernandez, S., Monson, G. D., & Ryan, J. C. (2018). Effect of biomass type, heating rate, and sample size on microwave-enhanced fast pyrolysis product yields and qualities. *Applied Energy*, 228(June), 535–545. <https://doi.org/10.1016/j.apenergy.2018.06.107>

- Koley, S., Khadase, M. S., Mathimani, T., Raheman, H., & Mallick, N. (2018). Catalytic and non-catalytic hydrothermal processing of *Scenedesmus obliquus* biomass for bio-crude production – A sustainable energy perspective. *Energy Conversion and Management*, 163(February), 111–121. <https://doi.org/10.1016/j.enconman.2018.02.052>
- Kretzschmar, N., Busse, O., & Seifert, M. (2024). Controlling the reaction network of Ni/silica derived conversion of bio-oil surrogate guaiacol. *Carbon Resources Conversion*, 7(1), 1-13. <https://doi.org/10.1016/j.crcon.2023.05.006>
- Kubička, D., Horáček, J., Setnička, M., Bulánek, R., Zukal, A., & Kubičková, I. (2014). Effect of support-active phase interactions on the catalyst activity and selectivity in deoxygenation of triglycerides. *Applied Catalysis B: Environmental*, 145, 101–107. <https://doi.org/10.1016/j.apcatb.2013.01.012>
- Kumar, A., Daw, P., & Milstein, D. (2022). Homogeneous Catalysis for Sustainable Energy: Hydrogen and Methanol Economies, Fuels from Biomass, and Related Topics. *Chemical Reviews*, 122(1), 385–441. <https://doi.org/10.1021/acs.chemrev.1c00412>
- Kumar, N. (2017). Oxidative stability of biodiesel: Causes, effects and prevention. *Fuel*, 190, 328–350. <https://doi.org/10.1016/j.fuel.2016.11.001>
- Kurnia, I., Karnjanakom, S., Bayu, A., Yoshida, A., Rizkiana, J., Prakoso, T., Abudula, A., & Guan, G. (2017). In-situ catalytic upgrading of bio-oil derived from fast pyrolysis of lignin over high aluminum zeolites. *Fuel Processing Technology*, 167(June), 730–737. <https://doi.org/10.1016/j.fuproc.2017.08.026>
- Labeckas, G., Slavinskas, S., & Kanapkienė, I. (2017). The individual effects of cetane number, oxygen content or fuel properties on the ignition delay, combustion characteristics, and cyclic variation of a turbocharged CRDI diesel engine – Part 1. *Energy Conversion and Management*, 148(2017), 1003–1027. <https://doi.org/10.1016/j.enconman.2017.06.050>
- Lahiri, I., Oh, S. M., Hwang, J. Y., Kang, C., Choi, M., Jeon, H., Banerjee, R., Sun, Y. K., & Choi, W. (2011). Ultrathin alumina-coated carbon nanotubes as an anode for high capacity Li-ion batteries. *Journal of Materials Chemistry*, 21(35), 13621–13626. <https://doi.org/10.1039/c1jm11474c>
- Lai, F. ying, Chang, Y. chao, Huang, H. jun, Wu, G. qiang, Xiong, J. bo, Pan, Z. qian, & Zhou,

- C. fei. (2018). Liquefaction of sewage sludge in ethanol-water mixed solvents for bio-oil and biochar products. *Energy*, 148, 629–641. <https://doi.org/10.1016/j.energy.2018.01.186>
- Leng, L., Zhang, W., Peng, H., Li, H., Jiang, S., & Huang, H. (2020). Nitrogen in bio-oil produced from hydrothermal liquefaction of biomass: A review. *Chemical Engineering Journal*, 401, 1-18. <https://doi.org/10.1016/j.cej.2020.126030>
- Li, N., Bi, Y., Xia, X., Chen, H., & Hu, J. (2017). Hydrodeoxygenation of methyl laurate over Ni catalysts supported on hierarchical HZSM-5 zeolite. *Catalysts*, 7(12), 1-13. <https://doi.org/10.3390/catal7120383>
- Li, X., Yan, B., Zhang, J., Xu, N., Tao, J., Zhang, R., Liu, B., Sun, Z., & Chen, G. (2018). Hydrogen production by aqueous phase reforming of phenol derived from lignin pyrolysis over NiCe/ZSM-5 catalysts. *International Journal of Hydrogen Energy*, 43(2), 649–658. <https://doi.org/10.1016/j.ijhydene.2017.09.096>
- Li, Y., Zhu, C., Jiang, J., Yang, Z., Feng, W., Li, L., & Guo, Y. (2021). Bioresource Technology Catalytic hydrothermal liquefaction of Gracilaria corticata macroalgae: Effects of process parameter on bio-oil up-gradation. *Bioresource Technology*, 319(August 2020), 124163. <https://doi.org/10.1016/j.biortech.2020.124163>
- Limarta, S. O., Ha, J. M., Park, Y. K., Lee, H., Suh, D. J., & Jae, J. (2018). Efficient depolymerization of lignin in supercritical ethanol by a combination of metal and base catalysts. *Journal of Industrial and Engineering Chemistry*, 57, 45–54. <https://doi.org/10.1016/j.jiec.2017.08.006>
- Liu, B., Wang, Z., & Feng, L. (2021). Effects of reaction parameter on catalytic hydrothermal liquefaction of microalgae into hydrocarbon rich bio-oil. *Journal of the Energy Institute*, 94, 22–28. <https://doi.org/10.1016/j.joei.2020.10.008>
- Liu, C., Kong, L., Wang, Y., & Dai, L. (2018). Catalytic hydrothermal liquefaction of spirulina to bio-oil in the presence of formic acid over palladium-based catalysts. *Algal Research*, 33(May), 156–164. <https://doi.org/10.1016/j.algal.2018.05.012>
- Liu, J., Wei, Y., Li, R., Liu, Y., Yu, H., Zhou, X., Wu, B., Lin, T., & Zhong, L. (2024). Isolated Ni sites anchored on zeolites for direct synthesis of acetic acid from methane oxidative

- carbonylation. *Applied Catalysis B: Environmental*, 350(December 2023), 1–9. <https://doi.org/10.1016/j.apcatb.2024.123951>
- Liu, S. N., Cao, J. P., Zhao, X. Y., Wang, J. X., Ren, X. Y., Yuan, Z. S., Guo, Z. X., Shen, W. Z., Bai, J., & Wei, X. Y. (2019). Effect of zeolite structure on light aromatics formation during upgrading of cellulose fast pyrolysis vapor. *Journal of the Energy Institute*, 92(5), 1567–1576. <https://doi.org/10.1016/j.joei.2018.07.017>
- Liu, S., Wei, W., Wu, S., & Zhang, F. (2020). Preparation of hierarchical porous activated carbons from different industrial lignin for highly efficient adsorption performance. *Journal of Porous Materials*, 27(5), 1523–1533. <https://doi.org/10.1007/s10934-020-00926-9>
- Liu, T., Yang, L., Jiao, H., Jin, Z., Chen, P., Leng, S., & Zhou, W. (2022). Fractional distillation of biocrude from hydrothermal liquefaction of microalgae: Upgrading of fuel properties. *Algal Research*, 68(May), 1-12. <https://doi.org/10.1016/j.algal.2022.102888>
- Liu, X. Y., Huang, M., Ma, H. L., Zhang, Z. Q., Gao, J. M., Zhu, Y. L., Han, X. J., & Guo, X. Y. (2010). Preparation of a carbon-based solid acid catalyst by sulfonating activated carbon in a chemical reduction process. *Molecules*, 15(10), 7188–7196. <https://doi.org/10.3390/molecules15107188>
- Loong, C., Yusup, S., & Udomsap, P. (2014). Stabilization of Empty Fruit Bunch (EFB) derived Bio-oil using Antioxidants. In *24 European Symposium on Computer Aided Process Engineering* (Vol. 33, Issue Heinzerling 2010). Elsevier. <https://doi.org/10.1016/B978-0-444-63456-6.50038-7>
- Lu, J., Zhang, Z., Fan, G., Zhang, L., & Wu, Y. (2020). Enhancement of microalgae bio-oil quality via hydrothermal liquefaction using functionalized carbon nanotubes. *Journal of Cleaner Production*, 285, 1-13. <https://doi.org/10.1016/j.jclepro.2020.124835>
- Ma, Q., Wang, K., Sudibyo, H., Tester, J. W., Huang, G., Han, L., & Goldfarb, J. L. (2021). Production of upgraded biocrude from hydrothermal liquefaction using clays as in situ catalysts. *Energy Conversion and Management*, 247(September), 1-10. <https://doi.org/10.1016/j.enconman.2021.114764>

- Maia, A. A. D., & de Morais, L. C. (2016). Kinetic parameters of red pepper waste as biomass to solid biofuel. *Bioresource Technology*, 204, 157–163. <https://doi.org/10.1016/j.biortech.2015.12.055>
- Malins, K. (2017). Production of bio-oil via hydrothermal liquefaction of birch sawdust. *Energy Conversion and Management*, 144, 243–251. <https://doi.org/10.1016/j.enconman.2017.04.053>
- Manjare, S. D., & Dhingra, K. (2019). Supercritical fluids in separation and purification: A review. *Materials Science for Energy Technologies*, 2(3), 463–484. <https://doi.org/10.1016/j.mset.2019.04.005>
- Martins, F., Felgueiras, C., Smitkova, M., & Caetano, N. (2019). Analysis of fossil fuel energy consumption and environmental impacts in european countries. *Energies*, 12(6), 1–11. <https://doi.org/10.3390/en12060964>
- Matin, N. H., & Aydin, E. (2022). Reviewing the effect of pyrolysis temperature on the fourier-transform infrared spectra of biochars. 2022(2), 160–173. <https://doi.org/10.2478/ahr-2022-0020>
- Meng, Q., Hou, M., Liu, H., Song, J., & Han, B. (2017). Synthesis of ketones from biomass-derived feedstock. *Nature Communications*, 8, 1-8. <https://doi.org/10.1038/ncomms14190>
- Mishra, R. K., Kumar, V., Kumar, P., & Mohanty, K. (2022). Hydrothermal liquefaction of biomass for bio-crude production: A review on feedstocks, chemical compositions, operating parameters, reaction kinetics, techno-economic study, and life cycle assessment. *Fuel*, 316(January), 1-15. <https://doi.org/10.1016/j.fuel.2022.123377>
- Mlonka-m, A., Evangelopoulos, P., Zajemska, M., & Magdziarz, A. (2021). Pyrolysis of agricultural waste biomass towards production of gas fuel and high-quality char : Experimental and numerical investigations. 296(March), 1-9. <https://doi.org/10.1016/j.fuel.2021.120611>
- Mohiuddin, E., Isa, Y. M., Mdleleni, M. M., Sincadu, N., Key, D., & Tshabalala, T. (2016). Synthesis of ZSM-5 from impure and beneficiated Grahamstown kaolin: Effect of kaolinite content, crystallisation temperatures and time. *Applied Clay Science*, 119, 213–

221. <https://doi.org/10.1016/j.clay.2015.10.008>

Mortensen, P. M., Grunwaldt, J. D., Jensen, P. A., Knudsen, K. G., & Jensen, A. D. (2011). A review of catalytic upgrading of bio-oil to engine fuels. *Applied Catalysis A: General*, 407(1–2), 1–19. <https://doi.org/10.1016/j.apcata.2011.08.046>

Munnik, P., De Jongh, P. E., & De Jong, K. P. (2015). Recent Developments in the Synthesis of Supported Catalysts. *Chemical Reviews*, 115(14), 6687–6718. <https://doi.org/10.1021/cr500486u>

Nagappan, S., Bhosale, R. R., Duc, D., Thuy, N., & Chi, L. (2021). Catalytic hydrothermal liquefaction of biomass into bio-oils and other value-added products – A review. *Fuel*, 285(August 2020), 1–19. <https://doi.org/10.1016/j.fuel.2020.119053>

Nakagawa, T., Ozaki, H., Kamitanaka, T., Takagi, H., Matsuda, T., Kitamura, T., & Harada, T. (2003). Reactions of supercritical alcohols with unsaturated hydrocarbons. *Journal of Supercritical Fluids*, 27(3), 255–261. [https://doi.org/10.1016/S0896-8446\(02\)00269-3](https://doi.org/10.1016/S0896-8446(02)00269-3)

Neto, J. M., Komesu, A., Martins, L. H. da S., Gonçalves, V. O. O., Oliveira, J. A. R. de, & Rai, M. (2019). Third generation biofuels: An overview. *Sustainable Bioenergy: Advances and Impacts*, 283–298. <https://doi.org/10.1016/B978-0-12-817654-2.00010-1>

Nguyen, S. T., Le, T. M., & Nguyen, H. Van. (2021). Iron-catalyzed fast hydrothermal liquefaction of *Cladophora socialis* macroalgae into high quality fuel precursor. *Bioresource Technology*, 337, 1–10. <https://doi.org/10.1016/j.biortech.2021.125445>

Nolte, M. W., & Shanks, B. H. (2017). A Perspective on Catalytic Strategies for Deoxygenation in Biomass Pyrolysis. *Energy Technology*, 5(1), 7–18. <https://doi.org/10.1002/ente.-201600096>

Oasmaa, A., & Meier, D. (2015). Norms, Standards, and Legislation for Fast Pyrolysis Bio-oils from Lignocellulosic Biomass. *Energy Fuels*, 2015(29) 2471–2484 <https://doi.org/10.1021/acs.energyfuels.5b00026>

Ochoa, A., Bilbao, J., Gayubo, A. G., & Castaño, P. (2020). Coke formation and deactivation during catalytic reforming of biomass and waste pyrolysis products: A review. *Renewable and Sustainable Energy Reviews*, 119(October), 1–29. <https://doi.org/10.1016/j.rser>

.2019.109600

- Ong, H. C., Chen, W. H., Farooq, A., Gan, Y. Y., Lee, K. T., & Ashokkumar, V. (2019). Catalytic thermochemical conversion of biomass for biofuel production: A comprehensive review. *Renewable and Sustainable Energy Reviews*, 113(July), 1-12. <https://doi.org/10.1016/j.rser.2019.109266>
- Ooi, X. Y., Gao, W., Ong, H. C., Lee, H. V., Juan, J. C., Chen, W. H., & Lee, K. T. (2019). Overview on catalytic deoxygenation for biofuel synthesis using metal oxide supported catalysts. *Renewable and Sustainable Energy Reviews*, 112(December 2018), 834–852. <https://doi.org/10.1016/j.rser.2019.06.031>
- Osman, A. I., Mehta, N., Elgarahy, A. M., Al-Hinai, A., Al-Muhtaseb, A. H., & Rooney, D. W. (2021). Conversion of biomass to biofuels and life cycle assessment: A review. *Environmental Chemistry Letters*, 19(6), 4075–4118. <https://doi.org/10.1007/s10311-021-01273-0>
- Panwar, V., Kumar, P., Bansal, A., Ray, S. S., & Jain, S. L. (2015). PEGylated magnetic nanoparticles (PEG@Fe₃O₄) as cost effective alternative for oxidative cyanation of tertiary amines via C-H activation. *Applied Catalysis A: General*, 498, 25–31. <https://doi.org/10.1016/j.apcata.2015.03.018>
- Papageridis, K. N., Charisiou, N. D., Douvartzides, S., Sebastian, V., Hinder, S. J., Baker, M. A., AlKhoori, S., Polychronopoulou, K., & Goula, M. A. (2020). Promoting effect of CaO-MgO mixed oxide on Ni/γ-Al₂O₃ catalyst for selective catalytic deoxygenation of palm oil. *Renewable Energy*, 162, 1793–1810. <https://doi.org/10.1016/j.renene.2020.09.133>
- Park, C. W., Kim, J. W., Kim, H. U., Park, Y.-K., Lam, S. S., Ha, J.-M., & Jae, J. (2021). Bimetallic Ni-Re catalysts for the efficient hydrodeoxygenation of biomass-derived phenols. *International Journal of Energy Research*, 45(11), 16349 – 16361. <https://doi.org/10.1002/er.6882>
- Park, J. Y., Jeon, W., Lee, J. H., Nam, B., & Lee, I. G. (2019). Effects of supercritical fluids in catalytic upgrading of biomass pyrolysis oil. *Chemical Engineering Journal*, 377, 1-9. <https://doi.org/10.1016/j.cej.2018.11.010>

- Patience, O., Ilo, S., Nkomo, L., Malusi, N., Onisimo, M., & Simatele, M. D. (2022). *Optimisation of process parameters using response surface methodology to improve the liquid fraction yield from pyrolysis of water hyacinth*. 30, 6681–6704. <https://doi.org/10.1007/s11356-022-22639-z>
- Patil, M. L., Lali, A. M., & Dalai, A. K. (2019). Catalytic hydrodeoxygenation of bio-oil model compound for production of fuel grade oil. *Asia-Pacific Journal of Chemical Engineering*, 14(4). <https://doi.org/10.1002/apj.2317>
- Penghui Yan. (2019). *Hydrodeoxygenation of biocrude oil to value-added products. Master's degree of Physical Chemistry (University of Chinese Academy of Science)*.
- Priya, N. S. C., Sandhya, K., & Rajendran, D. N. (2018). Study on Electrical conductivity and Activation Energy of doped Ceria nanostructures. *Electrochemical Energy Technology*, 3(1), 49–53. <https://doi.org/10.1515/eetech-2017-0004>
- Rachel-Tang, D. Y., Islam, A., & Taufiq-Yap, Y. H. (2017). Bio-oil production via catalytic solvolysis of biomass. *RSC Advances*, 7(13), 7820–7830. <https://doi.org/10.1039/c6ra27824h>
- Ratnasari, D. K., Bijl, A., Yang, W., & Jönsson, P. G. (2020). Effect of H-ZSM-5 and Al-MCM-41 proportions in catalyst mixtures on the composition of bio-oil in ex-situ catalytic pyrolysis of lignocellulose biomass. *Catalysts*, 10(8). 1-18. <https://doi.org/10.3390/catal10080868>
- Rezaei, P. S., Oh, D., Hong, Y., Kim, Y. M., Jae, J., Jung, S. C., Jeon, J. K., & Park, Y. K. (2017). In-situ catalytic co-pyrolysis of yellow poplar and high-density polyethylene over mesoporous catalysts. *Energy Conversion and Management*, 151(June), 116–122. <https://doi.org/10.1016/j.enconman.2017.08.073>
- Riaz, A., Kim, C. S., Kim, Y., & Kim, J. (2016). High-yield and high-calorific bio-oil production from concentrated sulfuric acid hydrolysis lignin in supercritical ethanol. *Fuel*, 172, 238–247. <https://doi.org/10.1016/j.fuel.2015.12.051>
- Riyanto, C. A., Ampri, M. S., & Martono, Y. (2020). Synthesis and Characterization of Nano Activated Carbon from Annatto Peels (*Bixa orellana L.*) Viewed from Temperature Activation and Impregnation Ratio of H₃PO₄. *EKSAKTA: Journal of Sciences and Data*

Analysis, May, 44–50. <https://doi.org/10.20885/eksakta.vol1.iss1.art7>

- Rodrigues, S. C., Silva, M. C., Torres, J. A., & Bianchi, M. L. (2020). Use of Magnetic Activated Carbon in a Solid Phase Extraction Procedure for Analysis of 2,4-dichlorophenol in Water Samples. *Water, Air, and Soil Pollution*, 231(6), 1–14. <https://doi.org/10.1007/s11270-020-04610-1>
- Rorrer, J. E., Bell, A. T., & Toste, F. D. (2019). Synthesis of Biomass-Derived Ethers for Use as Fuels and Lubricants. *ChemSusChem*, 12(13), 2835–2858. <https://doi.org/10.1002/cssc.201900535>
- Ross, D. S., & Blessing, J. E. (1979). Alcohols as H-donor media in coal conversion. 2. Base-promoted H-donation to coal by methyl alcohol. *Fuel*, 58(6), 438–442. [https://doi.org/10.1016/0016-2361\(79\)90085-1](https://doi.org/10.1016/0016-2361(79)90085-1)
- Saber, M., Golzary, A., Hosseinpour, M., Takahashi, F., & Yoshikawa, K. (2016). Catalytic hydrothermal liquefaction of microalgae using nanocatalyst. *Applied Energy*, 183, 566–576. <https://doi.org/10.1016/j.apenergy.2016.09.017>
- Saghir, M., Zafar, S., Tahir, A., Ouadi, M., Siddique, B., & Hornung, A. (2019). Unlocking the potential of biomass energy in Pakistan. *Frontiers in Energy Research*, 7(Mar), 1–18. <https://doi.org/10.3389/fenrg.2019.00024>
- Sangnikul, P., Phanpa, C., Xiao, R., Zhang, H., Reubroycharoen, P., Kuchonthara, P., Vitidsant, T., Pattiya, A., & Hinchiranan, N. (2019). Role of copper- or cerium-promoters on NiMo/γ-Al₂O₃ catalysts in hydrodeoxygenation of guaiacol and bio-oil. *Applied Catalysis A: General*, 574, 151 – 160. <https://doi.org/10.1016/j.apcata.2019.02.004>
- Santos, J., Ouadi, M., Jahangiri, H., & Hornung, A. (2019). Integrated intermediate catalytic pyrolysis of wheat husk. *Food and Bioproducts Processing*, 114, 23–30. <https://doi.org/10.1016/j.fbp.2018.11.001>
- Schimming, S. M., Lamont, O. D., König, M., Rogers, A. K., D’Amico, A. D., Yung, M. M., & Sievers, C. (2015). Hydrodeoxygenation of guaiacol over ceria-zirconia catalysts. *ChemSusChem*, 8(12), 2073 – 2083. <https://doi.org/10.1002/cssc.201500317>

- Schmitt, C. C., Raffelt, K., Zimina, A., Krause, B., Otto, T., Rapp, M., Grunwaldt, J. D., & Dahmen, N. (2018). Hydrotreatment of Fast Pyrolysis Bio-oil Fractions Over Nickel-Based Catalyst. *Topics in Catalysis*, 61(15–17), 1769–1782. <https://doi.org/10.1007/s11244-018-1009-z>
- Şenol, O. I., Viljava, T. R., & Krause, A. O. I. (2005). Hydrodeoxygenation of methyl esters on sulphided NiMo/ γ -Al₂O₃ and CoMo/ γ -Al₂O₃ catalysts. *Catalysis Today*, 100(3–4), 331–335. <https://doi.org/10.1016/j.cattod.2004.10.021>
- Serrano-Ruiz, J. C., Braden, D. J., West, R. M., & Dumesic, J. A. (2010). Conversion of cellulose to hydrocarbon fuels by progressive removal of oxygen. *Applied Catalysis B: Environmental*, 100(1–2), 184–189. <https://doi.org/10.1016/j.apcatb.2010.07.029>
- Shafaghat, H., Kim, J. M., Lee, I. G., Jae, J., Jung, S. C., & Park, Y. K. (2019). Catalytic hydrodeoxygenation of crude bio-oil in supercritical methanol using supported nickel catalysts. *Renewable Energy*, 159–166. <https://doi.org/10.1016/j.renene.2018.06.096>
- Shah, Z., Veses, R. C., Vagheti, J. C. P., Amorim, V. D. A., & Silva, R. da. (2019). Preparation of jet engine range fuel from biomass pyrolysis oil through hydrogenation and its comparison with aviation kerosene. *International Journal of Green Energy*, 16(4), 350–360. <https://doi.org/10.1080/15435075.2019.1566730>
- Shakya, R., Whelen, J., Adhikari, S., Mahadevan, R., & Neupane, S. (2015). Effect of temperature and Na₂CO₃ catalyst on hydrothermal liquefaction of algae. *Algal Research*, 12, 80–90. <https://doi.org/10.1016/j.algal.2015.08.006>
- Shu, R., Jiang, H., Xie, L., Liu, X., Yin, T., Tian, Z., Wang, C., & Chen, Y. (2023). Efficient hydrodeoxygenation of lignin-derived phenolic compounds by using Ru-based biochar catalyst coupled with silicotungstic acid. *Renewable Energy*, 202, 1160–1168. <https://doi.org/10.1016/j.renene.2022.11.092>
- Shuping, Z., Yulong, W., Mingde, Y., Kaleem, I., Chun, L., & Tong, J. (2010). Production and characterization of bio-oil from hydrothermal liquefaction of microalgae *Dunaliella tertiolecta* cake. *Energy*, 35(12), 5406–5411. <https://doi.org/10.1016/j.energy.2010.07.013>

- Singh, A., Prajapati, P., Vyas, S., Gaur, V. K., Sindhu, R., Binod, P., Kumar, V., Singhania, R. R., Awasthi, M. K., Zhang, Z., & Varjani, S. (2023). A Comprehensive Review of Feedstocks as Sustainable Substrates for Next-Generation Biofuels. *Bioenergy Research*, 16(1), 105–122. <https://doi.org/10.1007/s12155-022-10440-2>
- Singh, R., Bhaskar, T., Dora, S., & Balagurumurthy, B. (2013). Catalytic hydrothermal upgradation of wheat husk. *Bioresource Technology*, 149, 446–451. <https://doi.org/10.1016/j.biortech.2013.09.092>
- Song, Z., Ren, D., Wang, T., Jin, F., Jiang, Q., & Huo, Z. (2016). Highly selective hydrothermal production of cyclohexanol from biomass-derived cyclohexanone over Cu powder. *Catalysis Today*, 274, 94–98. <https://doi.org/10.1016/j.cattod.2015.11.016>
- Srinivasan, V., Adhikari, S., Chattanathan, S. A., Tu, M., & Park, S. (2014). Catalytic Pyrolysis of Raw and Thermally Treated Cellulose Using Different Acidic Zeolites. *Bioenergy Research*, 7(3), 867–875. <https://doi.org/10.1007/s12155-014-9426-8>
- Steinbusch, K. J. J. (2010). *Liquid biofuel production from volatile fatty acids*.
- Sun, L., Wang, Z., Chen, L., Yang, S., Xie, X., Gao, M., Zhao, B., Si, H., Li, J., & Hua, D. (2020). Catalytic Fast Pyrolysis of Biomass into Aromatic Hydrocarbons over Mo-Modified ZSM-5 Catalysts. *Catalysts*, 10(9), 1–10. <https://doi.org/10.3390/catal10091051>
- Syed, M. W., Kazmi, W. W., Hussain, A., Shah, S. F. A., Kariim, I., Mehdi, A. M., Omer, A., Bhatti, A. H., Eze, F., & Bhatti, U. H. (2024). Lignin Liquefaction: Unraveling the effect of process conditions and sustainable pathways for biofuel production– A comprehensive review. *Energy Conversion and Management*, 313(May), 1-39. <https://doi.org/10.1016/j.enconman.2024.118615>
- Taghvaei, H., & Rahimpour, M. R. (2019). Catalytic hydrodeoxygenation of bio-oil using in situ generated hydrogen in plasma reactor: Effects of alumina supported catalysts and plasma parameters. *Process Safety and Environmental Protection*, 121, 221 – 228. <https://doi.org/10.1016/j.psep.2018.10.020>
- Tao, H. X., Xie, X. A., Tang, C. Z., & Tian, W. G. (2013). Mechanism of ketones formation from cellulose liquefaction in sub- and supercritical ethanol. *Ranliao Huaxue*

- Xuebao/Journal of Fuel Chemistry and Technology*, 41(1), 60–66. [https://doi.org/10.1016/s1872-5813\(13\)60010-9](https://doi.org/10.1016/s1872-5813(13)60010-9)
- Tekin, K., & Karagöz, S. (2013). Non-catalytic and catalytic hydrothermal liquefaction of biomass. *Research on Chemical Intermediates*, 39(2), 485–498. <https://doi.org/10.1007/s11164-012-0572-3>
- TermehYousefi, A., Bagheri, S., Shinji, K., Rouhi, J., Rusop Mahmood, M., & Ikeda, S. (2014). Fast Synthesis of Multilayer Carbon Nanotubes from Camphor Oil as an Energy Storage Material. *BioMed Research International*, 2014, 1-6. <https://doi.org/10.1155/2014/691537>
- Titirici, M. M., Thomas, A., Yu, S. H., Müller, J. O., & Antonietti, M. (2007). A direct synthesis of mesoporous carbons with bicontinuous pore morphology from crude plant material by hydrothermal carbonization. *Chemistry of Materials*, 19(17), 4205–4212. <https://doi.org/10.1021/cm0707408>
- Toor, S. S., Rosendahl, L., & Rudolf, A. (2011). Hydrothermal liquefaction of biomass: A review of subcritical water technologies. *Energy*, 36(5), 2328–2342. <https://doi.org/10.1016/j.energy.2011.03.013>
- Uhler, A. D., Stout, S. A., Douglas, G. S., Healey, E. M., & Emsbo-Mattingly, S. D. (2016). Chemical Character of Marine Heavy Fuel Oils and Lubricants. In *Standard Handbook Oil Spill Environmental Forensics: Fingerprinting and Source Identification: Second Edition* (Second Edi). Elsevier Inc. <https://doi.org/10.1016/B978-0-12-809659-8.00013-9>
- Van Nam, H., Viet, D. Q., Tam, T. T., & Tho, V. D. S. (2020). Chemical composition of pyrolysis oil through thermal decomposition of sugarcane biomass. *Vietnam Journal of Chemistry*, 58(6), 770–778. <https://doi.org/10.1002/vjch.202000077>
- Velaga, B., Doley, R., & Peela, N. R. (2021). Rapid synthesis of hierarchical ZSM-5 zeolites for the reactions involving larger reactant molecules. *Advanced Powder Technology*, 32(4), 1033–1046. <https://doi.org/10.1016/j.appt.2021.02.002>
- Verma, A. M., & Kishore, N. (2017). Platinum catalyzed hydrodeoxygenation of guaiacol in illumination of cresol production: A density functional theory study. *Royal Society Open Science*, 4(11), 1-12. <https://doi.org/10.1098/rsos.170650>

- Vu, X. H., & Armbruster, U. (2019). Designing Hierarchical ZSM-5 Materials for Improved Production of LPG Olefins in the Catalytic Cracking of Triglycerides. *Advances in Materials Science and Engineering*, 2019, 1-7. <https://doi.org/10.1155/2019/3198421>
- Wądrzyk, M., Korzeniowski, Ł., Plata, M., Janus, R., Lewandowski, M., Borówka, G., & Maziarka, P. (2023). Solvothermal Liquefaction of Blackcurrant Pomace in the Water-Monohydroxy Alcohol Solvent System. *Energies*, 16(3), 1–15. <https://doi.org/10.3390/en16031127>
- Wang, G., Li, N., Xing, X., Sun, Y., Zhang, Z., & Hao, Z. (2020). Gaseous adsorption of hexamethyldisiloxane on carbons: Isotherms, isosteric heats and kinetics. *Chemosphere*, 247, 1-9. <https://doi.org/10.1016/j.chemosphere.2020.125862>
- Wang, K., Kim, K. H., & Brown, R. C. (2014). Catalytic pyrolysis of individual components of lignocellulosic biomass. *Green Chemistry*, 16(2), 727–735. <https://doi.org/10.1039/c3gc41288a>
- Wang, Q., Wang, S., Li, X., & Guo, L. (2013). Hydrogen production via acetic acid steam reforming over HZSM-5 and Pd/HZSM-5 catalysts and subsequent mechanism studies. *BioResources*, 8(2), 2897–2909. <https://doi.org/10.15376/biores.8.2.2897-2909>
- Wang, W., Xu, Y., Wang, X., Zhang, B., Tian, W., & Zhang, J. (2018). Bioresource Technology Hydrothermal liquefaction of microalgae over transition metal supported TiO₂ catalyst. *Bioresource Technology*, 250(October 2017), 474–480. <https://doi.org/10.1016/j.biortech.2017.11.051>
- Wang, X., & Chen, J. (2017). Effects of indium on Ni/SiO₂ catalytic performance in hydrodeoxygenation of anisole as model bio-oil compound: Suppression of benzene ring hydrogenation and C-C bond hydrogenolysis. *Cuihua Xuebao/Chinese Journal of Catalysis*, 38(11), 1818–1830. [https://doi.org/10.1016/S1872-2067\(17\)62910-3](https://doi.org/10.1016/S1872-2067(17)62910-3)
- Wang, X., Xie, X. an, Sun, J., & Liao, W. (2019). Effects of liquefaction parameters of cellulose in supercritical solvents of methanol, ethanol and acetone on products yield and compositions. *Bioresource Technology*, 275(December 2018), 123–129. <https://doi.org/10.1016/j.biortech.2018.12.047>

- Wauton, I., & Ogbeide, S. E. (2021). Characterization of pyrolytic bio-oil from water hyacinth (*Eichhornia crassipes*) pyrolysis in a fixed bed reactor. *Biofuels*, 12(8), 899–904. <https://doi.org/10.1080/17597269.2018.1558838>
- Wei, H., Liu, W., Chen, X., Yang, Q., Li, J., & Chen, H. (2019). Renewable bio-jet fuel production for aviation: A review. *Fuel*, 254(January), 1375-1384. <https://doi.org/10.1016/j.fuel.2019.06.007>
- Weyrich, P. A., Treviño, H., Hölderich, W. F., & Sachtler, W. M. H. (1997). Characterization of Ce promoted, zeolite supported Pd catalysts. *Applied Catalysis A: General*, 163(1–2), 31–44. [https://doi.org/10.1016/S0926-860X\(97\)00114-2](https://doi.org/10.1016/S0926-860X(97)00114-2)
- Wu, X., Zhang, J., Li, M., Bian, J., & Peng, F. (2019). Catalytic hydrothermal liquefaction of eucalyptus to prepare bio-oils and product properties. *Energy Conversion and Management*, 199(August), 1-9. <https://doi.org/10.1016/j.enconman.2019.111955>
- Xin, H., Hu, X., Cai, C., Wang, H., Zhu, C., Li, S., Xiu, Z., Zhang, X., Liu, Q., & Ma, L. (2020). Catalytic Production of Oxygenated and Hydrocarbon Chemicals From Cellulose Hydrogenolysis in Aqueous Phase. *Frontiers in Chemistry*, 8(May), 1–20. <https://doi.org/10.3389/fchem.2020.00333>
- Xu, J., Dong, X., & Wang, Y. (2020). Industrial Crops & Products Hydrothermal liquefaction of macroalgae over various solids, basic or acidic oxides and metal salt catalyst: Products distribution and characterization. *Industrial Crops & Products*, 151(April), 1-10. <https://doi.org/10.1016/j.indcrop.2020.112458>
- Xue, X., Liu, Y., Wu, L., Pan, X., Liang, J., & Sun, Y. (2019). Catalytic fast pyrolysis of maize straw with a core–shell ZSM-5@SBA-15 catalyst for producing phenols and hydrocarbons. *Bioresource Technology*, 289(June), 1-7. <https://doi.org/10.1016/j.biortech.2019.121691>
- Yan, H. L., Zong, Z. M., Li, Z. K., Kong, J., Zheng, Q. X., Li, Y., & Wei, X. Y. (2017). Sweet sorghum stalk liquefaction in supercritical methanol: Effects of operating conditions on product yields and molecular composition of soluble fraction. *Fuel Processing Technology*, 155, 42–50. <https://doi.org/10.1016/j.fuproc.2016.02.011>

- Yan, X., Wang, W., Zhao, Y., & Zhou, J. (2018). *The Effect of Different Catalysts and Process Parameters on the Chemical Content of Bio-oils from Hydrothermal Liquefaction of Sugarcane Bagasse*. *Bioresource*, 13(1), 997–1018.
- Yang, Y., Tian, Z., Lan, Y., Wang, S., & Chen, H. (2021). An overview of biofuel power generation on policies and finance environment, applied biofuels, device and performance. *Journal of Traffic and Transportation Engineering (English Edition)*, 8(4), 534–553. <https://doi.org/10.1016/j.jtte.2021.07.002>
- Yao, L., Wang, Y., Galvez, M. E., Hu, C., & da Costa, P. (2017). γ -Alumina-Supported Ni-Mo Carbides as Promising Catalysts for CO₂ Methanation. *Modern Research in Catalysis*, 06(04), 135–145. <https://doi.org/10.4236/mrc.2017.64010>
- Yin, S., & Tan, Z. (2012). Hydrothermal liquefaction of cellulose to bio-oil under acidic , neutral and alkaline conditions. *Applied Energy*, 92, 234–239. <https://doi.org/10.1016/j.apenergy.2011.10.041>
- Yun, J., Kim, S., Jung, W., & Jung, J. C. (2024). Plastic-Derived Solid Acid Catalysts for the Production of Methyl 2-Hydroxyisobutyrate via Esterification. *Korean Journal of Chemical Engineering*, 41, 2297–2306, <https://doi.org/10.1007/s11814-024-00154-w>
- Zhang, J., & Zhang, X. (2019). The thermochemical conversion of biomass into biofuels. In *Biomass, Biopolymer-Based Materials, and Bioenergy: Construction, Biomedical, and other Industrial Applications*. Woodhead Publishing, Elsevier Ltd. 327–368. <https://doi.org/10.1016/B978-0-08-102426-3.00015-1>
- Zhang, L., Li, C. J., Zhou, D., Zhang, S. C., & Chen, J. M. (2013). Hydrothermal liquefaction of water hyacinth: Product distribution and identification. *Energy Sources, Part A: Recovery, Utilization and Environmental Effects*, 35(14), 1349–1357. <https://doi.org/10.1080/15567036.2012.677937>
- Zhang, L., Xu, C. (Charles), & Champagne, P. (2010). Overview of recent advances in thermochemical conversion of biomass. *Energy Conversion and Management*, 51(5), 969–982. <https://doi.org/10.1016/j.enconman.2009.11.038>
- Zhang, M., Hu, Y., Wang, H., Li, H., Han, X., Zeng, Y., & Xu, C. C. (2021). A review of bio-oil upgrading by catalytic hydrotreatment: Advances, challenges, and prospects.

- Molecular Catalysis*, 504(February), 1-11. <https://doi.org/10.1016/j.mcat.2021.111438>
- Zhang, X. (2016). Essential scientific mapping of the value chain of thermochemically converted second-generation bio-fuels. *Green Chemistry*, 18(19), 5086–5117. <https://doi.org/10.1039/c6gc02335e>
- Zhang, X., Lei, H., Chen, S., & Wu, J. (2016). Catalytic co-pyrolysis of lignocellulosic biomass with polymers: A critical review. *Green Chemistry*, 18(15), 4145–4169. <https://doi.org/10.1039/c6gc00911e>
- Zhang, Y., Chen, F., Chen, D., Cen, K., Zhang, J., & Cao, X. (2020). Upgrading of biomass pellets by torrefaction and its influence on the hydrophobicity, mechanical property, and fuel quality. *Biomass Conversion and Biorefinery*, 12(6), 2061–2070. <https://doi.org/10.1007/s13399-020-00666-5>
- Zhang, Y., Li, M., Xing, E., Luo, Y., & Shu, X. (2018). Protective desilication of highly siliceous H-ZSM-5 by sole tetraethylammonium hydroxide for the methanol to propylene (MTP) reaction. *RSC Advances*, 8(66), 37842–37854. <https://doi.org/10.1039/C8RA06786D>
- Zhang, Y., Xue, M., Zhou, Y., Zhang, H., Wang, W., Wang, Q., & Sheng, X. (2016). Propane dehydrogenation over Ce-containing ZSM-5 supported platinum–tin catalysts: Ce concentration effect and reaction performance analysis†. *RSC Advances*, 6(35), 29410–29422. <https://doi.org/10.1039/c6ra04173f>
- Zhang, Y., Zhai, X., Zhang, H., & Zhao, J. (2017). Enhanced selectivity in the conversion of glycerol to pyridine bases over HZSM-5/11 intergrowth zeolite. *RSC Advances*, 7(38), 23647–23656. <https://doi.org/10.1039/c7ra02311a>
- Zhao, B., Li, H., Wang, H., Hu, Y., Gao, J., Zhao, G., Ray, M. B., & Xu, C. C. (2021). Synergistic effects of metallic Fe and other homogeneous/heterogeneous catalysts in hydrothermal liquefaction of woody biomass. *Renewable Energy*, 176, 543–554. <https://doi.org/10.1016/j.renene.2021.05.115>
- Zheng, J. L. (2008). Pyrolysis oil from fast pyrolysis of maize stalk. *Journal of Analytical and Applied Pyrolysis*, 83(2), 205–212. <https://doi.org/10.1016/j.jaap.2008.08.005>

- Zheng, Y., Wang, F., Yang, X., Huang, Y., Liu, C., Zheng, Z., & Gu, J. (2017). Study on aromatics production via the catalytic pyrolysis vapor upgrading of biomass using metal-loaded modified H-ZSM-5. *Journal of Analytical and Applied Pyrolysis*, 126(May), 169–179. <https://doi.org/10.1016/j.jaap.2017.06.011>
- Zheng, Y., Wang, J., Wang, Y., Zhou, H., Pu, Z., Yang, Q., & Huang, W. (2020). The combination of MoS₂/WO₃ and its adsorption properties of methylene blue at low temperatures. *Molecules*, 25(1), 1–13. <https://doi.org/10.3390/molecules25010002>
- Zhu, Z., Toor, S. S., Rosendahl, L., Yu, D., & Chen, G. (2015). Influence of alkali catalyst on product yield and properties via hydrothermal liquefaction of barley straw. *Energy*, 80, 284–292. <https://doi.org/10.1016/j.energy.2014.11.071>
- Zormpa, F. F., Margellou, A. G., Karakoulia, S. A., Delli, E., & Triantafyllidis, K. S. (2024). Hydrodeoxygenation of lignin bio-oil model compounds and surrogate mixtures over zeolite supported nickel catalysts. *Catalysis Today*, 433, 1-8. <https://doi.org/10.1016/j.cattod.2024.114654>

RESEARCH OUTPUTS

(i) Publication papers

- Kariim, I., Park, J. Y., Kazmi, W. W., Swai, H., Lee, I. G., & Kivevele, T. (2024). Solvothermal liquefaction of orange peels into biocrude: An experimental investigation of biocrude yield and energy compositional dependency on process variables. *Bioresource Technology*, 391, 129928. <https://doi.org/10.1016/j.biortech.2023.129928>
- Kariim, I., Swai, H., & Kivevele, T. (2023). Bio-Oil Upgrading over ZSM-5 Catalyst: A Review of Catalyst Performance and Deactivation. *International Journal of Energy Research*, 2023(1), 1-33. <https://doi.org/10.1155/2023/4776962>
- Kariim, I., Waidi, Y. O., Swai, H., & Kivevele, T. (2023). Catalytic hydrothermal liquefaction of orange peels into biocrude: An optimization approach by central composite design. *Journal of Analytical and Applied Pyrolysis*, 173, 106032. <https://doi.org/10.1016/j.jaap.2023.106032>
- Kariim, I., Swai, H., & Kivevele, T. (2022). Recent advances in thermochemical conversion of biomass into drop-in fuel: A review. *Scientific African*, 17, 1-27. <https://doi.org/10.1016/j.sciaf.2022.e01352>

(ii) Poster Presentation



PASET
Partnership for Applied Sciences,
Engineering & Technology

Solvothermal liquefaction of orange peels and catalytic upgrading of biocrude into transportation fuel over a hybrid catalyst

Ishaq Kariim^{1,2}, Hulda Swai³, In-Gu Lee², Thomas Kivevele¹

¹ School of Materials, Energy, Water, and Environmental Sciences (MEWES), The Nelson Mandela African Institution of Science and Technology (NM-AIST), P.O. Box 447, Tanzania
² Bioresource Circulation Laboratory, Korea Institute of Energy Research (KIER), Yuseong -gu, Daejeon 34129, South Korea
³ School of Life Sciences and Bioengineering (LISBE), Nelson Mandela African Institution of Science and Technology, P.O Box 447, Arusha, Tanzania
 *Contact: kariimi@nm-aist.ac.tz/+2348179612145



Introduction

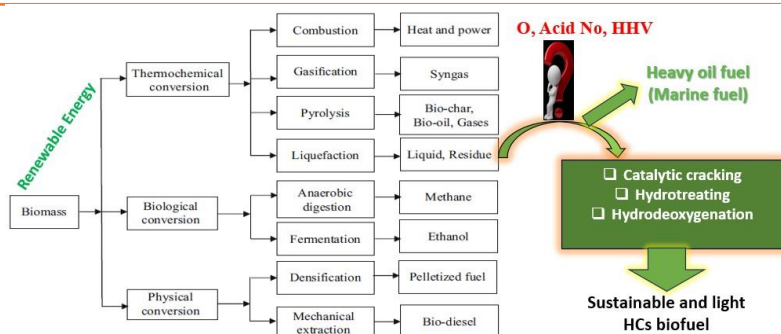


Fig. 1 Alternatives energy sources from biomass valorization

Energy demand and environmental pollution have been a major challenge in the present world due to the overdependence on the conventional fuel. The valorization of biomass via solvothermal liquefaction process produces biocrude with high oxygen contents which retards its direct application in the combustion engine. The removal of oxygen is essential to portray biomass as an excellent and eco-friendly energy source.

Materials and Methods



Fig. 2: Ni/kaolin catalyst synthesis

- ❖ Wet impregnation method was adopted
- ❖ The drying process removes water molecules
- ❖ The calcination process decomposes the nitrates

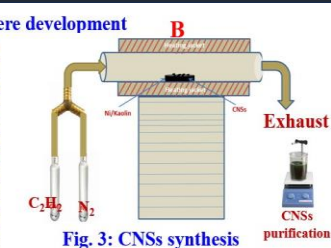


Fig. 3: CNSs synthesis

- ❖ The catalyst enhances the carbon nucleation
- ❖ N₂ serves as a purge/carrier gas
- ❖ Acetylene serves as carbon source

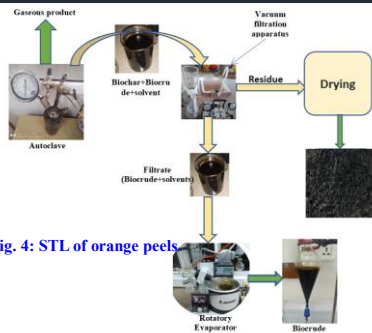


Fig. 4: STL of orange peels

Results and Discussion

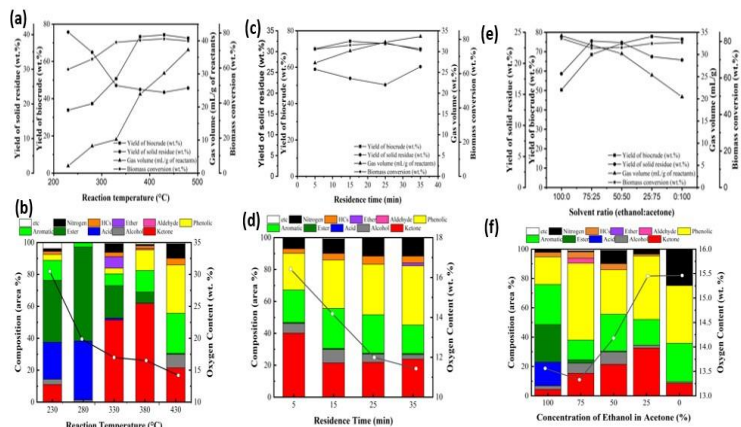


Fig. 4: Effects of reaction temperature on (a) bio-products' yield (b) biocrude compositions; residence time on: (c) bio-products' yield (d) biocrude compositions and solvent ratio on: (e) bio-products' yield (f) biocrude compositions.

Conclusion

- ❖ The noncatalytic STL produced high HHV of 38.81 KJ/kg at 430 °C, 35 mins and 50:50 EtOH: Acetone
- ❖ The NiCeMo supported HZSM-5-CNSs promotes HCs formation, and adversely affects the HHV due to side reactions

Acknowledgement

This work was funded by the Partnership for Applied Sciences, Engineering, & Technology-Regional Scholarship and Innovation Fund (PASET- RSIF)